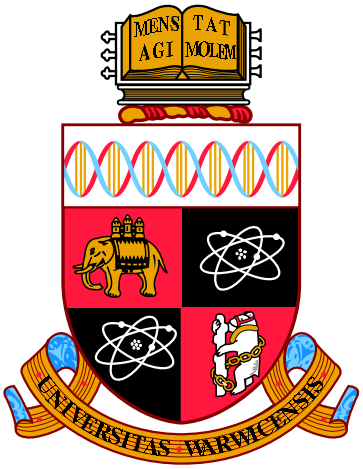

Fluctuation-driven firing in spatially extended neuron models

by

Robert Gowers

Thesis

Submitted to the University of Warwick

for the degree of

Doctor of Philosophy

Mathematics for Real-World Systems Centre for Doctoral Training

November 2019

Contents

Acknowledgments

I would like to thank my supervisors Magnus Richardson and Yulia Timofeeva for their guidance and expertise over the course of my PhD. I would also like to acknowledge everyone in MathSys for creating an enjoyable and productive environment. In particular, I would like to thank Sami Al-Izzi and Roger Hill for reading through drafts of my thesis.

Declarations

I declare this thesis to be my own original work.

Many of the results from Chapter 2 can be found in the pre-print, *Low-rate firing limit for neurons with axon, soma and dendrites driven by spatially distributed stochastic synapses* (RP Gowers, Y Timofeeva, MJE Richardson), which is currently under review.

Similarly, an article using the results from Chapter 3 is in preparation, titled *How neuronal structure affects the dynamic firing-rate response* (RP Gowers, Y Timofeeva, MJE Richardson), which is due to be submitted shortly.

The findings in Chapters 4 and 5 are also currently in preparation for a journal article, *The effect of linearised active currents on fluctuation-driven firing in spatial-neuron models* (RP Gowers, Y Timofeeva, MJE Richardson).

Abstract

This thesis explores how spatially extended neuron models integrate synaptic drive and how morphology affects the firing-rate response. Particular emphasis is placed on the low-rate limit that represents the activity of most cortical neurons. Chapter 1 first introduces the basics of neuronal electrophysiology, highlighting how synaptic drive and active currents affect the membrane properties of spatially extended neurons. The second half of the chapter gives an overview of neuronal firing and how a level-crossing approach can be used to approximate the low-rate limit of integrate-and-fire models. With the neuron's dynamics and an approach to approximating the firing rate explained, Chapter 2 starts by examining the calculation of temporal and spatial correlators in the simpler models to give some intuition to how the synaptic drive is integrated. We then proceed to calculate the steady-state upcrossing rate for progressively more complex neuronal morphologies. Next, Chapter 3 investigates how neuronal morphology influences the patterning of the time-varying firing-rate response to sinusoidally modulated synaptic drive. Three different forms of modulation are applied to each model and focus is placed on finite frequency phase zeros of the firing-rate response as this indicates synchrony between the input modulation and the output firing-rate response. Finally in Chapters 4 and 5, we extend the previous analyses for both steady-state and sinusoidally modulated drive to neurons with membranes made quasi-active via linearisation of an active current such as I_h.

Abbreviations and Symbols

Abbreviations

AIS axon initial segment

AMPA α-amino-3-hydroxy-5-methyl-4-isoxazolepropionic acid

AP action potential

EIF exponential integrate-and-fire

EPSP excitatory postsynaptic potential

GABA γ-aminobutyric acid

IF integrate-and-fire

IPSP inhibitory postsynaptic potential

LIF leaky integrate-and-fire

QIF quadratic integrate-and-fire

SDE stochastic differential equation

SPDE stochastic partial differential equation

Mathematical Symbols

Quantity	Description	Typical units
E_L	Leak current reversal potential	mV
V	Transmembrane potential	mV
v	Transmembrane potential measured from E_L	mV
τ_v	Membrane time constant	ms
τ_s	Synaptic time constant	ms
σ_{WN}	Intensity of white synaptic noise	mV
σ_s	Intensity of coloured synaptic noise	mV
β_s	Relative synaptic time constant τ_s/τ_v	-
μ	Mean component of synaptic drive	mV
λ_j	Electrotonic length constant of neurite j	μm
G_{λ_j}	Characteristic conductance of a neurite j	nS
ρ_j	Ratio of G_λ for neurite j to the somatic leak conductance	-
β_σ	Relative somatic time constant τ_σ/τ_v	-
β_α	Relative axonal time constant τ_α/τ_v	-
τ_w	Quasi-active time constant	ms
κ	Quasi-active coupling parameter	-
β_w	Relative quasi-active time constant	-
X_{th}	Dimensionfull trigger position for firing initiation	μm
x_{th}	Dimensionless trigger position for firing initiation	-
v_{th}	Threshold potential measured from E_L	mV
v_{re}	Reset potential measured from E_L	mV
σ_v	Standard deviation of the membrane potential	mV
$\sigma_{\dot{v}}$	Standard deviation of $\partial v/\partial t$	mV
r_0	Steady-state mean upcrossing rate	Hz
Λ	Magnitude of modulated upcrossing rate relative to r_0	-
ψ	Phase of modulated upcrossing rate relative to input modulation	-

Chapter 1

Neuronal Anatomy and Electrophysiology

1.1 Motivation

Computational neuroscience is a broad discipline which seeks to understand various aspects of the nervous system via data analysis, statistics, modelling and simulations. It covers a range of spatial scales from the whole brain to molecular dynamics at ion channels, as shown in Figure 1.1. There are numerous applications of the field, from improving understanding and thus treatment for neuropathologies such as epilepsy, schizophrenia, and Parkinson's disease [1–3]; and also translating how the nervous system learns and computes to create better artificial intelligence systems [4]. The diversity of scale, approaches and applications attracts many researchers from a range of backgrounds to the field.

Being able to predict how neuronal populations convert input signals into their output activity is fundamental to understanding neuronal function. Modelling approaches have considered the constituent neurons in the population to have similar (or identical) properties with the population activity being taken as the output [5–9]. The integrative properties of the constituent neurons thus determine the overall output activity. Most studies to date have considered these constituent cells with a point-like structure or as two compartments [10–12].

This thesis considers theoretical models of single neurons with spatial structure. These model neurons are considered representative of a wider population. By creating a framework to calculate the activity of these neurons, we infer the effect that neuronal morphology has on how the population processes input signals.

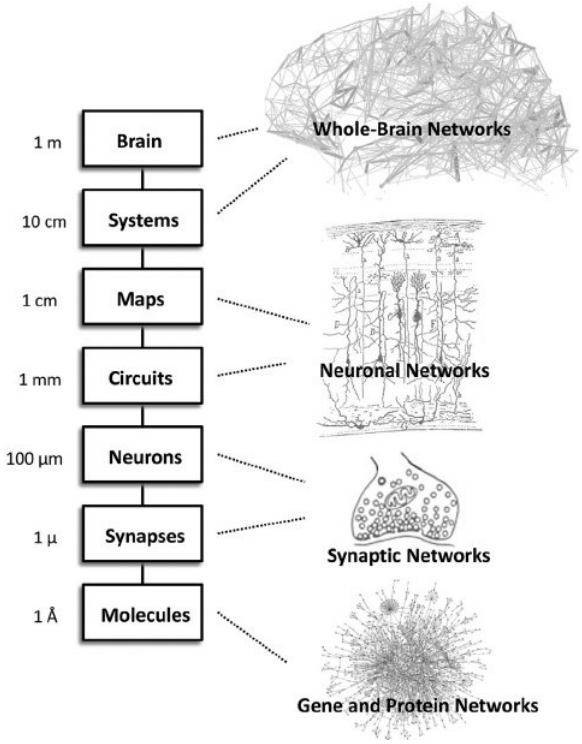

Figure 1.1: The different spatial scales investigated by computational neuroscience. This thesis focuses on modelling at the single neuron level. Image from [13].

1.2 Neuronal Structure

Observations by Cajal in the late 19th century using Golgi's staining method first revealed that not only are neurons discrete cells, but also that they have an intricate branching structure [14]. In general, dendrites emanate in a tree-like fashion from the cell body (the soma), as we can see from the various dendritic arbours shown in Figure 1.2. The axon also usually originates from the soma, but it has occasionally been observed to branch off a dendrite, especially in certain types of cells [15, 16]. What differentiates the axon from the dendrites is the presence of presynaptic terminals containing neurotransmitters at various positions along its length. These are positioned close to areas on other neurons (typically dendrites), forming chemical synapses.

In brief, the dendrites receive inputs from other neurons, which are integrated in the axon initial segment (AIS), yielding an output signal which is transmitted by the axon to other neurons. However, we must note that this is an over-simplification for numerous reasons, such as: the existence of electrical synapses between dendrites (and between axons [17]), the fact that dendrites themselves are capable of process-

ing information by various means [18–22], axons from chandelier cells form synapses onto other axons [23], and that neurons may influence each other via the electric fields created by their transmembrane currents [24].

While the framework outlined in this thesis can in principle be applied to any neuronal structure, we outline a few neuronal classes in the cerebral cortex for context. Cortical cells are functionally interesting because they are involved in various important tasks, including processing sensory information (visual [25], auditory, [26], olfactory [27]), and cognitive processes [25] (e.g. working memory [28]).

Pyramidal neurons, named due to the pyramidal shape of the cell body, are the principal cortical excitatory cells, comprising ∼75% of all neurons in the mammalian cortex [29]. These cells are highly extended neurons with a long apical dendritic trunk, oblique dendrites, apical tuft dendrites, and a multitude of basal dendrites, as shown in Figure 1.2(a, b). Also present in the cortex are various interneurons whose dendrites and axons only project locally rather than to other areas of the brain [23]. Stellate cells are an interneuron type found in layer IV of the cortex and their dendrites form a star-like shape about the soma, Figure 1.2(c). Excitatory synapses are located throughout the dendritic arbour of cortical cells [30], while inhibitory synapses are clustered at specific regions depending on the presynaptic cell type [23]. These cells differ morphologically: between different cortical layers [31, 32], between cells in the same layer [31, 33], and between mammalian species [34, 35].

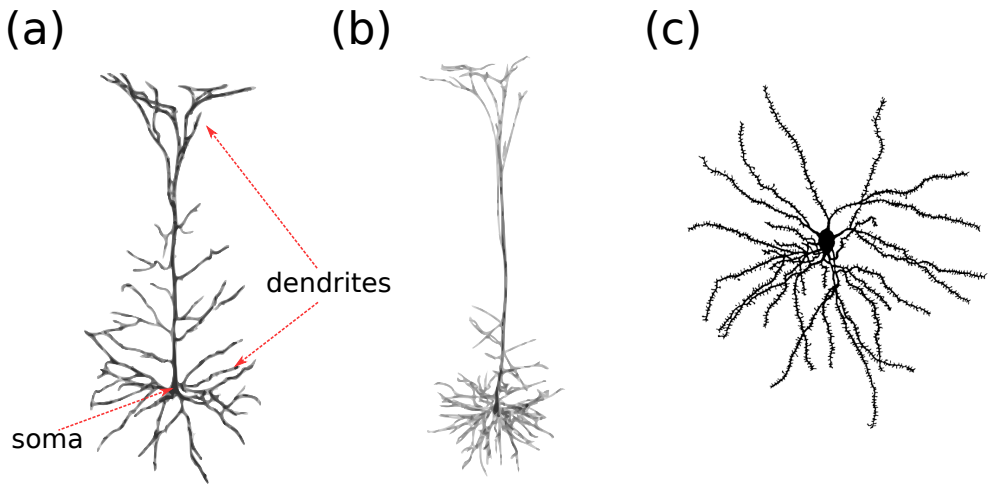

Figure 1.2: Dendritic arbours of different types of neuron: (a) cortical layer 3 and (b) layer 5 pyramidal neurons (from [19]), (c) cortical stellate cell (from [36]).

1.3 Neuronal Electrophysiology

1.3.1 Transmembrane Potential

A neuronal membrane consists of a lipid bilayer that is impermeable to ions inside and outside the cell. Ions such as K^+, Na^+, Cl^- and Ca^{2+} freely exist in the extracellular medium and the intracellular cytoplasm. At certain locations on the membrane are ion channels, which allow specific ionic species to traverse through the membrane. The difference in electrical potential between the intracellular cytoplasm and the extracellular medium, $V = V_i - V_e$, is termed the transmembrane potential. The transmembrane potential is the key state variable for determining neuronal activity, as we shall see later. Due to ionic concentration differences, the transmembrane potential is negative. The concentration differences arise from sodium/potassium pumps, which pump 3 Na^+ out of the cell and 2 K^+ into the cell. In response, we obtain a current for each ionic species from ionic fluxes caused by diffusion (due to concentration gradients) and drift (due to electric charge). The ionic currents collectively sum to zero at equilibrium, resulting in the equilibrium transmembrane potential.

For a single ionic species, j, the potential at which this equilibrium occurs is given by the Nernst potential [37, 38]

$$E_j = \frac{k_B T}{zq} \log\left(\frac{[N_j^+]^e}{[N_j]^i}\right), \tag{1.1}$$

where k_B is the Boltzmann constant, T is the absolute temperature, z is the valency of the ion, q is the elementary charge and $[N_j]^{e,i}$ is the external/internal ionic concentration. As examples $E_{Na^+} \sim 60\text{mV}$ and $E_{K^+} \sim -80\text{mV}$. With multiple ionic species, the equilibrium potential is described by the Goldman-Hodgkin-Katz voltage equation, which is akin to the logarithm of the weighted sum of the concentrations for all the constituent species [39, 40].

1.3.2 Transmembrane Currents

Denoting a channel's conductance as G_j, the outward current I_j through a given channel can often be approximated as Ohmic

$$I_j = G_j(V - E_j), \tag{1.2}$$

where E_j is called the reversal potential of the channel. Multiple (n) Ohmic currents written as (1.2) can be combined into an overall membrane leakage current I_L with

effective conductance G_L and reversal potential E_L

$$I_L = G_L(V - E_L), \tag{1.3}$$

where G_L is simply the sum of the n component conductances and $E_L \sim -70$ mV [41, 42] is the weighted average of the n reversal potentials

$$G_L = \sum_{j=1}^{n} G_j, \quad E_L = \frac{\sum_{j=1}^{n} G_j E_j}{G_L}. \tag{1.4}$$

Since the lipid bilayer is an insulator separating two regions of charge, it acts as a capacitor with capacitance C_m. By conservation of current, the capacitive I_c, leakage I_L, and any other outward transmembrane I_add currents sum to zero, and thus for a patch of membrane

$$I_c = C_\mathrm{m}\frac{\mathrm{d}V}{\mathrm{d}T}, \quad C_\mathrm{m}\frac{\mathrm{d}V}{\mathrm{d}T} = G_L(E_L - V) - I_\mathrm{add}. \tag{1.5}$$

From this equation, we define the membrane time constant $\tau_v = C_\mathrm{m}/G_L$.

1.3.3 Axial Current and Cable Equation

As the main objective of this thesis is finding how spatial extent affects neuronal function, we need to look at how the potential changes in space. The various neuron types in Figure 1.2 illustrate that neurons are highly branched structures with neurites far greater in length than radius. Since variations in the transmembrane potential are far greater longitudinally than radially [43], this means that we model each dendrite and axon as a one-dimensional spatial structure. The next assumption we introduce is that the intracellular cytoplasm is a pure Ohmic resistance, resistivity r_a, with no capacitive or inductive properties [44]. We treat the neurite as a cylinder with radius a, capacitance per unit area c_m and transmembrane leak conductance per unit area g_L. All parameters are treated as constant with length, however one can generalise them to vary with length. An example would be the variations in radius resulting from branching and tapering [45–48], but this is beyond the scope of this thesis. First we take a segment of neurite Δ_X which is sufficiently short so that the incoming axial current I_a is equal to the outgoing axial current, as shown in Figure 1.3(a). The axial resistance of this segment is $r_a\Delta_X/(\pi a^2)$ and hence Ohm's law gives the difference in potential across this segment as

$$V(X,T) - V(X+\Delta_X,T) = \frac{r_\mathrm{a}\Delta_X}{\pi a^2} I_\mathrm{a}(X,T), \tag{1.6}$$

which if we rearrange and let $\Delta_X \to 0$ yields

$$I_{\mathrm{a}}(X,T) = -\frac{\pi a^2}{r_{\mathrm{a}}}\frac{\partial V}{\partial X}. \tag{1.7}$$

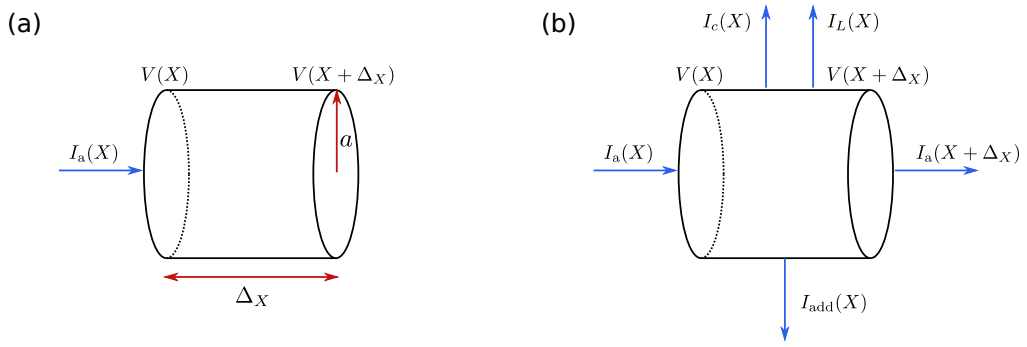

Figure 1.3: Cylindrical sections of length Δ_X showing the axial and transmembrane currents.

To extract the time dependence of V, we consider another section Δ_X long enough such that transmembrane currents are no longer negligible, Figure 1.3(b). With the addition of an arbitrary outward transmembrane $I_{\mathrm{add}}(X,T)$, conservation of current on this section Δ_X gives

$$\frac{\pi a^2}{r_{\mathrm{a}}}\left[\left.\frac{\partial V}{\partial X}\right|_{X+\Delta_X} - \left.\frac{\partial V}{\partial X}\right|_{X}\right] = I_{\mathrm{add}}(X,T) + 2\pi a \Delta_X \left[c_{\mathrm{m}}\frac{\partial V}{\partial T} + g_L(V-E_L)\right]. \tag{1.8}$$

Letting $\Delta_X \to 0$ and defining the electrotonic length constant as $\lambda^2 = a/(2r_{\mathrm{a}}g_{\mathrm{m}})$, we arrive at the uniform cable equation

$$\tau_v \frac{\partial V}{\partial T} = E_L - V + \lambda^2 \frac{\partial^2 V}{\partial X^2} - \frac{I_{\mathrm{add}}}{2\pi a \Delta_X g_L}, \tag{1.9}$$

where the length constant λ represents the length of cable for which the transmembrane conductance and the axial conductance are equal to the characteristic conductance G_λ. A larger value of λ thus means that local changes in potential will spread further along the neurite. Expressing the axial current in terms of the characteristic conductance thus gives

$$I_{\mathrm{a}}(X,T) = -\lambda G_\lambda \frac{\partial V}{\partial X}, \quad G_\lambda = 2\pi a \lambda g_L. \tag{1.10}$$

Mathematically, the cable equation (1.9) is a one-dimensional reaction-diffusion

equation and a special form of the Telegrapher's equation for transmission lines [49]. As shall be detailed in Chapter 2, various methods exist for analysing the cable equation (1.9).

At various points in this thesis we will compare the differences in response between a point-neuron model governed by (1.5) and a spatially extended neuron obeying the cable equation (1.9). In this chapter we will next outline how active currents and synaptic drive can be incorporated into both models.

1.3.4 Active Currents

Voltage-activated currents have a channel conductance which changes in response to the transmembrane potential V. Denoting the proportion of channels of type j which are open at time T as $p_j(V,T)$ and the conductance when all channels are open as $\overline{G}_j$, the active current I_j is given by

$$I_j = p_j(V,T)\overline{G}_j(V - E_j). \tag{1.11}$$

The proportion of open channels p_j may be the product of several gating variables which each take time in adapting to changes in the membrane potential, a formalism introduced in the Hodgkin-Huxley model [50].

An active current of particular interest for this thesis is the depolarising hyperpolarisation-activated current, simply referred to as I_h. I_h channels are opened when V becomes more negative (hyperpolarisation-activated) but have a reversal potential $E_h \sim -40$ mV, greater than the leakage potential $E_L \sim -70$ mV (depolarising) [51–53]. As we shall see later, this provides a form of negative feedback. Since this negative feedback controls the excitability of the neuron, it has been found that enhancing I_h through anticonvulsants may play a role in the treatment of epilepsy [54–56].

I_h channels are common in pyramidal neurons and other neurons such as cerebellar Purkinje cells, with the density of channels increasing with distance from the soma in hippocampal CA1 [57] and cortical layer 5 pyramidal cells [51,58], while in Purkinje cells, the channels are almost uniformly distributed in the dendrites [59]. I_h has been experimentally observed to add subthreshold voltage resonance [60–62], and modelling of I_h has shown that it can explain the electrical field sensitivity resonance observed in the apical dendrites of pyramidal cells [63]. A nonlinear model for I_h is given in terms of a single gating variable $n(V)$ with $p_h = n(V)$ [64]

$$I_h = \overline{G}_h n(V)(V - E_h), \quad \tau_n(V)\frac{\partial n}{\partial T} = n_\infty(V) - n. \tag{1.12}$$

Here $n_\infty(V)$ is the steady-state fraction of open channels at voltage V, while $\tau_n(V)$ is a measure of how quickly the channels open and close in response to changes in voltage. The shape of $n_\infty(V)$ is shown in Figure 1.4 as sigmoidal. Since I_h is hyperpolarisation activated, this means that n_∞ tends to 1 as V decreases and 0 as V increases.

Quasi-Active Approximation

For the small deviations around the equilibrium potential which we consider in this thesis, we can approximate I_h via linearisation about the equilibrium point for V and n, denoted (V^*, n^*). This is termed a quasi-active approximation, which transforms the current I_h in terms of a new variable w which is linearly coupled to the transmembrane potential V [65, 66]. We demonstrate this linearisation first for the point neuron and then show it carries over to the spatially extended neuron.

Quasi-active point neuron
For the point neuron we substitute $I_{\text{add}} = I_h$ into (1.5)

$$C_{\text{m}}\frac{\mathrm{d}V}{\mathrm{d}T} = G_L(E_L - V) + \overline{G}_h n(V)(E_h - V). \tag{1.13}$$

At an equilibrium potential V^*, $\mathrm{d}V/\mathrm{d}T = 0$. When this is satisfied, we can rearrange (1.13) in terms of $n(V)$, yielding the V-nullcline

$$n_2(V) = -\frac{G_L(E_L - V)}{\overline{G}_h(E_h - V)}. \tag{1.14}$$

The n-nullcine is given by $n_\infty(V)$ by setting $\partial n/\partial T = 0$ in (1.12). The intersection of the two nullclines $n_\infty(V)$ and $n_2(V)$ gives the equilibria of the system, as shown in Figure 1.4.

For small deviations about this equilibrium with $(V, n) = (V^* + \delta V, n^* + \delta n)$, we can expand (1.12) to give

$$I_h(V^* + \delta V) = \overline{G}_h(n^* + \delta n)(V^* + \delta V - E_h), \tag{1.15}$$

$$\left[\tau_n(V^*) + \delta V \left.\frac{\partial \tau_n}{\partial V}\right|_{V^*} + O(\delta V^2)\right]\frac{\partial \delta n}{\partial T} = \delta V \left.\frac{\partial n}{\partial V}\right|_{V^*} + O(\delta V^2) - \delta n, \tag{1.16}$$

which we can simplify by taking to first order in δV, and δn, thus neglecting higher

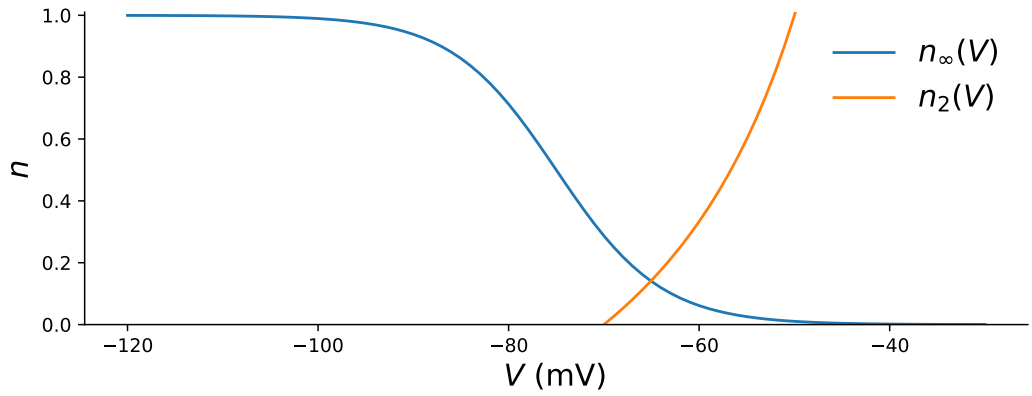

Figure 1.4: The intersection of $n_\infty(V)$ and $n_2(V)$ provides the equilibria (V^*, n^*) of the neuron with an active current. For a hyperpolarisation-activated, depolarising current there is only a single intersection and hence a unique equilibrium.

order terms of the form δV^2 or $\delta n \times \delta V$

$$I_h(V^* + \delta V) \approx \overline{G}_h n^*(V^* + \delta V - E_h) + \overline{G}_h \delta n(V^* - E_h) \tag{1.17}$$

$$\tau_n(V^*)\frac{\partial \delta n}{\partial T} = \delta V \left.\frac{\partial n}{\partial V}\right|_{V^*} - \delta n. \tag{1.18}$$

Defining the quasi-active variable, time constant and current coupling coefficient as $w = \delta n[\partial n/\partial V|_{V^*}]^{-1}$, $\tau_w = \tau_n(V^*)$ and $K = -\partial n/\partial V|_{V^*}\overline{G}_h(E_h - V^*)$ respectively, we obtain

$$I_h(V) \approx \overline{G}_h n^*(V - E_h) + Kw, \quad \tau_w \frac{\partial w}{\partial T} = (V - V^*) - w, \tag{1.19}$$

where we note that since $\partial n/\partial V$ is always negative due to I_h being hyperpolarisation-activated, and $E_h > V^*$, K is always positive. From (1.19) we can see that this means that an increase in w resulting from an increase of V away from V^*, will in turn increase $I_h(V)$, which will ultimately act to decrease V back towards V^*. Such currents are termed restorative as they seek to restore the system back to its original state after being perturbed [66]. Substitution of this quasi-active current (1.19) into the membrane potential equation (1.13) yields

$$C_\mathrm{m}\frac{\mathrm{d}V}{\mathrm{d}T} = G_L(E_L - V) + \overline{G}_h n^*(E_h - V) - Kw. \tag{1.20}$$

This gives us an effective membrane conductance $G_{Lh} = G_L + n^*G_h$ and reversal potential $E_{Lh} = (G_L E_L + n^*\overline{G}_h E_h)/G_{Lh}$. Defining the new membrane time constant as $\tau_v = C_\mathrm{m}/G_{Lh}$ and the voltage coupling coefficient as $\kappa = K/G_{Lh}$, we finally arrive

at the equations for the point-neuron model with a single linearised active current

$$\tau_v \frac{\mathrm{d}V}{\mathrm{d}T} = E_{Lh} - V - \kappa w, \quad \tau_w \frac{\partial w}{\partial T} = V - E_{Lh} - w, \tag{1.21}$$

where one can check by setting $\partial V/\partial T = 0$ that the equilibrium potential $V^* = E_{Lh}$.

Quasi-active spatial neuron

Adding I_h to the earlier cable equation (1.9) with $I_{\mathrm{add}} = I_h$ gives

$$c_{\mathrm{m}} \frac{\partial V}{\partial T} = g_L(E_L - V) + \overline{g}_h n(V)(E_h - V) + g_L \lambda^2 \frac{\partial^2 V}{\partial X^2}, \tag{1.22}$$

where $\overline{g}_h = \overline{G}_h/(2\pi a \Delta_X)$. This time at the equilibrium potential V^*

$$n_2(V^*) = -\frac{g_L}{\overline{g}_h(E_h - V^*)} \left[(E_L - V^*) + \lambda^2 \frac{\partial^2 V}{\partial X^2}\bigg|_{V^*} \right], \tag{1.23}$$

where for all of the spatial systems we analyse, we linearise the cable about a position which satisfies $\partial^2 V/\partial X^2|_{V^*} = 0$. Expanding to linear order in the same way as for the point neuron, we will again obtain I_h as defined in (1.19). Substituting this into our earlier cable equation (1.22) yields

$$c_{\mathrm{m}} \frac{\partial V}{\partial T} = g_L(E_L - V) + \overline{g}_h n^*(E_h - V) + g_L \lambda^2 \frac{\partial^2 V}{\partial X^2} - \frac{Kw}{2\pi a \Delta_X}. \tag{1.24}$$

In a similar manner to the point neuron, this gives us a new effective membrane conductance per unit area $g_{Lh} = g_L + n^* \overline{g}_h$ and reversal potential $E_{Lh} = (g_L E_L + \overline{g}_h n^* E_h)/g_{Lh}$. The new time and space constants are given by $c_{\mathrm{m}}/g_{Lh} \to \tau_v$, and $\lambda^2 g_L/g_{Lh} \to \lambda^2$. With the voltage coupling coefficient as $\kappa = K/(2\pi a \Delta_X g_{Lh})$, our cable equation with a quasi-active membrane is given by

$$\tau_v \frac{\partial V}{\partial T} = E_{Lh} - V + \lambda^2 \frac{\partial V^2}{\partial X^2} - \kappa w, \quad \tau_w \frac{\partial w}{\partial T} = V - E_{Lh} - w. \tag{1.25}$$

Here $V^* = E_{Lh}$, as is the case for spatial models with a spatially homogeneous mean voltage and I_h present across the whole spatial model. Even when the mean voltage is not spatially homogeneous or I_h is not present across the whole neuron model (e.g. when an axon is present), $V^* = E_{Lh}$ is taken for simplicity by assuming that spatial variations of V^* in (1.23) are small compared to $E_L - V^*$. Furthermore, the quasi-active parameters τ_w and κ have the same meanings for both the point and spatial neuron models.

There are many other active currents present in neurons which we could

linearise about the equilibrium potential such as persistent sodium [67,68] and slow potassium currents [67]. We do not consider multiple quasi-active currents for the sake of simplicity, though they can each be added linearly in a similar fashion. Other active currents, such as the calcium currents found in pyramidal cells that enable burst firing [69–72], are also not considered due to them being largely inactive at potentials near E_L. This makes them inactive in the subthreshold regime we confine ourselves to in this thesis.

1.4 Synaptic Integration

Depolarisation at a presynaptic bouton from an arriving action potential (AP) opens voltage gated Ca^{2+} channels. The incoming Ca^{2+} in turn activates proteins on synaptic vesicles containing neurotransmitters, which causes the vesicles to fuse with the presynaptic membrane. This releases neurotransmitters into the synaptic cleft, which bind to postsynaptic receptors, activating them. This activation usually opens the associated ion channels, allowing ions to flow into the postsynaptic neuron [73]. This process can be seen in the drawing of Figure 1.5. With the ion channel current given by (1.2), for excitatory synapses $E_e > E_L$, and so opening these channels depolarises the neuron. While for inhibitory synapses, usually $E_i < E_L$, meaning that opening these channels hyperpolarises the neuron.

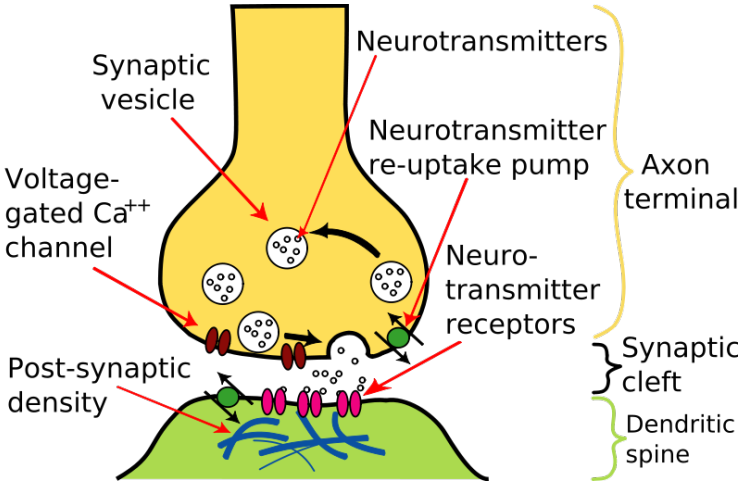

Figure 1.5: Diagram of a chemical synapse, showing the presynaptic bouton with vesicles containing neurotransmitters and voltage-gated Ca^{2+} channels; and the postsynaptic dendritic spine with neurotransmitter receptors that open ion channels. Image taken from [74].

1.4.1 Synaptic Bombardment

Cells in the neocortex receive input from thousands of synapses. This stream of input is highly complex and variable, but empirical evidence suggests that the arrival statistics of synaptic input can be captured by stochastic processes [75–78]. Furthermore, the process of synaptic transmission we saw in Figure 1.5 involves many highly variable processes, adding an additional source of stochasticity [78,79]. Each synaptic input causes the membrane conductance to initially rise rapidly as the channels open before decaying more slowly as the channels close. This can be modelled as causing a step increase in the synaptic conductance of Δ_g followed by exponential decay with time constant τ_s [80], giving

$$\tau_s \frac{\partial G_s}{\partial T} = -G_s + \tau_s \Delta_g \sum_{\{T_{sk}\}} \delta(T - T_{sk}), \tag{1.26}$$

where $\{T_{sk}\}$ denotes the set of synaptic pulse arrival times. Due to the number of synapses from various different presynaptic neurons, the arrival times are assumed to follow a Poisson process with a presynaptic arrival rate r_s, which approximately corresponds to some *in vivo* experimental observations [75,81,82]. r_s is either taken as constant (as in Chapters 2 and 4) or as consisting of a constant and sinusoidally oscillating term (as in Chapters 3 and 5).

Letting N_s be the mean number of pulses arriving in a time window Δ_T, if the rate of arrivals is high and the ratio between the standard deviation and the mean of G_s is much less than 1, we can simplify the Poisson process to a Gaussian process via the diffusion approximation [83,84]

$$\tau_s \frac{\partial G_s}{\partial T} \approx -G_s + \frac{\tau_s \Delta_g}{\Delta_T}(N_s + \sqrt{N_s}\zeta), \tag{1.27}$$

where ζ is a unit-variance zero-mean Gaussian random number. This diffusion approximation is tested in Appendix C.1 for spatial models. As in the quasi-active case, we will first look at simplifying this equation for synaptic drive arriving at a point before moving on to spatially distributed synaptic drive.

Point neuron synaptic drive

For a total number of synapses n_s, we can substitute $N_s = n_s r_s \Delta_T$ as the mean number of pulses arriving in a window Δ_T. This means that the synaptic conductance

in (1.27) evolves as

$$\tau_s \frac{\partial G_s}{\partial T} = -G_s + \tau_s \Delta_g n_s r_s + \tau_s \Delta_g \sqrt{n_s r_s} \frac{\zeta}{\sqrt{\Delta_T}}. \tag{1.28}$$

Here we introduce the temporal Gaussian white noise process $\xi_s(T)$, which is delta-correlated with itself in time

$$\xi_s(T) = \lim_{\Delta_T \to 0} \frac{\zeta}{\sqrt{\Delta_T}}, \quad \langle \xi_s(T) \xi_s(T') \rangle = \delta(T - T'). \tag{1.29}$$

Given that ζ has mean zero, we can infer from (1.28) that the steady-state mean $\langle G_s \rangle = \tau_s \Delta_g n_s r_s$. Defining the synaptic conductance standard deviation $\sigma_G = \Delta_G \sqrt{n_s r_s \tau_s / 2}$, we arrive at an Ornstein-Uhlenbeck process for the synaptic conductance

$$\tau_s \frac{\partial G_s}{\partial T} = \langle G_s \rangle - G_s + \sigma_G \sqrt{2\tau_s} \xi_s(T). \tag{1.30}$$

Since $\tau_s > 0$, correlations will exist between G_s at different times. Thus, this represents temporally coloured noise.

Spatially distributed synaptic drive

Given a number of synapses per unit area of ϱ_s, over a distance Δ_X we can substitute $N_s = 2\pi a \Delta_X \varrho_s r_s \Delta_T$. This means that the synaptic conductance per unit area g_s evolves as

$$\tau_s \frac{\partial g_s}{\partial T} = -g_s + \tau_s \Delta_g \varrho_s r_s + \tau_s \Delta_g \sqrt{\frac{\varrho_s r_s}{2\pi a}} \frac{\zeta}{\sqrt{\Delta_X \Delta_T}}. \tag{1.31}$$

Now we have a spatio-temporal Gaussian white-noise process, $\xi_s(X, T)$ which is delta-correlated with itself

$$\begin{aligned} \xi_s(X, T) &= \lim_{\Delta_X, \Delta_T \to 0} \frac{\zeta}{\sqrt{\Delta_X \Delta_T}}, \\ \langle \xi_s(X, T) \xi_s(X', T') \rangle &= \delta(X - X') \delta(T - T'). \end{aligned} \tag{1.32}$$

Similar to the point neuron, we can infer that $\langle g_s \rangle = \tau_s \Delta_g \varrho_s r_s$. Also defining $\sigma_g = \frac{1}{2} \Delta_g \sqrt{\varrho_s r_s \tau_s / (2\pi a \lambda)}$, we obtain a form of the conductance equation that can be compared to the Ornstein-Uhlenbeck process

$$\tau_s \frac{\partial g_s}{\partial T} = \langle g \rangle_s - g_s + 2\sigma_g \sqrt{\lambda \tau_s} \xi_s(X, T). \tag{1.33}$$

Like the point-neuron case (1.30), g_s is temporally coloured noise. However the conductance is not filtered with respect to X and thus g_s is spatially white.

We can let $s = e, i$ for two distinct synaptic currents representing excitatory and inhibitory synapses respectively. However, in this thesis for simplicity we will only consider a single synaptic process s which represents the combination of excitatory and inhibitory drive. Since the time constants for excitatory AMPA receptors and inhibitory GABA receptors are 2-3 ms and 10 ms respectively, we take $\tau_s = 5$ ms throughout this work. This value is also widely used in experiments when a single type stochastic input, mimicking background synaptic drive, is applied *in vitro* [85–88]. It is important to note that considering a combined synaptic drive s rather than just excitatory or inhibitory drive alone allows us to more justifiably adjust $\langle g \rangle_s$ and σ_g independently.

1.4.2 Effect of Synaptic Drive on Membrane Properties

Synaptic drive does not just allow current into the cell, but also effects the integrative properties of the neuron. We show this first for the point-neuron model and then for the spatially extended neuron.

Point neuron membrane properties
Using the transmembrane current convention of outward currents being positive, we add the synaptic current $I_s = G_s(E_s - V)$ by substituting for $-I_{\text{add}}$ in (1.5)

$$C_{\text{m}}\frac{\text{d}V}{\text{d}T} = G_L(E_L - V) + G_s(E_s - V), \tag{1.34}$$

where G_s is described by (1.28). For synaptic conductance fluctuations G_{sF} about the mean $\langle G_s \rangle$, we substitute $G_s = \langle g_s \rangle_s + g_{sF}$. Similarly, the potential can be split into the response from the mean and fluctuations as $V = \langle V \rangle + v_F$. This means that we can write the mean response as

$$C_{\text{m}}\frac{\text{d}\langle V \rangle}{\text{d}T} = 0 = G_L(E_L - \langle V \rangle) + \langle G_s \rangle(E_s - \langle V \rangle) \tag{1.35}$$

which from (1.4), we can see that the opening of channels due to synaptic input increases the overall conductance of the cell to $G_0 = G_L + \langle G_s \rangle$ and changes the resting membrane potential to $E_0 = \langle V \rangle = (G_L E_L + \langle G_s \rangle E_s)/G_0$. From our earlier definition of $\tau_v = C_{\text{m}}/G_0$, this has the effect of decreasing the effective membrane time constant.

For the fluctuating components, we assume that the product $G_{sF} \times v_F$ is

small, which means

$$\tau_v \frac{\mathrm{d}v_F}{\mathrm{d}T} = -v_F + \frac{G_{sF}}{G_0}(E_s - E_0). \tag{1.36}$$

Hence we can simplify the voltage (1.36) and synaptic (1.30) equations with the change of variables, $s = G_{sF}(E_s - E_0)/G_0$ and $\sigma_s = \sigma_G(E_s - E_0)/G_0$

$$\tau_v \frac{\mathrm{d}v_F}{\mathrm{d}T} = -v_F + s, \quad \tau_s \frac{\partial s}{\partial T} = -s + \sigma_s\sqrt{2\tau_s}\xi_s(T). \tag{1.37}$$

Adding the mean voltage E_0 to v_F, defining the voltage measured from the leakage potential v as $v = V - E_L$ and the mean voltage component of the synaptic drive $\mu = E_0 - E_L$, we finally obtain

$$\tau_v \frac{\mathrm{d}v}{\mathrm{d}T} = \mu - v + s, \quad \tau_s \frac{\partial s}{\partial T} = -s + \sigma_s\sqrt{2\tau_s}\xi_s(T). \tag{1.38}$$

Spatial neuron membrane properties
For a dendrite with leak conductance and a single type of synaptic input with conductance described by (1.33), we have the cable equation

$$c_\mathrm{m}\frac{\partial V}{\partial T} = g_L(E_L - V) + g_s(E_s - V) + g_L\lambda^2\frac{\partial^2 V}{\partial X^2}. \tag{1.39}$$

Substituting $g_s = \langle g\rangle_s + g_{sF}$ and $V = \langle V\rangle + v_F$ as in the point-neuron model, the mean potential response thus follows

$$c_\mathrm{m}\frac{\partial\langle V\rangle}{\partial T} = 0 = g_L(E_L - \langle V\rangle) + \langle g_s\rangle(E_s - \langle V\rangle) + g_L\lambda^2\frac{\partial^2\langle V\rangle}{\partial X^2}, \tag{1.40}$$

increasing the average overall conductance per unit area of the cell to $g_0 = g_L + \langle g_s\rangle$. Updating our earlier definitions of τ_v and λ with $c_\mathrm{m}/g_0 \to \tau_v$ and $g_L\lambda^2/g_0 \to \lambda^2$, when we reformulate the cable equation for the mean component into (1.9) the conductance increase reduces both the membrane time and length constants. These effects have been found experimentally [89–92], and have been described through mathematical models [93, 94] and simulations [95].

Again assuming that the product $g_{sF} \times v_F$ is small, v_F evolves as

$$\tau_v \frac{\partial v_F}{\partial T} = -v_F + \frac{g_{sF}}{g_0}(E_s - \langle V\rangle) + \lambda^2\frac{\partial^2 v_F}{\partial X^2}. \tag{1.41}$$

We again simplify the voltage and synaptic equations with the change of variable $s = g_{sF}(E_s - E_0)/g_0$. Letting $\sigma_s = \sigma_g(E_s - E_0)/g_0$, and assuming $\langle V\rangle$ is close to

E_0 with position X, $(E_s - \langle V(X)\rangle)/(E_s - E_0) \approx 1$, this yields

$$\tau_v \frac{\partial v_F}{\partial T} = -v_F + \lambda^2 \frac{\partial^2 v_F}{\partial X^2} + s, \quad \tau_s \frac{\partial s}{\partial T} = -s + 2\sigma_s \sqrt{\lambda \tau_s}\xi_s(X,T). \tag{1.42}$$

Reintroducing the mean component in the synaptic drive in the same manner as the point neuron with $v = V - E_L$, $\mu = E_0 - E_L$ gives

$$\tau_v \frac{\partial v}{\partial T} = \mu - v + \lambda^2 \frac{\partial^2 v}{\partial X^2} + s, \quad \tau_s \frac{\partial s}{\partial T} = -s + 2\sigma_s \sqrt{\lambda \tau_s}\xi_s(X,T), \tag{1.43}$$

where we note that μ is only equal to the voltage mean when $\langle v\rangle$ is spatially homogeneous. Furthermore, while σ_g and σ_G are parametrised differently, σ_s has the same meaning for the point and spatial neurons: σ_s represents the standard deviation of the synaptic conductance relative to the membrane conductance multiplied by the synaptic driving force $(E_s - E_0)$.

White-noise limit

If the synapses close rapidly, $\tau_s \to 0$ and for the point neuron (1.30) becomes

$$G_s = \langle G_s\rangle + \sigma_G \sqrt{2\tau_s}\xi_s(T), \tag{1.44}$$

meaning that the fluctuating component of the synaptic current is simply scaled white noise. Using the same scaling of G_{sF} as before, the equation for the membrane potential is

$$\tau_v \frac{\mathrm{d}v}{\mathrm{d}T} = \mu - v + \sigma_{\mathrm{WN}} \sqrt{2\tau_v}\xi_s(T), \quad \sigma_{\mathrm{WN}} = \sigma_s \sqrt{\frac{\tau_s}{\tau_v}}. \tag{1.45}$$

Similarly for the spatially distributed synaptic drive, (1.33) becomes

$$g_s = \langle g_s\rangle + 2\sigma_g \sqrt{\lambda \tau_s}\xi_s(X,T), \tag{1.46}$$

and after extracting g_{sF}, this means that our cable equation now becomes

$$\tau_v \frac{\partial v}{\partial T} = \mu - v + \lambda^2 \frac{\partial^2 v}{\partial X^2} + 2\sigma_{\mathrm{WN}} \sqrt{\lambda \tau_v}\xi_s(X,T), \tag{1.47}$$

with σ_{WN} defined as before. In this thesis most of the focus is on coloured-noise drive (1.38),(1.43) rather than white noise, because it is both more biophysically realistic and easier to extract an approximation for the firing rate for the approach that we will use. However, the white-noise limit is occasionally useful as a comparison,

as it gives statistics of the voltage in a typically simpler form, and is used in most of the existing literature on stochastic neuronal firing for point-neuron models [7,96].

Quasi-active currents and synaptic drive
By starting from (1.39) and adding the I_h current, it is straightforward to include the linearised active current and synaptic drive, along with the effects on τ_v and λ. The effective conductance per unit area is now $g_{0h} = g_L + \langle g_s \rangle + \overline{g}_h n^*$ while the new resting potential is $E_{0h} = (g_L E_L + \langle g_s \rangle E_s + \overline{g}_h n^* E_h)/g_{0h}$, where E_h and g_h are defined as before in subsection 1.3.4. This means that the new time constant is $\tau_v = c_\mathrm{m}/g_{0h}$ and the length constant from the original cable equation (1.9) is changed to $g_L\lambda^2/g_{0h} \to \lambda^2$.

With E_{Lh} as the resting potential of the quasi-active membrane in the absence of synaptic drive, defining $v = V - E_{Lh}$ and $\mu = E_{0h} - E_{Lh}$ in a similar manner to the passive membrane with synaptic drive (1.43) gives for the point neuron

$$\tau_v \frac{\mathrm{d}v}{\mathrm{d}T} = \mu - v - \kappa w + s, \quad \tau_w \frac{\partial w}{\partial T} = v - \mu - w, \tag{1.48}$$

while for the spatial neuron we obtain the cable equation

$$\tau_v \frac{\partial v}{\partial T} = \mu - v + \lambda^2 \frac{\partial^2 v}{\partial X^2} - \kappa w + s, \quad \tau_w \frac{\partial w}{\partial T} = v - \mu - w. \tag{1.49}$$

In this thesis we will often remove the dimensions from space and time with $x = X/\lambda$ and $t = T/\tau_v$. This convention of denoting the dimensionless variables as (x, t) and the dimensionfull variables as (X, T) is adopted throughout this thesis. The dimensionless variables are used in the analysis of the equations, while the dimensionfull parameters are reintroduced in figures to indicate how the analytically calculated result translate to biophysically relevant quantities.

1.5 The Significance of Spiking

The vast majority of neurons in the mammalian brain are capable of producing APs. An AP is a large and rapid increase and then subsequent decrease in a neuron's membrane potential. APs are initiated within the first 50μm of the axon, the AIS [97,98]. Spiking allows for depolarisation large enough to propagate along the axon and in turn depolarise presynaptic terminals. Non-spiking potentials in the AIS are much smaller in magnitude, decay rapidly along the long axon, and thus have no influence on the presynaptic terminals. Therefore, spiking is significant because it produces a sequence of events necessary for communication between neurons via

chemical synapses that we introduced in section 1.4.

The production of APs is possible due to the high density of voltage-gated ion channels at the AIS. The most significant of these ion channels for APs are Na^+ channels and K^+ channels. When the membrane potential of the AIS depolarises sufficiently, both the Na^+ and K^+ channels begin to open. However, the Na^+ channels open more quickly, allowing ions to flow in and the potential depolarises rapidly. As the membrane potential increases, the Na^+ channels inactivate, allowing no more ions through. The ions flowing outwards due to the open K^+ channels then causes the potential to decrease, often hyperpolarising the AIS. This decrease in potential closes the K^+ channels and the neuron returns to rest. An AP recorded *in vitro* is shown in Figure 1.6.

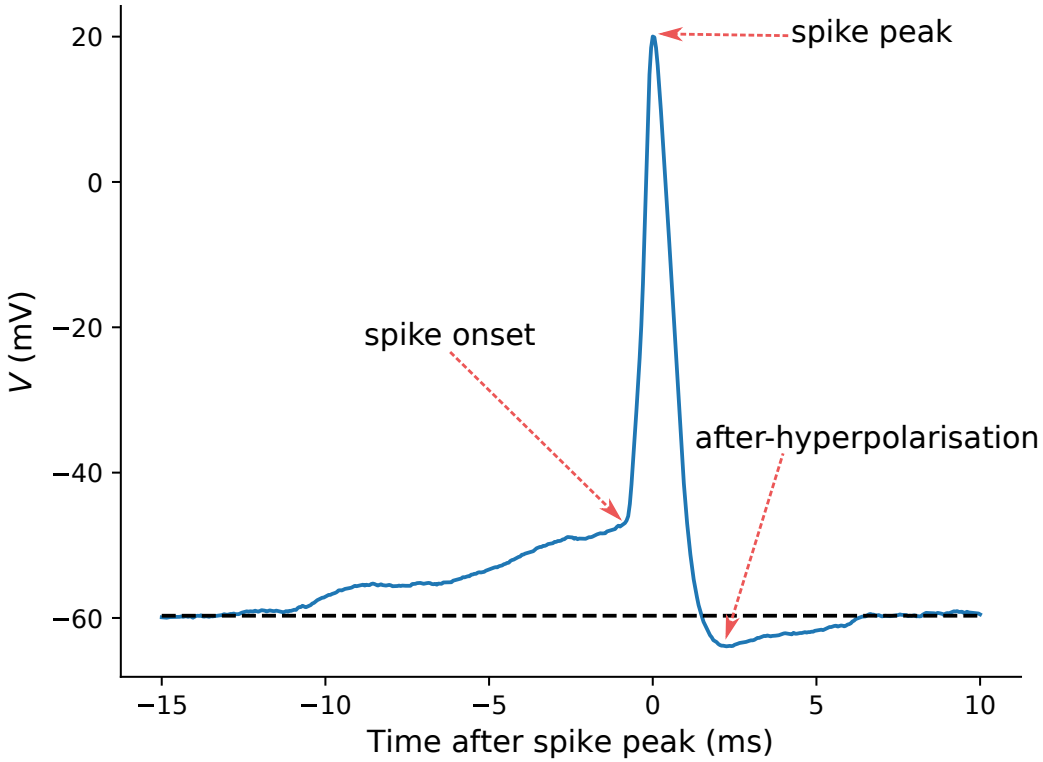

Figure 1.6: Example of a recorded action potential, showing how V rises rapidly upon spike onset and hyperpolarises after peaking [99]. The dashed line shows the resting potential of the cell.

The complexity of neuronal spiking has led to a multitude of models being developed to characterise different aspects of neuronal firing. The appropriate model to choose depends on the phenomena that one wishes to accurately capture.

1.6 The Hodgkin-Huxley Model

The Hodgkin-Huxley model includes three different channel types (leakage, sodium and potassium) with four differential equations which characterise the voltage, two activation variables (n, m), and one inactivation variable h [50]

$$c_{\mathrm{m}}\frac{\partial V}{\partial T} = g_L(E_L - V) + \overline{g}_K n^4(E_K - V) + \overline{g}_{\mathrm{Na}} m^3 h(E_{\mathrm{Na}} - V) + g_L\lambda^2\frac{\partial^2 V}{\partial X^2} - \frac{I_{\mathrm{add}}(X,T)}{2\pi a\Delta_X}, \tag{1.50}$$

$$\frac{\partial q}{\partial T} = \alpha_q(V)(1-q) - \beta_q(V)q, \quad q = (n, m, h). \tag{1.51}$$

However, the complexity of the Hodgkin-Huxley model which arises from the numerous independent parameters and non-linearities means that it is invariably difficult to approach analytically.

1.7 Integrate-and-Fire Models

Integrate-and-fire (IF) models simplify the spiking dynamics of neurons by introducing a threshold voltage v_{th} and a reset voltage v_{re}. Once the membrane potential reaches threshold, it is instantly changed to the reset voltage. This simplification makes IF models much easier to analyse analytically, and is appropriate when the voltage dynamics immediately after a spike peak are not relevant. IF models with input $I_{\mathrm{in}}(T)$ have the general form

$$\tau_v\frac{\mathrm{d}v}{\mathrm{d}T} = F(v) + I_{\mathrm{in}}(T), \tag{1.52}$$

where $F(v)$ determines the type of IF model and is used in point-neuron models to characterise the dynamics of the system [7].

1.7.1 Leaky Integrate-and-Fire Model

For the leaky integrate-and-fire model (LIF), there is no spike-generating current and $F(v) = \mu - v$. This makes it a straightforward model to analyse, and requires the spike-onset dynamics to be irrelevant or very fast to be appropriate. If we impose a finite threshold v_{th} and reset v_{re} to our cable equation with synaptic drive (1.43), we obtain a form of the LIF model. The spiking dynamics for the LIF model are instantaneous, which is represented by the abrupt transitions from v_{th} to v_{re} in Figure 1.7.

In this thesis, we will predominantly use the simulated LIF firing rate as a reference to compare the upcrossing rate, which we introduce later. This is because our focus on stochastic neuronal firing is in the fluctuation-driven regime where usually the spiking dynamics are unimportant due to the time between firing events being much longer than the duration of an AP. Should the spike-onset dynamics be of interest, other IF models must be employed such as the quadratic integrate-and-fire (QIF) [100] or exponential integrate-and-fire (EIF) [101] models, but this is beyond the scope of this thesis.

While there is only a single voltage to reach threshold and reset for point-neuron models, for spatial models how threshold and reset are applied across space depends on the context of the problem. For this thesis, we will check whether threshold has been reached at a single spatial position, X_{th}, termed the trigger position. This represents a location of high Na^+ channel density required to initiate APs. Due to the backpropagation of the AP throughout the dendritic arbour, we reset the potential at all spatial locations to v_{re} after threshold is reached at X_{th}. Since this of a much shorter timescale than the average time between firing events in the low-rate regime considered here, this reset is applied simultaneously at all locations for simplicity.

1.7.2 Deterministic Limit

If the mean current by itself is sufficient to cause the voltage to exceed v_{th} and the effect of noise is negligible, then we can invert the IF equations to obtain an expression for the firing rate. Letting $I_{\text{in}} = 0$, we reduce (1.52) to the ODE

$$\tau_v \frac{\mathrm{d}v}{\mathrm{d}T} = F(v). \tag{1.53}$$

We require the potential in the long-time limit to exceed threshold, $v_\infty > v_{\text{th}}$, for any firing to occur in the deterministic limit. For the LIF model $F(v) = \mu - v$, meaning that the deterministic suprathreshold firing rate is

$$r_{\text{det}} = \left[\tau_v \ln\left(\frac{\mu - v_{\text{re}}}{\mu - v_{\text{th}}}\right)\right]^{-1}. \tag{1.54}$$

When μ is no longer constant in space or there are multiple neuronal structures to consider with different properties, we cannot neglect the spatial aspect of the problem and (1.54) no longer holds in general.

1.7.3 Resonate and Fire Models

The term resonate-and-fire has been used for a broad class of models which have the common theme of second-order dynamics in time of v [102]. Here we will focus strictly on linear models which can be derived from our quasi-active current approximation in section 1.3.4

$$\tau_v \frac{\mathrm{d}v}{\mathrm{d}T} = \mu - v - \kappa w + I_{\mathrm{in}}(T), \quad \tau_w \frac{\partial w}{\partial T} = v - \mu - w. \tag{1.55}$$

Such systems can express a subthreshold voltage resonance, which has been well-explored for both point- and extended-neuron models [65, 103, 104]. For an input $I_{\mathrm{in}}(T)$ with time-varying moments, this system can also express resonances in the firing rate. While this has been studied for point-neuron models [105–107], far less work exists for spatial models which is confined to suprathreshold firing [108, 109].

1.8 Upcrossing Approximation

Provided that $\mu < v_{\mathrm{th}}$ and the time derivative $\dot{v} = \partial v/\partial t$ is well-defined, we can approximate the firing rate for a LIF neuron by the mean rate at which a process without reset crosses v_{th} with $\dot{v} > 0$. Figure 1.7 shows for sufficiently long time in between firing events, the voltage traces for these two processes converge. This is expected because the models studied in this thesis are linear between reset events. Known as the upcrossing method, the theory underlying this result was outlined by Rice [110] and has recently been applied to point neuron models [9, 106, 107, 111, 112]. Level-crossing methods have also been employed in other fields, such as wireless communication channels [113], fluctuating sea surfaces [114] and rough grown surfaces [115].

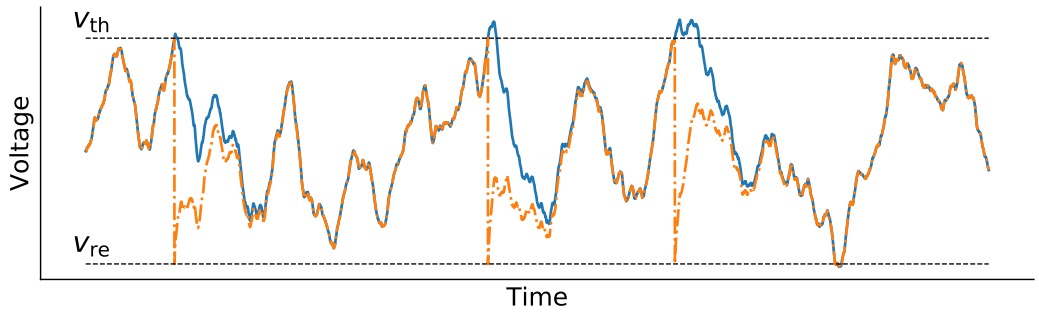

Figure 1.7: A simulated example of two voltage traces with the same input drive, where one has a reset (orange) and the other does not (blue). As well as the correspondence between the upcrossing and reset events, the voltage traces for the two processes converge between reset events.

For Gaussian distributed v and $\dot{v}$, which we have due to the diffusion limit taken for the synaptic drive (1.27), one can derive a formula for the general upcrossing rate. We use the term general here to stress that this upcrossing rate is applicable when the moments of v and $\dot{v}$ are time-varying. This derivation is provided in more detail in Appendix A.1. Here we give the resulting formula and an explanation of the parameters involved. Denoting the standard deviations of v and $\dot{v}$ as σ_v and $\sigma_{\dot{v}}$ respectively, and using the subscript "th" to denote quantities evaluated at threshold (e.g. $[\sigma_{\dot{v}}]_{\text{th}}$ means $\sigma_{\dot{v}}$ given $v = v_{\text{th}}$), the general upcrossing formula for Gaussian distributed v and $\dot{v}$ is itself Gaussian-like in shape with respect to v_{th}

$$r_{\text{uc}} = \frac{[\sigma_{\dot{v}}]_{\text{th}}}{2\pi\sigma_v} \exp\left[-\frac{(v_{\text{th}} - \langle v\rangle)^2}{2\sigma_v^2}\right] [e^{-\eta^2} + \eta\sqrt{\pi}(1 + \operatorname{erf}\eta)], \tag{1.56}$$

where $\eta = \langle\dot{v}\rangle_{\text{th}}/([\sigma_{\dot{v}}]_{\text{th}}\sqrt{2})$. These moments conditioned at threshold are given by

$$\langle\dot{v}\rangle_{\text{th}} = \langle\dot{v}\rangle + \frac{\operatorname{cov}(v,\dot{v})(v_{\text{th}} - \langle v\rangle)}{\sigma_v^2}, \quad [\sigma_{\dot{v}}^2]_{\text{th}} = \sigma_{\dot{v}}^2 - \frac{\operatorname{cov}(v,\dot{v})^2}{\sigma_v^2}. \tag{1.57}$$

In Chapters 2 and 4, the presynaptic arrival rate r_s is set to be constant in time, causing all the moments to be time-independent, while in Chapters 3 and 5, weak sinusoidal modulation is applied to the presynaptic arrival rate, causing the moments of v and $\dot{v}$ to also vary sinusoidally in time at the same frequency.

The upcrossing approximation is particularly desirable because it works well for temporally coloured synaptic drive, which is not directly tractable using the standard Fokker-Planck approaches used for IF models - even for point-neuron models (though see [116–118]). The requirement that the time interval between spikes is

long compared to the membrane time constant is, for example, satisfied for most neocortical pyramidal cells, which spike irregularly at low firing rates [119, 120].

1.9 Overview

In this chapter we have explored the basic concepts of neuronal electrophysiology, such as the transmembrane potential, synaptic integration, and active currents. Importantly, we derived the cable equation with stochastic synaptic drive (1.9), the analysis of which forms a necessary part of this thesis. The LIF model of neuronal firing was discussed, however due to the low irregular firing rates of many neurons and its analytical tractability, we will instead use the upcrossing approach to approximate the firing rate.

With the biophysical background and necessary equations established, in Chapter 2 we will calculate the upcrossing rate in response to steady-state drive for a range of simple spatial neuron models. This is to see the effect of morphology on the population-averaged fluctuation-driven firing rate. In Chapter 3, sinusoidal modulation of the presynaptic firing rate and external oscillatory currents are included to calculate the dynamic firing-rate response of spatially extended neurons. Quasi-active currents representing I_h are included in Chapters 4 and 5, which investigate the steady-state and dynamic response respectively of quasi-active neurons.

Chapter 2

Steady-State Firing Rate

2.1 Introduction

The impact of morphology on neuronal computation is an active area of neuroscience research, with recent studies investigating the effect of the axon [121–123], and morphological differences between rodents and humans [34, 35, 42]. The hope is that these studies could give functional explanations for the various neuronal morphologies observed [18]. Given that neurons are highly spatially extended, vary morphologically [31–35], and often show low irregular firing rates *in vivo* thought to be responsible for rate coding [81, 124], it is surprising that there are few theoretical results of the morphological effects on fluctuation-driven firing (although results obtained via simulation exist [125–128]). The existing literature concerning this largely focuses on two-compartmental models [10–12] or synaptic drive applied to a single point in space [127].

In this chapter we use the upcrossing approach to approximate the steady-state fluctuation-driven firing rate of several spatial-neuron models. We start with the point neuron (section 2.2), introduce spatial extent with an infinite dendrite (section 2.3), before making the structure progressively more complex by adding an axon (section 2.6), then an electrically substantial soma as in Rall's ball-and-stick model [129] (section 2.7), and finally we consider multiple dendrites (section 2.8). In each case we calculate the voltage variances (a term used to collectively refer to the voltage variance, the variance of the voltage time-derivative, the time-autocovariance and the spatial-autocovariance) for white- and coloured-noise input, and the upcrossing rate in the latter case. For our calculation of the variances, we assume that the synaptic input has been ongoing for a sufficiently long time such that any initial transients are negligible. Hence all the quantities required for the

upcrossing rate are time-independent. Many of the results shown here can be found in [130], but some of the notation may differ.

2.1.1 Steady-State Upcrossing Rate

In the steady state with coloured-noise drive, it is always the case that $\langle \dot{v} \rangle = 0$ and $\mathrm{cov}(v, \dot{v}) = 0$. The former is easy to verify by taking expectations of the stochastic cable equation (1.43), since by design $\langle s \rangle = 0$. For the same-time covariance, $\mathrm{cov}(v, \dot{v}) = \langle v\dot{v} \rangle = \frac{1}{2}\frac{\mathrm{d}}{\mathrm{d}t}\langle v^2 \rangle$, which is zero for drive with constant mean and intensity. In reference to the general upcrossing equation (1.56), this means that $\eta = 0$ and $[\sigma_{\dot{v}}^2]_{\mathrm{th}} = \sigma_{\dot{v}}^2$. Hence the upcrossing rate due to steady-state drive is given simply as [110]

$$r_0 = \frac{\sigma_{\dot{v}}}{2\pi\sigma_v} \exp\left[-\frac{(\langle v \rangle - v_{\mathrm{th}})^2}{2\sigma_v^2}\right]. \tag{2.1}$$

2.2 Point Neuron

To demonstrate the methods later used in spatial models, we calculate the upcrossing approximation of the fluctuation-driven firing rate for the point-neuron model. We recall from Chapter 1 that the potential measured from the leak potential $v = V - E_L$ and the synaptic variable s are given by (1.38)

$$\tau_v \frac{\mathrm{d}v}{\mathrm{d}T} = \mu - v + s, \quad \tau_s \frac{\partial s}{\partial T} = -s + \sigma_s\sqrt{2\tau_s}\xi_s(T), \tag{2.2}$$

where τ_v is the membrane time constant, μ is the mean component of the synaptic drive, τ_s is the synaptic time constant and σ_s is the intensity of the stochastic drive. For ease of analysis, we remove the time dimension with the substitution $t = T/\tau_v$ and introduce the relative time constant parameter $\beta_s = \tau_s/\tau_v$. This changes the voltage and synaptic equations to

$$\frac{\mathrm{d}v}{\mathrm{d}t} = \mu - v + s, \quad \beta_s \frac{\mathrm{d}s}{\mathrm{d}t} = -s + \sigma_s\sqrt{2\beta_s}\xi_s(t). \tag{2.3}$$

2.2.1 Point Neuron Variances, White-Noise

While there are many ways to calculate the variance of v for the point-neuron model, we utilise the temporal Fourier transform here. In this thesis we use the convention

$$\tilde{f}(\omega) = \int_{-\infty}^{\infty} f(t)e^{-i\omega t}\mathrm{d}t, \quad f(t) = \frac{1}{2\pi}\int_{-\infty}^{\infty} \tilde{f}(\omega)e^{i\omega t}\mathrm{d}\omega. \tag{2.4}$$

Our strategy is to write $v(t)$ in terms of the inverse Fourier transform of $\tilde{v}(\omega)$, multiply this integral by a different realisation of the same process over the same time window, and then take the expectation. This approach is chosen because the integrals often resolve more easily in the Fourier domain, and because it generalises straightforwardly to spatial-neuron models.

In the white-noise limit, taking the Fourier transform of $v(t)$ yields

$$\tilde{v}(\omega) = 2\pi\delta(\omega)\mu + \frac{\sigma_{\mathrm{WN}}\sqrt{2}\tilde{\xi}_s(\omega)}{1+i\omega}, \tag{2.5}$$

where $\tilde{\xi}_s(\omega)$ is the Fourier transform of the white-noise process $\xi_s(t)$. This means the potential is given by the inverse transform

$$v(t) = \mu + \frac{\sigma_{\mathrm{WN}}\sqrt{2}}{2\pi}\int_{-\infty}^{\infty}\frac{\tilde{\xi}_s(\omega)e^{i\omega t}}{1+i\omega}\mathrm{d}\omega, \tag{2.6}$$

from $\langle v\rangle = \mu$, as expected from the original equation (2.3). In order to compute the variance, we need the white-noise correlator in the frequency domain. Recalling the correlator in time for $\xi_s(t)$ (1.29), we can use Fourier transforms to obtain the correlator in terms of angular frequency

$$\langle\tilde{\xi}_s(\omega)\tilde{\xi}_s(-\omega')\rangle = 2\pi\delta(\omega-\omega'). \tag{2.7}$$

Denoting v_F as the fluctuating component of v, $v_F = v - \langle v\rangle$, we subtract the mean from (2.6) and multiply it by a copy of v_F at time t' with $-\omega'$ in the integrand. Taking the expectation of this yields

$$\begin{aligned}\langle v_F(t)v_F(t')\rangle &= \frac{\sigma_{\mathrm{WN}}^2}{\pi}\int_{-\infty}^{\infty}\frac{e^{i\omega t}}{1+i\omega}\mathrm{d}\omega\int_{-\infty}^{\infty}\delta(\omega-\omega')\frac{e^{-i\omega' t'}}{1-i\omega'}\mathrm{d}\omega' \\ &= \frac{\sigma_{\mathrm{WN}}^2}{\pi}\int_{-\infty}^{\infty}\frac{e^{i\omega(t-t')}}{1+\omega^2}\mathrm{d}\omega,\end{aligned} \tag{2.8}$$

which is a known integral that gives an exponential temporal autocovariance

$$\langle v_F(t)v_F(t')\rangle = \sigma_{\mathrm{WN}}^2 e^{-|t-t'|}. \tag{2.9}$$

Since v_F is zero-mean, setting $t = t'$ simply gives us the variance $\sigma_v^2 = \sigma_{\mathrm{WN}}^2$. We note that since: (i) the mean is constant in time, (ii) the temporal autocovariance depends only on the time difference rather than the absolute times, and (iii) that the variance is finite, $v(t)$ is a wide-sense stationary stochastic process. In addition, denoting the complex conjugate by *, we also have that $\tilde{v}(\omega)^* = \tilde{v}(-\omega)$. This means

we could have utilised the Wiener-Khinchin theorem, which states that the temporal autocovariance $K(\tau)$ and power spectral density $S(\omega)$ form a Fourier transform pair [131]

$$K(\tau) \equiv \langle v(t)v(t+\tau)\rangle, \quad S(\omega) \equiv |\tilde{f}(\omega)|^2, \quad K(\tau) = \frac{1}{2\pi}\int_{-\infty}^{\infty} S(\omega)e^{i\omega\tau}\mathrm{d}\omega. \tag{2.10}$$

Since this will apply in all of the steady-state cases, we utilise these relations as a shortcut for deriving the variances in later models.

2.2.2 Point Neuron Variances, Coloured-Noise

For coloured noise, taking Fourier transforms of v and s of the point neuron equations (2.3) gives the power spectral density

$$\tilde{v}_F(\omega) = \frac{\tilde{s}(\omega)}{1+i\omega}, \quad \tilde{s} = \frac{\sigma_s\sqrt{2\beta_s}\tilde{\xi}(\omega)}{1+i\omega\beta_s}, \quad S(\omega) = \frac{2\sigma_s^2\beta_s}{(1+\omega^2)(1+\omega^2\beta_s^2)}, \tag{2.11}$$

where it is useful for future models to define $\gamma = \sqrt{1+i\omega}$, which for the point neuron means $\gamma^2\tilde{v}_F(\omega) = \tilde{s}(\omega)$. Integrating $S(\omega)$ yields the temporal autocovariance, which can be resolved by splitting into partial fractions

$$\begin{aligned}
\langle v_F(t)v_F(t')\rangle &= \frac{\sigma_s^2\beta_s}{\pi}\int_{-\infty}^{\infty}\frac{e^{i\omega(t-t')}}{(1+\omega^2)(1+\omega^2\beta_s^2)}\mathrm{d}\omega \\
&= \frac{\sigma_s^2\beta_s}{\pi(1-\beta_s^2)}\left[\int_{-\infty}^{\infty}\frac{e^{i\omega(t-t')}}{1+\omega^2}\mathrm{d}\omega - \beta_s^2\int_{-\infty}^{\infty}\frac{e^{i\omega(t-t')}}{1+\beta_s^2\omega^2}\mathrm{d}\omega\right] \\
&= \frac{\sigma_s^2\beta_s}{1-\beta_s^2}\left[e^{-|t-t'|} - \beta_s e^{-|t-t'|/\beta_s}\right] = K(t-t').
\end{aligned} \tag{2.12}$$

In comparison with white-noise drive, the temporal autocovariance curve is broadened. The peak value is lower and decreases with increasing β_s, while the correlations for large time differences are higher. Setting $t = t'$ gives us the variance σ_v^2 since v_F is zero-mean

$$\sigma_v^2 = \frac{\sigma_s^2\beta_s}{1+\beta_s}. \tag{2.13}$$

We note that in comparison with the variance when driven by white-noise (2.9), as $\sigma_{\mathrm{WN}}^2 = \beta_s\sigma_s^2$, increasing $\beta_s = \tau_s/\tau_v$ (slower synapses) increases the variance towards a maximum of σ_s^2.

To calculate the variance of the time derivative $\dot{v}$, we use differentiation

property of the Fourier transform, $\tilde{\dot{v}}(\omega) = i\omega\tilde{v}(\omega)$. This means that $\dot{v}(t)$ written as an inverse Fourier transform is

$$\dot{v}(t) = \frac{\sigma_s\sqrt{2\beta_s}}{2\pi}\int_{-\infty}^{\infty}\frac{i\omega\tilde{\xi}(\omega)e^{i\omega t}}{(1+i\omega)(1+i\omega\beta_s)}\mathrm{d}\omega, \tag{2.14}$$

which, upon repeating the same process as before, shows that the temporal autocovariance is the inverse Fourier transform of $\omega^2 S(\omega)$ and yields

$$\langle\dot{v}(t)\dot{v}(t')\rangle = \frac{\sigma_s^2}{1-\beta_s^2}\left[e^{-|t-t'|/\beta_s} - \beta_s e^{-|t-t'|}\right]. \tag{2.15}$$

Therefore, the variance of the time derivative $\sigma_{\dot{v}}^2$ is

$$\sigma_{\dot{v}}^2 = \frac{\sigma_s^2}{1+\beta_s}. \tag{2.16}$$

Note that there is no comparable calculation for the white-noise limit as the integral of $\omega^2 S(\omega)$ does not converge in this case; for white noise $\dot{v}$ is undefined. Furthermore, we also notice that the derivative variance is proportional to the difference between variances from coloured- and white-noise drive (when we let $\sigma_{\mathrm{WN}}^2 = \beta_s\sigma_s^2$), labelled $[\sigma_v^2]_c$ and $[\sigma_v^2]_{\mathrm{WN}}$ respectively

$$\beta_s^2\sigma_{\dot{v}}^2 = [\sigma_v^2]_{\mathrm{WN}} - [\sigma_v^2]_c. \tag{2.17}$$

This relation holds for all cases where the variances in question are derived via the integrals with the same function $F(\omega)$

$$[\sigma_v^2]_{\mathrm{WN}} = \int_{-\infty}^{\infty}F(\omega)\mathrm{d}\omega, \quad [\sigma_v^2]_c = \int_{-\infty}^{\infty}\frac{F(\omega)\mathrm{d}\omega}{1+\omega^2\beta_s^2}, \quad \sigma_{\dot{v}}^2 = \int_{-\infty}^{\infty}\frac{\omega^2 F(\omega)\mathrm{d}\omega}{1+\omega^2\beta_s^2}. \tag{2.18}$$

All variances in this thesis can be expressed in this way. The relation between these variances in (2.17) often gives a shortcut to derive $[\sigma_v^2]_c$ since $[\sigma_v^2]_{\mathrm{WN}}$ and $\sigma_{\dot{v}}^2$ are more straightforwardly calculated.

2.2.3 Point Neuron, Firing Rate

With σ_v^2 and $\sigma_{\dot{v}}^2$, we can now calculate the steady-state upcrossing rate as derived earlier (2.1). For the point neuron this yields

$$r_{\mathrm{uc}} = \frac{1}{2\pi\sqrt{\beta_s}}\exp\left(-\frac{\beta_s(v_{\mathrm{th}}-\mu)^2}{2\sigma_s^2(1+\beta_s)}\right), \tag{2.19}$$

which shows: first, that $r_{\rm uc}$ depends on $(v_{\rm th}-\mu)/\sigma_s$ rather than the absolute value of the threshold $v_{\rm th}$ and second, that decreasing β_s results in a higher *dimensionless* upcrossing rate. Converting this result back to *dimensionfull* quantities, when we alter β_s we can choose whether to fix τ_v or τ_s. The time constants for a particular type of synapse are generally fixed, whereas the effective membrane time constant decreases with increasing transmembrane conductance. Hence we fix τ_s and vary τ_v when we alter β_s. As mentioned in Chapter 1, we keep $\tau_s = 5$ ms throughout this thesis. When $v_{\rm th} > \langle v \rangle$ (μ for the point-neuron model) and the effect of noise is negligible, we can calculate the deterministic limit using equation (1.54). This is shown as the black line in Figure 2.1(a).

Figure 2.1(a) shows that the upcrossing method for the particular parameters chosen can approximate firing rates less than 20Hz. When $v < \langle v \rangle$ and $\tau_s < \tau_v$, the upcrossing method tends to overestimate threshold-reset rate (see Appendix C.2.1). Figure 2.1(b) shows that the dimensionfull upcrossing rate increases with β_s (from decreasing τ_v), which is also reflected in the threshold-reset rate, and that the upcrossing method provides a good approximation for the threshold-reset rate over a range of β_s. Similar to the analysis performed in [9], the accuracy of the upcrossing method is seen in greater detail in Appendix C.2.1, Figure C.3(a).

In the subthreshold regime ($v < \langle v \rangle$) throughout this thesis we typically choose a membrane parameter set that is biophysically plausible, for which the upcrossing method is reasonably accurate, and shows a wide range of the mathematically predicted behaviours. Therefore for reasons of biophysical plausibility combined with the analysis of the upcrossing approximation's accuracy in Appendix C.2.1, we usually choose $\beta_s = 0.5$ and $(v_{\rm th} - \langle v \rangle)/\sigma_v \sim 3$ when we fix the mean.

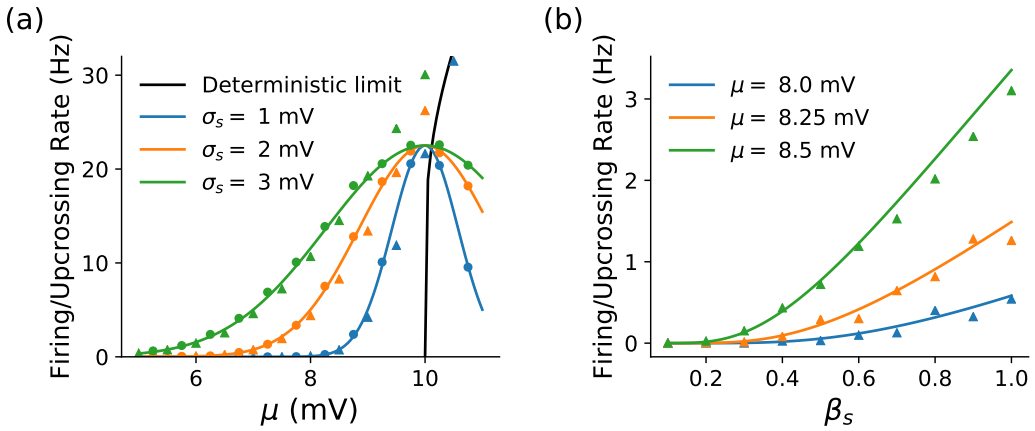

Figure 2.1: (a) For the point-neuron model, the upcrossing method (2.19) (solid lines) approximates the subthreshold firing rate well for rates lower than 20Hz. As a convention used throughout this thesis, numerical simulations of the upcrossing rate are shown as circles, while those of the threshold-reset rate are shown as triangles. (b) Increasing β_s by decreasing τ_v increases the fluctuation-driven firing rate as predicted by the upcrossing approximation. Other parameters: (a-b) $v_{\text{th}} = 10\text{mV}$, (a) $\tau_v = 10\text{ms}$. (b) $\sigma_s = 1\text{mV}$.

2.3 Infinite Dendrite

The first spatial model we introduce is the infinite dendrite, as it is spatially homogeneous and can be straightforwardly compared with the point-neuron model. The infinite dendrite can be interpreted as two long identical dendrites with identically distributed drive radiating from a soma with negligible electrical properties (hereafter referred to as a "nominal" soma). This model has the cable equation derived in Chapter 1 (1.43). Removing the dimensions from space with $X = \lambda x$ along with time as before, we find

$$\frac{\partial v}{\partial t} = \mu - v + \frac{\partial^2 v}{\partial x^2} + s(x,t), \quad \beta_s \frac{\partial s}{\partial t} = -s + 2\sigma_s \sqrt{\beta_s}\xi_s(x,t). \tag{2.20}$$

Since the cable is infinite, we have the boundary conditions that the potential cannot continually grow with distance

$$|v(\pm\infty, t)| < \infty. \tag{2.21}$$

As the infinite dendrite is uniformly driven by synaptic drive, we should expect the mean to also be uniform with x. Since by construction $\langle s \rangle = 0$, and we are in the

steady state, in general the mean can be obtained by solving the equation

$$\langle v \rangle - \mu = \frac{\partial^2 \langle v \rangle}{\partial x^2}, \tag{2.22}$$

which has the solution $\langle v \rangle = \mu$ due to the spatial homogeneity of the synaptic drive.

2.3.1 Infinite Dendrite Variances, White-Noise

There are many ways of calculating the variances of an infinite dendrite. For white noise, previous analysis exists for this model by Fourier series [125]. In this chapter, we will start with simple spatial models using Fourier transforms in both space and time, with the spatial Fourier transform pair used here as

$$\hat{f}(k) = \int_{-\infty}^{\infty} e^{-ikx} f(x) \mathrm{d}x, \quad f(x) = \frac{1}{2\pi} \int_{-\infty}^{\infty} e^{ikx} \hat{f}(k) \mathrm{d}k. \tag{2.23}$$

With white noise, performing Fourier transforms in space and time gives

$$\hat{v}_F(k, \omega) = \frac{2\sigma_{\mathrm{WN}} \hat{\xi}_s(k, \omega)}{1 + k^2 + i\omega}, \tag{2.24}$$

where $\hat{\xi}_s(k, \omega)$ is the Fourier transform of the white-noise process in space and time. For an infinite cable, this has the correlator

$$\langle \hat{\xi}_s(k, \omega) \hat{\xi}_s(-k', -\omega') \rangle = 4\pi^2 \delta(k - k') \delta(\omega - \omega'), \tag{2.25}$$

however, as we shall note in future models, the spatial component of this correlator is affected by the boundary conditions of the cable. Since (i) the mean is constant in space, (ii) the spatial autocovariance depends only on the spatial difference rather than the absolute spatial positions, and (iii) the variance is finite, $v(x, t)$ is wide-sense stationary in space in addition to time. This means that we can utilise a spatial form of the Wiener-Khinchin theorem

$$K(\Delta, \tau) \equiv \langle v(x, t)(x + \Delta, t + \tau) \rangle, \quad S(k, \omega) \equiv |\hat{f}(k, \omega)|^2, \tag{2.26}$$

$$K(\Delta, \tau) = \frac{1}{4\pi^2} \int_{-\infty}^{\infty} e^{ik\Delta} \mathrm{d}k \int_{-\infty}^{\infty} S(k, \omega) e^{i\omega\tau} \mathrm{d}\omega. \tag{2.27}$$

Hence for white-noise drive, substituting (2.24) for $\hat{f}(k,\omega)$ in (2.26-2.27) gives the full autocovariance by the double inverse-transform

$$\langle v_F(x,t)v_F(x',t')\rangle = \frac{\sigma_{\text{WN}}^2}{\pi^2}\int_{-\infty}^{\infty} e^{ik(x-x')}\mathrm{d}k \int_{-\infty}^{\infty} \frac{e^{i\omega(t-t')}}{(1+k^2)^2+\omega^2}\mathrm{d}\omega. \tag{2.28}$$

While the infinite cable is one of the rare spatial cases where it is possible to compute this integral for the full autocovariance [125], it is more instructive to show the temporal and spatial autocovariance separately. $K(t-t')$ and $K(x-x')$ are given by setting $x=x'$ and $t=t'$ respectively

$$K(t-t') = \frac{\sigma_{\text{WN}}^2}{\pi}\int_{-\infty}^{\infty} \frac{e^{-|t-t'|(1+k^2)}}{1+k^2}\mathrm{d}k = \sigma_{\text{WN}}^2\,\mathrm{erfc}(\sqrt{|t-t'|}), \tag{2.29}$$

$$K(x-x') = \frac{\sigma_{\text{WN}}^2}{\pi}\int_{-\infty}^{\infty} \frac{e^{ik(x-x')}}{1+k^2}\mathrm{d}k = \sigma_{\text{WN}}^2 e^{-|x-x'|}. \tag{2.30}$$

We can take $t=t'$ in the temporal autocovariance or $x=x'$ in the spatial autocovariance to give $\sigma_v^2 = \sigma_{\text{WN}}^2$ as expected. These autocovariances also show that synaptic input is being filtered differently in time than in space. $K(t-t')$ in Figure 2.2(a, b) shows, in comparison with the point neuron, voltage fluctuations from synaptic drive decorrelate more rapidly in the infinite cable. Reintroducing dimensions with $X = x\lambda$ in (2.30) reveals that the range of spatial correlations increases with λ. Finally, multiplying the integrand of (2.28) by ω^2 shows that the derivative variance is still undefined as white-noise fluctuations are present at every spatial position.

2.3.2 Infinite Dendrite Variances, Coloured-Noise

With coloured-noise drive, taking Fourier transforms in time and space of (2.20) gives the fluctuating voltage as

$$\hat{v}_F(k,\omega) = \frac{2\sigma_s\sqrt{\beta_s}\hat{\xi}_s(k,\omega)}{(1+k^2+i\omega)(1+i\omega\beta_s)}. \tag{2.31}$$

Substituting $S(k,\omega) = |\hat{v}_F(k,\omega)|^2$ into (2.27) thus gives the full correlator as

$$K(x-x',t-t') = \frac{\sigma_s^2\beta_s}{\pi^2}\int_{-\infty}^{\infty} e^{ik(x-x')}\mathrm{d}k \int_{-\infty}^{\infty} \frac{e^{i\omega(t-t')}\mathrm{d}\omega}{[(1+k^2)^2+\omega^2](1+\omega^2\beta_s^2)}. \tag{2.32}$$

To find the temporal autocovariance, we set $x = x'$, and first calculate the ω-integral

$$K(t-t') = \frac{\sigma_s^2}{\pi}\int_{-\infty}^{\infty} \frac{(1+k^2)e^{-|t-t'|\beta_s^{-1}} - \beta_s^{-1}e^{-|t-t'|(1+k^2)}}{(1+k^2)(1+k^2+\beta_s^{-1})(1+k^2-\beta_s^{-1})}\mathrm{d}k, \tag{2.33}$$

which can also be resolved to give a closed-form solution that is functionally distinct from the point neuron coloured-noise autocovariance (2.12). This is due to spatial extent narrowing the profile as we saw earlier for white-noise drive. However, since this "narrowing" occurs on a combination of membrane and synaptic timescales, $K(t-t')$ is algebraically complex and is hence given in Appendix A.4.2.

We compare the temporal covariances for the passive models explored so far for both white and coloured synaptic drive in Figure 2.2(a, b). We see that for both types of synaptic drive, the autocovariance profile is narrower for the infinite dendrite when compared to the point-neuron model, meaning that fluctuations at a specific position along the cable decorrelate more quickly. Furthermore, as expected, Figure 2.2 shows that coloured synaptic drive causes the autocovariance to be broader and decay less rapidly for both models.

For the spatial autocovariance we let $t = t'$ and integrate with respect to ω to obtain

$$K(x-x') = \frac{\sigma_s^2}{\pi}\int_{-\infty}^{\infty} \frac{e^{ik(x-x')}}{(1+k^2)(1+\beta_s^{-1}+k^2)}\mathrm{d}k, \tag{2.34}$$

which itself integrates to

$$K(x-x') = \sigma_s^2\beta_s\left(e^{-|x-x'|} - \frac{e^{-|x-x'|\sqrt{1+\beta_s^{-1}}}}{\sqrt{1+\beta_s^{-1}}}\right). \tag{2.35}$$

This shows that the magnitude of correlations for all $x-x'$ increases with increasing β_s, but $K(x-x'=0)$ is always lower when compared with the white-noise spatial autocovariance (2.30) with the substitution $\sigma_{\mathrm{WN}}^2 = \sigma_s^2\beta_s$ (1.45). However, when we compare the spatial autocovariance with the variance with $K(x-x')/K(0)$, Figure 2.2(c) shows that increasing β_s increases the extent of correlations. This can be verified by checking the limits $\beta_s \to 0$ (white noise) and $\beta_s \to \infty$ (frozen noise) for $K(x-x')/K(0)$. Since increasing β_s broadens temporal correlations for a single location, intuitively there is more time for this temporally correlated voltage to diffuse spatially, thus increasing β_s broadens the extent of spatial correlations.

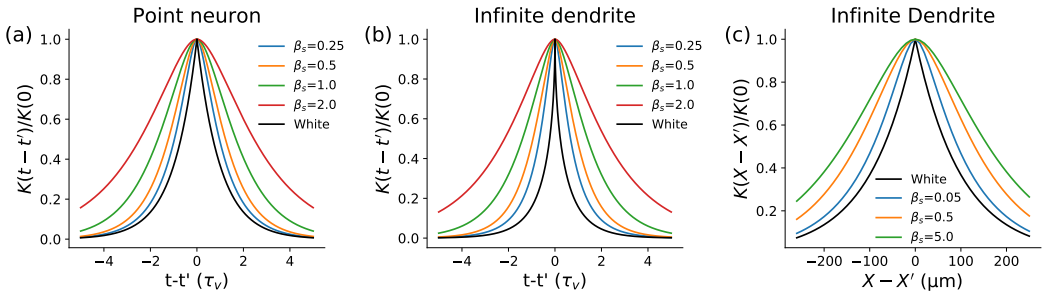

Figure 2.2: Given the same membrane and synaptic time constants, the time autocovariance for (a) the point neuron (2.8, 2.12) has wider profile than (b) the infinite dendrite (2.29, A.44). (c) The relative spatial autocovariance in the infinite dendrite (2.30, 2.35) increases with the relative timescale synaptic drive β_s. Other parameters: (b-c) $\lambda = 100\mu$m.

Finally, taking $t = t'$ and $x = x'$, the variance and derivative variance can be obtained by splitting the integrand of (2.32) into partial fractions giving

$$\sigma_v^2 = \sigma_s^2 \beta_s \left(1 - \sqrt{\frac{\beta_s}{1+\beta_s}}\right), \quad \sigma_{\dot{v}}^2 = \frac{\sigma_s^2}{\beta_s}\sqrt{\frac{\beta_s}{1+\beta_s}}. \tag{2.36}$$

The first aspect to note about these variances is that despite coming from a spatial model, the spatial parameter λ is not present. For spatial models λ indicates the length scale over which synaptic drive contributes to voltage fluctuations. However, the lack of X dependence means that no other variables carry units of length so λ cannot be present on dimensional grounds. Secondly, in comparison with the point neuron (2.13, 2.16), the variances have a qualitatively different dependence on β_s. For all β_s this results in σ_v^2 being lower for the infinite dendrite while $\sigma_{\dot{v}}^2$ is higher.

2.3.3 Infinite Dendrite, Firing Rate

With the variances now obtained, we can substitute into the formula for the steady-state upcrossing rate (2.1), which gives a different dependence on the input parameters than the point neuron (2.19)

$$r_{\text{uc}} = \frac{1}{2\pi\beta_s}\sqrt{\frac{\sqrt{\beta_s}}{\sqrt{1+\beta_s}-\sqrt{\beta_s}}}\exp\left[-\frac{(v_{\text{th}}-\langle v\rangle)^2\sqrt{1+\beta_s}}{2\sigma_s^2\beta_s(\sqrt{1+\beta_s}-\sqrt{\beta_s})}\right]. \tag{2.37}$$

For the threshold-reset simulation, we set $x_{\text{th}} = 0$ without loss of generality and reset the potential to v_{re} at all locations when $v(x_{\text{th}}, t) = v_{\text{th}}$ as described in 1.7.1.

With the same parameters (μ, σ_s, β_s) for which the upcrossing rate gives

a good approximation, both the upcrossing and threshold-reset rates are lower for the infinite dendrite than the point neuron, Figure 2.3(a). Furthermore, even if we adjust σ_s such that σ_v is the same for the point neuron and infinite dendrite, the upcrossing rates will not be the same because the ratio $\sigma_{\dot{v}}/\sigma_v$ differs between the two models, where we see that the infinite dendrite's upcrossing rate is always higher, Figure 2.3(b). In contrast, since the mean in the infinite dendrite is homogeneous and also equal to μ, the deterministic limit for the infinite dendrite is the same as the point neuron.

Measuring the relative error between the upcrossing and threshold-reset processes, Figure C.3(b) in Appendix C.2.1 shows that the upcrossing method for the infinite dendrite has a narrower range of parameters for which it acts as a good approximation of the threshold-reset firing rate, and that this range is shifted to higher β_s. This is because spatial extent gives a the narrower profile of $K(t-t')$, as we saw in Figure 2.2, leading to the upcrossing approximation overestimating the threshold-reset rate by a greater margin for $\beta_s < 1$ and $\langle v \rangle < v_{\text{th}}$.

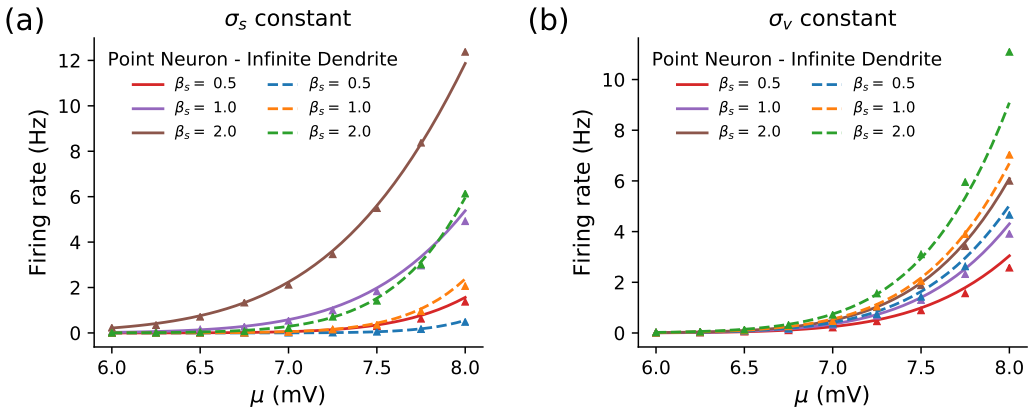

Figure 2.3: The upcrossing rates of the point neuron (2.19) and infinite dendrite (2.37), with triangles representing simulations of the threshold-reset process. (a) When σ_s (here $\sigma_s = 1.5$ mV) is kept constant, the point neuron upcrossing rate is considerably higher than that of the infinite dendrite. (b) On the other hand, when σ_v is kept fixed (here $\sigma_v = 1$mV) the infinite neuron has a higher upcrossing rate for a range of β_s.

2.4 Semi-Infinite Dendrite

We now consider the case of a semi-infinite dendrite with a sealed end at $X = 0$, which provides a boundary condition of zero axial current, requiring $\partial V/\partial X|_{X=0} = 0$. This can be interpreted as a toy model of the long apical dendrite in pyramidal

cells. Like the infinite dendrite, we can infer from (2.22) that the mean potential is spatially homogeneous, $\langle v \rangle = \mu$.

2.4.1 Semi-Infinite Dendrite Variances, White-Noise

While the double Fourier transform of v is exactly the same as the infinite case (2.24), the zero-current boundary condition at $x = 0$ changes the correlator of $\hat{\xi_s}(k, \omega)$. The effect of the sealed end can be replicated with an "image" cable from $x = 0$ to $-\infty$, with the added condition that the potential in the image reflects that in the original cable: $v(-x, t) = v(x, t)$. The reflected potential means that a white-noise process at x is delta-correlated with itself and an image at $-x$

$$\langle \xi_s(x,t)\xi_s(x',t') \rangle = \delta(t-t')[\delta(x-x') + \delta(x+x')]. \tag{2.38}$$

Applying Fourier transforms gives the correlator in the Fourier domain as

$$\langle \hat{\xi}_s(k,\omega)\hat{\xi}_s(-k',-\omega') \rangle = 4\pi^2\delta(\omega-\omega')[\delta(k-k') + \delta(k+k')]. \tag{2.39}$$

The effect of this change in correlator means that we can no longer simply use the space-time Wiener-Khinchin theorem (2.26) because the spatial correlator $K(x, x')$ depends on the absolute positions of x and x' rather than just the difference.

With this new correlator in Fourier space, we now have for $\langle v_F(x,t)^2 \rangle$

$$\begin{aligned}
\langle v_F(x,t)^2 \rangle &= \frac{\sigma_{\text{WN}}^2}{\pi^2} \int_{-\infty}^{\infty} e^{ikx} \mathrm{d}k \int_{-\infty}^{\infty} e^{i\omega t} \mathrm{d}\omega \int_{-\infty}^{\infty} e^{-ik'x} \mathrm{d}k' \\
&\quad \times \int_{-\infty}^{\infty} \frac{\delta(\omega-\omega')[\delta(k-k') + \delta(k+k')]}{(1+k^2+i\omega)(1+k'^2-i\omega')} e^{-i\omega' t} \mathrm{d}\omega \\
&= \frac{\sigma_{\text{WN}}^2}{\pi^2} \int_{-\infty}^{\infty} (1+e^{2ikx}) \mathrm{d}k \int_{-\infty}^{\infty} \frac{\mathrm{d}\omega}{(1+k^2)^2+\omega^2} = \frac{\sigma_{\text{WN}}^2}{\pi} \int_{-\infty}^{\infty} \frac{1+e^{2ikx}}{1+k^2} \mathrm{d}k \\
\sigma_v^2 &= \sigma_{\text{WN}}^2 (1+e^{-2x}).
\end{aligned} \tag{2.40}$$

Hence at $x = 0$ the variance of the semi-infinite cable is double the infinite case. We can also see that if we modify the spatio-temporal Wiener-Khinchin theorem by placing a factor $e^{ik(x-x')} + e^{ik(x+x')}$ in the integrand, this approach will also work for other semi-infinite sealed cables.

2.4.2 Semi-Infinite Dendrite Variances, Coloured-Noise

Using the same approach as for white noise, for coloured noise we can infer that the variance is given by

$$\begin{aligned}\sigma_v^2 &= \frac{\sigma_s^2\beta_s}{\pi^2}\int_{-\infty}^{\infty}(1+e^{2ikx})\mathrm{d}k\int_{-\infty}^{\infty}\frac{\mathrm{d}\omega}{[(1+k^2)^2+\omega^2](1+\omega^2\beta_s^2)}\\ &= \frac{\sigma_s^2}{\pi}\int_{-\infty}^{\infty}\frac{1+e^{2ikx}}{(1+k^2)(1+\beta_s^{-1}+k^2)}\mathrm{d}k,\\ \sigma_v^2(x) &= \sigma_s^2\beta_s\left[1+e^{-2x}-\sqrt{\frac{\beta_s}{1+\beta_s}}\left(1+e^{-2x\sqrt{1+\beta_s^{-1}}}\right)\right],\end{aligned} \tag{2.41}$$

from which we notice that unlike for white noise (2.40), the variance for coloured noise is not simply the infinite variance (2.36) multiplied by a single spatial factor (e.g. $1+e^{-2x}$). Rather, each component is multiplied by a distinct spatial factor. In contrast, for the derivative variance we have

$$\sigma_{\dot{v}}^2(x) = \frac{\sigma_s^2}{\pi\beta_s}\int_{-\infty}^{\infty}\frac{1+e^{2ikx}}{1+\beta_s^{-1}+k^2}\mathrm{d}k = \frac{\sigma_s^2}{\beta_s}\sqrt{\frac{\beta_s}{1+\beta_s}}\left(1+e^{-2x\sqrt{1+\beta_s^{-1}}}\right), \tag{2.42}$$

which is just the infinite derivative variance (2.36) multiplied by $1+e^{-2x\sqrt{1+\beta_s^{-1}}}$.

We note that when evaluated at $x=0$, the σ_v^2 and $\sigma_{\dot{v}}^2$ at $x=0$ are twice as high for the semi-infinite dendrite in comparison with the infinite dendrite. As the semi-infinite and infinite dendrite models can represent one and two-dendrite models emanating from a nominal soma respectively [130], this means that two identical dendrites with independent stochastic drive give half the sealed-end variance of a single dendrite. Hence despite more sources of synaptic drive in the infinite model, this is counteracted by the fact that fluctuations in one dendrite can diffuse freely to the other rather than being reflected at the boundary. This finding generalises to n identical dendrites driven by synaptic drive, where one can show using the approach outlined here that the variances at $x=0$ are $1/n$ the semi-infinite case (2.41, 2.42).

2.4.3 Semi-Infinite Dendrite, Firing Rate

Placing the trigger position at the nominal soma, $x_{\mathrm{th}}=0$, the higher variances for the semi-infinite dendrite has implications for both the upcrossing approximation and the firing rate, as we illustrate in Figure 2.4. Firstly the $\sigma_{\dot{v}}/\sigma_v$ prefactor for the upcrossing rate (2.1) will be the same for the two models. However the doubling of σ_v^2 in the exponent leads to the semi-infinite dendrite having a much higher upcrossing

rate given the same fluctuation strength σ_s. Since the mean is equal to μ everywhere in these two models, this means that this is the only change in the upcrossing rate between them. Furthermore, it implies that if we instead fix σ_v for the two models, the upcrossing rate will be the same in each case, as we see in Figure 2.5(a).

In the suprathreshold regime, as the mean of both models is uniform and equal to μ, the deterministic limit for the two models is the same, as we also see in Figure 2.4. Moreover, in the subthreshold regime after the upcrossing approximation becomes inaccurate, the semi-infinite model retains a higher firing rate for the same value of σ_s (Figure 2.4) but the same firing rate as the infinite model for fixed σ_v, Figure 2.5(b). This shows that σ_v^2 being the only difference for the firing of the two models is not just limited to specific limiting cases of μ but applies across the whole voltage range.

As in the case for the infinite dendrite, both the upcrossing rate and the simulated firing rate for the semi-infinite dendrite are independent of the length constant λ, as seen in Figure 2.5(a).

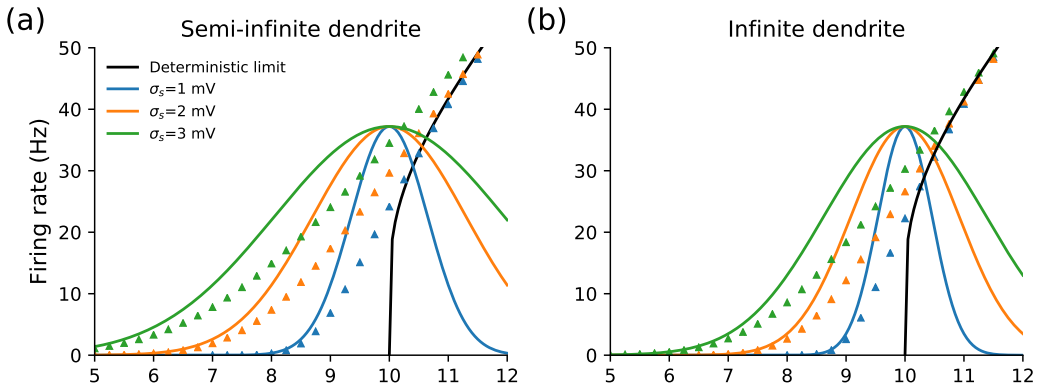

Figure 2.4: Comparing the firing rates of the semi-infinite (a) and infinite (b) dendrites subject to coloured noise, with solid lines representing the upcrossing approximation (2.37) and triangles threshold-reset simulations, reveals that the firing rate is significantly higher in the subthreshold range ($\mu < 10$mV) for the semi-infinite dendrite. This applies even in the region where the upcrossing approximation is no longer accurate (e.g. $\mu = 9$-10 mV). However, for $\mu > v_{\text{th}}$, the firing rates for both structures converge to the same deterministic limit. Other parameters: $\tau_v = 10$ms, $\tau_s = 5$ms, $v_{\text{th}} = 10$mV, $v_{\text{re}} = 0$mV.

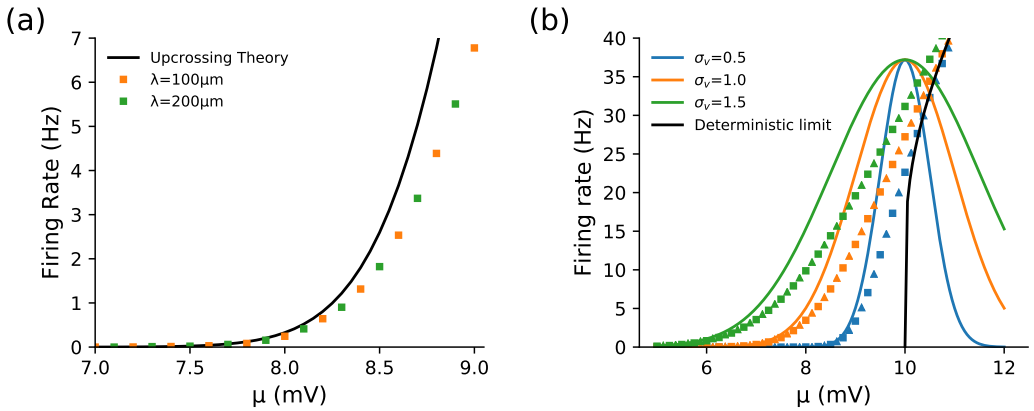

Figure 2.5: (a) Both the upcrossing and simulated threshold-reset rates are independent of λ for the semi-infinite dendrite model, $\sigma_s = 1\text{mV}$. (b) For fixed σ_v, the infinite and semi-infinite models show not only the same upcrossing rate but the same firing rate across the whole voltage range. Here squares denote threshold-reset simulations of the semi-infinite model while triangles denote the infinite model. Other parameters: $\tau_v = 10\text{ms}$, $\tau_s = 5\text{ms}$, $v_{\text{th}} = 10\text{mV}$, $v_{\text{re}} = 0\text{mV}$.

2.5 Finite Sealed Dendrite

For the previous two spatial models, we have assumed that the dendrites are so long that the effects of the distal ends can be ignored. Here we analyse the variances a finite dendrite of length L, where the dendrite is sealed at both ends: $\partial V/\partial X|_{X=0} = 0$ and $\partial V/\partial X|_{X=L} = 0$. We represent the non-dimensional length as $l = L/\lambda$. The upcrossing rate is not calculated or shown in this section since we found no distinguishing features in comparison with the infinite and semi-infinite models.

Since there are now two reflecting boundaries, this changes the noise correlator further to become an infinite summation

$$\langle \xi_s(x,t)\xi_s(x',t')\rangle = \delta(t-t') \sum_{m=-\infty}^{\infty} \delta(x-x'+2ml) + \delta(x+x'+2ml). \tag{2.43}$$

In the Fourier domain, the correlator is also a summation, given by

$$\langle \hat{\xi}_s(\omega,k)\hat{\xi}_s(-\omega',-k')\rangle = 4\pi^2\delta(\omega-\omega') \sum_{m=-\infty}^{\infty} [\delta(k-k') + \delta(k+k')]e^{2ik'ml}, \tag{2.44}$$

where a derivation can be found in Appendix A.4.1.

2.5.1 Sealed Dendrite Variances, White-Noise

For a sealed cable driven by white-noise, the variance can be calculated from the following steps

$$\begin{aligned}\sigma_v^2 &= \frac{\sigma_{\text{WN}}^2}{\pi^2}\sum_{m=-\infty}^{\infty}\int_{-\infty}^{\infty}e^{ikx}\mathrm{d}k\int_{-\infty}^{\infty}\frac{e^{i\omega t}\mathrm{d}\omega}{1+k^2+i\omega}\int_{-\infty}^{\infty}e^{-ik'x}\mathrm{d}k'\int_{-\infty}^{\infty}\frac{e^{-i\omega' t}\mathrm{d}\omega}{1+k'^2-i\omega'}\\ &\times\delta(\omega-\omega')[\delta(k-k')+\delta(k+k')]e^{2ik'ml}\\ &= \frac{\sigma_{\text{WN}}^2}{\pi^2}\sum_{m=-\infty}^{\infty}\int_{-\infty}^{\infty}e^{ikx}\mathrm{d}k\int_{-\infty}^{\infty}[e^{-ikx}e^{2ikml}+e^{-2ikml}e^{ikx}]\frac{\mathrm{d}\omega}{(1+k^2)+\omega^2}\\ &= \frac{\sigma_{\text{WN}}^2}{\pi}\sum_{m=-\infty}^{\infty}\int_{-\infty}^{\infty}\frac{e^{2ikml}+e^{2ik(x-2ml)}}{1+k^2}\mathrm{d}k = \sigma_{\text{WN}}^2\sum_{m=-\infty}^{\infty}e^{-2|ml|}+e^{-2|x-ml|},\end{aligned} \tag{2.45}$$

from which we can resolve this summation and rearrange to give

$$\sigma_v^2 = \frac{2\sigma_{\text{WN}}^2\cosh(l-x)\cosh x}{\sinh l}. \tag{2.46}$$

Since this form of expression appears frequently for the sealed dendrite, we define the function

$$C(x,\zeta) = \frac{2\cosh[(l-x)\sqrt{1+\zeta}]\cosh(x\sqrt{1+\zeta})}{\sqrt{1+\zeta}\sinh(l\sqrt{1+\zeta})}, \tag{2.47}$$

allowing us to write the variance as $\sigma_v^2 = \sigma_{\text{WN}}^2 C(x,0)$.

As we see in Figure 2.6(a), this variance is highest at the sealed ends and symmetric about $l/2$, where the variance is lowest. We introduce the ratio of the bulk to edge variance, $\sigma_v^2(l/2)/\sigma_v^2(0)$, as a measure of the similarity between the sealed dendrite and the semi-infinite dendrite. Substituting our result for white noise (2.46), we find

$$\frac{\sigma_v^2(l/2)}{\sigma_v^2(0)} = \frac{1}{1+\tanh^2(l/2)}, \tag{2.48}$$

which converges to $1/2$ as $l\to\infty$, the case of the semi-infinite dendrite (2.40), and 1 as $l\to 0$, an isopotential neuron. We see in Figure 2.6(b) that the relative variance profile $\sigma_v^2(X)/\sigma_v^2(0)$ for the first half of the sealed dendrite is highly similar to the semi-infinite dendrite for $\lambda \le 200\mu$m (i.e. $l \ge 5$ for $L = 1000\mu$m).

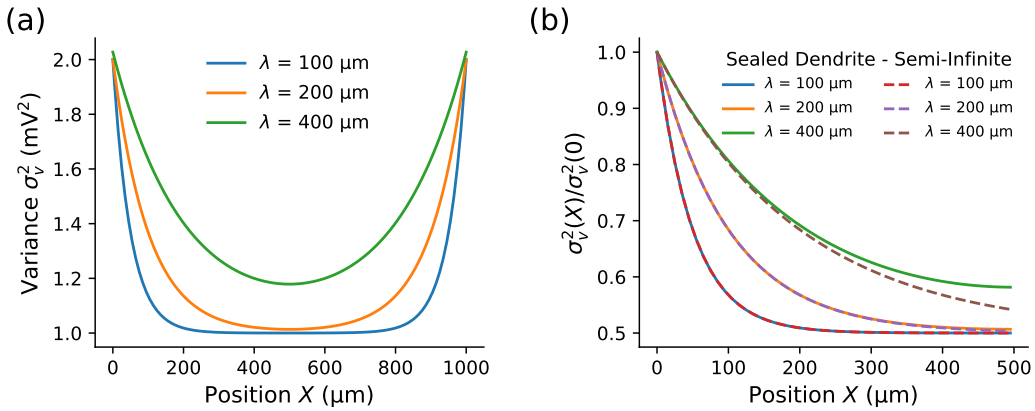

Figure 2.6: (a) Increasing λ increases the white-noise variance (2.46) at all points in a sealed dendrite and leads to a flatter variance profile near the centre. (b) In the first half of the sealed dendrite, we see that for $\lambda \leq 200\mu$m, the ratio $\sigma_v^2(X)/\sigma_v^2(0)$ is highly similar between the sealed dendrite (solid line) and the semi-infinite dendrite (2.40) (dashed). Other parameters $L = 1000\mu$m, $\sigma_{\text{WN}} = 1$mV.

2.5.2 Sealed Dendrite Variances, Coloured-Noise

Based on the approach we used for coloured noise in a semi-infinite dendrite and white noise in a sealed dendrite, the variance for coloured noise in a sealed dendrite proceeds from

$$\begin{aligned}\sigma_v^2 &= \frac{\sigma_s^2}{\pi}\sum_{m=-\infty}^{\infty}\int_{-\infty}^{\infty}\frac{e^{2ikml}+e^{-2ikml}e^{2ikx}}{(1+k^2)(1+\beta_s^{-1}+k^2)}\mathrm{d}k \\ &= \frac{\sigma_s^2\beta_s}{\pi}\sum_{m=-\infty}^{\infty}\int_{-\infty}^{\infty}(e^{2ikml}+e^{-2ikml}e^{2ikx})\left(\frac{1}{1+k^2}-\frac{1}{1+\beta_s^{-1}+k^2}\right)\mathrm{d}k, \quad (2.49)\end{aligned}$$

where we can see that the first term of the integral with denominator $1/(1+k^2)$ will simply give us the white-noise variance (2.46). For the second term with denominator $1/(1+\beta_s^{-1}+k^2)$, we find an analogous form

$$\frac{1}{\sqrt{1+\beta_s^{-1}}}\sum_{m=-\infty}^{\infty} e^{-2|ml|\sqrt{1+\beta_s^{-1}}}+e^{-2|x-ml|\sqrt{1+\beta_s^{-1}}}, \quad (2.50)$$

which we can infer from the previous summation reduces to

$$\frac{2\cosh[(l-x)\sqrt{1+\beta_s^{-1}}]\cosh(x\sqrt{1+\beta_s^{-1}})}{\sqrt{1+\beta_s^{-1}}\sinh(l\sqrt{1+\beta_s^{-1}})}. \quad (2.51)$$

Recalling $C(x, \zeta)$ (2.47), this means that the coloured-noise variance is given by

$$\sigma_v^2 = \sigma_s^2 \beta_s [C(x, 0) - C(x, \beta_s^{-1})]. \tag{2.52}$$

Putting the spatial dimensions back into (2.52) with $X = x\lambda$ and $L = l\lambda$, in $C(x, \beta_s^{-1})$ the synaptic drive changes the length constant to $\lambda/\sqrt{1 + \beta_s^{-1}}$.

As with white noise, the coloured-noise variance is greatest at the ends of the cable and lowest at the centre, with λ determining the extent to which the ends affect the variance at the centre. The effective membrane time constant τ_v also plays a role however, with Figure 2.7(a) showing that increasing $\tau_v/\tau_s = \beta_s^{-1}$ decreases the effective length constant. Here the white-noise profile is the limit of $\tau_v \to \infty$, which is analogous to how the the white-noise profile of $K(x - x')$ for the infinite dendrite was narrowest in Figure 2.2.

For the derivative variance, we can use the same approach as before or simply use the relation between the white- and coloured-noise variances given earlier (2.17) to obtain

$$\sigma_{\dot{v}}^2 = \frac{\sigma_s^2}{\beta_s} C(x, \beta_s^{-1}). \tag{2.53}$$

Like the variance, λ and β_s determine the extent to which the cable ends affect the derivative variance throughout the cable. Figure 2.7(b) shows that the $\sigma_{\dot{v}}^2$ decays more rapidly than σ_v^2 as x increases above zero, since it only has the length constant altered by synaptic filtering, $\lambda/\sqrt{1 + \beta_s^{-1}}$. Furthermore, we also see increasing τ_v (and hence decreasing β_s) reduces the end effects on $\sigma_{\dot{v}}^2$.

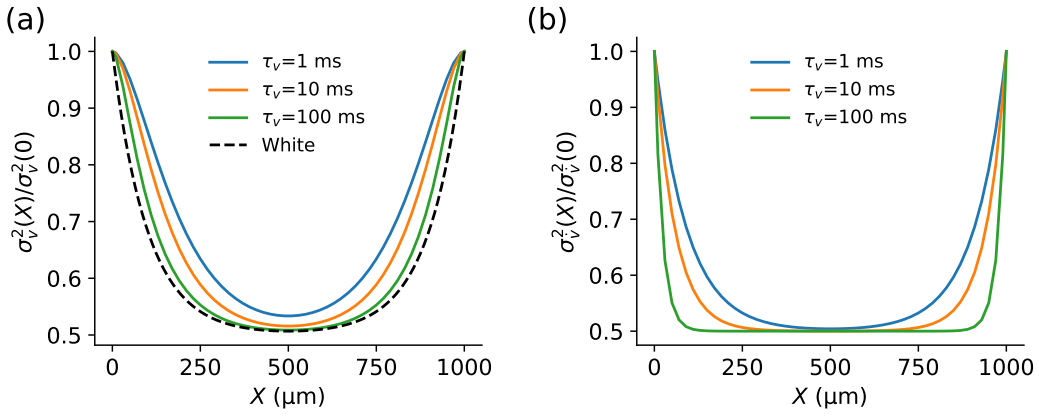

Figure 2.7: (a) For the coloured-noise variance in the sealed dendrite (2.52), increasing τ_v causes end effects to decrease. (b) This is also observed for the derivative variance (2.53). Other parameters: $L = 1000\mu$m, $\tau_s = 5$ms, $\sigma_s = 1$mV, $\lambda = 200\mu$m.

From this analysis, we can see that we can approximate the variances of the first half of a long dendrite with $L \sim 1000\mu$m from the semi-infinite variances if $\lambda \leq 200\mu$m. However, we note that slower relative synaptic drives (higher β_s) reduces the accuracy of this approximation.

2.6 Dendrite-and-Axon Model

Here we expand the model to consider two cables, a dendrite receiving synaptic drive as before and an unmyelinated passive axon receiving no synaptic drive, as detailed in Figure 2.8. We do not consider the effects of myelination because we are interested in the rate at which spikes are triggered, as calculated from voltage statistics of the unmyelinated axon initial segment (AIS), rather than propagation of spikes through the myelinated axon. However, myelination will lower the load conductance of the axon, and it is possible to deal with myelination in this framework using a model similar to [132].

As described in section 1.5, the action potential (AP) is initiated a short distance down the axon in the AIS, a distance which has some variation both between different types of neurons [122, 133, 134], neurons of the same type [16], and can be altered by electrical activity [121]. This model allows us to vary the site of AP initiation, which we will hereafter term the trigger position denoted by X_{th}, and observe how this affects the firing properties. Furthermore, as axons are typically thinner than dendrites [16], these two cables will have different properties, which again will affect the firing rate.

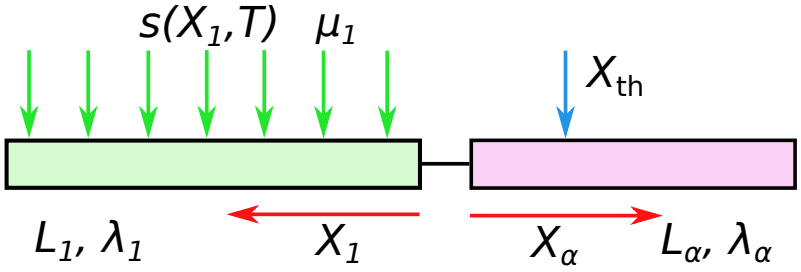

Figure 2.8: Model of a dendrite receiving synaptic drive (green arrows) connected to a passive axon receiving no input. The trigger position along the axon, X_{th}, is shown by the blue arrow. For semi-infinite neurites we take $L_1 = \infty = L_\alpha$.

With a dendrite receiving synaptic drive connected at its end to a passive axon receiving no drive, we denote the dendritic and axonal properties by the subscripts 1 and α respectively. Measuring the voltages v_1 and v_α both from E_L (as-

sumed the same in both neurites), our general dendrite-and-axon model is

$$\tau_1 \frac{\partial v_1}{\partial T} = \mu_1 - v_1 + \lambda_1^2 \frac{\partial^2 v_1}{\partial X_1^2} + s_1, \quad \tau_\alpha \frac{\partial v_\alpha}{\partial T} = -v_\alpha + \lambda_\alpha^2 \frac{\partial^2 v_\alpha}{\partial X_\alpha^2}, \tag{2.54}$$

where the neurites meet at $x_1 = 0 = x_\alpha$, representing a nominal soma. Since we choose to measure v_1 and v_α from the same level E_L, the boundary conditions of continuity of potential and conservation of current are

$$v_1(0,T) = v_\alpha(0,T), \quad \lambda_1 G_{\lambda_1} \frac{\partial v_1}{\partial X_1}(0,T) + \lambda_\alpha G_{\lambda_\alpha} \frac{\partial v_\alpha}{\partial X_\alpha}(0,T) = 0. \tag{2.55}$$

We will treat the dendrite and axon as semi-infinite and reasonably assume (as is typically done in other models [98, 135, 136]) that the membrane capacitance per unit area, leak conductance per unit area and leak current reversal potential is the same in both the dendrite and axon.

We rescale the spatial dimension with respect to each neurite, so that $x_1 = X_1/\lambda_1$ and $x_\alpha = X_\alpha/\lambda_\alpha$. However we rescale time in both neurites with respect to the dendritic time constant. Defining $\beta_\alpha = \tau_\alpha/\tau_1$, our rescaled equations are

$$\frac{\partial v_1}{\partial t} = \mu_1 - v_1 + \frac{\partial v_1^2}{\partial x_1^2} + s_1, \quad \beta_\alpha \frac{\partial v_\alpha}{\partial t} = -v_\alpha + \frac{\partial v_\alpha^2}{\partial x_\alpha^2}, \tag{2.56}$$

where since we assume the same capacitance per unit area in the dendrite and unmyelinated axon, then $\beta_\alpha = g_1/g_\alpha$, where g_α is the membrane conductance per unit area of the axon.

2.6.1 Dendrite-and-Axon, Green's Functions

For more general boundary conditions that exist with neuronal sections with different properties, we cannot use the method of taking Fourier transforms in space and time. Instead we use Green's functions in space and frequency. Integration of these Green's functions with the stochastic drive can then yield the mean, variances, and later in Chapter 3 these quantities under modulation. For a space-time delta input to the dendrite at location y_1 at time t', the Green's functions $\mathcal{G}_{11}(x_1, y_1; t, t')$ and $\mathcal{G}_{\alpha 1}(x_\alpha, y_1; t, t')$ satisfy

$$\frac{\partial \mathcal{G}_{11}}{\partial t} = -\mathcal{G}_{11} + \frac{\partial^2 \mathcal{G}_{11}}{\partial x_1^2} + \delta(x_1 - y_1)\delta(t - t'), \quad \beta_\alpha \frac{\partial \mathcal{G}_{\alpha 1}}{\partial t} = -\mathcal{G}_{\alpha 1} + \frac{\partial^2 \mathcal{G}_{\alpha 1}}{\partial x_\alpha^2}, \tag{2.57}$$

where the notation $\mathcal{G}_{jk}$ denotes the response in neurite j due to an input in neurite k. As the Fourier domain also allows for treatment of the soma and quasi-active

currents [103, 104], the Green's function in the Fourier domain $\tilde{\mathcal{G}}(x_i, y_j; \omega)$ is more appropriate. Taking the temporal Fourier transform of (2.57) and defining $\gamma_1 = \sqrt{1 + i\omega}$ and $\gamma_\alpha = \sqrt{1 + i\omega\beta_\alpha}$ gives a second order differential equation in x_j for each neurite

$$\gamma_1^2 \tilde{\mathcal{G}}_{11}(x_1, y_1; \omega) = \frac{\partial^2 \tilde{\mathcal{G}}_{11}}{\partial x_1^2} + \delta(x_1 - y_1), \quad \gamma_\alpha^2 \tilde{\mathcal{G}}_{\alpha 1}(x_\alpha, y_1; \omega) = \frac{\partial^2 \tilde{\mathcal{G}}_{\alpha 1}}{\partial x_\alpha^2}, \tag{2.58}$$

where the boundary conditions for the Green's functions are inherited from the cable equations (2.55)

$$\tilde{\mathcal{G}}_{11}(0, y_1; \omega) = \tilde{\mathcal{G}}_{\alpha 1}(0, y_1; \omega), \quad G_{\lambda 1} \frac{\partial \tilde{\mathcal{G}}_{11}}{\partial x_1} + G_{\lambda_\alpha} \frac{\partial \tilde{\mathcal{G}}_{\alpha 1}}{\partial x_\alpha} = 0. \tag{2.59}$$

Noting our earlier definitions of λ and G_λ in section 1.3.3, and assuming that the axial resistivity r_a is constant in both neurites, we can express $G_{\lambda_\alpha}/G_{\lambda 1}$ in terms of the ratio of length constants and β_α

$$\frac{G_{\lambda_\alpha}}{G_{\lambda 1}} = \frac{2\pi a_\alpha \lambda_\alpha g_\alpha}{2\pi a_1 \lambda_1 g_1} = \frac{\lambda_\alpha^3}{\beta_\alpha^2 \lambda_1^3}. \tag{2.60}$$

Here we will introduce the sum-over-trips formalism described in [103, 104, 137] because it generalises to any number of dendrites. This approach is explained in more detail in the Appendix A.2 and can be used to derive the time- or Fourier-domain Green's function of an arbitrary neuronal branching structure by considering all possible paths from a measurement location x_i to an input location y_j.

Since all the morphologies we consider with multiple neurites have them all as semi-infinite, we only need to consider two situations: the response at x_i from an input on the same neurite at y_i, Figure 2.9(a), and the response at x_i from an input on a different neurite at y_j, Figure 2.9(b). With $\gamma_i = \sqrt{1 + i\omega\beta_i}$, the Green's functions for these two cases are given by

$$\begin{aligned} \tilde{\mathcal{G}}_{ii}(x_i, y_i; \omega) &= \frac{e^{-|x_i - y_i|\gamma_i}}{2\gamma_i} + (2\tilde{f}_i - 1)e^{-|x_i + y_i|\gamma_i}, \\ \tilde{\mathcal{G}}_{ij}(x_i, y_j; \omega) &= \tilde{f}_j \frac{e^{-(x_i\gamma_i + y_j\gamma_j)}}{\gamma_j}, \end{aligned} \tag{2.61}$$

where the segment factor $\tilde{f}_j$ represents the relative admittance of neurite j compared to the whole node. For m neurites that emanate from a node with a soma (denoted

by the subscript σ), it is given by [103, 104]

$$\tilde{f}_j = \frac{Y_j(\omega)}{Y_\sigma(\omega) + \sum_{i=1}^{m} Y_i(\omega)}, \quad Y_j(\omega) = G_{\lambda_j}\gamma_j, \quad Y_\sigma(\omega) = G_\sigma \gamma_\sigma^2. \tag{2.62}$$

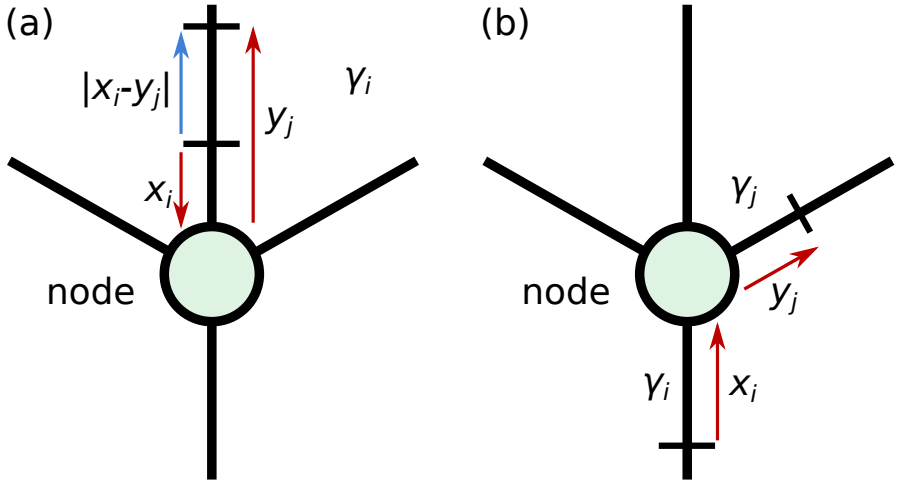

Figure 2.9: Examples of different trips on semi-infinite neurites from output x_i to input y_j: (a) There are two trips from x_i to y_j on the same neurite, one of length $|x_i + y_j|$ (red) and another of length $|x_i - y_j|$ (blue). (b) There is a single trip from x_i to y_j on different neurites.

With the dendrite-and-axon model there are only two neurites, and since input only arrives at the dendrite, we only need consider $\tilde{\mathcal{G}}_{11}$ and $\tilde{\mathcal{G}}_{\alpha 1}$. Thus we only the segment factor $\tilde{f}_1(\omega)$ is required, which is given by

$$\tilde{f}_1(\omega) = \frac{G_{\lambda_1}\gamma_1}{G_{\lambda_1}\gamma_1 + G_{\lambda_\alpha}\gamma_\alpha} = \frac{\beta_\alpha^2 \lambda_1^3 \gamma_1}{\beta_\alpha^2 \lambda_1^3 \gamma_1 + \lambda_\alpha^3 \gamma_\alpha}, \tag{2.63}$$

and hence we can conclude that the Green's functions are

$$\tilde{\mathcal{G}}_{11}(x_1, y_1; \omega) = \frac{e^{-|x_1 - y_1|\gamma_1}}{2\gamma_1} + \frac{e^{-|x_1 + y_1|\gamma_1}}{2\gamma_1}\left(\frac{\beta_\alpha^2 \lambda_1^3 \gamma_1 - \lambda_\alpha^3 \gamma_\alpha}{\beta_\alpha^2 \lambda_1^3 \gamma_1 + \lambda_\alpha^3 \gamma_\alpha}\right), \tag{2.64}$$

$$\tilde{\mathcal{G}}_{\alpha 1}(x_\alpha, y_1; \omega) = \frac{\beta_\alpha^2 \lambda_1^3 e^{-(x_\alpha \gamma_\alpha + y_1 \gamma_1)}}{\beta_\alpha^2 \lambda_1^3 \gamma_1 + \lambda_\alpha^3 \gamma_\alpha}. \tag{2.65}$$

With these Green's functions and an arbitrary input $\tilde{I}(y_1; \omega)$, the potential in neurite

j in the Fourier domain is

$$\tilde{v}_j(x_j,\omega) = \int_0^\infty \tilde{\mathcal{G}}_{j1}(x_j,y_1;\omega)\tilde{I}(y_1;\omega)\mathrm{d}y_1. \tag{2.66}$$

Taking the inverse Fourier transform yields the potential in the time domain

$$v_j(x_j,t) = \frac{1}{2\pi}\int_{-\infty}^\infty e^{i\omega t}\mathrm{d}\omega \int_0^\infty \tilde{\mathcal{G}}_{j1}(x_j,y_1;\omega)\tilde{I}(y_1;\omega)\mathrm{d}y_1. \tag{2.67}$$

From this general expression we will proceed to compute the mean and variances in the axon.

2.6.2 Dendrite-and-Axon, Mean

Due to the lack of synaptic drive in the axon, the mean is no longer spatially uniform in either the dendrite and axon. Recall from section 1.4.2 that we scaled the synaptic drive and intensity according to

$$s = \frac{g_{sF}(E_s - \langle V_1\rangle)}{g_1}, \quad \sigma_s = \frac{\sigma_g(E_s - \langle V_1\rangle)}{g_1}. \tag{2.68}$$

Now that $\langle V_1\rangle \neq E_L + \mu$, if we rescale in the same way, and keep all other quantities constant, this would imply that σ_s is now spatially dependent. However since E_s is typically much larger than $\langle V_1\rangle$ and E_L when its value is dominated by excitatory synapses ($E_s \sim 0\text{mV}$, $E_L \sim -70\text{mV}$), (2.68) can be approximated by our spatially homogeneous definitions of s and σ_s used earlier in (1.43). Nevertheless, the methods we present here can account for spatially varying σ_s.

To obtain the mean, we could simply take the expectation of each term in (2.56) and solve the second order ODE. However, it is simple to use the Green's functions we just derived (2.64) if we note that the input into dendrite is given by

$$\tilde{I}(y_1,\omega) = 2\pi\mu_1\delta(\omega) + \tilde{s}(y_1,\omega). \tag{2.69}$$

Substituting this into (2.67), we get the potential in neurite j as

$$\begin{aligned} v_j(x_j,t) = \mu_1 &\int_0^\infty \tilde{\mathcal{G}}_{j1}(x_j,y_1;0)\mathrm{d}y_1 \\ &+ \frac{1}{2\pi}\int_{-\infty}^\infty e^{i\omega t}\mathrm{d}\omega \int_0^\infty \tilde{\mathcal{G}}_{j1}(x_j,y_1;\omega)\tilde{s}(y_1;\omega)\mathrm{d}y_1, \end{aligned} \tag{2.70}$$

which after we take the expectation, and recalling that $\langle \tilde{s} \rangle = 0$, we obtain the mean

$$\langle v_j(x_j) \rangle = \mu_1 \int_0^\infty \tilde{\mathcal{G}}_{j1}(x_j, y_1; 0) \mathrm{d}y_1. \tag{2.71}$$

For the dendrite, this gives the mean as

$$\langle v_1(x_1) \rangle = \mu_1 \left(1 - \frac{\lambda_\alpha^3 e^{-x_1}}{\beta_\alpha^2 \lambda_1^3 + \lambda_\alpha^3} \right), \tag{2.72}$$

while for the axon the mean is

$$\langle v_\alpha(x_\alpha) \rangle = \frac{\mu_1 \beta_\alpha^2 \lambda_1^3}{\beta_\alpha^2 \lambda_1^3 + \lambda_\alpha^3} e^{-x_\alpha} = \mu_1 \tilde{f}_1(0) e^{-x_\alpha}. \tag{2.73}$$

This shows that the mean monotonically decreases for decreasing x_1 and increasing x_α. This is shown in Figure 2.10(a), with the mean in the axon decaying much more rapidly with distance from $x = 0$ than in the dendrite.

2.6.3 Dendrite-and-Axon Variances, White-Noise

Since APs are initiated in the axon [97,98], to calculate the upcrossing rate we need only find the variances in the axon. Since we have taken the Fourier transform in time and not in space, we utilise the correlator

$$\langle \tilde{\xi}_s(y, \omega) \tilde{\xi}_s(y', -\omega') \rangle = 2\pi \delta(y - y') \delta(\omega - \omega'). \tag{2.74}$$

The variance in neurite j can be found from subtracting the mean from (2.70), squaring and taking the expectation, yielding

$$\begin{aligned} \sigma_{v_j}^2(x_j) = \frac{1}{(2\pi)^2} \int_{-\infty}^\infty e^{i\omega t} \mathrm{d}\omega \int_0^\infty \tilde{\mathcal{G}}_{j1}(x_j, y_1; \omega) \mathrm{d}y_1 \\ \times \int_{-\infty}^\infty e^{-i\omega' t} \mathrm{d}\omega' \int_0^\infty \tilde{\mathcal{G}}_{j1}(x_1, y_1'; -\omega') \langle \tilde{s}(y_1, \omega) \tilde{s}(y_1', -\omega') \rangle \mathrm{d}y_1'. \end{aligned} \tag{2.75}$$

For both white and coloured noise, the expectation of the fluctuating synaptic component has the form

$$\langle \tilde{s}(y_1, \omega) \tilde{s}(y_1', -\omega') \rangle = 2\pi \delta(y - y') \delta(\omega - \omega') |\tilde{s}(y_1, \omega)|^2, \tag{2.76}$$

and hence the variance integral reduces to

$$\sigma^2_{v_j}(x_j) = \frac{1}{2\pi}\int_{-\infty}^{\infty} \mathrm{d}\omega \int_0^{\infty} |\tilde{\mathcal{G}}_{j1}(x_j, y_1; \omega)|^2 |\tilde{s}(y_1;\omega)|^2 \mathrm{d}y_1. \tag{2.77}$$

The notation $|\tilde{s}|^2$ here is used to express the frequency-domain power spectral density of the synaptic drive. Similarly for the derivative variance, noting that for steady state input $\langle \tilde{\dot{v}}_j \rangle = 0$, we obtain $\sigma^2_{\dot{v}_j}$ via the integral

$$\sigma^2_{\dot{v}_j}(x_j) = \frac{1}{2\pi}\int_{-\infty}^{\infty} \omega^2 \mathrm{d}\omega \int_0^{\infty} |\tilde{\mathcal{G}}_{j1}(x_j, y_1; \omega)|^2 |\tilde{s}(y_1;\omega)|^2 \mathrm{d}y_1. \tag{2.78}$$

For white noise $|\tilde{s}(y_1,\omega)|^2 = 4\sigma^2_{\mathrm{WN}}$. Noting that $\gamma_j(-\omega) = \gamma_j^*(\omega)$, where * denotes the complex conjugate, to express $|\tilde{\mathcal{G}}_{\alpha 1}|^2$ we introduce the term

$$z_j = \gamma_j + \gamma_j^* = \sqrt{2 + 2\sqrt{1 + \omega^2 \beta_j^2}}, \tag{2.79}$$

meaning that

$$|\tilde{\mathcal{G}}_{\alpha 1}(x_\alpha, y_1; \omega)|^2 = \frac{\beta_\alpha^4 \lambda_1^6 e^{-(x_\alpha z_\alpha + y_1 z_1)}}{|\beta_\alpha \lambda_1^3 \gamma_1 + \lambda_\alpha^3 \gamma_\alpha|^2}. \tag{2.80}$$

Hence the variance is obtained through integration of the expression

$$\sigma^2_{v_\alpha}(x_\alpha) = \frac{2\sigma^2_{\mathrm{WN}}}{\pi}\int_{-\infty}^{\infty} \frac{\beta_\alpha^4 \lambda_1^6 e^{-x_\alpha z_\alpha}}{z_1 |\beta_\alpha^2 \lambda_1^3 \gamma_1 + \lambda_\alpha^3 \gamma_\alpha|^2} \mathrm{d}\omega, \tag{2.81}$$

which in general we must resolve numerically. In the special case of equal transmembrane conductances, which results in $\gamma_1 = \gamma_\alpha$ and $\beta_\alpha = 1$, we can move the terms involving λ_1 and λ_α outside the integral to give

$$\sigma^2_{v_\alpha}(x_\alpha) = \frac{2\sigma^2_{\mathrm{WN}}}{\pi}\left(\frac{\lambda_1^3}{\lambda_1 + \lambda_\alpha}\right)^2 \int_{-\infty}^{\infty} \frac{e^{-x_\alpha z}}{z|\gamma|^2} \mathrm{d}\omega, \tag{2.82}$$

which for $x_\alpha = 0$ yields

$$\sigma^2_{v_\alpha}(0) = 2\sigma^2_{\mathrm{WN}}\left(\frac{\lambda_1^3}{\lambda_1^3 + \lambda_\alpha^3}\right)^2. \tag{2.83}$$

Note that in the limit $\lambda_1/\lambda_\alpha \to \infty$, (2.83) tends to the variance for the semi-infinite dendrite (2.40), while for $\lambda_1/\lambda_\alpha = 1$ we obtain $\sigma^2_{\mathrm{WN}}/2$, half the infinite value. It is possible to obtain the white-noise driven variance for any x_α in terms of special functions, but only for the specific case of $g_1 = g_\alpha$ (Appendix A.4.3).

More interestingly, due to the spatial filtering of fluctuations in the axon (represented by $e^{-x_\alpha z_\alpha}$), the derivative variance is finite in the axon (but not in the dendrite) for white noise. Thus the derivative variance is given by

$$\sigma^2_{\dot{v}_\alpha}(x_\alpha) = \frac{2\sigma^2_{\mathrm{WN}}}{\pi}\int_{-\infty}^{\infty} \frac{\omega^2\beta_\alpha^4\lambda_1^6 e^{-x_\alpha z_\alpha}}{z_1|\beta_\alpha^2\lambda_1^3\gamma_1 + \lambda_\alpha^3\gamma_\alpha|^2}\mathrm{d}\omega, \tag{2.84}$$

where in the special case of $g_1 = g_\alpha$ this can be reduced to closed-form in terms of special functions, Appendix A.4.3 (A.50). An important consequence of the derivative variance being calculable in the axon for white noise is that it allows the upcrossing method to be used, as we shall calculate later.

In general, we find that at a given *dimensionfull* axonal position X_α and dendritic length constant λ_1, σ_v^2 varies non-monotonically with λ_α, as shown in Figure 2.10(b). This is also the case for $\sigma_{\dot{v}}^2$, but only very near $X_\alpha = 0$ with extremely high values of λ_α and is thus not depicted. When the ratio of the standard deviations, $\sigma_{\dot{v}}/\sigma_v$, is plotted for different λ_α we see in Figure 2.10(c) that this ratio increases with increasing λ_α, which is significant for the upcrossing rate as we shall see later.

2.6.4 Dendrite-and-Axon Variances, Coloured-Noise

With coloured noise we have $|\tilde{s}(y_1;\omega)|^2 = 4\sigma_s^2\beta_s/(1+\omega^2\beta_s^2)$ as in all previous coloured-noise spatial cases. This means that the variance is given by a simple modification to the white-noise integral equation

$$\sigma^2_{v_\alpha}(x_\alpha) = \frac{2\sigma_s^2\beta_s}{\pi}\int_{-\infty}^{\infty} \frac{\beta_\alpha^4\lambda_1^6 e^{-x_\alpha z_\alpha}}{z_1(1+\omega^2\beta_s^2)|\beta_\alpha^2\lambda_1^3\gamma_1 + \lambda_\alpha^3\gamma_\alpha|^2}\mathrm{d}\omega, \tag{2.85}$$

which must be computed numerically, as must also the case for $\gamma_1 = \gamma_\alpha$.

2.6.5 Dendrite-and-Axon, Firing Rate

White-Noise Firing Rate

With white-noise input, the upcrossing approximation can be used for $X_{\mathrm{th}} > 0$, however it generally gives a poorer fit than for coloured noise, as seen in Figure 2.10(d) (compare with coloured noise in Figure 2.11(a)). Nevertheless both the simulated firing rate and the upcrossing rate show a non-monotonic dependence of the firing rate on the axonal length constant λ_α. We saw earlier that the axonal mean (Figure 2.10(a)) and prefactor $\sigma_{\dot{v}}/\sigma_v$ (Figure 2.10(c)) increase with λ_α, which by themselves would increase the upcrossing rate. However, the dependence of σ_v^2

on λ_α eventually causes the upcrossing rate to decrease as λ_α increases, as $2\sigma_v^2$ is the denominator of the exponent for the upcrossing rate (2.1). The effect of λ_α on σ_v^2 eventually dominates the effect of the length constant on the firing rate, explaining the decrease seen in Figure 2.10(d) for $\lambda_\alpha = 150\mu$m.

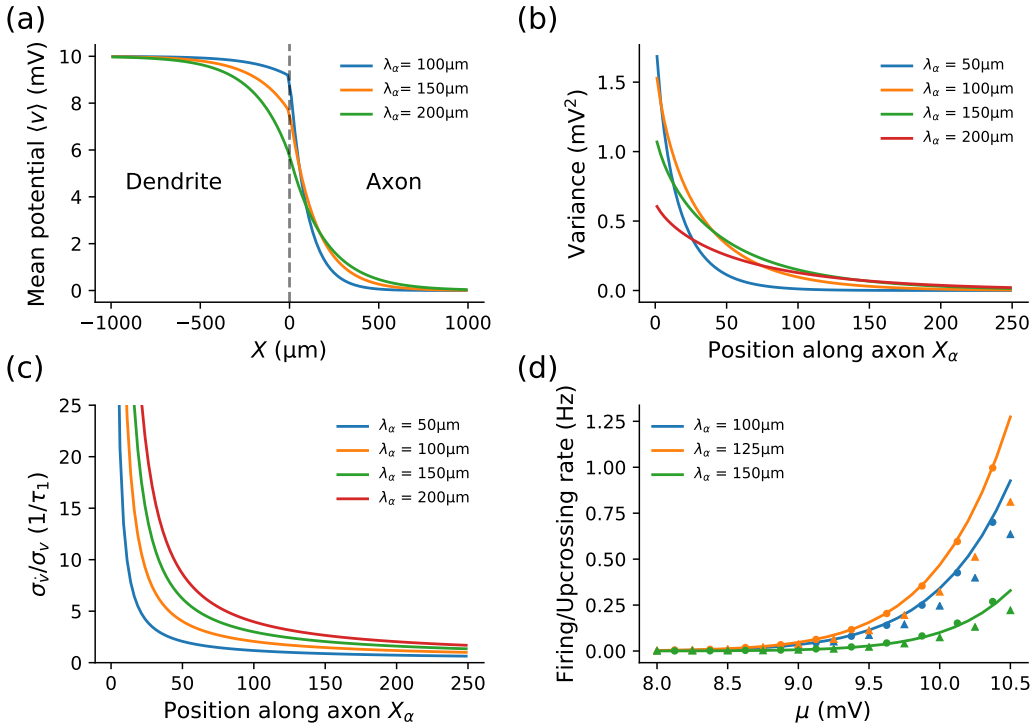

Figure 2.10: For the dendrite-and-axon model, (a) when λ_α is lower than λ_1 the mean potential (2.72, 2.73) decays more rapidly in the axon. (b) With white-noise drive, increasing λ_α always lowers the variance (2.81) at $x_\alpha = 0$, but can increase it further down the axon. (c) The derivative variance (2.84) exists for $x_\alpha > 0$ and the ratio $\sigma_{\dot{v}}/\sigma_v$ monotonically increases with λ_α at all positions. (d) Both the firing rate (triangles) and the upcrossing approximation (theory calculated from (2.1): solid line, simulation: circles) vary non-monotonically with λ_α. Other parameters: $\tau_v = 10$ms, $\lambda_1 = 200\mu$m (d) $X_{\rm th} = 35\mu$m, $v_{\rm th} = 10$mV, $\sigma_{\rm WN} = 1.5$mV.

Coloured-Noise Firing Rate

The effect of a passive axon on the fluctuation-driven firing rate with coloured-noise input can be evaluated by placing the trigger position at $X_{\rm th} = 0$ and calculating the ratio of the firing rate with the axon to that with sealed semi-infinite dendrite, $r_{\rm axon}/r_{\rm sealed}$. The axon acts as a passive conductance load, which can be changed by keeping λ_1 constant and varying the ratio of the axonal and dendritic radii, a_α/a_1. $a_\alpha/a_1 = 0$ corresponds to the sealed semi-infinite dendrite as the axon has zero

radius. Keeping v_{th} as measured from E_L the same for each value of a_α/a_1, Figure 2.11(a) shows that even a narrow axon significantly reduces the firing rate. This effect results from the mean and variance at $x = 0$ being reduced from the increase in λ_α caused by increasing a_α (section 1.3.3). If we kept $v_{\text{th}} - \langle v(0) \rangle$ constant instead to eliminate the mean contribution, the same effect would be present but the decrease in $r_{\text{axon}}/r_{\text{sealed}}$ would be slower with increasing a_α/a_1.

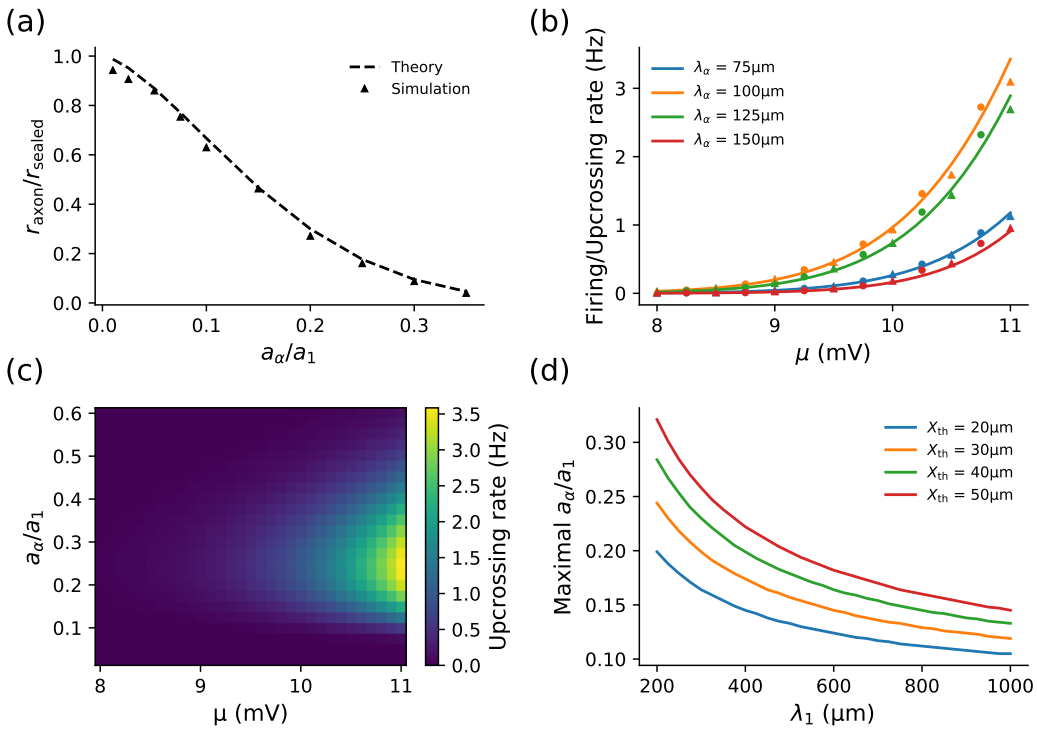

Figure 2.11: For the dendrite-and-axon model subject to coloured noise: (a) With $X_{\text{th}} = 0$, increasing the axonal radius a_α reduces both the simulated threshold-reset firing rate and upcrossing rate (2.1). (b) When $X_{\text{th}} = 30\mu$m the firing rate varies non-monotonically with λ_α. (c) For $\lambda_1 = 200\mu$m, the radius ratio for maximising the upcrossing rate is $a_\alpha/a_1 \sim 0.25$, while (d) shows that increasing λ_1 and decreasing X_{th} decreases the ratio for maximal upcrossing. Other parameters: (a-d) $\beta_s = 0.5$, $\sigma_s = 3$mV, $v_{\text{th}} = 10$mV, (a-c) $\lambda_1 = 200\mu$m, (a) $\mu_1 = 5$mV (b-c) $X_{\text{th}} = 30\mu$m, (d) $\mu = 10$mV, $\lambda_\alpha = 100\mu$m.

For a fixed dimensionfull trigger position $X_{\text{th}} > 0$, we find that, like white-noise input in Figure 2.10(d), the fluctuation-driven firing rate also varies non-monotonically with the ratio of length constants λ_α/λ_1 for coloured-noise input, Figure 2.11(b). We investigated this non-monotonic effect further in terms of the axon to dendrite radius ratio a_α/a_1, and μ, Figure 2.11(c). In this instance ($\lambda_1 = 200\mu$m),

the ratio that maximises firing is ~ 0.25, which is similar to the ratio between the AIS and apical dendrite in pyramidal cells [16,138]. When λ_1 is increased, this ratio decreases as shown in Figure 2.11(d) (i.e. favouring a thinner axon), but a_α/a_1 is still in a physiologically reasonable range. In the same panel, we also see that the ratio for maximising the firing rate is higher for trigger positions further from the nominal soma (X_{th} increasing).

Intuitively, the non-monotonic dependence of the upcrossing rate on a_α/a_1 can be understood from the definition of λ_α, which is proportional to $\sqrt{a_\alpha}$ (section 1.3.3). Thus the decay length of voltage fluctuations that enter the axon from the dendritic stimulation increases, which can increase both $\langle v_\alpha(X_{\text{th}})\rangle$ and $\sigma^2_{v_\alpha}(X_{\text{th}})$ by lowering the exponent x_{th} in (2.73) and (2.85). On the other hand, a larger λ_α increases the input conductance of the neuron, which will act to decrease both $\langle v_\alpha(X_{\text{th}})\rangle$ and $\sigma^2_{v_\alpha}(X_{\text{th}})$ by lowering the prefactor in (2.73) and (2.85). For smaller λ_α, the decay length effect is more significant, whereas for larger λ_α the increase input conductance plays a larger role.

2.7 Ball-and-Stick Model

The ball-and-stick model neuron, first proposed by Rall [129], adds an isopotential soma with transmembrane conductance G_σ, capacitance C_σ to the end of a dendrite. The soma is now electrically significant, which we will hereafter term "substantial" in contrast to the "nominal" soma with negligible electrical properties. Here we will choose the end $x = 0$ of the dendrite to place the soma. Denoting the potential at $x = 0$ as $V_\sigma(T)$, the somatic boundary condition is found via the conservation of current at $x = 0$

$$C_\sigma \frac{\mathrm{d}V_\sigma}{\mathrm{d}T} = G_\sigma(E_L - V_\sigma) + G_\lambda \lambda \left.\frac{\partial V}{\partial X}\right|_{X=0}. \tag{2.86}$$

As mentioned earlier, for this thesis we will not consider synaptic drive at the soma. This is done to allow for comparison between the ball-and-stick model and the other spatial models with a nominal soma. The mean and variance contributions from somatic drive would simply add linearly and not qualitatively change the nature of the results. A description of how to incorporate synaptic drive at the soma is given in Appendix A.5.

Dividing (2.86) by G_σ and defining the neuritic dominance factor as [44]

$$\rho = \frac{G_\lambda}{G_\sigma}, \tag{2.87}$$

we obtain

$$\tau_\sigma \frac{\mathrm{d}V_\sigma}{\mathrm{d}T} = E_L - V_\sigma + \rho\lambda \left.\frac{\partial V}{\partial X}\right|_{X=0}, \tag{2.88}$$

where $\tau_\sigma = C_\sigma/G_\sigma$ is the somatic membrane time constant. Here we can rescale space and time in terms of the dendrite, defining $\beta_\sigma = \tau_\sigma/\tau_v$ and measuring all voltages from E_L (assuming the dendrite and soma have the same leak current rest potential E_L)

$$\beta_\sigma \frac{\mathrm{d}v_\sigma}{\mathrm{d}t} = -v_\sigma + \rho \left.\frac{\partial v}{\partial x}\right|_{x=0}. \tag{2.89}$$

Adding an axon to this model changes the current conservation condition at the soma to

$$\beta_\sigma \frac{\mathrm{d}v_\sigma}{\mathrm{d}t} = -v_\sigma + \rho_\alpha \left.\frac{\partial v_\alpha}{\partial x_\alpha}\right|_{x_\alpha=0} + \rho_1 \left.\frac{\partial v_1}{\partial x_1}\right|_{x_1=0}, \tag{2.90}$$

where there is now a neuritic dominance factor for each cable with $\rho_j = G_{\lambda_j}/G_\sigma$. If we know G_σ, λ_1 and λ_α, then ρ_α can be expressed in terms of ρ_1 via

$$\frac{\rho_\alpha}{\rho_1} = \frac{a_\alpha \lambda_\alpha g_\alpha}{a_1 \lambda_1 g_1} = \frac{\lambda_\alpha^3}{\beta_\alpha^2 \lambda_1^3}, \tag{2.91}$$

where λ_1 and λ_α differ due to both differences in membrane conductance and radius. In the case with no axon, the limits $\rho \to 0$ and $\rho \to \infty$ converge to a killed ($v(0,t)$ constant) and sealed end respectively. With an axon, the limit $\rho \to \infty$ corresponds to the nominal soma condition we explored in the section 2.6.

2.7.1 Ball-and-Stick Model, Green's Function

Semi-Infinite Dendrite Only

Defining $\gamma_\sigma = \sqrt{1 + i\omega\beta_\sigma}$, the segment factor is

$$\tilde{f}_{1\sigma}(\omega) = \frac{\rho\gamma_1}{\gamma_\sigma^2 + \rho_1\gamma_1}, \tag{2.92}$$

hence we can derive the Green's function from (2.61) as

$$\tilde{\mathcal{G}}(x, y; \omega) = \frac{e^{-|x-y|\gamma_1}}{2\gamma_1} + \frac{e^{-|x+y|\gamma_1}}{2\gamma_1}\left(\frac{\rho\gamma_1 - \gamma_\sigma^2}{\rho\gamma_1 + \gamma_\sigma^2}\right). \tag{2.93}$$

From (2.93) we can see that $|\tilde{\mathcal{G}}|^2$ will have a term equivalent to that of the infinite cable, $|\tilde{\mathcal{G}}_\infty|^2 = e^{-|x-y|z_1}/(4|\gamma_1|^2)$. This implies that, while the soma applies temporal filtering, the derivative variance $\sigma_{\dot{v}}^2$ will still be undefined for distributed white-noise input. Thus we will focus on coloured-noise input in this section.

Dendrite and Axon

With the addition of an axon, the segment factor for dendrite 1 is

$$\tilde{f}_{1\sigma}(\omega) = \frac{G_{\lambda_1}\gamma_1}{G_\sigma\gamma_\sigma^2 + G_{\lambda_\alpha}\gamma_\alpha + G_{\lambda_1}\gamma_1} = \frac{\rho_1\gamma_1}{\gamma_\sigma^2 + \rho_\alpha\gamma_\alpha + \rho_1\gamma_1}, \tag{2.94}$$

which after substitution into the sum-over-trips equations (2.61) yields

$$\begin{aligned}
\tilde{\mathcal{G}}_{11}(x_1, y_1; \omega) &= \frac{(\rho_1\gamma_1 + \rho_\alpha\gamma_\alpha + \gamma_\sigma^2)e^{-|x_1-y_1|\gamma_1} + (\rho_1\gamma_1 - \rho_\alpha\gamma_\alpha - \gamma_\sigma^2)e^{-|x_1+y_1|\gamma_1}}{2\gamma_1(\gamma_\sigma^2 + \rho_\alpha\gamma_\alpha + \rho_1\gamma_1)}, \\
\tilde{\mathcal{G}}_{\alpha 1}(x_\alpha, y_1; \omega) &= \frac{\rho_1 e^{-(x_\alpha\gamma_\alpha + y_1\gamma_1)}}{\gamma_\sigma^2 + \rho_\alpha\gamma_\alpha + \rho_1\gamma_1}.
\end{aligned} \tag{2.95}$$

2.7.2 Ball-and-Stick Model, Mean

Similar to the dendrite-and-axon model, the lack of synaptic drive at the soma causes the mean potential to be spatially varying, even when there is no axon.

Semi-Infinite Dendrite Only

With a semi-infinite dendrite and soma, the mean is given by

$$\begin{aligned}
\langle v(x)\rangle &= \frac{\mu}{2}\int_0^\infty e^{-|x-y|} + e^{-|x+y|}\left(\frac{\rho-1}{\rho+1}\right)\mathrm{d}y \\
&= \frac{\mu}{2}\left[2 - e^{-x} + e^{-x}\left(\frac{\rho-1}{\rho+1}\right)\right],
\end{aligned} \tag{2.96}$$

which implies that the mean is always greatest in the bulk of the dendrite and lowest at the soma, with $\langle v(x)\rangle$ monotonically increasing with the distance from the soma x. As expected, in the sealed end limit ($\rho \to \infty$) $\langle v(x)\rangle = \mu$ while in the killed end limit ($\rho \to 0$) $\langle v(x)\rangle = 0$. This is shown in Figure 2.12(a).

Dendrite and Axon

When an axon is present, we are most interested in the mean either in the axon or soma ($x_\alpha = 0$) since it is in the AIS that firing occurs. Using the axonal Green's

function (2.95) we find that, as in the dendrite, decreasing ρ_1 also lowers the mean in the axon

$$\langle v_\alpha(x_\alpha)\rangle = \mu\tilde{f}_{10}(0)e^{-x_\alpha} = \frac{\mu\rho_1}{1+\rho_\alpha+\rho_1}e^{-x_\alpha}. \tag{2.97}$$

2.7.3 Ball-and-Stick Model Variances

Semi-Infinite Dendrite Only

Calculating the variance using the same method as before (2.77), Figure 2.12(b) shows that the variance increases at all locations as the dendrite-to-soma conductance ratio ρ increases towards the value for a nominal soma ($\rho \to \infty$), with the value in the bulk of the dendrite ($x \to \infty$) unaffected by the somatic load. The variance profile with length is generally non-monotonic except for low ρ, with a peak in σ_v^2 within a fraction of λ of the soma.

Dendrite and Axon

The variance profile in the dendrite still varies non-monotonically with x_1 for larger ρ_1, but always decreases with x_α in the axon, as shown in Figure 2.13(a).

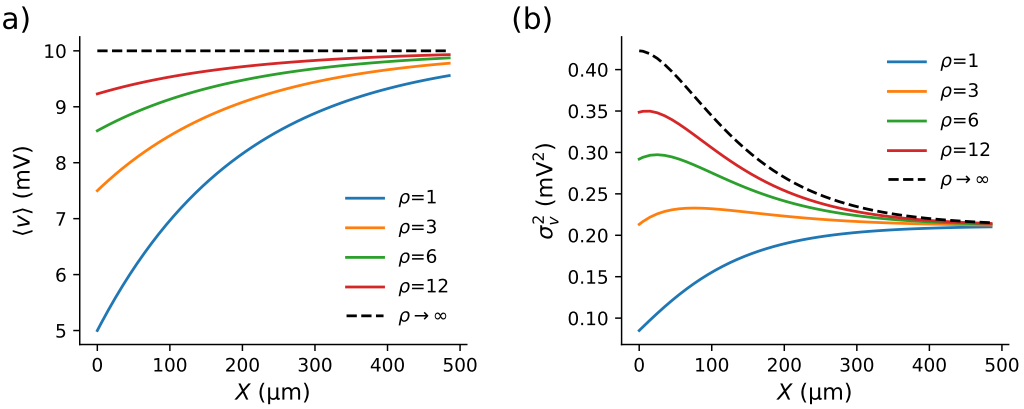

Figure 2.12: (a) A larger soma (decreasing ρ) reduces the mean (2.96) near the soma. (b) Increasing ρ changes the variance (2.77) from being lowest to highest near the soma. Other parameters: $\lambda_1 = 200\mu$m, $\beta_\alpha = 7/6$ $\mu = 10$mV, $\sigma_s = 1$mV.

2.7.4 Ball-and-Stick Model, Firing Rate

As we might expect from the reduction in both the mean and variance, a larger soma (lower ρ_1) reduces the steady-state firing rate, Figure 2.13(b). To see how the soma affects the axonal load, we set the trigger position at $X_{\text{th}} = 0$ and repeated

the analysis in Figure 2.11(a) with various conductance ratios ρ_1. The upcrossing rate with no axon was fixed at 1Hz for each somatic size by adjusting σ_s. This was to account for the soma's effect on the firing rate in Figure 2.13(b), ensuring that we focus solely on the effect of the axonal load. Figure 2.13(c) shows that lower ρ_1 causes $r_{\text{axon}}/r_{\text{no axon}}$ to decrease more slowly with increasing a_α/a_1, as the same axonal load is smaller in relative terms when the somatic conductance is larger.

Finally, the effect of the soma on the axonal radius that maximises the firing rate is shown in Figure 2.13(d). As mentioned in section 2.6.5 when had a nominal soma, increasing the axonal trigger position increases the ratio a_α/a_1 that maximises the upcrossing rate. Decreasing ρ_1 also increases the maximal value of a_α/a_1. This is because the mean-increasing effect at X_{th} of a larger axon is more significant than the reduction in variance for the upcrossing rate with a larger soma.

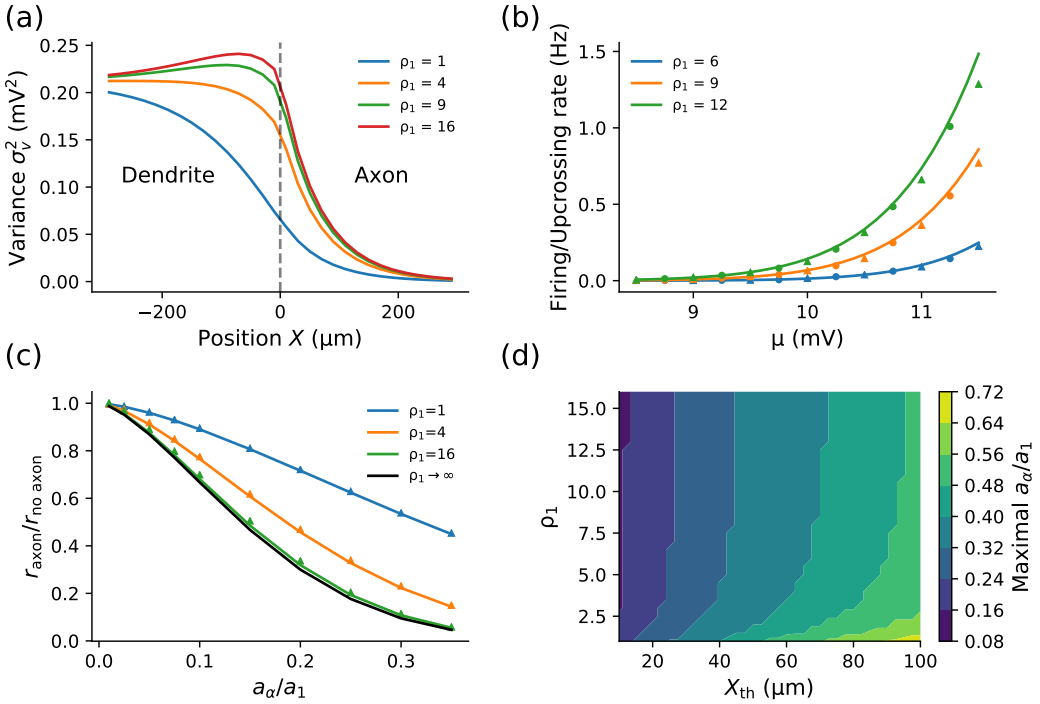

Figure 2.13: The somatic conductance reduces the variance (2.77) and hence the fluctuation-driven firing rate, where lower ρ_1 indicates a larger soma. (a) Dendritic variance varies non-monotonically for larger ρ_1, but always decreases with axonal position. (b) The reduction in σ_v^2 from smaller ρ_1 decreases both the simulated firing rate (triangles), theoretical (solid lines) and simulated upcrossing rates (circles). (c) The relative effect of the axonal load on the firing rate is reduced with decreasing ρ_1. (d) Decreasing ρ_1 increases the relative axonal radius that maximises the upcrossing rate for $X_{\text{th}} > 0$. Parameters used: (a-d) $\lambda_1 = 200\mu$m, $\beta_s = 0.5$, $v_{\text{th}} = 10$mV, (a) $\lambda_\alpha = 150\mu$m. $\sigma_s = 1$mV (b) $X_{\text{th}} = 30\mu$m, $\lambda_\alpha = 100\mu$m, $\sigma_s = 3$mV (d) $\mu = 10$mV, $\sigma_s = 3$mV.

2.8 Multiple Dendrites and Axon

Most neurons have multiple dendrites radiating from the soma rather than just a single branch. For example, many basal dendrites radiate from the soma of a pyramidal cell. The functional effects of a neuron's dendritic topology has been explored in various theoretical and modelling studies [139–142]. Here we analyse a model that has n dendrites and an axon, where the dendrites have with identical membrane properties and identically distributed but independent synaptic drive. First we will consider the soma to have negligible electrical load (nominal), and later we will examine the effects of a electrically substantial soma as in section 2.7.

Each dendrite obeys the cable equation

$$\tau_j \frac{\partial v_j}{\partial T} = \mu_j - v_j + \lambda_j^2 \frac{\partial^2 v_j}{\partial X_j^2} + s_j, \quad j = 1, 2, ..., n \tag{2.98}$$

and due to the identical membrane properties and identical mean synaptic drive $\tau_1 = \tau_2 = ... = \tau_n$, $\lambda_1 = \lambda_2 = ... = \lambda_n$, and $\mu_1 = \mu_2 = ... = \mu_n$. Hence we will hereafter refer to dendritic properties with the subscript 1. The fluctuating component of the synaptic drive in each dendrite is described by

$$\beta_s \frac{\partial s_j}{\partial t} = -s_j + 2\sigma_s \sqrt{\beta_s} \xi_j(x_j, t). \tag{2.99}$$

While the parameters β_s and σ_s are the same for each dendrite, the independence of synaptic drive means that there is zero correlation between ξ_j and ξ_k for different dendrites. Mathematically this can be written as

$$\langle \xi_j(x_j, t) \xi_k(x_k, t') \rangle = \delta_{jk} \delta(x_j - x_k) \delta(t - t'), \tag{2.100}$$

where δ_{jk} is the Kronecker delta function. The current conservation condition with a nominal soma is given by

$$\lambda_\alpha^3 \frac{\partial v_\alpha}{\partial x_\alpha}\bigg|_{x_\alpha = 0} + \sum_{j=1}^{n} \beta_\alpha^2 \lambda_1^3 \frac{\partial v_j}{\partial x_j}\bigg|_{x_j = 0} = 0, \tag{2.101}$$

where β_α is as defined in section 2.6. With an electrically substantial soma, the current conservation condition becomes

$$\beta_\sigma \frac{\mathrm{d}v_\sigma}{\mathrm{d}t} = -v_\sigma + \rho_\alpha \frac{\partial v_\alpha}{\partial x_\alpha}\bigg|_{x_\alpha = 0} + \sum_{j=1}^{n} \rho_1 \frac{\partial v_j}{\partial x_j}\bigg|_{x_j = 0}. \tag{2.102}$$

2.8.1 Multiple Dendrites and Axon, Green's Functions

Nominal Soma

With a nominal soma, we start by deriving the Green's function for the axon in response to input in dendrite 1, $\tilde{\mathcal{G}}_{\alpha 1}$. Using the fact that all the dendrites have identical membrane properties, the segment factor for the trip from x_α to y_1 is given by

$$\tilde{f}_1 = \frac{G_{\lambda_1} \gamma_1}{G_{\lambda_\alpha} \gamma_\alpha + \sum_{m=1}^{n} G_{\lambda_m} \gamma_m} = \frac{\beta_\alpha^2 \lambda_1^3 \gamma_1}{\lambda_\alpha^3 \gamma_\alpha + n \beta_\alpha^2 \lambda_1^3 \gamma_1}. \tag{2.103}$$

Hence the Green's function is

$$\tilde{\mathcal{G}}_{\alpha 1}(x_\alpha, y_1; \omega) = \frac{\tilde{f}_1(\omega)}{\gamma_1} e^{-(x_\alpha \gamma_\alpha + y_1 \gamma_1)} = \frac{\beta_\alpha^2 \lambda_1^3 e^{-(x_\alpha \gamma_\alpha + y_1 \gamma_1)}}{\lambda_\alpha^3 \gamma_\alpha + n \beta_\alpha^2 \lambda_1^3 \gamma_1}, \tag{2.104}$$

which we can see reduces to the Green's function for a dendrite and axon for $n = 1$ (2.64). Furthermore, since all dendrites have identical properties, the axonal response Green's functions are the same: $\tilde{\mathcal{G}}_{\alpha 1} = \tilde{\mathcal{G}}_{\alpha 2} = ... = \tilde{\mathcal{G}}_{\alpha n}$.

For the dendrites there are two different Green's functions to consider; the response in dendrite 1 due to input at a different dendrite, $\tilde{\mathcal{G}}_{12}$, and the response due to an input in the same dendrite, $\tilde{\mathcal{G}}_{11}$. For $\tilde{\mathcal{G}}_{12}$, there is only a single trip and we use the same segment factor as before (2.103) but with a different complex length

$$\tilde{\mathcal{G}}_{12}(x_1, y_2; \omega) = \frac{\beta_\alpha^2 \lambda_1^3 e^{-|x_1 + y_2| \gamma_1}}{\lambda_\alpha^3 \gamma_\alpha + n \beta_\alpha^2 \lambda_1^3 \gamma_1}. \tag{2.105}$$

Whilst for $\tilde{\mathcal{G}}_{11}$ substituting the parameters into (2.61) yields

$$\tilde{\mathcal{G}}_{11}(x_1, y_1; \omega) = \frac{e^{-|x_1 - y_1| \gamma_1}}{2\gamma_1} - \frac{\lambda_\alpha^3 \gamma_\alpha + (n-2) \beta_\alpha^2 \lambda_1^3 \gamma_1}{\lambda_\alpha^3 \gamma_\alpha + n \beta_\alpha^2 \lambda_1^3 \gamma_1} \frac{e^{-|x_1 + y_1| \gamma_1}}{2\gamma_1}. \tag{2.106}$$

Substantial Soma

When the soma is electrically substantial, we must change the segment factor to include the somatic admittance

$$\tilde{f}_{10} = \frac{G_{\lambda_1} \gamma_1}{G_{\lambda_\alpha} \gamma_\alpha + G_\sigma \gamma_\sigma^2 + n G_{\lambda_1} \gamma_1} = \frac{\rho_1 \gamma_1}{\rho_\alpha \gamma_\alpha + \gamma_\sigma^2 + n \rho_1 \gamma_1}, \tag{2.107}$$

from which we substitute into (2.61) to obtain the Green's functions.

2.8.2 Multiple Dendrites and Axon, Mean

With multiple input dendrites, due to the linearity of the system, the response in a neurite is calculated as the sum of the contributions from each dendrite. For input $\tilde{I}_j(y_j; \omega)$, this means that

$$v_i(x_i, t) = \sum_{j=1}^{n} \frac{1}{2\pi} \int_{-\infty}^{\infty} e^{i\omega t} \mathrm{d}\omega \int_0^{l_j} \tilde{\mathcal{G}}_{ij}(x_i, y_j; \omega) \tilde{I}_j(y_j; \omega) \mathrm{d}y_j. \tag{2.108}$$

With $\tilde{I}_j(y_j;\omega) = 2\pi\mu_j\delta(\omega) + \tilde{s}_j$, the mean is given by

$$\langle v_i(x_i)\rangle = \sum_{j=1}^{n} \mu_j \int_0^{l_j} \tilde{\mathcal{G}}_{ij}(x_i, y_j; 0)\mathrm{d}y_j, \tag{2.109}$$

which simplifies further for the axon since all dendrites have the same properties and mean drive. Thus for semi-infinite dendrites with a nominal soma

$$\langle v_\alpha(x_\alpha)\rangle = n\mu_1 \int_0^{\infty} \frac{\beta_\alpha^2\lambda_1^3 e^{-(x_\alpha+y_1)}}{\lambda_\alpha^3 + n\beta_\alpha^2\lambda_1^3} = n\mu_1 \frac{\beta_\alpha^2\lambda_1^3 e^{-x_\alpha}}{\lambda_\alpha^3 + n\beta_\alpha^2\lambda_1^3}, \tag{2.110}$$

which shows that the mean always increases by increasing the number of synaptically driven dendrites n, to a maximum of $\mu_1 e^{-x_\alpha}$ as $n \to \infty$. With an electrically substantial soma the mean in the axon is

$$\langle v_\alpha(x_\alpha)\rangle = \frac{n\mu_1\rho_1 e^{-x_\alpha}}{1 + \rho_\alpha + n\rho_1}. \tag{2.111}$$

2.8.3 Multiple Dendrites and Axon Variances

Given that (2.108) implies that the contribution to the axonal voltage from each dendrite sum linearly, the fluctuating component from each dendrite also sum linearly, hence

$$v_{\alpha F} = \sum_{j=1}^{n} v_{\alpha F j} = \sum_{j=1}^{n} \frac{1}{2\pi} \int_{-\infty}^{\infty} e^{i\omega t}\mathrm{d}\omega \int_0^{\infty} \tilde{\mathcal{G}}_{\alpha j}(x_\alpha, y_j; \omega)\tilde{s}_j(y_j;\omega)\mathrm{d}y_j. \tag{2.112}$$

If the synaptic drive is independent between dendrites, then the variance contributions from each dendrite also sum linearly

$$\sigma_{v_\alpha}^2 = \sum_{j=1}^{n} \langle v_{\alpha F j}^2\rangle, \quad \langle v_{\alpha F j}^2\rangle = \frac{1}{2\pi}\int_{-\infty}^{\infty}\mathrm{d}\omega \int_0^{\infty} |\tilde{\mathcal{G}}_{\alpha j}(x_\alpha, y_j;\omega)|^2 |\tilde{s}_j|^2 \mathrm{d}y_j. \tag{2.113}$$

Therefore for coloured noise and identical dendrites with identically distributed noise, each dendrite contributes equally to the whole, giving

$$\sigma_{v_\alpha}^2 = \frac{2n\sigma_s^2}{\pi} \int_{-\infty}^{\infty}\mathrm{d}\omega \int_0^{\infty} \frac{|\tilde{\mathcal{G}}(x_\alpha, y_1;\omega)|^2}{1 + \omega^2\beta_s^2}\mathrm{d}y_1, \tag{2.114}$$

and the derivative variance is found simply via multiplication of the integrand by ω^2. While for brevity we have neglected the more difficult problem of the synaptic drive being correlated across dendrites, the framework developed here can accommodate certain types of correlated drive. Noting that our axonal Green's function 2.104 has

$|\tilde{\mathcal{G}}_{\alpha 1}|^2$ as

$$|\tilde{\mathcal{G}}_{\alpha 1}(x_\alpha, y_1; \omega)|^2 = \frac{|\tilde{f}_1(\omega)|^2}{|\gamma_1|^2} e^{-(x_\alpha z_\alpha + y_1 z_1)}, \tag{2.115}$$

the y-integral can be easily evaluated to give the variance

$$\sigma^2_{v_\alpha} = \frac{2n\sigma_s^2}{\pi} \int_{-\infty}^{\infty} \frac{|\tilde{f}_1(\omega)|^2}{z_1 |\gamma_1|^2 (1 + \omega^2 \beta_s^2)} e^{-x_\alpha z_\alpha} \mathrm{d}\omega. \tag{2.116}$$

While this integral in general must be calculated numerically, it gives some insight into how the σ_v^2 varies with n. For large n with both a nominal and substantial soma, $|\tilde{f}_1(\omega)|^2 \sim 1/n^2$ and hence we should expect that $\sigma^2_{v_\alpha} \sim 1/n$ for large n. This large n tendency also applies to the derivative variance $\sigma^2_{\dot{v}_\alpha}$ and is very clearly seen for the nominal soma when both time constants are equal, making the segment factor independent of ω with $\tilde{f}_1(\omega) = \tilde{f}_1(0)$. This result is a generalisation of what we found in section 2.4.2 with the variance of the infinite dendrite model being half that of the semi-infinite model at $x = 0$.

For a nominal soma, both axonal variances monotonically decrease with n across a large range of λ_α, β_α and x_α, Figure 2.14(a). The ratio between the variances, $\sigma_{\dot{v}}/\sigma_v$, is also remarkably similar (if not quite constant) with n as seen in Figure 2.14(b). Thus, we should expect the number of dendrites n to affect the upcrossing rate mainly through changes in mean and variance σ_v^2. Note also that the non-monotonicity of σ_v^2 with the ratio of the length constants λ_α/λ_1 seen for the single dendrite case is retained for n dendrites and that this relationship changes as the dendritic number increases.

However, for a substantial soma, the variances no longer monotonically decrease with n but instead peak at an intermediate value, Figure 2.14)(c, d). Moreover, the value of n that maximises σ_v^2 is in general different to the n that maximises $\sigma_{\dot{v}}^2$, implying that the ratio $\sigma_{\dot{v}}/\sigma_v$ is no longer approximately constant as was the case for the nominal soma. This is because the frequency dependence of the segment factor $\tilde{f}_1$ differs for a substantial soma due to the γ_σ^2 term in the denominator (2.107). Thus increasing the number of dendrites for small n has a smaller effect on $|\tilde{f}_1|^2$ while scaling the prefactor of (2.116). Note that the absolute value of both variances decreases with decreasing dendrite-to-soma conductance ratio ρ_1 for any number of dendrites. Therefore, from this we should expect the number of dendrites to affect the upcrossing rate differently when the soma size is changed.

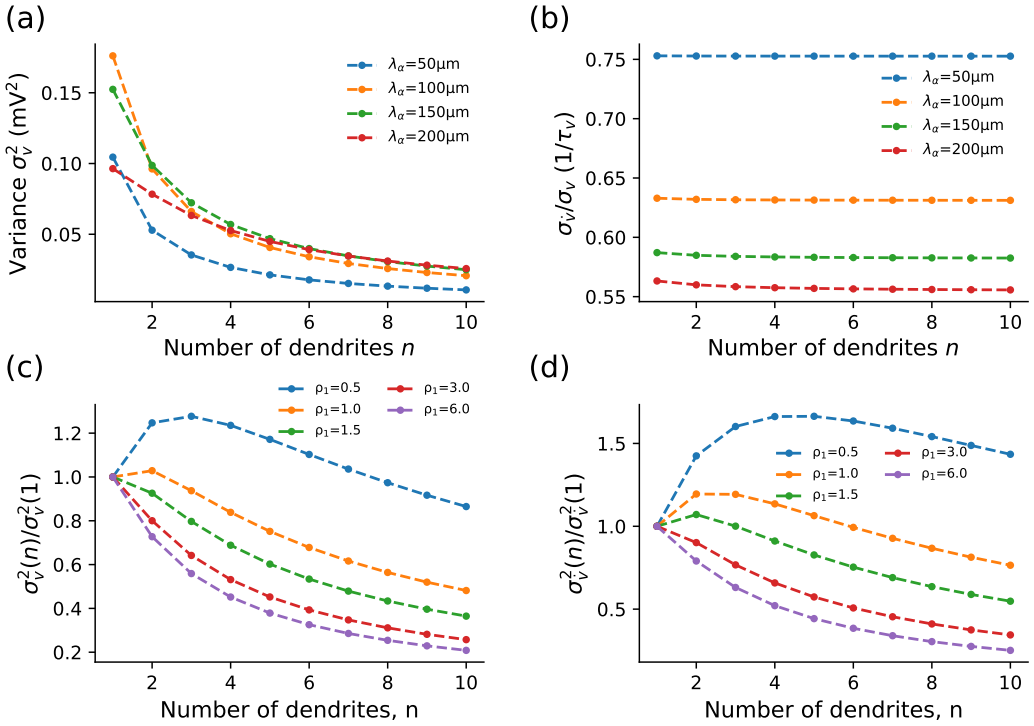

Figure 2.14: The variances decrease as $1/n$ for a large number of dendrites n, but for a small number of dendrites the presence of a substantial soma can make this dependence non-monotonic. (a) For a nominal soma the variance decreases monotonically with n. (b) The ratio between the standard deviations is surprisingly close to constant, even when the axonal and dendritic time constants differ. (c) With a substantial soma, the variance peaks for a small dendritic number. (d) $\sigma_{\dot{v}}^2$ generally peaks for a larger dendritic number than σ_v^2 and does not require as small a value of ρ_1 for non-monotonicity to occur. The variances in each case are calculated using (2.116). Parameters used: (a-d) $X_\alpha = 30\mu$m, $\lambda_1 = 200\mu$m, $\beta_s = 0.5$, $\beta_\alpha = 7/6$, $\sigma_s = 1.0$mV, (c-d) $\lambda_\alpha = 150\mu$m.

2.8.4 Multiple Dendrites and Axon, Firing Rate

Nominal Soma

For the nominal soma, we have seen that increasing the number of dendrites n increases $\langle v \rangle$ (2.110), decreases σ_v^2 (Figure 2.14(a)), while $\sigma_{\dot{v}}/\sigma_v$ remains roughly constant (Figure 2.14(b)). Since the upcrossing rate (2.1) for $\langle v \rangle < v_{\rm th}$ increases with increasing $\langle v \rangle$ and decreases with decreasing σ_v^2, the effect of dendritic number n on the fluctuation-driven firing will depend on whether the mean increasing or variance decreasing effect is stronger.

For smaller mean drive μ or lower λ_α, the decrease in σ_v from additional

dendrites affects fluctuation-driven firing than increases in $\langle v \rangle$, hence the firing rate decreases as shown in Figure 2.15(a). On the other hand, when the mean is more significant for fluctuation-driven firing (larger μ or λ_α), the firing rate is initially increased by additional dendrites, with Figure 2.15(b) showing the firing rate is maximised with $n = 2$ for lower μ and $n = 3$ with higher μ. Note that since the axonal mean converges to a finite limit as $n \to \infty$ while the variance decreases to zero, the fluctuation-driven firing rate will always eventually decrease with the number of dendrites when n is large enough.

The dendritic number for which maximises the upcrossing rate, $n_{\max}$, is shown in more detail as a function of axon to dendrite radius ratio a_α/a_1 and mean drive μ in Figure 2.15(c). Intuitively, a relatively wider axon allows the increased mean drive component from additional dendrites to propagate further along the axon, increasing $\langle v_\alpha(x_{\text{th}}) \rangle$ and hence increasing $n_{\max}$. Increasing μ increases $\langle v_\alpha(x_{\text{th}}) \rangle$ linearly (2.110), hence increasing $n_{\max}$.

In the previous simulations, the total leak conductance of the neuron increased with the number of added dendrites, and one may presume that the increase in leak is responsible for the decrease in firing rate with n. To this further, we fixed the leak conductance of the cell by varying the dendritic radius a_1 with n. Given that the total input conductance for n dendrites and an axon is

$$G_{\text{in}} = n(2\pi a_1 \lambda_1) g_1 + 2\pi a_\alpha \lambda_\alpha g_\alpha, \tag{2.117}$$

we can keep the total input conductance the same as the one dendrite case, $G_{\text{in}}(n = 1)$ using the relationship $\lambda_1(n) = \lambda_1(n = 1)/n^{1/3}$. This gives the segment factor as

$$\tilde{f}_1(\omega) = \frac{g_1^2 \lambda_1^3 (n = 1)\gamma_1}{n(g_1^2 \lambda_1^3 (n = 1)\gamma_1 + g_\alpha^2 \lambda_\alpha^3 \gamma_\alpha)}. \tag{2.118}$$

Since we found earlier that the integrands for the variances are proportional to $|\tilde{f}_1(\omega)|^2$ (2.116), this shows that the variances and hence the firing rate for fixed λ_α still decrease with n for lower μ and λ_α as shown in Figure 2.15(d). Thus the reduction in fluctuation-dominated firing due to additional dendrites is not simply due to the fact that adding more dendrites increases the cell size, but because the relative admittance of each dendrite compared to the total cell admittance, $\tilde{f}_1(\omega)$, decreases. This relative admittance decrease with n represents voltage fluctuations from one dendrite being able to diffuse to the $n - 1$ other dendrites as well as the axon.

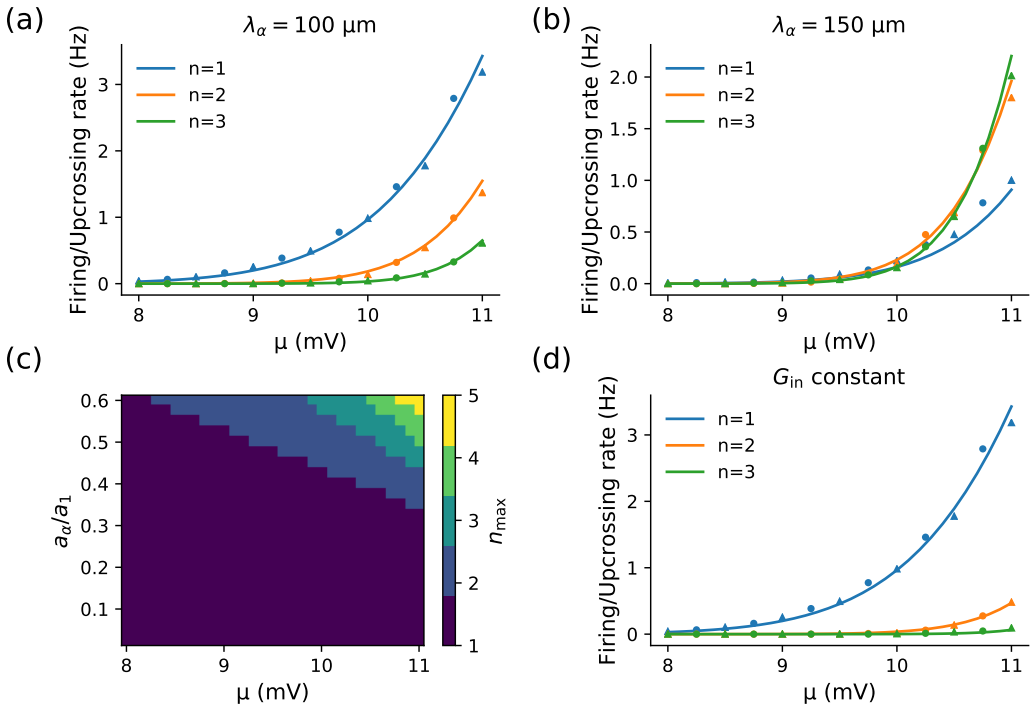

Figure 2.15: Increasing the number of dendrites (a) decreases the firing rate for smaller λ_α, while (b) increases it for larger λ_α. (c) Higher μ and relative axon size a_α/a_1 increases the number of dendrites that maximises dendritic firing. (d) Increasing the number of dendrites while keeping the total cell conductance equal to the $n = 1$ case in (2.117) results in an even faster reduction in the firing rate with n than (a). In panels (a, b, d) solid lines indicate the theoretically predicted upcrossing rate (2.1), while circles and triangles show upcrossing and threshold-reset simulations respectively. Parameters used: (a) $\lambda_\alpha = 100\mu$m, (b) $\lambda_\alpha = 150\mu$m (d) $\lambda_1(n = 1) = 200\mu$m, $\lambda_\alpha = 100\mu$m, (a-c) $\lambda_1 = 200\mu$m, (a-d) $X_{\text{th}} = 30\mu$m, $\beta_s = 0.5$, $\beta_\alpha = 7/6$, $\sigma_s = 3$mV, $v_{\text{th}} = 10$mV.

Substantial Soma

For a substantial soma and using the same parameters as the nominal soma in Figure 2.15(a), Figure 2.16(a-d) shows that smaller ρ_1 increases the number of dendrites that maximise firing. A contributing factor why this is the case is because since the somatic load is fixed, the relative impact on the conductance of adding more dendrites is smaller. However, a smaller conductance ratio ρ_1 always reduces the overall firing rate for the same input drive.

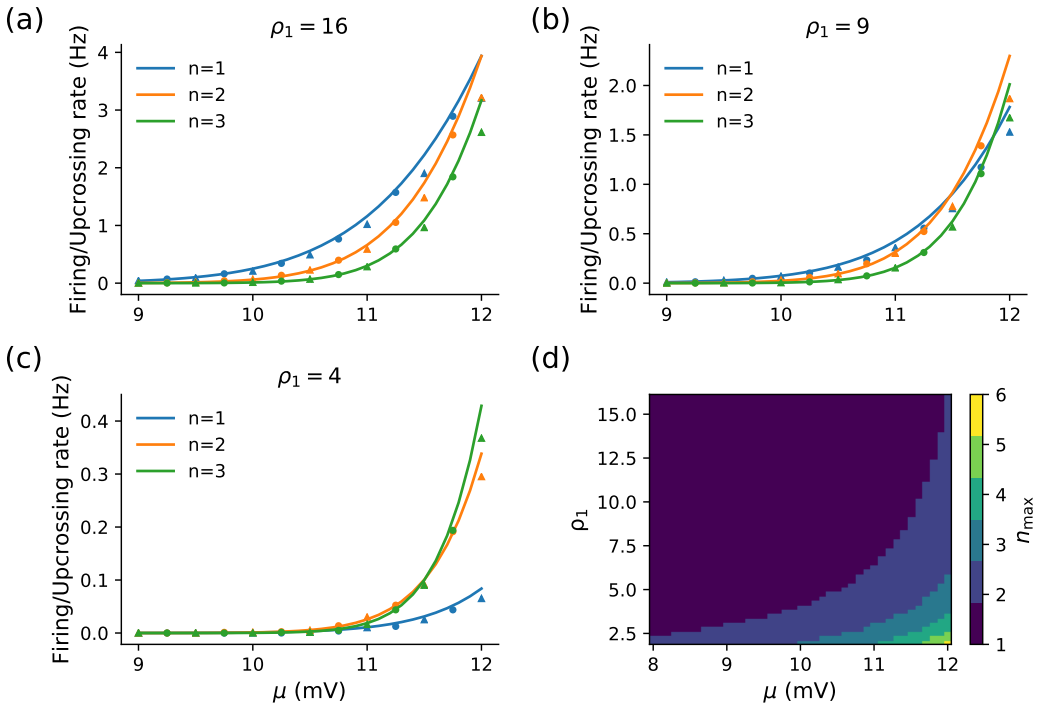

Figure 2.16: A larger axon and soma (smaller ρ_1) increase the number of dendrites that maximises the fluctuation-driven firing rate. The theoretical upcrossing rate (solid lines) (2.1) is compared with the simulated upcrossing (circles) and threshold-reset rates (triangles) for three different somatic sizes: (a) $\rho_1 = 16$, (b) $\rho_1 = 9$, (c) $\rho_1 = 4$. (d) The number of dendrites that maximises the upcrossing rate, $n_{\max}$, increases with increasing μ and decreasing ρ_1 (larger somata). Other parameters: (a-d) $\lambda_1 = 200\mu$m, $\lambda_\alpha = 100\mu$m, $X_{\text{th}} = 30\mu$m, $\sigma_s = 3$mV, $v_{\text{th}} = 10$mV.

2.9 Summary

This chapter has demonstrated that in the fluctuation-driven low firing-rate regime, the upcrossing approximation allows for analytical study of spatially extended neuron models that need not be limited to a single dendrite nor with stochastic synaptic drive confined to a single point, but distributed as is the case *in vivo*. The only requirements for the upcrossing rate to be defined are the calculation of the voltage mean, variance and rate-of-change of variance at the AP trigger position. The upcrossing method provided a good approximation for these simple models in the low-rate limit with firing rates <5 Hz, which is representative of the slow average firing rates of neocortical pyramidal cells [119,120], with more detailed analysis of the validity of the upcrossing approximation in Appendix C.2.1. Despite the structures being relatively simple compared to full neuronal morphologies, they demonstrate

considerable richness in the steady-state beyond what point-like or even compartmental models capture.

For the infinite and semi-infinite dendrite models (sections 2.3 and 2.4), the upcrossing rate was shown to be independent of the electrotonic length constant, which was surprising given that λ sets the range over which synaptic drive contributes to voltage fluctuations. The intuitive explanation for this was that λ is the only parameter with units of length, and thus cannot be present in the firing rate. Furthermore we also found that fixing the output voltage standard deviation between the two models by adjusting the synaptic standard deviation, the upcrossing rate and the simulated firing rate beyond the range of the upcrossing approximation was the same. This suggests that there is a universal functional form for the firing rate parametrised by σ_v that is independent of λ and the number of dendrites. This functional form for both coloured noise and in the white-noise limit is distinct from the point neuron LIF model and merits further mathematical analysis.

The addition of an axon allows the trigger position for firing to be placed in the AIS and causes the mean potential to spatially vary across the structure, leading to various interesting effects (section 2.6). When the trigger position was placed at the nominal soma, the load conductance provided by a thin axon led to a considerable reduction in the upcrossing rate. In addition, we saw that placing the trigger position a short distance down the AIS gave rise to a non-monotonic dependence of the upcrossing rate on the axonal radius.

The framework was next applied to consider an electrically substantial soma with a lumped conductance and capacitance (section 2.7). Because we did not consider synaptic drive at the soma, it acted as a conductance sink which reduced both the mean and variance across the neuron, significantly reducing the firing rate. For the ball-and-stick model with a dendrite only, the mean became spatially varying. When an axon was added, a larger soma increased the axonal radius which maximised the upcrossing rate.

Our approach was also then extended to multiple dendrites connected to an axon (section 2.8). Since the addition of more dendrites decreased the voltage variance but increased the mean in the axon, this led in general to a non-monotonic dependency of the output firing rate on the number of dendrites. The number of dendrites for maximal fluctuation-driven firing increased for a higher mean synaptic drive, a wider axon, a larger soma, and the trigger position being located further along the axon.

Chapter 3

Dynamic Response

3.1 Introduction

The average firing rate of neuronal networks *in vivo* often fluctuates periodically. These oscillations were first measured from areas of the brain via EEG, from which we get the well-known frequency bands (delta, theta, alpha, beta, gamma) [143,144]. Oscillatory behaviour has also been observed at smaller scales, such as from micro-electrode array measurements [145–147]. From a neuropathological perspective, the spread of oscillations is fundamental to understanding seizure propagation in epilepsy [147], and reduced synchrony plays an integral role in schizophrenia [2].

As an important step in understanding firing-rate dynamics in neuronal networks, the response of individual neurons - representative of a wider population - to oscillatory drive has been the subject of prior research. Importantly, it has been found that neuronal populations can respond to oscillatory drive at frequencies orders of magnitude higher than the mean firing rate [85, 86, 88, 148, 149]. This gives rise to the idea of neuronal populations being able to encode information much faster than single neurons [6, 87, 150]. The exact reasons why neuronal population firing can respond such high frequency oscillations remains an active area of research. Studies indicate that the spike dynamics [86], the load conductance of the dendritic arbour [11, 127, 149], and the axonal load conductance [126] all contribute to this high bandwidth.

In this chapter we focus purely on the firing-rate *response* of spatial neuron models to sinusoidally modulated drive. Two types of modulation that together represent modulation of the presynaptic firing rate are considered; modulation of the mean and the variance of the synaptic drive. In addition we also consider local current modulation applied at a single point on the structure, representing

an external modulating current. We show that the upcrossing method can be used to calculate an approximation for the oscillatory firing rate and we utilise this in the limit of small amplitude modulation. This approach is first applied to the previously studied passive point-neuron model, before moving on to spatial models with progressively more complex morphologies.

3.1.1 Oscillatory Presynaptic Drive

Many collections of neurons are thought to be able to encode information through their mean firing rate [81, 124, 150]. Since Fourier's theorem states that any time-varying signal can be represented as a sum of sinusoids, calculating the firing-rate response of the postsynaptic neuron to small-amplitude sinusoidal presynaptic background activity allows us to infer the firing-rate response of the neuron to any weak time-varying modulation of the presynaptic firing rate. For sinusoidal modulation at angular frequency Ω, the mean presynaptic firing rate is written as

$$r_s = r_{s0} + r_{s1}e^{i\Omega t}, \tag{3.1}$$

where r_{s0} is the steady-state component of the presynaptic firing rate and r_{s1} is the amplitude of oscillations about this level.

If we assume that r_{s1} is small compared to r_{s0}, then substitution of (3.1) into the equation for the synaptic conductance (1.27) yields terms oscillating at the same frequency Ω which modulate the mean and variance of the neuron. This derivation is given fully in Appendix A.3. For clarity we let the membrane potential $V = \langle V\rangle_0 + u$, where $\langle V\rangle_0$ is the steady state mean component and u is the combined fluctuating and oscillatory voltage. Defining the stochastic synaptic drive s in the same manner as section 1.4.2, our dimensionless time equations for the point neuron in terms of u are

$$\frac{\mathrm{d}u}{\mathrm{d}t} = -u + \frac{\epsilon_m}{1+i\Omega\beta_s}e^{i\Omega t} + s, \quad \beta_s\frac{\mathrm{d}s}{\mathrm{d}t} = -s + \sigma_s\sqrt{2\beta_s}(1+\epsilon_v e^{i\Omega t})\xi_s(t), \tag{3.2}$$

where ϵ_m and ϵ_v are the real-valued coefficients for the resulting synaptic mean and variance modulation respectively. This form agrees with that found in [9]. Adding $\mathrm{d}\langle v\rangle_0/\mathrm{d}t$ to (3.2) would allow us to assess the voltage measured from rest with no synaptic drive, $v = V - E_L$. However, since we have studied changes in the steady-state mean in detail in the previous chapter, we will restrict our analysis here to the variable u which both oscillates and fluctuates about $\langle v\rangle_0$.

Similarly for spatial-neuron models we arrive at the equations

$$\begin{aligned}\frac{\partial u}{\partial t} &= -u + \frac{\epsilon_m}{1+i\Omega\beta_s}e^{i\Omega t} + \frac{\partial^2 u}{\partial x^2} + s \\ \beta_s\frac{\partial s}{\partial t} &= -s + 2\sigma_s\sqrt{\beta_s}(1+\epsilon_v e^{i\Omega t})\xi_s(x,t),\end{aligned} \tag{3.3}$$

where ϵ_m and ϵ_v are spatially uniform since we apply a spatially uniform modulation of the presynaptic drive.

3.1.2 Oscillating External Currents

Another form of modulation comes from external currents. These can arise from local-field potentials or gap junctions, and affect the voltage directly without synaptic filtering. Much of the existing experimental [85, 86, 148] and theoretical literature [126, 127] has used this type of modulation. With a magnitude of ϵ_c for the point neuron, this current modulation is represented as

$$\frac{\mathrm{d}u}{\mathrm{d}t} = -u + \epsilon_c e^{i\Omega t} + s. \tag{3.4}$$

For spatially extended neurons, an electrode can apply current modulation to a specific position x_c, which we write as

$$\frac{\partial u}{\partial t} = -u + \epsilon_c\delta(x-x_c)e^{i\Omega t} + \frac{\partial^2 u}{\partial x^2} + s. \tag{3.5}$$

3.1.3 Linear Frequency Response

Due to the linearity of the system, the synaptic mean, variance and current modulation components can be analysed in isolation from each other, and then linearly combined to give the overall response. Furthermore, provided that the modulation amplitudes $\epsilon_{c,m,v}$ are small, this means that we can approximate the firing rate response to first order, hence for modulation type j

$$r_j = r_0 + r_{1j}\epsilon_j e^{i\Omega t} + O(\epsilon_j^2), \tag{3.6}$$

where r_0 represents the steady-state firing rate, which for the upcrossing approximation is given by 2.1. Therefore when all three modulation types present we can sum the first order contributions linearly to yield

$$r_{c,m,v} = r_0 + r_{1c}\epsilon_c e^{i\Omega t} + r_{1m}\epsilon_m e^{i\Omega t} + r_{1v}\epsilon_v e^{i\Omega t}. \tag{3.7}$$

Simulations were performed to verify both the validity of the linear frequency response and upcrossing approximations, with the specific details of the approach used in Appendix B.2. Hence in each figure we show values from both dynamic upcrossing and threshold-reset simulations. Each model was simulated with modulation for a fixed time period, with the existence of an upcrossing or threshold-reset event noted at each time step. This was repeated for many different random realisations ($\sim 10^6$–10^8) to give the time-varying ensemble-averaged firing rate as a function of time. A discrete Fourier transform method was finally used to extract the amplitude, $|r_{1j}|$, and phase, $\angle r_{1j}$, of the firing-rate response.

An example of the dynamic firing-rate response due to an oscillatory input signal with frequency Ω is shown in Figure 3.1. We will now look at calculating the complex coefficients $r_{1c,m,v}$.

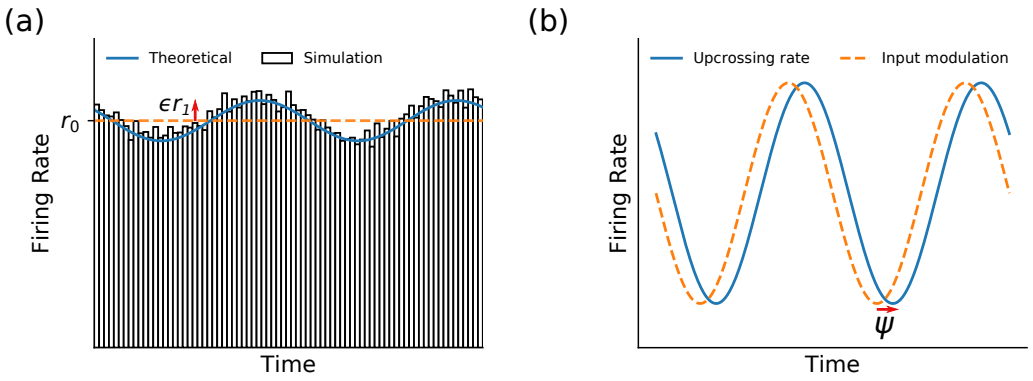

Figure 3.1: Example of input current modulation causing oscillations in the firing rate. (a) Averaging over realisations of the time-dependent firing rate yields a histogram which oscillates about the steady-state level r_0 with amplitude ϵr_1. (b) The theoretical upcrossing-rate response is compared with the input modulation, showing a small phase lag ψ.

3.1.4 Current/Synaptic Mean Modulation Upcrossing Rate

When looking at current or synaptic mean modulation only, the general upcrossing rate derived in Chapter 1 (1.56) differs from the steady state mainly in that $\langle \dot{u} \rangle \neq 0$; however, we still have for the covariance $\mathrm{cov}(u, \dot{u}) = 0$ (since we are only changing the mean value and not altering stochastic fluctuations). Recalling the earlier notation from section 1.8, this means that $\langle \dot{u} \rangle_{\mathrm{th}} = \langle \dot{u} \rangle$, $[\sigma_{\dot{u}}]_{\mathrm{th}} = \sigma_{\dot{u}}$, and hence $\eta = \langle \dot{u} \rangle / (\sigma_{\dot{u}} \sqrt{2})$. Denoting our modulation prefactor as $\epsilon_{c,m}$, for small $\epsilon_{c,m}$,

the now time-dependent first moments will take the form

$$\langle u(t)\rangle = \langle u\rangle_0 + \langle u\rangle_1 \epsilon_{c,m} e^{i\Omega t}, \quad \langle \dot{u}(t)\rangle = \langle \dot{u}\rangle_0 + \langle \dot{u}\rangle_1 \epsilon_{c,m} e^{i\Omega t}, \tag{3.8}$$

where $\langle u\rangle_0 = 0$ by definition, and as we saw in the steady state $\langle \dot{u}\rangle_0 = 0$. Substituting these expressions into the general formula for the upcrossing rate (1.56), letting $u_{\text{th}} = v_{\text{th}} - \langle v\rangle_0$, and expanding to first order in $\epsilon_{c,m}$, we find

$$\begin{aligned} r(t) &= \frac{\sigma_{\dot{u}}}{2\pi\sigma_u} \exp\left[-\frac{(u_{\text{th}} - \langle u\rangle_1 \epsilon_{c,m} e^{i\Omega t})^2}{2\sigma_u^2}\right] \left\{ \exp\left(-\frac{\langle \dot{u}\rangle_1^2 \epsilon_{c,m}^2 e^{2i\Omega t}}{2\sigma_{\dot{u}}^2}\right) \right. \\ &\quad \left. + \frac{\langle \dot{u}\rangle_1 \epsilon_{c,m} e^{i\Omega t}\sqrt{\pi}}{\sigma_{\dot{u}}\sqrt{2}} \left[1 + \operatorname{erf}\left(\frac{\langle \dot{u}\rangle_1 \epsilon_{c,m} e^{i\Omega t}}{\sigma_{\dot{u}}\sqrt{2}}\right)\right] \right\} \\ r(t) &\approx \frac{\sigma_{\dot{u}}}{2\pi\sigma_u} \exp\left[-\frac{u_{\text{th}}^2}{2\sigma_u^2}\right] \left[1 + \left(\frac{u_{\text{th}}\langle u\rangle_1}{\sigma_u^2} + \frac{\langle \dot{u}\rangle_1}{\sigma_{\dot{u}}}\sqrt{\frac{\pi}{2}}\right) \epsilon_{c,m} e^{i\Omega t}\right], \end{aligned} \tag{3.9}$$

where the variances of u and v are equivalent, $\sigma_u^2 = \sigma_v^2$. We note that the prefactor for $r(t)$ is equal to the steady state upcrossing rate r_0 (2.1). Thus for current or synaptic mean modulation we have

$$r_{c,m}(t) = r_0 + r_{1c,m}\epsilon_{c,m} e^{i\Omega t}, \quad \frac{r_{1c,m}}{r_0} = \frac{u_{\text{th}}\langle u\rangle_1}{\sigma_u^2} + \frac{\langle \dot{u}\rangle_1}{\sigma_{\dot{u}}}\sqrt{\frac{\pi}{2}}. \tag{3.10}$$

3.1.5 Variance Modulation Upcrossing Rate

When only variance modulation is considered, the calculation of the upcrossing rate involves the calculation of the oscillatory variances, with the first moments stationary as in the steady state. Again, if ϵ_v is small we can write the variances as

$$\begin{aligned} \sigma_u^2 = [\sigma_u^2]_0 + [\sigma_u^2]_1 \epsilon_v e^{i\Omega t}, \quad \sigma_u^2 = [\sigma_{\dot{u}}^2]_0 + [\sigma_{\dot{u}}^2]_1 \epsilon_v e^{i\Omega t}, \\ \operatorname{cov}(u, \dot{u}) = [\sigma_{u\dot{u}}]_1 \epsilon_v e^{i\Omega t}, \end{aligned} \tag{3.11}$$

where the zeroth order term for the covariance is omitted since we explained in the steady-state chapter that this is always zero, section 2.1.1. The terms that make up η in (1.56) are thus given by

$$\begin{aligned} \langle \dot{u}\rangle_{\text{th}} &= \frac{[\sigma_{u\dot{u}}]_1 u_{\text{th}} \epsilon_v e^{i\Omega t}}{[\sigma_u^2]_0 + [\sigma_u^2]_1 \epsilon_v e^{i\Omega t}}, \\ [\sigma_{\dot{u}}^2]_{\text{th}} &= [\sigma_{\dot{u}}^2]_0 + [\sigma_{\dot{u}}^2]_1 \epsilon_v e^{i\Omega t} - \frac{[\sigma_{u\dot{u}}^2]_1 \epsilon_v^2 e^{2i\Omega t}}{[\sigma_u^2]_0 + [\sigma_u^2]_1 \epsilon_v e^{i\Omega t}}, \end{aligned} \tag{3.12}$$

which can be expanded to first order in ϵ_v

$$\begin{aligned}\langle \dot{u} \rangle_{\text{th}} &= \frac{[\sigma_{u\dot{u}}]_1}{[\sigma_u^2]_1} u_{\text{th}} \epsilon_v e^{i\Omega t} + O(\epsilon_v^2), \\ [\sigma_{\dot{u}}]_{\text{th}} &= [\sigma_{\dot{u}}]_0 \left(1 + \frac{[\sigma_{\dot{u}}^2]_1}{2[\sigma_{\dot{u}}^2]_0} \epsilon_v e^{i\Omega t}\right) + O(\epsilon_v^2),\end{aligned} \tag{3.13}$$

and hence $\eta = \langle \dot{u} \rangle_{\text{th}} / ([\sigma_{\dot{u}}]_{\text{th}} \sqrt{2})$ from section 1.8 is given by

$$\eta = \frac{[\sigma_{u\dot{u}}]_1 u_{\text{th}} \epsilon_v e^{i\Omega t}}{[\sigma_u^2]_0 [\sigma_{\dot{u}}]_0 \sqrt{2}} + O(\epsilon_v^2). \tag{3.14}$$

Therefore, in a similar manner to current and synaptic mean modulation, we obtain the dynamic upcrossing rate as

$$\begin{aligned} r_v &= r_0 + r_{1v} \epsilon_v e^{i\Omega t}, \quad \frac{r_{1v}}{r_0} = r_{11} + r_{12} + r_{13} \\ r_{11} &= \frac{[\sigma_{u\dot{u}}]_1 u_{\text{th}}}{[\sigma_u^2]_0 [\sigma_{\dot{u}}]_0} \sqrt{\frac{\pi}{2}}, \quad r_{12} = \frac{1}{2} \left(\frac{[\sigma_{\dot{u}}^2]_1}{[\sigma_{\dot{u}}^2]_0} - \frac{[\sigma_u^2]_1}{[\sigma_u^2]_0} \right), \quad r_{13} = \frac{u_{\text{th}}^2 [\sigma_u^2]_1}{2[\sigma_u^4]_0}. \end{aligned} \tag{3.15}$$

where we have broken down the upcrossing-rate response into three parts, (r_{11}, r_{12}, r_{13}) for ease of analysis.

The magnitude of the dynamic upcrossing-rate response will hereafter be denoted by $\Lambda = |r_1/r_0|$, with the shorthand Λ_0 and Λ_∞ to denote the low and high frequency limits

$$\Lambda_0 = \lim_{\Omega \to 0} \left| \frac{r_1}{r_0} \right|, \quad \Lambda_\infty = \lim_{\Omega \to \infty} \left| \frac{r_1}{r_0} \right|. \tag{3.16}$$

Similarly, the phase shift of the dynamic response is denoted as $\psi = \angle r_1/r_0$, with $\psi < 0$ denoting that the firing rate response lags the input. As with Λ, ψ_0 and ψ_∞ are given by the phase at the limits of $\Omega = 0$ and $\Omega = \infty$ respectively.

Of particular interest in our analysis is whether $\psi(\Omega) = 0$ at finite, non-zero frequencies. If the modulation is generated by the firing of population of similar neurons, then these phase zeros represent the frequencies at which firing-rate oscillations in this population are in synchrony with the input drive. While in general synchrony is also possible for $\psi = 2\pi n$, we typically find that for $n \neq 0$ that Λ is very small at these frequencies.

Furthermore, when we have $\Lambda_\infty = 0$, the bandwidth of the firing rate response represents the range of frequencies for which the neuron can transmit information about the incoming waveform effectively through its firing rate. Here

we use the convention of the cutoff angular frequency Ω_c being the value at which $\Lambda(\Omega_c)/\Lambda_0 = 1/\sqrt{2}$ and the half-amplitude frequency by $\Lambda(\Omega_{1/2})/\Lambda_0 = 1/2$. "Resonance" in this thesis refers to local maxima or minima of the amplitude Λ.

3.2 Point Neuron Modulation

3.2.1 Point Neuron, Current Modulation

We can calculate $\langle u(t)\rangle$ and $\langle \dot{u}(t)\rangle$ for the point neuron with zero steady-state mean value by taking the temporal Fourier transform

$$\tilde{u}(\omega) = \frac{\sigma_s\sqrt{2\beta_s}\tilde{\xi}_s(\omega)}{(1+i\omega)(1+i\omega\beta_s)} + \frac{\epsilon_c\delta(\omega-\Omega)}{1+i\omega}. \tag{3.17}$$

By taking the inverse Fourier transform and the expectation, we get the two oscillating first moments

$$\langle u(t)\rangle = \frac{\epsilon_c e^{i\Omega t}}{1+i\Omega}, \quad \langle \dot{u}(t)\rangle = \frac{i\Omega\epsilon_c e^{i\Omega t}}{1+i\Omega}. \tag{3.18}$$

Substituting these expressions into (3.10) we find

$$\frac{r_1}{r_0} = \frac{1}{1+i\Omega}\left(\frac{u_{\mathrm{th}}}{\sigma_u^2} + \frac{i\Omega}{\sigma_{\dot{u}}}\sqrt{\frac{\pi}{2}}\right). \tag{3.19}$$

In the low- and high-frequency limits, the dynamic response reads

$$\Lambda_0 = \frac{u_{\mathrm{th}}}{\sigma_u^2}, \quad \Lambda_\infty = \frac{1}{\sigma_{\dot{u}}}\sqrt{\frac{\pi}{2}}, \tag{3.20}$$

which shows that there is a finite high-frequency limit. This has been found before in point neurons for the upcrossing rate [9,151] and also for the threshold-reset firing rate for LIF neurons subject to the coloured noise [117]. However this was not found for white noise which instead acts as a low-pass filter with a high-frequency phase limit of $-\pi/4$ [5, 96] or for EIF or QIF point neurons subject to white or coloured noise [101].

This finite high-frequency limit implies that a population of these neurons can encode information carried by current modulation arbitrarily quickly. Experiments that have used noisy input and current modulation demonstrate that this is not the case for pyramidal cells [85, 88, 152]. These differences arise from the dynamic time course of the AP [86, 153] and the fact that most *in vitro* experimental studies typically apply the oscillation at a single point, which can make a difference as when

shall explore in spatial models.

The presence of a single zero and pole in 3.19 means that a resonant peak is unattainable for current modulation in the point neuron. In comparison, previous studies found point LIF neurons subject to white noise show no fluctuation-driven firing-rate resonance when $\langle u \rangle_0 << u_{\text{th}}$ [96, 154], but that resonances appear for larger yet still subthreshold $\langle u \rangle_0$ [6].

Furthermore, by substituting in the steady state values for σ_u^2 and $\sigma_{\dot{u}}$, we can obtain a condition on u_{th}/σ_u for which the dynamic response decreases with frequency

$$\frac{u_{\text{th}}}{\sigma_u}\sqrt{\frac{2}{\pi\beta_s}} > 1, \tag{3.21}$$

which is typically satisfied for values for which the upcrossing approximation is valid (higher u_{th}/σ_u, $\beta_s \sim 1$). We shall refer to this as a quasi-low-pass filter.

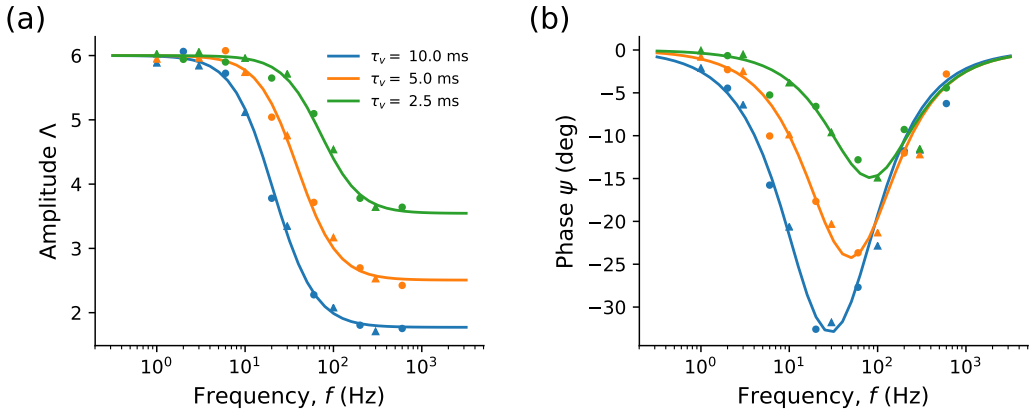

Figure 3.2: For the point neuron subject to current modulation, decreasing τ_v (higher β_s) increases the high-frequency limit Λ_∞ (3.20). Solid lines show the theoretical predicted amplitude (a) and phase (b) of the dynamic upcrossing rate response (3.19), while circles and triangles denote upcrossing and threshold-reset simulations respectively. Other parameters: (a-b) $\tau_s = 5$ms, $u_{\text{th}}/\sigma_v = 3$.

3.2.2 Point Neuron, Synaptic Mean Modulation

Synaptic mean modulation gives a very similar response to current modulation for the point neuron, with the only difference being a denominator of $(1 + i\Omega\beta_s)$ to the modulated term of $\tilde{u}(\omega)$

$$\tilde{u}(\omega) = \frac{\sigma_s\sqrt{2\beta_s}\tilde{\xi}_s(\omega)}{(1+i\omega)(1+i\omega\beta_s)} + \frac{\epsilon_c\delta(\omega-\Omega)}{(1+i\Omega\beta_s)(1+i\omega)}, \tag{3.22}$$

and hence the first moment coefficients are given by

$$\langle u \rangle_1 = \frac{1}{(1+i\Omega\beta_s)(1+i\Omega)}, \quad \langle \dot{u} \rangle_1 = \frac{i\Omega}{(1+i\Omega\beta_s)(1+i\Omega)}. \tag{3.23}$$

Our upcrossing-rate response to synaptic mean modulation therefore also is changed by having a denominator of $(1+i\Omega\beta_s)$

$$\frac{r_{1m}}{r_0} = \frac{1}{(1+i\Omega\beta_s)(1+i\Omega)} \left(\frac{u_{\text{th}}}{\sigma_u^2} + \frac{i\Omega}{\sigma_{\dot{u}}} \sqrt{\frac{\pi}{2}} \right), \tag{3.24}$$

which shows that while Λ_0 is the same as in current modulation, the high-frequency limit tends to zero as Ω^{-1}

$$\Lambda_0 = \frac{u_{\text{th}}}{\sigma_u^2}, \quad \Lambda_\infty = \frac{1}{\Omega\beta_s\sigma_{\dot{u}}} \sqrt{\frac{\pi}{2}}, \quad \psi_\infty = -\frac{\pi}{2}. \tag{3.25}$$

This shows that the upcrossing-rate response behaves as a first-order low-pass filter with respect to the modulation frequency Ω and there is no longer a finite high-frequency limit. Furthermore the cutoff frequency is well-defined, and can be increased by decreasing τ_v (increasing β_s), giving neurons with faster voltage dynamics a larger effective bandwidth to carrying the modulation frequency in their firing rate. This can be seen in Figure 3.3(a), and is later compared against the infinite dendrite in Figure 3.6(c).

In terms of dynamical systems, since r_1/r_0 given by (3.24) has two poles and one zero, one might imagine that a resonant peak is possible for certain parameters. A necessary condition for this is that the zero has to be smaller than the two poles, i.e.

$$\frac{u_{\text{th}}\sigma_{\dot{u}}}{\sigma_u^2} \sqrt{\frac{2}{\pi}} < \min(1, \beta_s^{-1}), \tag{3.26}$$

from which fixing u_{th}/σ_u and substituting in $\sigma_{\dot{u}}/\sigma_u$ yields

$$\frac{u_{\text{th}}}{\sigma_u} \sqrt{\frac{2}{\pi\beta_s}} < \min(1, \beta_s^{-1}), \quad \frac{u_{\text{th}}}{\sigma_u} \sqrt{\frac{2}{\pi}} < \min(\beta_s^{1/2}, \beta_s^{-1/2}). \tag{3.27}$$

This condition is most easily satisfied when $\beta_s = 1$. However, this indicates that $u_{\text{th}}/\sigma_u < \sqrt{\pi/2} \approx 1.25...$ is necessary for resonance, far below the value for which the upcrossing approach usually gives a good steady-state approximation. We examine the difficulty of achieving this theoretical resonance in more detail in comparison with the infinite dendrite, Figure 3.6(d).

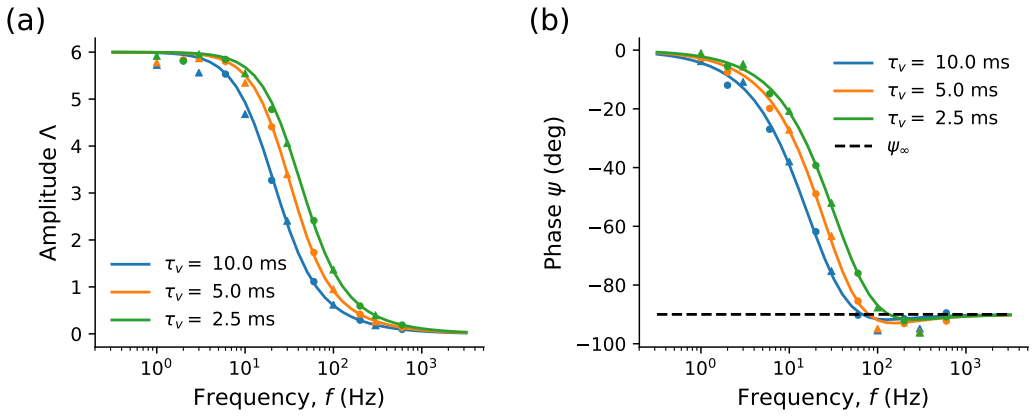

Figure 3.3: With synaptic mean modulation applied to a point neuron, decreasing τ_v (higher β_s) increases the cutoff frequency hence increases the bandwidth. Solid lines show the theoretical dynamic upcrossing-rate response (3.24), while circles and triangles denote upcrossing and threshold-reset simulations respectively. Other parameters: $\tau_s = 5\text{ms}$, $u_{\text{th}}/\sigma_u = 3$.

3.2.3 Point Neuron, Variance Modulation

As variance modulation causes the noise amplitude σ_s to be multiplied by the oscillatory term, a Fourier transform of the point neuron potential now introduces a convolution term denoted by $*$

$$\tilde{u}(\omega) = \frac{\sigma_s\sqrt{2\beta_s}}{(1+i\omega)(1+i\omega\beta_s)}\left[\tilde{\xi}_s(\omega) + \epsilon_v 2\pi\delta(\omega-\Omega) * \tilde{\xi}_s(\omega)\right]. \tag{3.28}$$

Since $2\pi\delta(\omega-\Omega) * \tilde{\xi}_s(\omega) = \tilde{\xi}_s(\omega-\Omega)$, the overall potential is given by

$$u(t) = \frac{\sigma_s\sqrt{2\beta_s}}{2\pi}\left[\int_{-\infty}^{\infty}\frac{\tilde{\xi}_s(\omega)e^{i\omega t}\mathrm{d}\omega}{(1+i\omega)(1+i\omega\beta_s)} + \epsilon_v\int_{-\infty}^{\infty}\frac{\tilde{\xi}_s(\omega-\Omega)e^{i\omega t}\mathrm{d}\omega}{(1+i\omega)(1+i\omega\beta_s)}\right], \tag{3.29}$$

from which we see that the first-order term in ϵ_v of the variance is given by the cross multiplication of the two integrals. Since our white-noise correlator implies that $\langle\tilde{\xi}_s(\omega-\Omega)\tilde{\xi}_s(-\omega')\rangle = 2\pi\delta(\omega'-\omega+\Omega)$, we have to first order in ϵ_v

$$\begin{aligned}\langle u(t)^2\rangle &= [\sigma_u^2]_0 + [\sigma_u^2]_1\epsilon_v e^{i\Omega t}\\ [\sigma_u^2]_1 &= \frac{2\sigma_s^2\beta_s}{\pi}\int_{-\infty}^{\infty}\frac{\mathrm{d}\omega}{[1+\omega^2+i\Omega(1+i\omega)][1+\omega^2\beta_s^2+i\Omega\beta_s(1+i\omega\beta_s)]},\end{aligned} \tag{3.30}$$

and hence

$$[\sigma_u^2]_1 = \frac{8i\sigma_s^2\beta_s}{(\Omega - 2i)(\beta_s\Omega - 2i)[\beta_s\Omega - i(1+\beta_s)]}. \tag{3.31}$$

Similarly for the derivative variance we find that

$$\begin{aligned}\langle \dot{u}(t)^2 \rangle &= [\sigma_{\dot{u}}^2]_0 + [\sigma_{\dot{u}}^2]_1 \epsilon_v e^{i\Omega t} \\ [\sigma_{\dot{u}}^2]_1 &= \frac{2\sigma_s^2\beta_s}{\pi}\int_{-\infty}^{\infty} \frac{(\omega^2 - \Omega\omega)\mathrm{d}\omega}{[1+\omega^2 + i\Omega(1+i\omega)][1+\omega^2\beta_s^2 + i\Omega\beta_s(1+i\omega\beta_s)]},\end{aligned} \tag{3.32}$$

and so

$$[\sigma_{\dot{u}}^2]_1 = \frac{4i\sigma_s^2[2 - \beta_s\Omega^2 + i\Omega(1+\beta_s)]}{(\Omega - 2i)(\beta_s\Omega - 2i)[\beta_s\Omega - i(\beta_s+1)]}. \tag{3.33}$$

Finally we must calculate the covariance by cross multiplying the integrals for u and $\dot{u}$, which yields the last term required

$$\begin{aligned}\langle u\dot{u} \rangle &= \frac{2\epsilon_v\sigma_s^2\beta_s e^{i\Omega t}}{\pi}\int_{-\infty}^{\infty} \frac{-i(\omega - \Omega)\mathrm{d}\omega}{[1+\omega^2 + i\Omega(1+i\omega)][1+\omega^2\beta_s^2 + i\Omega\beta_s(1+i\omega\beta_s)]}, \\ [\sigma_{u\dot{u}}]_1 &= \frac{-4\sigma_s^2\beta_s\Omega}{(\Omega - 2i)(\beta_s\Omega - 2i)[\beta_s\Omega - i(1+\beta_s)]}.\end{aligned} \tag{3.34}$$

In the low-frequency limit, each of the dynamic variance coefficients except the covariance is finite

$$\lim_{\Omega\to 0}[\sigma_u^2]_1 = \frac{2\sigma_s^2\beta_s}{1+\beta_s}, \quad \lim_{\Omega\to 0}[\sigma_{\dot{u}}^2]_1 = \frac{2\sigma_s^2}{1+\beta_s}, \quad \lim_{\Omega\to 0}[\sigma_{u\dot{u}}]_1 = 0, \tag{3.35}$$

where comparison with the steady-state variances shows that $[\sigma_u^2]_1 = 2[\sigma_u^2]_0$ and $[\sigma_{\dot{u}}^2]_1 = 2[\sigma_{\dot{u}}^2]_0$ in the low-frequency limit, which is general to variance modulation and not specific to the point neuron. This can be seen by letting $\Omega = 0$ in (3.29) and calculating $[\sigma_u^2]_1$. Therefore the dynamic upcrossing-rate response in the low-frequency limit is given by the r_{13} term of (3.15)

$$\Lambda_0 = \lim_{\Omega\to 0}\frac{u_{\mathrm{th}}^2[\sigma_u^2]_1}{2[\sigma_u^4]_0} = \frac{u_{\mathrm{th}}^2}{[\sigma_u^2]_0} = \frac{u_{\mathrm{th}}^2}{\sigma_s^2}\left(\frac{1+\beta_s}{\beta_s}\right). \tag{3.36}$$

While in the high-frequency limit, all dynamic variances coefficients decrease with modulation frequency

$$\lim_{\Omega\to\infty}[\sigma_u^2]_1 = \frac{8i\sigma_s^2}{\beta_s\Omega^3}, \quad \lim_{\Omega\to\infty}[\sigma_{\dot{u}}^2]_1 = -\frac{4i\sigma_s^2}{\beta_s\Omega}, \quad \lim_{\Omega\to\infty}[\sigma_{u\dot{u}}]_1 = \frac{4\sigma_s^2}{\beta_s\Omega^2}, \tag{3.37}$$

which shows that for large Ω, the $[\sigma_{\dot{v}}^2]_1$ term of r_{12} will dominate the dynamic upcrossing-rate response. This means that the high-frequency amplitude and phase limits

$$\Lambda_\infty = \frac{2\sigma_s^2}{\beta_s \Omega [\sigma_{\dot{u}}^2]_0}, \quad \psi_\infty = -\frac{\pi}{2}. \tag{3.38}$$

Hence unlike current modulation but like synaptic mean modulation, the amplitude of upcrossing-rate oscillations decays towards zero at high frequencies due to synaptic filtering. The high-frequency phase limit was found earlier for upcrossing in [9, 151], but differs from LIF neurons with white noise, which instead have $\psi_\infty = 0$ [6, 96].

The cutoff frequency for variance modulation is roughly twice that for synaptic mean modulation, as is later shown in comparison with the infinite dendrite, Figures 3.6(c) 3.7(c). This suggests that the bandwidth of variance-modulated signals is broader, allowing faster-changing signals to be transmitted in this way. This agrees with a previous study which suggest that neuronal populations can convey fast signals by changes variance than changes in the mean [150].

It is possible to obtain a resonant peak in the upcrossing rate with variance modulation applied to a passive point neuron (as has been found previously in [151], though their definition of variance modulation refers to modulation of s rather than σ_s). However, this resonance requires low u_{th} and high β_s, so is not observed with parameter ranges for which the upcrossing approximation is valid. The reason that this resonance requires low $u_{\text{th}}/[\sigma_u]_0$ (< 1.7 for $\beta_s = 0.5$) can be explained by noticing that $|r_{13}|$ decreases monotonically as a low-pass filter, while $|r_{11}|$ and $|r_{12}|$ peak at intermediate frequencies. Since $|r_{13}| \propto u_{\text{th}}^2/[\sigma_u^2]_0$ while $|r_{11}| \propto u_{\text{th}}/[\sigma_u]_0$ and $|r_{12}|$ has no dependence on the relative threshold, decreasing $u_{\text{th}}/[\sigma_u]_0$ more significantly decreases the low-pass filtering effect of $|r_{13}|$ than the other two terms. This means that a resonant peak emerges for as $u_{\text{th}}/[\sigma_u]_0$ is lowered which is otherwise masked by the low-pass response of $|r_{13}|$ when $u_{\text{th}}/[\sigma_u]_0$ is greater.

While it is possible that the threshold-reset rate does in fact exhibit resonance for lower $u_{\text{th}}/[\sigma_u]_0$, as has been found for white-noise input [96], the properties of such firing-rate resonances (resonant frequency, peak height, phase zero) cannot be reliably determined using the upcrossing method due to parameters required for which the steady-state upcrossing approximation is inaccurate. This inaccuracy is illustrated by disagreement between threshold-reset simulations and the theoretical upcrossing-rate response in Figure 3.4(a, b).

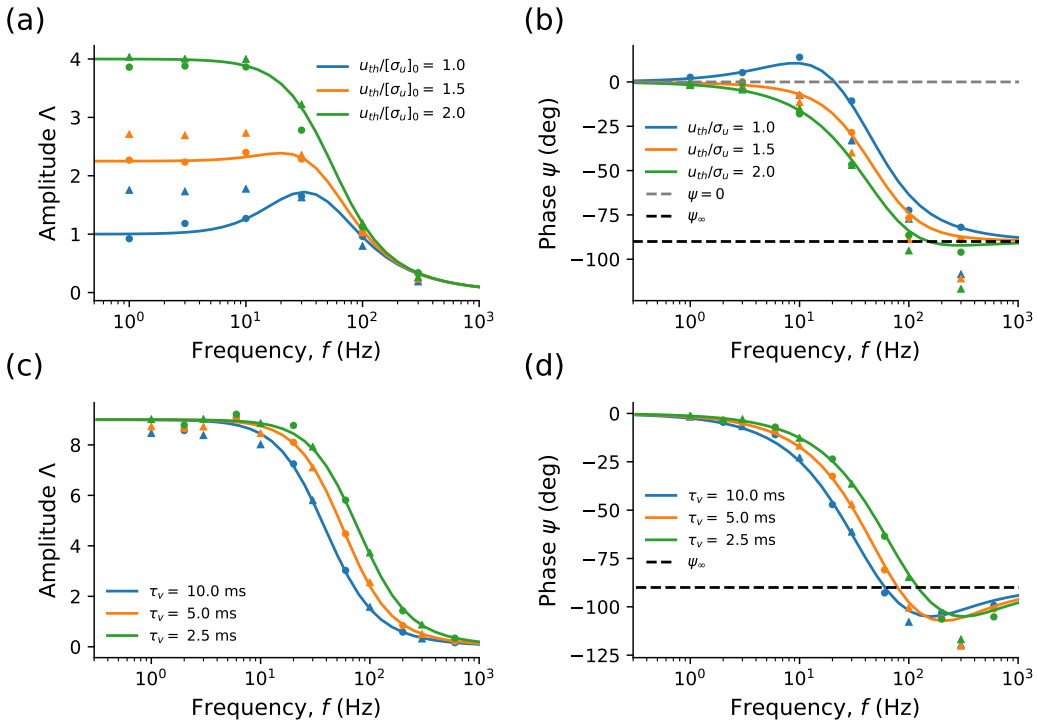

Figure 3.4: With variance modulation applied to the point neuron: (a-b) Decreasing $u_{\text{th}}/[\sigma_u]_0$ allows resonance to appear in the upcrossing rate, but this is not apparent in the simulated threshold-reset firing rate. (c-d) For $u_{\text{th}}/[\sigma_u]_0 = 3$, as τ_v decreases (higher β_s), the cutoff frequency of the upcrossing-rate response increases. Solid lines show the amplitude (a,c) and phase (b,d) of the theoretical upcrossing-rate response (3.15), whilst circles and triangles indicate upcrossing and threshold-reset simulations respectively. Parameters used: (a-d) $\tau_s = 5$ms, (a-b) $\tau_v = 10$ms (c-d) $u_{\text{th}}/[\sigma_u]_0 = 3$.

3.3 Infinite Dendrite Modulation

3.3.1 Infinite Dendrite, Local Current Modulation

For any spatial-neuron model, current modulation can be applied to a variety of different positions. When we apply modulation at a single location x_c, we can represent this in the cable equation as

$$\frac{\partial u}{\partial t} = -u + \frac{\partial^2 u}{\partial x^2} + s + \epsilon_c \delta(x - x_c) e^{i\Omega t}. \tag{3.39}$$

For clarity, we use the Fourier-domain Green's function $\tilde{\mathcal{G}}(x, y; \omega)$ to give $u(t)$

$$u(x,t) = \frac{1}{2\pi}\int_{-\infty}^{\infty} e^{i\omega t}\mathrm{d}\omega \int_{\mathcal{R}} \tilde{\mathcal{G}}(x,y;\omega)[\tilde{s}(y,\omega) + 2\pi\epsilon_c\delta(\omega-\Omega)\delta(y-x_c)]\mathrm{d}y. \quad (3.40)$$

Without loss of generality, we will measure at $x = 0$ and choose this as the trigger position. With the infinite dendrite Green's function $\tilde{\mathcal{G}} = e^{-|x-y|\gamma}/(2\gamma)$, the delta functions resolve the integrals for the modulation term, and thus the mean components have the form

$$\langle u(t)\rangle = \epsilon_c e^{i\Omega t}\tilde{\mathcal{G}}(0, x_c; \Omega) = \epsilon_c e^{i\Omega t}\frac{e^{-|x_c|\Gamma}}{2\Gamma}, \quad \Gamma = \sqrt{1+i\Omega}, \quad (3.41)$$

$$\langle u\rangle_1 = \frac{e^{-|x_c|\Gamma}}{2\Gamma}, \quad \langle \dot{u}\rangle_1 = i\Omega\langle u\rangle_1. \quad (3.42)$$

Since we have only used the fact that the dendrite is infinite in the substitution of the Green's function, for any spatial structure the oscillatory mean coefficients at x due to local current modulation at x_c are given by

$$\langle u\rangle_1 = \tilde{\mathcal{G}}(x, x_c; \Omega), \quad \langle \dot{u}\rangle_1 = i\Omega\tilde{\mathcal{G}}(x, x_c; \Omega). \quad (3.43)$$

The dynamic upcrossing-rate response is therefore

$$\frac{r_{1c}}{r_0} = \frac{e^{-|x_c|\Gamma}}{2\Gamma}\left(\frac{u_{\mathrm{th}}}{\sigma_u^2} + \frac{i\Omega}{\sigma_{\dot{u}}}\sqrt{\frac{\pi}{2}}\right). \quad (3.44)$$

For all modulation input positions, the low-frequency limit is

$$\Lambda_0 = \frac{u_{\mathrm{th}}e^{-|x_c|}}{2\sigma_u^2}, \quad (3.45)$$

where the exponential scaling with distance $|x_c|$ makes sense as modulation further away will decay and thus have a smaller effect. The high-frequency limit depends on x_c, with the special case of $x_c = 0$ yielding

$$\lim_{\Omega\to\infty}\frac{r_{1c}}{r_0} = \frac{i\sqrt{\pi\Omega}}{2(1+i)\sigma_{\dot{u}}}, \quad \Lambda_\infty = \frac{1}{2\sigma_{\dot{u}}}\sqrt{\frac{\pi\Omega}{2}}, \quad \psi_\infty = \pi/4, \quad (3.46)$$

showing that the dynamic response increases without bound with Ω. On the other hand, for $|x_c| > 0$, the complex exponential dominates at high Ω with

$$\lim_{\Omega\to\infty}\frac{r_{1c}}{r_0} = \frac{e^{-|x_c|(1+i)\sqrt{\Omega/2}}\sqrt{\pi\Omega}}{2(1+i)\sigma_{\dot{u}}}, \quad \Lambda_\infty = \frac{e^{-|x_c|\sqrt{\Omega/2}}}{2\sigma_{\dot{u}}}\sqrt{\frac{\pi\Omega}{2}}, \quad \psi_\infty \to -\infty, \quad (3.47)$$

hence the amplitude of modulation will eventually decay to zero and the high-frequency phase limit is undetermined. Interestingly, we find that for small $|x_c|$ (< 0.3 for the parameters in Figure 3.5), Λ is non-monotonic in shape, as shown in Figure 3.5(a). Initially Λ decreases with frequency due to the prefactor $1/\Gamma$, before increasing once the term with $i\Omega$ becomes prominent. Finally, for large Ω the exponential term dominates and Λ decreases again. Increasing $|x_c|$ decreases the frequency required for the exponential decay to have an effect. Λ is also at least half Λ_0 across frequencies at least up to 1kHz, qualitatively agreeing with experimental studies of somatically applied current modulation and stochastic drive [85, 88, 151].

This non-monotonic behaviour suggests the existence of non-trivial zero phase crossings, which can be seen from the plot of ψ, Figure 3.5(b). Two non-trivial zeros of ψ are present for small $|x_c| > 0$. For the parameters chosen the lower phase zero is in the high-gamma frequency band [143, 144].

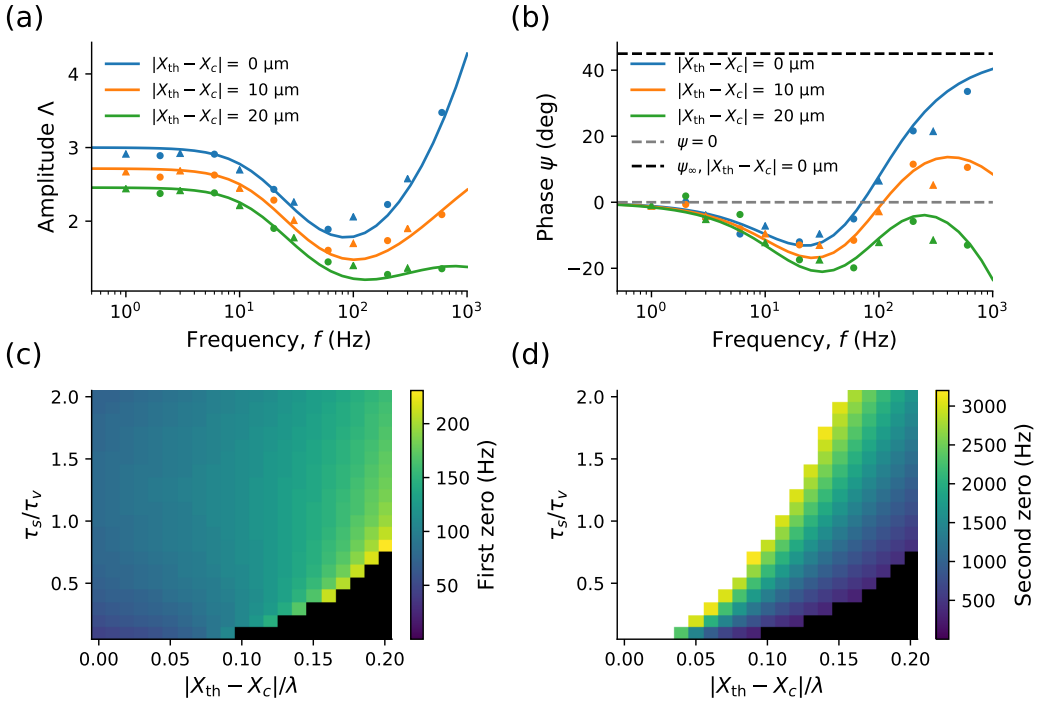

Figure 3.5: Local current modulation in the infinite dendrite gives a non-monotonic firing-rate response profile in amplitude (a) and phase (b). For sufficiently low spatial separation between the trigger position x_{th} and the location of modulation injection x_c, the upcrossing-rate response exhibits phase zeros. Solid lines show the amplitude and phase of the theoretical dynamic upcrossing-rate response (3.44), whilst circles and triangles denote upcrossing and threshold-reset simulations respectively. (c-d) Both phase zeros disappear for lower τ_s/τ_v and x_{th}. Black areas indicate that no phase zero is present and white areas indicate phase zeros in excess of 3200 Hz. Other parameters: (a-d) $\lambda = 100\mu$m, $u_{\text{th}}/\sigma_u = 3$, (a-b) $\tau_v = 10$ms, $\tau_s = 5$ms.

3.3.2 Infinite Dendrite, Synaptic Mean Modulation

Synaptic mean modulation for spatial models is most easily calculated using the Green's function $\tilde{\mathcal{G}}(x, y; \omega)$ and this approach can be generalised to all morphologies. For synaptic mean modulation, the total input is

$$\tilde{I}(y, \omega) = \tilde{s}(y, \omega) + \frac{2\pi\epsilon_m \delta(\omega - \Omega)}{1 + i\Omega\beta_s}, \tag{3.48}$$

and hence the voltage response is

$$u(x, t) = \frac{1}{2\pi} \int_{\mathcal{R}} \mathrm{d}y \int_{-\infty}^{\infty} e^{i\omega t} \tilde{\mathcal{G}}(x, y; \omega) \left[\tilde{s}(y, \omega) + \frac{2\pi\epsilon_m \delta(\omega - \Omega)}{1 + i\Omega\beta_s} \right] \mathrm{d}\omega, \tag{3.49}$$

where for the infinite dendrite $\mathcal{R} = (-\infty, \infty)$. Since $\langle \tilde{s} \rangle = 0$, we can deduce that the time-varying mean is given by

$$\langle u(x,t) \rangle = \frac{\epsilon_m e^{i\Omega t}}{1 + i\Omega\beta_s} \int_{\mathcal{R}} \tilde{\mathcal{G}}(x, y; \Omega) \mathrm{d}y, \tag{3.50}$$

and hence the oscillatory first-moment coefficients are

$$\langle u \rangle_1 = \frac{1}{1 + i\Omega\beta_s} \int_{\mathcal{R}} \tilde{\mathcal{G}}(x, y; \Omega) \mathrm{d}y, \quad \langle \dot{u} \rangle_1 = \frac{i\Omega}{1 + i\Omega\beta_s} \int_{\mathcal{R}} \tilde{\mathcal{G}}(x, y; \Omega) \mathrm{d}y. \tag{3.51}$$

This is a general formula for uniformly distributed synaptic mean modulation since we have made no assumptions about the morphology of the neuron.

The Green's function for an infinite cable is $\tilde{\mathcal{G}}(x, y; \omega) = e^{-|x-y|\gamma}/(2\gamma)$, which upon substitution yields spatially uniform $\langle u \rangle_1$ and $\langle \dot{u} \rangle_1$ that are exactly the same as the point-neuron model (3.18). Indeed, this will be common in many of the simpler spatial-neuron models we examine. Therefore, the dynamic upcrossing-rate response will have the same form as (3.19), as shown in Figure 3.6(a, b).

In the low-frequency limit, we again find that $\Lambda_0 = u_{\mathrm{th}}/\sigma_u^2$. Since we fix u_{th}/σ_u and σ_u in this chapter to maintain similar steady-state dynamics for the upcrossing approximation, we will obtain the same low-frequency limit for the infinite dendrite as the point neuron.

It is impossible to fix both σ_u and $\sigma_{\dot{u}}$ across the two models, however, as we saw for the steady-state comparison. We recall from section 2.3.3 that for fixed σ_u, $\sigma_{\dot{u}}$ was higher for the infinite dendrite compared with the point neuron, section 2.3.2. Since the high-frequency limit has the same form (3.25), this implies that the cutoff frequency is lower for the infinite dendrite. This is indeed shown in Figure 3.3(c), though the difference is revealed to be < 1Hz for the parameters chosen.

Finally, we again look at the possibility of firing-rate resonance due to synaptic mean modulation. Since we found in Chapter 2 that the ratio $\sigma_{\dot{u}}/\sigma_u$ is higher for the infinite dendrite than the point-neuron model (2.37), the necessary condition for resonance found earlier (3.26) will require an even lower value of u_{th}/σ_u. This is verified in Figure 3.6, and is even further from the region for which the upcrossing method can be applied to approximate the threshold-reset firing rate.

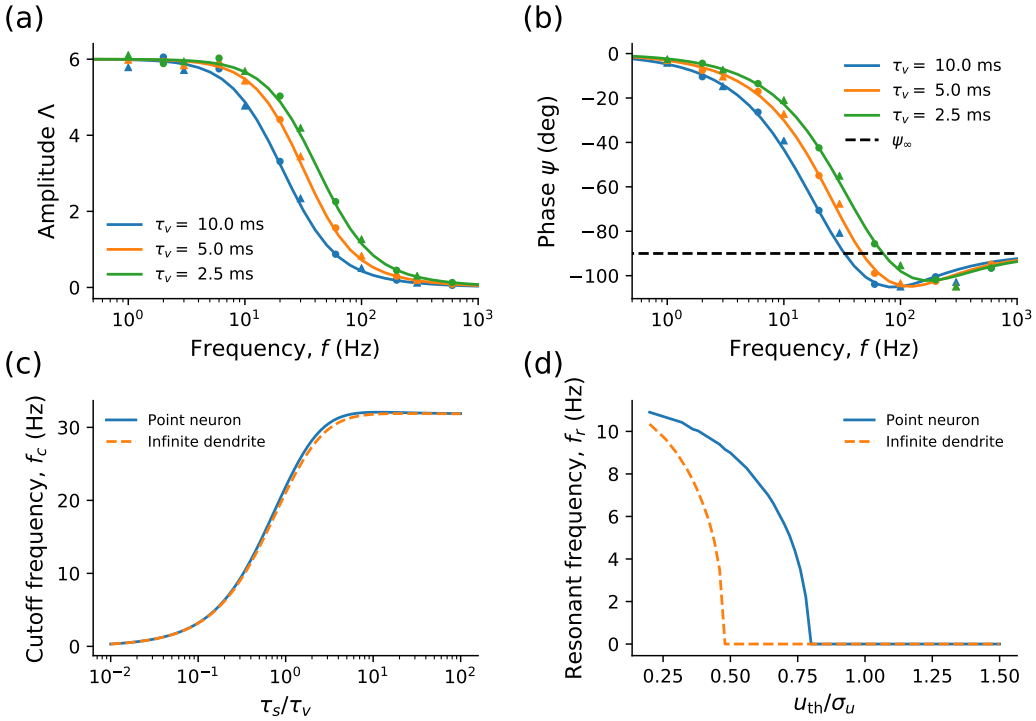

Figure 3.6: (a, b) Synaptic mean modulation in the infinite dendrite gives the same form of dynamic response as in the point neuron, however (c) the cutoff frequency is lowered by $<$ 1Hz for the chosen parameters. (d) Resonance in the dynamic upcrossing rate is theoretically possible, but it requires very low values of u_{th}/σ_u. The value of u_{th}/σ_u to initiate resonance is lower for the infinite dendrite than the point neuron. In (a,b) solid lines illustrate the theoretical dynamic upcrossing-rate response (3.24), while circles and triangles show upcrossing and threshold-reset simulations respectively. Other parameters: (a-d) $\lambda = 100\mu$m, $\tau_s = 5$ms, (a-b) $u_{\text{th}}/\sigma_s = 3$, $\tau_v = 10$ms.

3.3.3 Infinite Dendrite, Variance Modulation

Unlike current modulation and like synaptic mean modulation, variance modulation is intrinsically coupled to synaptic drive and is thus distributed with s. Performing the double Fourier transform on u yields

$$\hat{u}(k,\omega) = \frac{2\sigma_s\sqrt{\beta_s}}{(1+i\omega\beta_s)(1+k^2+i\omega)}(\hat{\xi}_s(k,\omega) + \epsilon_v\hat{\xi}_s(k,\omega-\Omega)), \tag{3.52}$$

from which we obtain the amplitude $[\sigma_u^2]_1$ from the integral

$$\begin{aligned}
[\sigma_u^2]_1 &= \frac{2\sigma_s^2\beta_s}{\pi^2}\int_{-\infty}^{\infty}\mathrm{d}\omega\int_{-\infty}^{\infty}\frac{\mathrm{d}k}{D_\infty(k,\omega,\Omega)} \\
D_\infty(k,\omega,\Omega) &= [1+\omega^2\beta_s^2+i\Omega\beta_s(1+i\omega\beta_s)] \\
&\quad\times[(1+k^2)^2+\omega^2+i\Omega(1+k^2+i\omega)]
\end{aligned} \tag{3.53}$$

Note the similarity to the point neuron (3.31), but now we replace one of the constant terms with $1+k^2$. Both the ω and k integrals can be resolved analytically to give

$$\begin{aligned}
[\sigma_u^2]_1 &= \frac{4\sigma_s^2}{(2+i\Omega\beta_s)M(\Omega)A(\Omega)} \\
A(\Omega) &\equiv \sqrt{1+\tfrac{1}{2}i\Omega}+\sqrt{1+\beta_s^{-1}+i\Omega}, \quad M(\Omega)\equiv\sqrt{1+\tfrac{1}{2}i\Omega}\sqrt{1+\beta_s^{-1}+i\Omega}.
\end{aligned} \tag{3.54}$$

Similarly, using $A(\Omega)$ and $M(\Omega)$ as defined for the variance (3.54), the oscillatory coefficient for the derivative variance follows from

$$\begin{aligned}
[\sigma_{\dot{u}}^2]_1 &= \frac{2\sigma_s^2\beta_s}{\pi^2}\int_{-\infty}^{\infty}\mathrm{d}\omega\int_{-\infty}^{\infty}\frac{(\omega^2-\Omega\omega)\mathrm{d}k}{D_\infty(k,\omega,\Omega)}, \\
[\sigma_{\dot{u}}^2]_1 &= \frac{2\sigma_s^2}{\beta_s A(\Omega)}\left[1+\frac{(2+i\Omega\beta_s)+i\Omega(1+i\Omega\beta_s)}{(2+i\Omega\beta_s)M(\Omega)}\right].
\end{aligned} \tag{3.55}$$

Finally the covariance is given by

$$\begin{aligned}
[\sigma_{u\dot{u}}]_1 &= \frac{2\sigma_s^2\beta_s}{\pi^2}\int_{-\infty}^{\infty}\mathrm{d}\omega\int_{-\infty}^{\infty}\frac{-i(\omega-\Omega)\mathrm{d}k}{D_\infty(k,\omega,\Omega)}, \\
[\sigma_{u\dot{u}}]_1 &= \frac{2i\sigma_s^2\Omega}{(2+i\Omega\beta_s)M(\Omega)A(\Omega)}.
\end{aligned} \tag{3.56}$$

In the low-frequency limit, we again have $\lim_{\Omega\to 0}[\sigma_u^2]_1 = 2[\sigma_u^2]_0$, $\lim_{\Omega\to 0}[\sigma_{\dot{u}}^2]_1 = 2[\sigma_{\dot{u}}^2]_0$, $\lim_{\Omega\to 0}[\sigma_{u\dot{u}}^2]_1 = 0$, meaning that Λ_0 is again given entirely in terms of the r_{13} term of (3.15)

$$\Lambda_0 = \frac{u_{\mathrm{th}}^2}{\sigma_s^2\beta_s\left[1-(1+\beta_s^{-1})^{-1/2}\right]}. \tag{3.57}$$

In the high-frequency limit, the dynamic variance coefficients tend to

$$\lim_{\Omega\to\infty}[\sigma_u^2]_1 = -\frac{4\sigma_s^2(1-i)}{\beta_s\Omega^{5/2}(1+1/\sqrt{2})}, \quad \lim_{\Omega\to\infty}[\sigma_{\dot{u}}^2]_1 = \frac{2\sigma_s^2(1-i)}{\beta_s\Omega^{1/2}},$$
$$\lim_{\Omega\to\infty}[\sigma_{u\dot{u}}]_1 = -\frac{2\sigma_s^2(1+i)}{\beta_s\Omega^{3/2}(1+1/\sqrt{2})}. \tag{3.58}$$

Again, we can see that the $[\sigma_{\dot{u}}^2]_1$ term in r_{12} (3.15) will dominate and thus Λ_∞ and ψ_∞ are given by

$$\Lambda_\infty = \lim_{\Omega\to\infty}\left|\frac{[\sigma_{\dot{u}}^2]_1}{2[\sigma_{\dot{u}}^2]_0}\right| = \frac{\sqrt{2(1+\beta_s^{-1})}}{\Omega^{1/2}}, \quad \psi_\infty = -\frac{\pi}{4}. \tag{3.59}$$

This shows a crucial difference from the point neuron in that the upcrossing-rate response decays as $\Omega^{-1/2}$ rather than Ω, and ψ_∞ is now $-\pi/4$ rather than $-\pi/2$, as shown in Figure 3.7(a, b). In comparison to synaptic mean modulation, the cutoff frequency is approximately twice as high, saturating for both the point neuron and infinite dendrite at ~ 60 Hz. The difference in the cutoff frequency with variance modulation between the point neuron and infinite dendrite is small however, Figure 3.7(c), with the cutoff frequency for the infinite dendrite being slightly higher at lower τ_s/τ_v and slightly lower at higher τ_s/τ_v.

While resonance is again theoretically possible, for the infinite dendrite an even lower relative threshold $u_{\rm th}/[\sigma_u]_0$ is required for upcrossing resonance than the point-neuron model, with $u_{\rm th}/[\sigma_u]_0 < 1.5$ required in Figure 3.7(d). This is because, while the profiles of $|r_{12}|$ and $|r_{13}|$ for the infinite dendrite are similar to the point neuron, the peak $|r_{11}|$ is lower for the infinite dendrite due to the smaller magnitude of $[\sigma_{u\dot{u}}]_1$.

Since the effects of synaptic mean and variance modulation sum linearly, we can deduce from the lack of firing rate resonance for either synaptic mean or variance modulation that modulation of the presynaptic firing rate will also not induce firing-rate resonance in the parameter region for which the upcrossing method provides a good approximation.

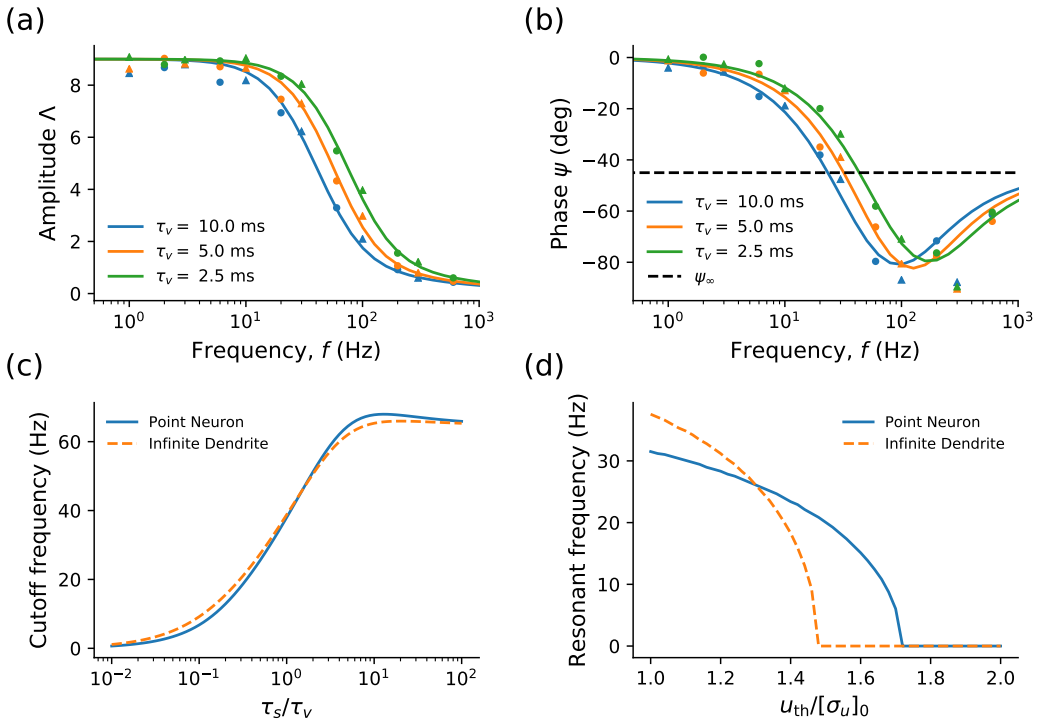

Figure 3.7: (a) The upcrossing-rate response amplitude of the infinite dendrite subject to variance modulation decreases to zero in the high-frequency limit, similar to the point neuron. (b) However, the high-frequency phase limit is $-\pi/4$ rather than the value of $-\pi/2$ found for the point neuron. (c) The cutoff frequency is similar between the point neuron and infinite dendrite, with the infinite dendrite having a higher cutoff for lower τ_s/τ_v and a lower cutoff for higher τ_s/τ_v. (d) An even lower value of $u_{\text{th}}/[\sigma_u]_0$ is required to observe resonance in the infinite dendrite when compared with the point neuron. In (a, b) solid lines show the theoretical upcrossing-rate response (3.15), while circles and triangles denote upcrossing and threshold-reset simulations respectively. Other parameters: (a-d) $\lambda = 100\mu$m, $\tau_s = 5$ms, (a-c) $u_{\text{th}}/[\sigma_u]_0 = 3$, (a,b,d) $\tau_v = 10$ ms.

3.4 Semi-Infinite Dendrite Modulation

When comparing the semi-infinite with the infinite dendrite, we fix the $[\sigma_u]_0$ and u_{th} so that both models have the same steady-state upcrossing rate. Thus we are testing how placing a sealed end at $x = 0$ affects only the dynamic properties of the firing rate. For all modulation types we place the trigger position at the sealed end, $x_{\text{th}} = 0$, as in section 2.4.3 for the steady-state firing rate.

3.4.1 Semi-Infinite Dendrite, Local Current Modulation

For a general output trigger position x_{th} and modulation input position x_c, we can substitute the semi-infinite Green's function, $\tilde{\mathcal{G}} = (e^{-|x-y|\gamma} + e^{-|x+y|\gamma})/(2\gamma)$, into (3.43) to yield the mean coefficient for local current modulation as

$$\langle u(x_{\text{th}}, x_c)\rangle_1 = \frac{1}{2\Gamma}(e^{-|x_{\text{th}}-x_c|\Gamma} + e^{-|x_{\text{th}}+x_c|\Gamma}), \tag{3.60}$$

where we see that reflection at the sealed end at $x = 0$ gives an additional $e^{-|x_{\text{th}}+x_c|}$ in comparison with the infinite dendrite. Fixing the trigger position at the nominal soma $x_{\text{th}} = 0$ yields r_1/r_0 that is simply double the infinite case (3.44)

$$\frac{r_{1c}}{r_0} = \frac{e^{-|x_c|\Gamma}}{\Gamma}\left(\frac{u_{\text{th}}}{\sigma_u^2} + \frac{i\Omega}{\sigma_{\dot{u}}}\sqrt{\frac{\pi}{2}}\right). \tag{3.61}$$

Furthermore, fixing σ_u across the two models means that $\sigma_{\dot{u}}$ will also be the same (section 2.4.2), hence for all frequencies and parameters with $x_{\text{th}} = 0$ we will have

$$\Lambda_{\text{semi}} = 2\Lambda_{\text{inf}}, \quad \psi_{\text{semi}} = \psi_{\text{inf}}. \tag{3.62}$$

This means that the only change to the response is a doubling of the amplitude of oscillations. For n semi-infinite dendrites radiating from $x = 0$ (where the semi-infinite and infinite cases are equivalent to $n = 1$ and $n = 2$ respectively) receiving current modulation at a single dendrite at x_c, the dynamic upcrossing-rate response can be generalised to

$$\frac{r_{1c}}{r_0} = \frac{e^{-|x_c|\Gamma}}{n\Gamma}\left(\frac{u_{\text{th}}}{\sigma_u^2} + \frac{i\Omega}{\sigma_{\dot{u}}}\sqrt{\frac{\pi}{2}}\right). \tag{3.63}$$

Therefore the addition of more dendrites has a divisive effect on the relative magnitude of upcrossing-rate oscillations.

3.4.2 Semi-Infinite Dendrite, Synaptic Mean Modulation

For spatially uniform synaptic mean modulation, the dynamic mean coefficient $\langle u\rangle_1$ will have the same form for the semi-infinite dendrite as the point neuron and the infinite dendrite (3.23). Since we are scaling σ_s to keep σ_u constant, this therefore means that we should expect exactly the same dynamic upcrossing-rate response for the semi-infinite dendrite as the infinite dendrite. This is shown in Figure 3.8(a-b).

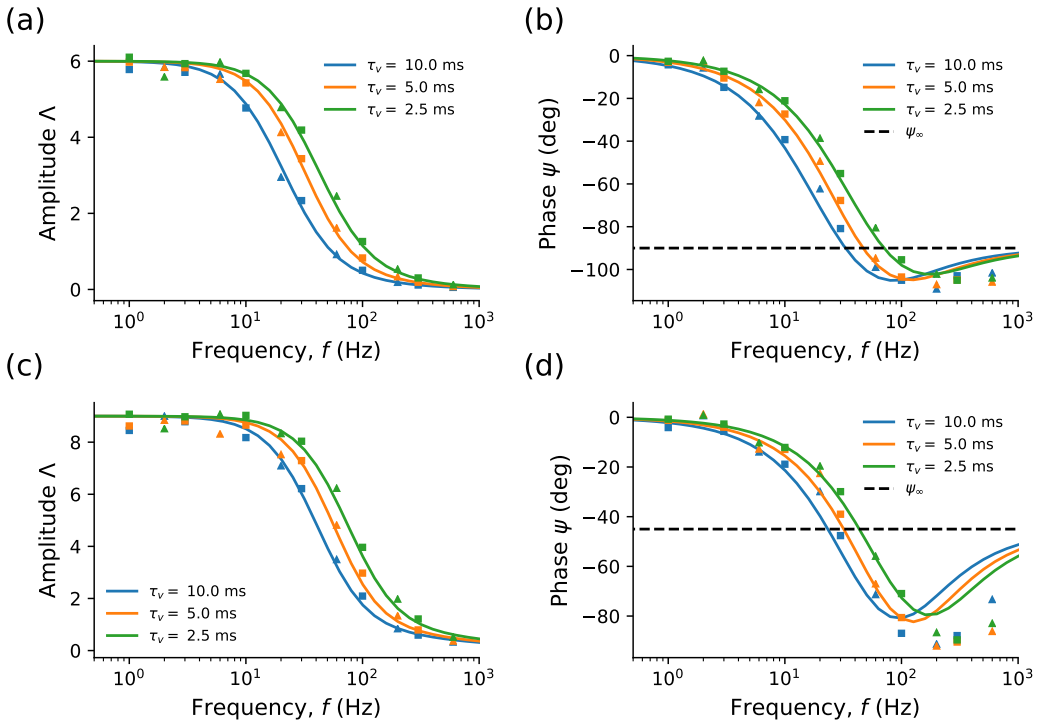

Figure 3.8: For a semi-infinite dendrite with mean (a-b) and variance (c-d) modulation, the response is exactly the same as an infinite dendrite for fixed u_{th} and $[\sigma_u]_0$. Solid lines show the theoretical upcrossing-rate response from (3.24) and (3.15) for synaptic mean and variance modulation respectively. Threshold-reset simulations of the semi-infinite and infinite dendrites are shown as triangles and squares respectively. Other parameters: (a-d) $\lambda = 100\mu$m, $\tau_s = 5$ms, $u_{\text{th}}/[\sigma_u]_0 = 3$

3.4.3 Semi-Infinite Dendrite, Variance Modulation

We can calculate the dynamic variance coefficients by using the correlator of $\langle\hat{\xi}(k,\omega)\hat{\xi}(-k',-\omega')\rangle$ for the semi-infinite dendrite. This means that for general x we have

$$[\sigma_u^2(x)]_1 = \frac{2\sigma_s^2\beta_s}{\pi^2}\int_{-\infty}^{\infty}\mathrm{d}\omega\int_{-\infty}^{\infty}\frac{(1+e^{2ikx})}{D_\infty(k,\omega,\Omega)}\mathrm{d}k, \tag{3.64}$$

where D_∞ has the same form as for the infinite dendrite (3.53). Since we wish to calculate the upcrossing rate at $x = 0$, (3.64) shows that the $[\sigma_u^2(0)]_1$ will be exactly double $[\sigma_u^2]_1$ for the infinite dendrite. Furthermore, this will also be true for the other dynamic variances $[\sigma_{\dot{u}}^2]_1$ and $[\sigma_{u\dot{u}}]_1$. Noting that this is the same scaling factor as the steady-state variances, it therefore follows that if σ_s is scaled to keep $[\sigma_u]_0$ constant between the two models, then $[\sigma_u]_1$ will also have the same value.

Thus, the dynamic upcrossing-rate response for variance modulation is the

same for the semi-infinite dendrite, Figure 3.8(c-d). We note that, just as in the steady-state firing rate, we can generalise this argument to show that the dynamic upcrossing-rate response at $x = 0$ will be the same for a neuron model with n identical semi-infinite dendrites with modulation distributed across all the dendrites provided that u_{th} and $[\sigma_u]_0$ are constant with n.

3.5 Ball-and-Stick Model Modulation

For the ball-and-stick neuron, synaptic drive is present on the dendrite only and we denote somatic quantities with subscript σ as in section 2.7. As with the steady-state, we must use the Green's function in frequency $\tilde{\mathcal{G}}(x, y; \omega)$ (2.93). Since by definition the steady-state mean $\langle v \rangle_0$ is given from

$$\langle v \rangle_0 = \mu + \frac{\mathrm{d}^2 \langle v \rangle_0}{\mathrm{d}x^2}, \quad \langle v_\sigma \rangle_0 = \rho \left. \frac{\mathrm{d}\langle v \rangle_0}{\mathrm{d}x} \right|_{x=0}, \tag{3.65}$$

the cable equation and somatic boundary condition in terms of the combined fluctuating and oscillating voltage u is

$$\frac{\partial u}{\partial t} = -u + \frac{\partial^2 u}{\partial x^2} + s, \quad \beta_\sigma \frac{\mathrm{d}u_\sigma}{\mathrm{d}t} = -u_\sigma + \rho \left. \frac{\partial u}{\partial x} \right|_{x=0}. \tag{3.66}$$

3.5.1 Ball-and-Stick Model, Local Current Modulation

First we look at current modulation applied to the soma for a semi-infinite dendrite. For easiest comparison to other points of application and other models, this is formulated as an oscillatory current applied at $x = 0$ on the dendrite

$$\frac{\partial u}{\partial t} = -u + \frac{\partial^2 u}{\partial x^2} + s + \epsilon_c \delta(x) e^{i\Omega t}. \tag{3.67}$$

As in Chapter 2, we will usually consider the time constant ratio $\beta_\sigma = 7/6$, arising from the increase in effective transmembrane conductance in the dendrite from the background synaptic drive. As this parameter could change the dynamic response, we will look at variations around this point. Such variations could be caused by differences in the leak conductance per unit area between the soma and axon for example. However, the relative difference between the mean and threshold $u_{\text{th}}/[\sigma_u]_0$ remains unchanged.

Using (3.43) we find the oscillatory mean coefficient at the soma is given by

$$\langle u \rangle_1 = \frac{\rho}{\rho\Gamma_1 + \Gamma_\sigma^2}, \quad \langle \dot{u} \rangle_1 = \frac{i\Omega\rho}{\rho\Gamma_1 + \Gamma_\sigma^2}, \tag{3.68}$$

which differs from previous cases of current modulation in the infinite dendrite as the high frequency limit for $\langle \dot{u} \rangle_1$ no longer increases without bound but instead has a finite limit. This is because at high frequencies the somatic term Γ_σ^2 dominates with $\lim_{\Omega\to\infty} \langle \dot{u} \rangle_1 = \rho/\beta_\sigma$. Hence, we have that

$$\frac{r_{1c}}{r_0} = \frac{\rho}{\rho\Gamma_1 + \Gamma_\sigma^2} \left(\frac{u_{\text{th}}}{\sigma_u^2} + \frac{i\Omega}{\sigma_{\dot{u}}} \sqrt{\frac{\pi}{2}} \right), \tag{3.69}$$

from which one can extract the low- and high-frequency limits

$$\Lambda_0 = \frac{\rho}{\rho + 1} \frac{u_{\text{th}}}{\sigma_u^2}, \quad \Lambda_\infty = \frac{\rho}{\beta_\sigma \sigma_{\dot{u}}} \sqrt{\frac{\pi}{2}}, \quad \psi_\infty = 0. \tag{3.70}$$

As one would expect, as $\rho \to \infty$, Λ_0 and Λ_∞ converge to the limits found for the semi-infinite dendrite with $x_c = 0$ (3.45, 3.46, 3.62). In comparison with current modulation in the semi-infinite dendrite at $x_c = 0$, Λ_∞ no longer increases without bound with Ω but has a finite limit due to the additional filtering of the soma. The low-frequency limit can be adjusted via changing ρ even when u_{th} and σ_u are fixed, as shown in Figure 3.9(a), where decreasing ρ decreases Λ at all frequencies.

Like modulation at the proximal end of a semi-infinite dendrite ($x_c = 0$), current modulation at the soma gives a single phase zero at non-zero frequency, as shown in Figure 3.9(b). Furthermore, we find that for smaller ρ (a larger soma) and larger β_σ (a more conductive dendrite) the frequency of the phase zero increases, Figure 3.9(c). This shows that the relative size and conductance per unit area of the soma to the dendrite can tune the frequency of synchronisation, which has been examined for two-compartmental models previously [11]. In addition, while for sufficiently low ρ the phase zero theoretically will disappear, this requires extremely low values of ρ (~ 0.01) and is hence not observed in the parameter range shown.

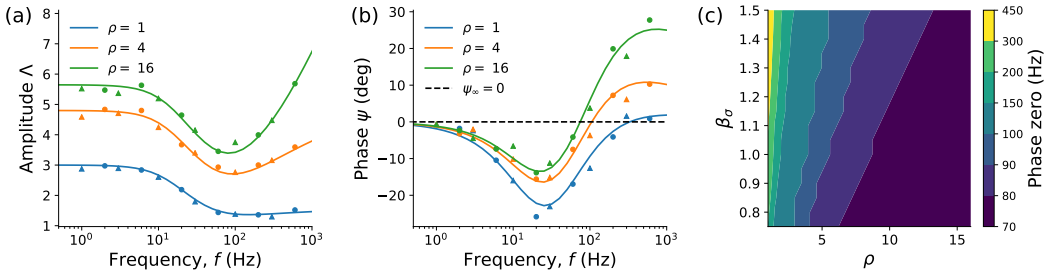

Figure 3.9: (a) With current modulation applied to the soma of a ball-and-stick neuron, decreasing ρ depresses both the dynamic amplitude Λ in the low- and high-frequency limits. (b) The phase zero also increases as ρ is decreased. (c) Decreasing ρ and increasing β_σ increases the frequency of the phase zero. In (a-b) solid lines show the theoretical upcrossing-rate response (3.69) while circles and triangles denote upcrossing and threshold-reset simulations respectively. Other parameters: (a-c) $\beta_s = 0.5$, $u_{\text{th}}/\sigma_u = 3$ (a-b) $\beta_\sigma = 7/6$.

3.5.2 Ball-and-Stick Model, Synaptic Mean Modulation

For synaptic mean modulation, the oscillating first-moment coefficients at the soma are

$$\langle u \rangle_1 = \frac{1}{1 + i\Omega\beta_s} \int_0^\infty \frac{e^{-y\Gamma_1}}{2\Gamma_1} \left(1 + \frac{\rho\Gamma_1 - \Gamma_\sigma^2}{\rho\Gamma_1 + \Gamma_\sigma^2}\right) \mathrm{d}y$$

$$\langle u \rangle_1 = \frac{\rho}{\Gamma_1(1 + i\Omega\beta_s)(\rho\Gamma_1 + \Gamma_\sigma^2)}, \tag{3.71}$$

$$\langle \dot{u} \rangle_1 = \frac{i\Omega\rho}{\Gamma_1(1 + i\Omega\beta_s)(\rho\Gamma_1 + \Gamma_\sigma^2)}, \tag{3.72}$$

which shows that $\langle \dot{u} \rangle_1$ decays to zero as $\Omega \to \infty$ more rapidly than previous models due to the somatic filtering term Γ_σ^2 dominating at high frequencies. Substituting these terms into the upcrossing-rate response (3.10), we find

$$\frac{r_{1m}}{r_0} = \frac{\rho}{\Gamma_1(1 + i\Omega\beta_s)(\rho\Gamma_1 + \Gamma_\sigma^2)} \left(\frac{u_{\text{th}}}{\sigma_u^2} + \frac{i\Omega}{\sigma_{\dot{u}}} \sqrt{\frac{\pi}{2}}\right), \tag{3.73}$$

for which the low- and high-frequency limits are

$$\Lambda_0 = \frac{\rho}{\rho + 1} \frac{u_{\text{th}}}{\sigma_u^2}, \quad \Lambda_\infty = \frac{\rho}{\Omega^{3/2}\beta_s\beta_\sigma\sigma_{\dot{u}}} \sqrt{\frac{\pi}{2}}, \quad \psi_\infty = -3\pi/4. \tag{3.74}$$

Note that for fixed u_{th}/σ_u^2, Λ_0 will decrease for increasing ρ. This is in marked contrast to synaptic mean modulation in previous models where the low-frequency limit remains unchanged with all parameters if u_{th}/σ_u^2 is kept constant. Figure 3.10(a)

shows the the reduction in Λ_0 with decreasing ρ, along with a slight decrease in the cutoff frequency (provided $\beta_\sigma \geq 1$) as we show later in Figure 3.11(c). Furthermore, we see that the high-frequency phase limit is now $-3\pi/4$, which differs from the semi-infinite dendrite limit of $\pi/2$. This implies that the ball-and-stick neuron population will attenuate very high-frequency modulations of the mean more strongly than previously examined models.

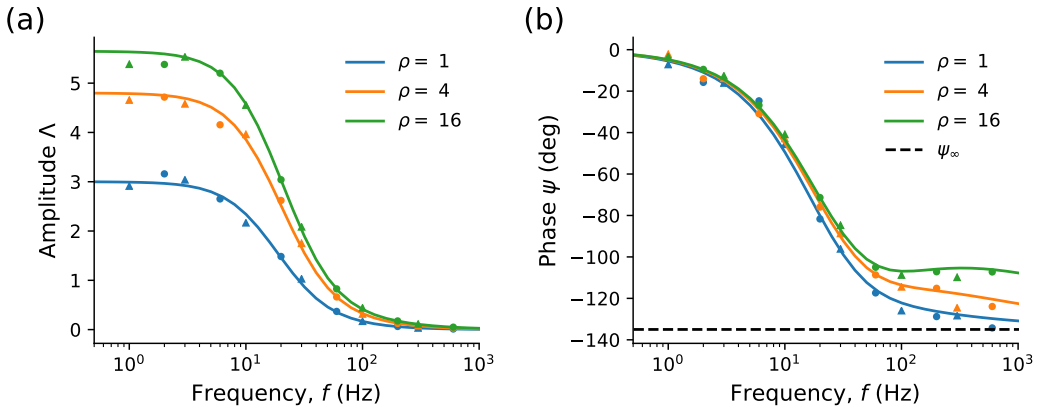

Figure 3.10: (a) Decreasing ρ decreases both the low-frequency limit and the cutoff frequency for synaptic mean modulation applied to the ball-and-stick neuron. (b) The ball-and-stick neuron shows a high-frequency phase limit of $\psi_\infty = -3\pi/4$ which is reached more quickly for lower ρ. Solid lines show the theoretical upcrossing rate (3.73) while circles and triangles are given by upcrossing and threshold-reset simulations respectively. Other parameters: $u_{\text{th}}/\sigma_u = 3$, $\lambda = 200\mu$m, $\tau_v = 10$ms, $\tau_s = 5$ms, $\beta_\sigma = 7/6$.

3.5.3 Ball-and-Stick Model, Variance Modulation

Since the somatic boundary condition makes it very difficult to interpret spatial Fourier transforms, we instead use the Green's function $\tilde{\mathcal{G}}(x, y; \omega)$ to understand variance modulation in the ball-and-stick model. In doing so, we develop a general approach that can be applied to any morphology. Using the convolution between the complex exponential and the Gaussian noise process used in section 3.2.3, the Fourier transform of the synaptic drive $\tilde{s}$ is

$$\tilde{s}(y;\omega) = \frac{2\sigma_s\sqrt{\beta_s}[\tilde{\xi}_s(y;\omega) + \epsilon_v\tilde{\xi}_s(y;\omega-\Omega)]}{1+i\omega\beta_s}. \tag{3.75}$$

Therefore the fluctuating component of the voltage response is given in terms of the Green's function integrals

$$u(x,t) = \frac{\sigma_s\sqrt{\beta_s}}{\pi}\int_{-\infty}^{\infty} e^{i\omega t}\mathrm{d}\omega \int_{\mathcal{R}} \frac{\tilde{\mathcal{G}}(x,y;\omega)}{1+i\omega\beta_s}[\tilde{\xi}_s(y;\omega)+\epsilon_v\tilde{\xi}_s(y;\omega-\Omega)]\mathrm{d}y. \tag{3.76}$$

Squaring and taking the expectation gives a steady-state term and fluctuating terms as outlined earlier (3.11)

$$\langle u(x,t)^2\rangle = [\sigma_u^2]_0 + [\sigma_u^2]_1\epsilon_v e^{i\Omega t} + O(\epsilon_v^2), \tag{3.77}$$

where the first-order term is given by

$$\begin{aligned}[\sigma_u^2]_1\epsilon_v e^{i\Omega t} = \epsilon_v\frac{\sigma_s^2\beta_s}{\pi^2}\int_{-\infty}^{\infty} e^{i\omega t}\mathrm{d}\omega\int_{\mathcal{R}}\frac{\tilde{\mathcal{G}}(x,y;\omega)}{1+i\omega\beta_s}\mathrm{d}y\int_{-\infty}^{\infty}e^{-i\omega' t}\mathrm{d}\omega'\times\\ \int_{\mathcal{R}}\frac{\tilde{\mathcal{G}}(x,y';-\omega')}{1-i\omega'\beta_s}[\langle\tilde{\xi}_s(y;\omega)\tilde{\xi}_s(y';-\omega'-\Omega)\rangle+\langle\tilde{\xi}_s(y';-\omega')\tilde{\xi}_s(y,\omega-\Omega)\rangle]\mathrm{d}y'.\end{aligned} \tag{3.78}$$

Similar to the point-neuron model, the white-noise correlators in space and time are

$$\begin{aligned}\langle\tilde{\xi}_s(y;\omega)\tilde{\xi}_s(y';-\omega'-\Omega)\rangle &= 2\pi\delta(y-y')\delta(\omega-\omega'-\Omega)\\ \langle\tilde{\xi}_s(y';-\omega')\tilde{\xi}_s(y;\omega-\Omega)\rangle &= 2\pi\delta(y-y')\delta(\omega-\omega'-\Omega),\end{aligned} \tag{3.79}$$

meaning we evaluate ω' at $\omega-\Omega$ and obtain the general expression

$$[\sigma_u^2]_1 = \frac{4\sigma_s^2\beta_s}{\pi}\int_{-\infty}^{\infty}\mathrm{d}\omega\int_{\mathcal{R}}\frac{\tilde{\mathcal{G}}(x,y;\omega)\tilde{\mathcal{G}}(x,y;\Omega-\omega)}{1+\omega(\omega-\Omega)\beta_s^2+i\Omega\beta_s}\mathrm{d}y. \tag{3.80}$$

For $\sigma_{\dot{u}}^2$ we multiply by $i\omega$ and $-i\omega'$

$$\begin{aligned}[\sigma_{\dot{u}}^2]_1 e^{i\Omega t} = \frac{\sigma_s^2\beta_s}{\pi^2}\int_{-\infty}^{\infty} i\omega e^{i\omega t}\mathrm{d}\omega\int_{\mathcal{R}}\frac{\tilde{\mathcal{G}}(x,y;\omega)}{1+i\omega\beta_s}\mathrm{d}y\int_{-\infty}^{\infty}-i\omega' e^{-i\omega' t}\mathrm{d}\omega'\times\\ \int_{\mathcal{R}}\frac{\tilde{\mathcal{G}}(x,y';-\omega')}{1-i\omega'\beta_s}[\langle\tilde{\xi}_s(y;\omega)\tilde{\xi}_s(y';-\omega'-\Omega)\rangle+\langle\tilde{\xi}_s(y';-\omega')\tilde{\xi}_s(y,\omega-\Omega)\rangle]\mathrm{d}y',\end{aligned} \tag{3.81}$$

which when we evaluate ω' at $\omega-\Omega$ gives

$$[\sigma_{\dot{u}}^2]_1 = \frac{4\sigma_s^2\beta_s}{\pi}\int_{-\infty}^{\infty}\omega(\omega-\Omega)\mathrm{d}\omega\int_{\mathcal{R}}\frac{\tilde{\mathcal{G}}(x,y;\omega)\tilde{\mathcal{G}}(x,y;\Omega-\omega)}{1+\omega(\omega-\Omega)\beta_s^2+i\Omega\beta_s}\mathrm{d}y. \tag{3.82}$$

Finally for the covariance $\sigma_{u\dot{u}}$ we can have $\dot{u}$ either in terms of (y,ω) or $(y',-\omega')$. Putting $\dot{u}$ in terms of (y,ω) and u in terms of $(y',-\omega')$ yields

$$[\sigma_{u\dot{u}}]_1 = \frac{4\sigma_s^2\beta_s}{\pi}\int_{-\infty}^{\infty} i\omega \mathrm{d}\omega \int_{\mathcal{R}} \frac{\tilde{\mathcal{G}}(x,y;\omega)\tilde{\mathcal{G}}(x,y;\Omega-\omega)}{1+\omega(\omega-\Omega)\beta_s^2+i\Omega\beta_s}\mathrm{d}y, \tag{3.83}$$

from which we can see that the change of variables $\omega \to \Omega - \omega$ yields the integral expression had we instead chosen to put $\dot{u}$ in terms of $(y',-\omega')$ and u in terms of (y,ω), showing the two ways are equivalent. We also note that all three oscillatory variances have the same y integral and differ only in the numerator for the ω-integral. Furthermore, for σ_u^2, swapping the order of integration reveals that the ω-integral is a convolution of $\tilde{\mathcal{G}}(x,y;\omega)/(1+i\omega\beta_s)$ with itself in terms of ω.

For $\beta_\sigma \geq 1$, increasing ρ initially increases the cutoff frequency for the dynamic firing-rate response, as shown in Figure 3.11(a, d). This is due to the stronger somatic filtering with a larger soma. For larger ρ, the cutoff frequency gradually decreases towards the frequency found for the infinite dendrite. We also note that the high-frequency limit when the soma is added is $\psi_\infty = -3\pi/4$, though convergence to this phase is slow and only seen at very high frequencies. This can be seen by evaluating the integrand of (3.82) for large ω and Ω with $x = 0$

$$\begin{aligned} J &= \frac{\rho^2\omega(\omega-\Omega)}{\overline{z}_1(\rho\gamma_1+\gamma_\sigma^2)(\rho\overline{\Gamma}_1+\overline{\Gamma}_\sigma^2)[1+\omega(\omega-\Omega)\beta_s^2+i\Omega\beta_s]}, \\ \overline{\Gamma}_1 &= \sqrt{1+i(\Omega-\omega)}, \quad \overline{\Gamma}_\sigma = \sqrt{1+i(\Omega-\omega)\beta_\sigma}, \quad \overline{z}_1 = \overline{\Gamma}_1+\overline{\Gamma}_\sigma, \\ J &\sim \frac{\rho^2}{i\Omega\beta_\sigma^2\beta_s\sqrt{i\Omega}}. \end{aligned} \tag{3.84}$$

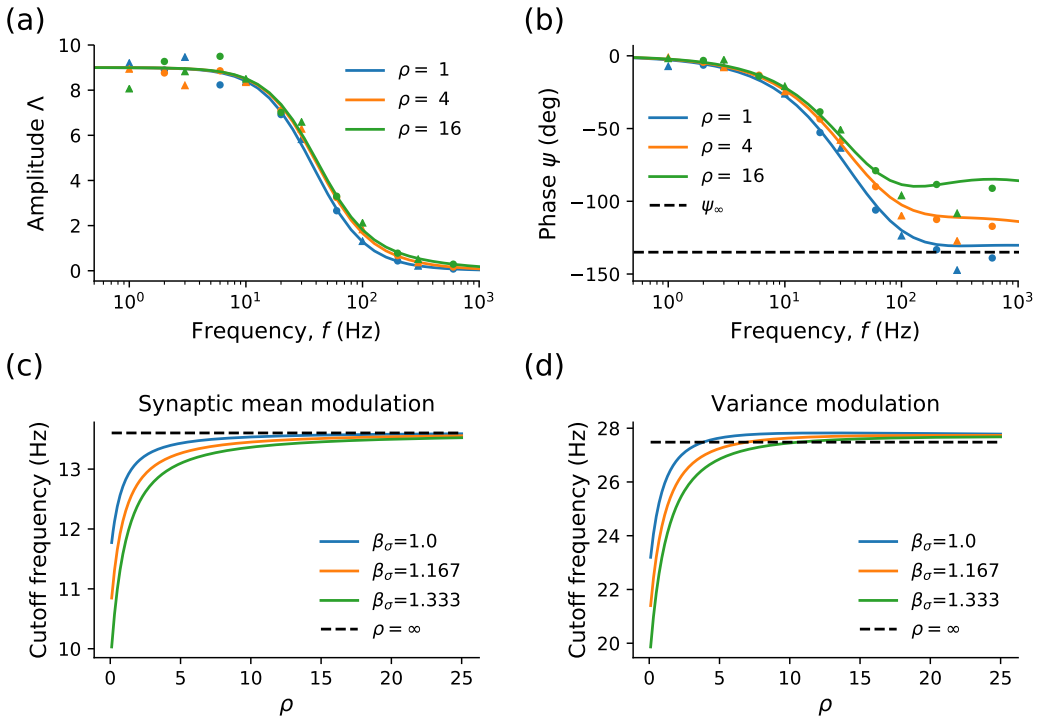

Figure 3.11: For variance modulation applied to the ball-and-stick neuron, a larger soma (smaller ρ) results in a lower cutoff frequency. (c) The cutoff frequency for synaptic mean modulation decreases with β_σ and converges towards the infinite dendrite value as ρ increases. (d) An almost identical trend is observed for variance modulation, except that the cutoff frequencies are approximately double that of synaptic mean modulation. Solid lines indicate the theoretical dynamic upcrossing-rate response from (3.73) for synaptic mean modulation and (3.15) for variance modulation, while circles and triangles denote upcrossing and threshold-reset simulations respectively. Other parameters: (a-d) $u_{\text{th}}/[\sigma_u]_0 = 3$, $\lambda = 200\mu$m, $\beta_s = 0.5$, (a-b) $\beta_\sigma = 7/6$.

3.6 Dendrite-and-Axon Model Modulation

Here we will explore the effect of modulated drive when a passive axon is included. In particular, we will vary the trigger position to see the spatial filtering effect of the axon on modulated signals. For simplicity, we will suppose the dendrite and axon are semi-infinite. Using the results from the steady state in section 2.6, it is straightforward to infer the effect of n identical dendrites on modulation from the single-dendrite case. Similarly, we will use a nominal soma in this analysis, but one can infer the effects of an electrically substantial soma from the previous section and the steady-state section 2.7.

3.6.1 Dendrite-and-Axon, Local Current Modulation

When current modulation is applied at the nominal soma, the oscillatory mean component is given by substitution of the Green's function $\tilde{\mathcal{G}}_{\alpha 1}$ (2.64) into (3.43)

$$\langle u \rangle_1 = \frac{\beta_\alpha^2 \lambda_1^3 e^{-x_{\text{th}}\Gamma_\alpha}}{\beta_\alpha^2 \lambda_1^3 \Gamma_1 + \lambda_\alpha^3 \Gamma_\alpha}, \tag{3.85}$$

hence giving the upcrossing-rate response as

$$\frac{r_{1c}}{r_0} = \frac{\beta_\alpha^2 \lambda_1^3 e^{-x_{\text{th}}\Gamma_\alpha}}{\beta_\alpha^2 \lambda_1^3 \Gamma_1 + \lambda_\alpha^3 \Gamma_\alpha} \left(\frac{u_{\text{th}}}{\sigma_u^2} + \frac{i\Omega}{\sigma_{\dot{u}}} \sqrt{\frac{\pi}{2}} \right). \tag{3.86}$$

Like other spatial cases, for $x_{\text{th}} = 0$ the upcrossing-rate response increases without bound for increasing Ω. However, similar to what was seen for local current modulation in the infinite cable, when $x_{\text{th}} > 0$, the high-frequency limit of Λ becomes zero, with faster decay for larger x_{th} (3.47).

For fixed steady-state mean and variance, when $X_{\text{th}} > 0$ decreasing λ_α by making the axon thinner leads to a reduction in the phase zero frequencies, eventually eliminating them, as shown in Figure 3.12(b). When $X_{\text{th}} = 0$ however, this effect is negligible. Since changing λ_α both changes the relative ratio of the length constants and the dimensionless trigger position $x_{\text{th}} = X_{\text{th}}/\lambda_\alpha$, we looked at how the first and second phase zeros depend on the axon to dendrite length constant ratio λ_α/λ_1 (representative of the relative axonal size, with higher λ_α/λ_1 indicating a wider axon) and the dimensionless trigger position x_{th}. Figure 3.12(c, d) shows that there is very little dependence of either phase zero on λ_α/λ_1 and thus most of the change we see from varying λ_α comes from changing x_{th}. Additionally, in comparison with the literature, increasing the relative dendritic size here (measured by λ_1/λ_α) does not significantly affect the cutoff or half-amplitude frequencies, unlike simulations in [126].

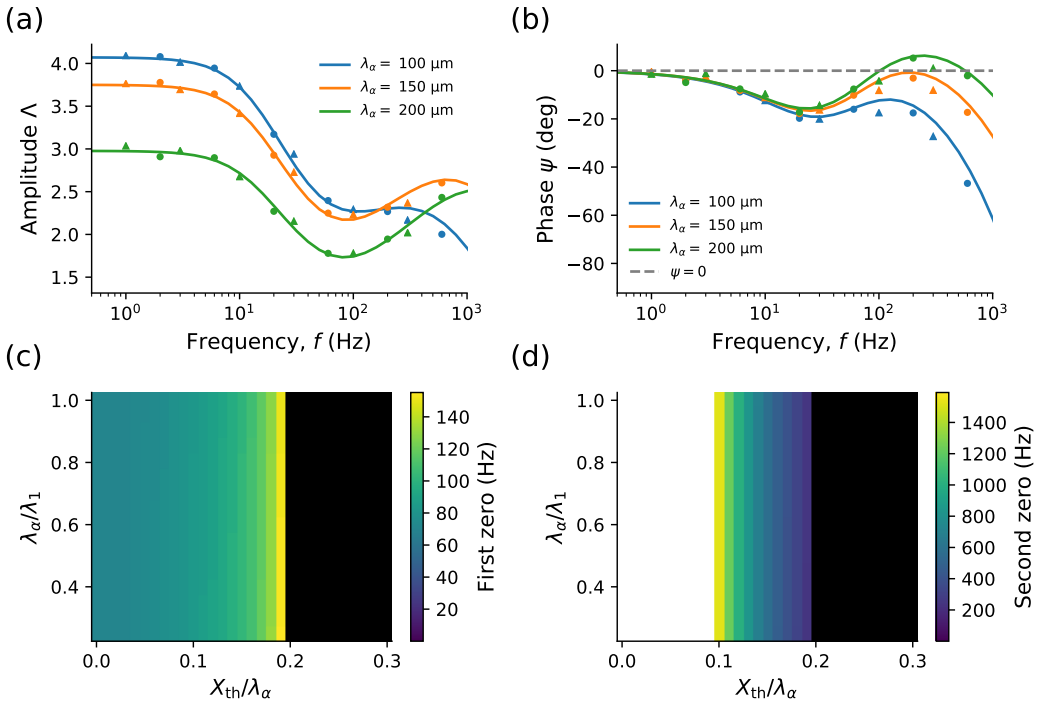

Figure 3.12: (a) For local current modulation applied to the dendrite-and-axon model at $x = 0$, we see sag in Λ at intermediate frequencies. (b) Increasing λ_α reduces both the height and frequency of the phase peak. (c) The first phase zero increases with $X_{\text{th}}/\lambda_\alpha$ until it vanishes but is virtually unaffected by relative axonal size λ_α/λ_1. (d) The second phase zero is similarly unaffected by λ_α/λ_1 and decreases with $X_{\text{th}}/\lambda_\alpha$ until it vanishes, annihilating the first phase zero in the process. Solid lines denote the theoretical upcrossing rate response (3.86) while circles and triangles represent upcrossing and threshold-reset simulations respectively. In (c, d), black regions indicate the absence of phase zeros, while white regions denote phase zeros in excess of 1600 Hz. Other parameters: $\lambda_1 = 200\mu$m $\beta_\alpha = 7/6$, $\tau_v = 10$ms $\tau_s = 5$ms, $X_{\text{th}} = 30\mu$m, $u_{\text{th}}/\sigma_u = 3$.

3.6.2 Dendrite-and-Axon, Synaptic Mean Modulation

Using the Green's function for the axonal response derived in the steady-state chapter $\tilde{\mathcal{G}}_{\alpha 1}$ (2.64), we can obtain the oscillatory component of the mean at the trigger position x_{th} as

$$\langle u \rangle_1 = \frac{\beta_\alpha^2 \lambda_1^3 e^{-x_{\text{th}}\Gamma_\alpha}}{\Gamma_1(1 + i\Omega\beta_s)(\beta_\alpha^2\lambda_1^3\Gamma_1 + \lambda_\alpha^3\Gamma_\alpha)}. \tag{3.87}$$

Substitution into the dynamic upcrossing-rate response (3.10) for synaptic mean modulation thus yields

$$\frac{r_{1m}}{r_0} = \frac{\beta_\alpha^2 \lambda_1^3 e^{-x_{\text{th}}\Gamma_\alpha}}{\Gamma_1(1+i\Omega\beta_s)(\beta_\alpha^2\lambda_1^3\Gamma_1 + \lambda_\alpha^3\Gamma_\alpha)} \left[\frac{u_{\text{th}}}{\sigma_u^2} + \frac{i\Omega}{\sigma_{\dot{u}}}\sqrt{\frac{\pi}{2}}\right]. \tag{3.88}$$

For the low-frequency limit this gives an amplitude dependent on the axonal length constant, time constant and trigger position

$$\Lambda_0 = \frac{\beta_\alpha^2 \lambda_1^3 e^{-x_{\text{th}}}}{\beta_\alpha^2\lambda_1^3 + \lambda_\alpha^3} \frac{u_{\text{th}}}{\sigma_u^2}, \tag{3.89}$$

which will tend to Λ_0 for synaptic mean modulation in the point neuron and infinite dendrite (3.25) when $x_{\text{th}} = 0$ and $\lambda_\alpha = 0$. For the high-frequency limit at $x_{\text{th}} = 0$, Λ will tend to zero with $\psi_\infty = -\pi/2$ as in the infinite dendrite case (3.25). However when $x_{\text{th}} > 0$, the exponential numerator will eventually dominate as frequency increases, causing Λ to decrease more rapidly towards zero and the phase to decrease without bound, $\psi_\infty \to -\infty$.

When we vary λ_α, Figure 3.13(a) shows that, while the response is still that of a low-pass filter, Λ_0 is maximised for intermediate length constant. This is because X_{th} has been fixed, hence increasing λ_α decreases the dimensionless distance in the exponential of (3.89) for Λ_0. On the other hand, increasing λ_α increases the magnitude of the denominator in (3.89). Thus for smaller λ_α, Λ initially increases with λ_α as the exponential effect is larger while as $x_{\text{th}} \to 0$ from larger λ_α, Λ will decrease due to the larger denominator. Variations in Λ are however relatively small, demonstrating a dynamic robustness of the upcrossing rate response to axonal size. Figure 3.13(b) shows that increasing λ_α increases the phase at high frequencies due to the smaller exponent.

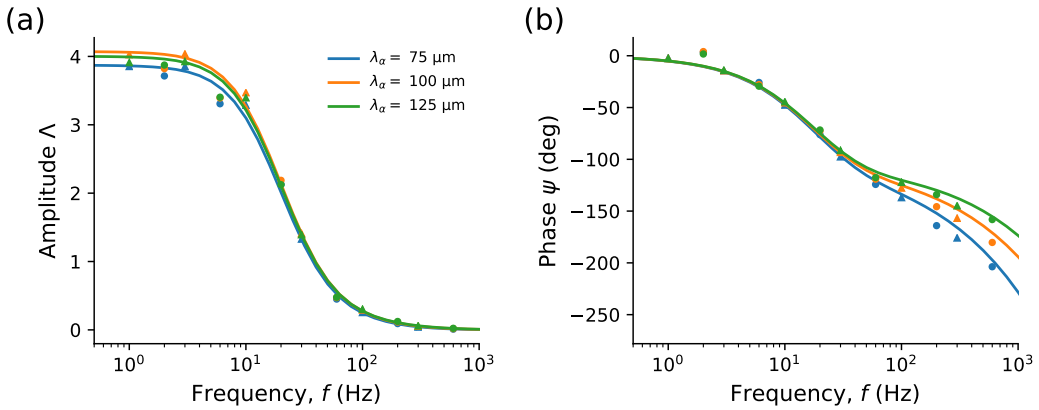

Figure 3.13: (a) For synaptic mean modulation applied to the dendrite-and-axon model, the dynamic firing-rate response in the axon varies non-monotonically at low frequencies with λ_α. (b) The phase of the dynamic response is almost identical with λ_α at lower frequencies and is lower for lower λ_α at higher frequencies. Solid lines show the theoretical upcrossing-rate response (3.88) while circles and triangles denote upcrossing and threshold-reset simulations respectively. Other parameters: $\tau_1 = 10\text{ms}$, $\tau_s = 5\text{ms}$, $\lambda_1 = 200\mu\text{m}$, $\beta_\alpha = 7/6$, $u_{\text{th}}/\sigma_u = 3$, $X_{\text{th}} = 30\mu\text{m}$

3.6.3 Dendrite-and-Axon, Variance Modulation

With a dendrite and an axon, we can obtain the dynamic variances by replacing $\tilde{\mathcal{G}}(x, y; \omega)$ with $\tilde{\mathcal{G}}_{\alpha 1}(x_\alpha, y_1; \omega)$ in equations (3.80,3.82,3.83). For example, the oscillating component of the voltage variance is given by

$$[\sigma_u^2]_1 = \frac{4\sigma_s^2\beta_s}{\pi}\int_{-\infty}^{\infty} \mathrm{d}\omega \int_0^{\infty} \frac{\tilde{\mathcal{G}}_{\alpha 1}(x_\alpha, y_1; \omega)\tilde{\mathcal{G}}_{\alpha 1}(x_\alpha, y_1; \Omega - \omega)}{1 + \omega(\omega - \Omega)\beta_s^2 + i\Omega\beta_s}\mathrm{d}y_1. \tag{3.90}$$

Using this approach, we found all the variances necessary to calculate the variance-modulated upcrossing rate. Due to the spatial separation between the dendritic drive and the trigger position for $x_{\text{th}} > 0$, the high-frequency phase limit is also undetermined ($\psi_\infty \to -\infty$) for variance modulation as we found for synaptic mean modulation in section 3.6.2. For fixed steady-state mean and variance, varying λ_α had negligible effect on the dynamic response. Increasing X_{th} also had little effect but reduced the cutoff frequency slightly as shown in Figure 3.14.

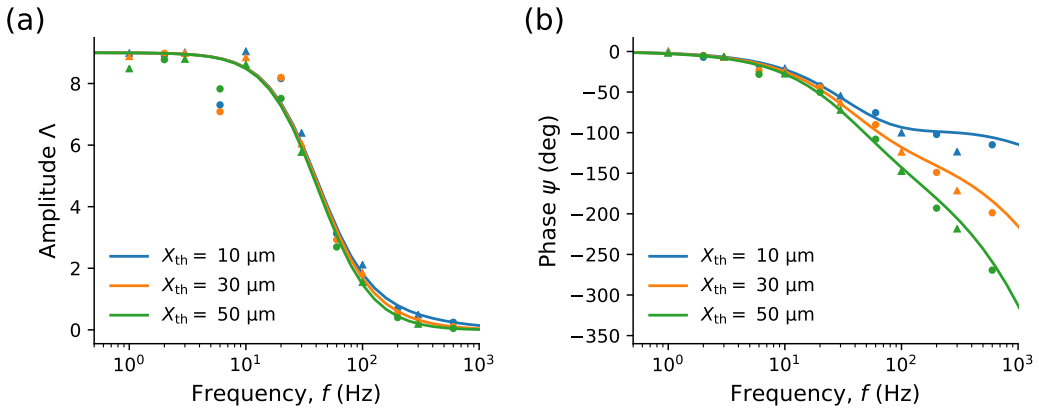

Figure 3.14: (a) For variance modulation applied to the dendrite-and-axon model, the amplitude is largely unchanged by increasing X_{th} and the cutoff frequency is slightly increased. (b) Increasing X_{th} causes the phase to decay more quickly as the modulation frequency increases. Solid lines indicate the theoretical upcrossing-rate response (3.15) while circles and triangles denote upcrossing and threshold-reset simulations respectively. Other parameters: $\tau_1 = 10\text{ms}$, $\tau_s = 5\text{ms}$, $\lambda_1 = 200\mu\text{m}$, $\lambda_\alpha = 100\mu\text{m}$, $\beta_\alpha = 7/6$, $u_{\text{th}}/\sigma_u = 3$.

Given the relatively minor effects from the axon on the amplitude and phase at low to moderate frequencies for synaptic mean and variance modulation, and our prior analysis of the semi-infinite dendrite in sections 3.4.2 and 3.4.3, we will not list the results of multiple dendrites in this chapter. Furthermore, the divisive effect on the amplitude for current modulation that multiple dendrites without an axon has also been discussed for the semi-infinite dendrite in section 3.4.1. The negligible effects that multiple dendrites have on the dynamic response been verified by analysis and simulation however, which we show in Appendix C.3.

3.7 Summary

In this chapter we have seen that the upcrossing method can be used to approximate the dynamic firing-rate response well in spatial neuron models, and that simple attributes of neuronal morphology change features of the dynamic response, such as the cutoff frequency, phase zeros and the high-frequency limit. Starting with the point neuron, we replicated results found in previous studies for the response from current, synaptic mean and variance modulation [9, 151].

Any spatially extended model allows for separation between the location of applied current modulation and the trigger position (sections 3.3.1, 3.4.1 3.5.1, 3.6.1), which produces a complex dynamic response which cannot be produced by

point-neuron models (section 3.2.1). This included a sag in the amplitude and phase zeros. The amplitude remained at least half of its low-frequency limit across a frequency range of several hundred Hz for the parameters chosen, in agreement with experimental studies with somatically applied current modulation [85, 87, 88]. However, unlike other modelling studies, nonlinear spike-generating currents were not required for this large bandwidth [86, 126]. Oscillation frequencies ∼100 Hz (sometimes called high-gamma or ultrafast) are physiologically relevant, having been observed in the neocortex on the macroscopic scale [155] and may play a role in neuropathologies such as schizophrenia [156].

For the infinite dendrite (section 3.3.1), the frequencies of the current modulation phase zeros could be adjusted by the position of the modulating input and the relative time scale of synaptic fluctuations, β_s. We saw for the ball-and-stick neuron (section 3.5.1) that increasing the size of the soma increased the frequency of phase zeros. Finally, with the dendrite-and-axon model (section 3.6.1) we saw that the phase zeros could be tuned by the dimensionless distance of the trigger position along but that the ratio of length constants had a negligible effect.

With synaptic mean and variance modulation, the cutoff frequency can be tuned by β_s, which is typically twice as high for variance modulation as compared with synaptic mean modulation (sections 3.3.2, 3.3.3, 3.5.3). For the ball-and-stick model (sections 3.5.2, 3.5.3), increasing somatic size and time constant decreased the cutoff frequency slightly for both modulation types. Changing the axonal length constant or the trigger position in the dendrite-and-axon model (sections 3.6.2, 3.6.3) mostly affected the phase at high frequencies and had a very small effect on the amplitude. The higher cutoff frequency for variance modulation has been produced experimentally *in vitro* [148], albeit at higher frequencies than in this chapter.

While resonances in the upcrossing-rate response were theoretically possible for synaptic mean and variance modulation, these were only enabled for parameter ranges outside the region for which the upcrossing approximation is applicable (sections 3.2.2, 3.2.3, 3.3.2, 3.3.3). From our analysis of the firing-rate response for the point neuron in this regime (section 3.2.3), it is unclear if the simulated threshold-reset firing rate displays these predicted resonances.

The common theme in this chapter is that for a fixed operating point where the steady-state variance and the relative threshold are held constant, it is the change from a point-like to a spatial model that makes the largest difference to the dynamic response rather than specific morphological details such as the number of dendrites or the size of the soma. The main differences are the high-frequency phase limit and phase zeros for local current modulation. Spatial extent does not confer

firing-rate resonances or phase zeros to modulation of the presynaptic drive in the regime for which the upcrossing approximation applies, but on the contrary, makes these resonance less easily attainable. This is due to the derivative variance relative to the voltage variance being higher for spatial models under than the point-neuron model under synaptic mean modulation, and due to the magnitude of the covariance being lower for variance modulation. The better theoretical candidate for a response in-phase with the input drive, which is unique to spatial-neuron models, comes from local current modulation, which allows for large bandwidths and phase zeros.

Chapter 4

Quasi-Active Neurons: Steady-State Firing Rate

4.1 Introduction

An advantage of the upcrossing approach is that it can be extended to include a variety of additional biophysical properties which affect the integration of spatio-temporal synaptic drive. In particular, non-passive effects from voltage-gated currents can be included, for example the hyperpolarisation-activated depolarising current I_h [106, 107]. I_h channels have been found to affect the subthreshold voltage frequency response [61, 157] and are expressed in different quantities between neuronal classes (compare [53, 57, 59, 158]) and mammalian species [42, 159]. From a neuropathological perspective, it has been found that due to its control of neuronal excitability, enhancing I_h may provide a part of epilepsy treatment [54–56].

This chapter thus applies the quasi-active approximation of voltage-gated ion channels introduced in section 1.3.4 to the spatial-neuron models seen in Chapter 2. The effect of a single type of linearised active current on the steady-state upcrossing rate is analysed for each model. This current is restorative, as it provides negative feedback to fluctuations about the steady-state mean. Only the dendrites are considered quasi-active in our models; electrically substantial somata or axons are taken as passive.

4.2 Quasi-Active Point Neuron

As shown in section 1.3.4, if we measure the potential about equilibrium with zero synaptic drive, $v = V - E_{Lh}$, the potential with a linearised current evolves as (1.48)

$$\tau_v \frac{\mathrm{d}v}{\mathrm{d}T} = \mu - v + s - \kappa w, \quad \tau_w \frac{\mathrm{d}w}{\mathrm{d}T} = v - \mu - w, \tag{4.1}$$

with the fluctuating component of the synaptic drive s defined as before 1.38. Physiologically representative values for κ and τ_w for a given active current are typically highly varied, so we vary both parameters widely. For reference, the dominant fast time constant of I_h is usually in the range $\tau_w \sim 20 - 50$ ms, while the coupling parameter $\kappa \sim 0.1 - 2$ [53, 57–59, 64].

Though we will mostly focus on coloured noise, white noise will be used to show the effect of the linearised current in isolation from the synaptic time scale. Rescaling time as before ($t = T/\tau_v$), we define $\beta_w = \tau_w/\tau_v$ and obtain

$$\beta_w \frac{\mathrm{d}w}{\mathrm{d}t} = v - \mu - w. \tag{4.2}$$

For a quasi-active membrane, we can employ the same strategy of taking Fourier transforms in time, rearranging in terms of $\tilde{v}(\omega)$, and then taking the inverse transform to get $v(t)$. Taking Fourier transforms in time gives

$$i\omega\tilde{v} = 2\pi\delta(\omega)\mu - \tilde{v} + \tilde{s} - \kappa\tilde{w}, \quad i\omega\beta_w\tilde{w} = \tilde{v} - 2\pi\delta(\omega)\mu - \tilde{w}, \tag{4.3}$$

which can be rearranged to give the potential in time as

$$v(t) = \mu + \frac{1}{2\pi}\int_{-\infty}^{\infty} e^{i\omega t}\frac{(1 + i\omega\beta_w)\tilde{s}}{(1 + i\omega)(1 + i\omega\beta_w) + \kappa}\mathrm{d}\omega. \tag{4.4}$$

Since $\langle\tilde{s}\rangle = 0$, for the quasi-active point neuron $\langle v\rangle = \mu$ as in the passive case. Recall that for the passive membrane we defined $\gamma = \sqrt{1 + i\omega}$ such that for the point neuron $\gamma^2\tilde{v}_F = \tilde{s}$ (section 2.2). Similarly for quasi-active membranes we define γ_h as

$$\gamma_h^2 = \frac{(1 + i\omega)(1 + i\omega\beta_w) + \kappa}{1 + i\omega\beta_w}, \tag{4.5}$$

such that $\gamma_h^2\tilde{v}_F = \tilde{s}$. Note that in either the limit of zero coupling, $\kappa = 0$, or when the active current response time becomes extremely slow, $\beta_w \to \infty$, γ_h converges to γ.

4.2.1 Point Neuron Variances, White-Noise

With white noise, $\tilde{s} = \sigma_{\text{WN}}\sqrt{2}\tilde{\xi}_s(\omega)$, the power spectral density is

$$S(\omega) = \frac{2\sigma_{\text{WN}}^2(1+\omega^2\beta_w^2)}{(1+\omega^2)(1+\omega^2\beta_w^2)+\kappa^2+2\kappa(1-\omega^2\beta_w)} = \frac{2\sigma_{\text{WN}}^2}{|\gamma_h|^4}, \tag{4.6}$$

from which we can obtain the time autocovariance and the variance using (2.10)

$$K(\tau) = \frac{1}{2\pi}\int_{-\infty}^{\infty} S(\omega)e^{i\omega\tau}\mathrm{d}\omega. \tag{4.7}$$

Even for the point neuron, the quasi-active current makes $K(\tau)$ algebraically complicated. With some manipulation of the integral of $S(\omega)$ (Appendix A.4.4), the temporal autocovariance can be found as

$$\begin{aligned} K(\tau) &= e^{-(1+\beta_w^{-1})\frac{\tau}{2}}\frac{(1+\beta_w+\kappa\beta_w)\cos(h\tau)+\frac{1}{2h}(1+\beta_w)(\beta_w^{-1}-1-\kappa)\sin(h\tau)}{(1+\beta_w)(1+\kappa)} \\ h &= \frac{1}{2\beta_w}\sqrt{4\beta_w(1+\kappa)-(1+\beta_w)^2}, \end{aligned} \tag{4.8}$$

while the variance is given by

$$\sigma_v^2 = \sigma_{\text{WN}}^2\frac{1+\beta_w(1+\kappa)}{(1+\beta_w)(1+\kappa)}. \tag{4.9}$$

We can infer from the form of $S(\omega)$ that σ_v^2 still does not exist, despite the addition of the active current which filters the voltage dynamics. This is because the quasi-active variable does not affect the dynamics at high frequencies as it is not coupled to the synaptic drive s. The variance decreases as β_w decreases and as κ increases, which makes sense as a faster acting or more strongly coupled restorative current will dampen fluctuations caused by noise more strongly.

4.2.2 Point Neuron Variances, Coloured-Noise

With coloured noise, taking Fourier transforms and inverting yields

$$v(t) = \mu + \frac{\sigma_s\sqrt{2\beta_s}}{2\pi}\int_{-\infty}^{\infty} e^{i\omega t}\frac{\tilde{\xi}_s(\omega)}{\gamma_h^2(1+i\omega\beta_s)}\mathrm{d}\omega, \tag{4.10}$$

and hence the power spectral density is given by

$$S(\omega) = \frac{2\sigma_s^2\beta_s}{(1+\omega^2\beta_s^2)|\gamma_h|^4}. \tag{4.11}$$

Some manipulation of the integration is required for the temporal autocovariance and variance, see Appendix (A.64). The presence of a restorative current narrows the temporal autocovariance profile $K(\tau)$ for both white and coloured noise with decreasing β_w and increasing κ, Figure 4.1. In general $K(\tau)$ is non-monotonic with small negative autocovariances possible for time differences of a few τ_v.

Setting $\tau = 0$, the the variance is given by (A.69)

$$\sigma_v^2 = \frac{\sigma_s^2 \beta_s}{(1+\beta_w)(1+\kappa)} \frac{\beta_w + \beta_s(1+\beta_w) + \beta_w^2(1+\kappa)}{\beta_w + \beta_s(1+\beta_w) + \beta_s^2(1+\kappa)}, \tag{4.12}$$

which agrees with the result in [107]. Like the white-noise variance, for coloured noise the variance decreases with decreasing β_w and increasing κ. For quasi-active membranes, the relationship between σ_v^2, $\sigma_{\dot{v}}^2$ and the variance resulting from white-noise drive from Chapter 2 still holds (2.17). Hence $\sigma_{\dot{v}}^2$ can be acquired by using (4.9) and (4.12)

$$\sigma_{\dot{v}}^2 = \frac{\sigma_s^2}{(1+\beta_w)} \frac{\beta_s + \beta_w(1+\beta_w) + \beta_s\beta_w(1+\kappa)}{\beta_w + \beta_s(1+\beta_w) + \beta_s^2(1+\kappa)}. \tag{4.13}$$

We will comment more on the variances later in comparison with the infinite dendrite, but we can see from (4.12) and (4.13) that w affects the variance in a non-trivial manner due to being coupled to v.

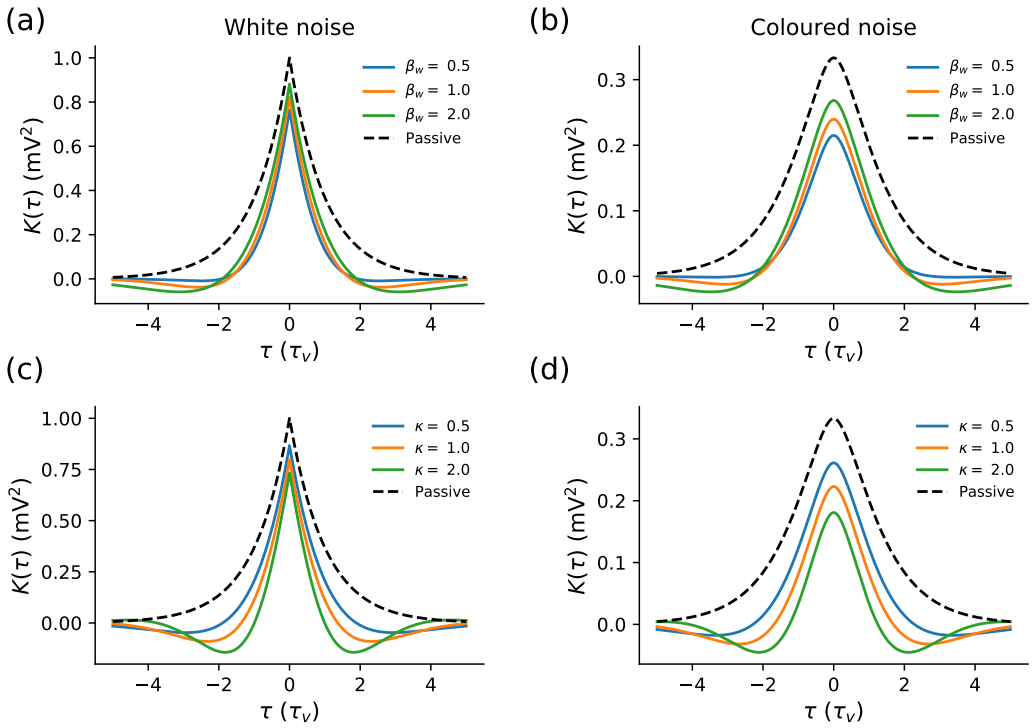

Figure 4.1: The temporal autocovariance $K(\tau)$ of quasi-active point neurons subject to white (4.8) and coloured noise (A.64), is narrowed by (a-b) decreasing β_w and (c-d) increasing κ. $K(\tau)$ for passive membranes is given by (2.8) and (2.12) for white and coloured noise respectively. Other parameters: $\beta_s = 0.5$, $\sigma_s = 1$mV.

4.2.3 Point Neuron, Firing Rate

Similar to the synaptic variable s, after v reaches v_{th} the quasi-active variable w is not reset in threshold-reset simulations, as in [105]. This is because the dynamics of w are much slower than those of the action potential. Due to the increase in the variance from increasing β_w, we would expect the upcrossing rate to increase as β_w increases, which is shown along with the threshold-reset rate in Figure 4.2(a, b). Similarly, as increasing κ decreases the variance, the upcrossing rate decreases as seen in Figure 4.2(c, d). Were we to fix σ_v by adjusting σ_s with either β_w or κ, then these effects would be reversed; larger β_w and smaller κ would instead decrease the upcrossing rate. Furthermore, we see that for $\mu < 9$mV, the upcrossing rate is lower for the quasi-active membrane than the passive membrane neuron, with convergence occurring as $\beta_w \to \infty$ or $\kappa \to 0$.

Curiously, when μ is just subthreshold ($9 < \mu < 10$mV in Figure 4.2(a, c)), the effects of increasing β_w and decreasing κ change from increasing the upcrossing rate to decreasing it. This occurs because the exponential term of the upcrossing

formula (2.1) becomes small, meaning that the increase in $\sigma_{\dot{v}}/\sigma_v$ with lower β_w and higher κ dominates. The effect is most pronounced at the maximum of the upcrossing rate when $\langle v \rangle = v_{\text{th}}$ and the exponential evaluates to 1, giving $r_{uc} = \sigma_{\dot{v}}/(2\pi\sigma_v)$. The threshold-reset rate is no longer well approximated by the upcrossing rate in this regime. We see in Figure 4.2(a) that increasing β_w always seems to increase the threshold-reset rate, while decreasing κ switches to decreasing the threshold-reset rate Figure 4.2(c).

We should finally note that, as the addition of a quasi-active current serves to dampen deviations away from the mean, the relative error of the upcrossing method as an approximation for the threshold-reset process is typically decreased. This is shown in more detail in Figure C.6 in Appendix C.2.2.

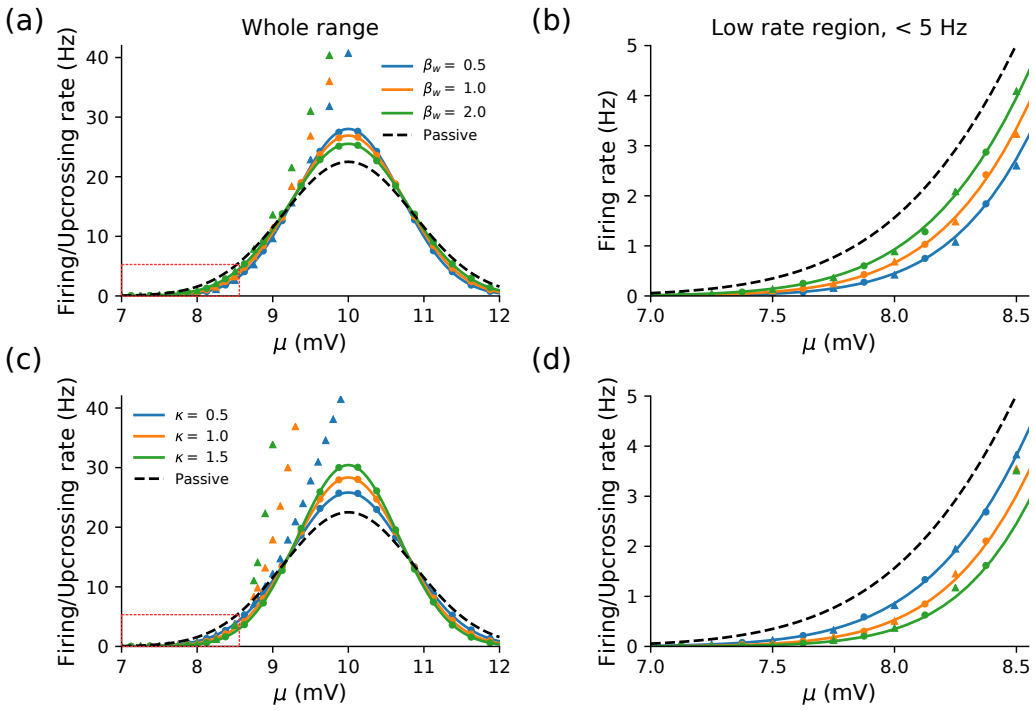

Figure 4.2: For the quasi-active point neuron, (a, b) decreasing β_w and (c, d) increasing κ lowers the subthreshold firing rate for fixed σ_s, but increases the near-threshold upcrossing rate. The low rate region is shown in more detail in panels (b) and (d), corresponding to the red boxes of panels (a) and (c) respectively. Solid lines show the theoretical upcrossing rate (2.1), dashed lines the upcrossing rate of the passive point neuron (2.19), while circles and triangles denote upcrossing and threshold-reset simulations respectively. Other parameters: (a-d) $\tau_s = 10$ms, $\tau_s = 5$ms, $\sigma_s = 1.5$mV, $v_{\text{th}} = 10$mV, (a-b) $\kappa = 0.55$, (c-d) $\beta_w = 1.5$.

4.3 Quasi-Active Infinite Dendrite

For the infinite dendrite and all further spatial models with quasi-active membranes, we will use the cable equation with the potential measured from the resting potential in the absence of synaptic drive E_{Lh} (1.49)

$$\frac{\partial v}{\partial t} = \mu - v + \frac{\partial^2 v}{\partial x^2} - \kappa w + s, \quad \beta_w \frac{\partial w}{\partial t} = v - \mu - w. \tag{4.14}$$

As with the passive membrane, the variances for the infinite dendrite are obtained here using Fourier transforms in space and time. Inverting the Fourier transform $\hat{v}(k,\omega)$ gives the potential as

$$v(x,t) = \mu + \frac{1}{4\pi^2}\int_{-\infty}^{\infty} e^{ikx}\mathrm{d}k \int_{-\infty}^{\infty} \frac{(1+i\omega\beta_w)\hat{s}(k,\omega)}{(1+i\omega+k^2)(1+i\omega\beta_w)+\kappa} e^{i\omega t}\mathrm{d}\omega, \tag{4.15}$$

which applies to any spatial structure for which the active current is uniform and the spatial Fourier transform makes sense. We can see from this that $\langle v \rangle = \mu$.

4.3.1 Infinite Dendrite Variances, White-Noise

Given the complexity of the temporal autocovariance for the passive membrane, we do not attempt to derive $K(\tau)$ for the quasi-active infinite dendrite here. The spatial autocovariance $K(x - x' = \Delta)$ is more tractable and of greater interest

$$\begin{aligned} K(\Delta) =& \frac{\sigma_{\mathrm{WN}}^2}{\pi^2}\int_{-\infty}^{\infty} e^{ik\Delta}\mathrm{d}k \\ &\times \int_{-\infty}^{\infty} \frac{(1+\omega^2\beta_w^2)\mathrm{d}\omega}{[(1+k^2)^2+\omega^2](1+\omega^2\beta_w^2)+\kappa^2+2\kappa(1+k^2-\omega^2\beta_w)}, \end{aligned} \tag{4.16}$$

which after performing the ω-integral (see Appendix A.4.5 for details) first yields

$$K(\Delta) = \frac{\sigma_{\mathrm{WN}}^2}{\pi}\int_{-\infty}^{\infty} \frac{1+\beta_w(1+\kappa+k^2)}{[1+\beta_w(1+k^2)](1+\kappa+k^2)} e^{ik\Delta}\mathrm{d}k, \tag{4.17}$$

which can be resolved by separating into partial fractions and then integrated separately to finally give

$$K(\Delta) = \frac{\sigma_{\mathrm{WN}}^2}{\kappa-\beta_w^{-1}}\left(\frac{\kappa}{\sqrt{1+\beta_w^{-1}}} e^{-|\Delta|\sqrt{1+\beta_w^{-1}}} - \frac{\beta_w^{-1}}{\sqrt{1+\kappa}} e^{-|\Delta|\sqrt{1+\kappa}}\right), \tag{4.18}$$

where the variance σ_v^2 results from letting $\Delta = 0$

$$\sigma_v^2 = \frac{\sigma_{\text{WN}}^2}{\kappa - \beta_w^{-1}} \left(\frac{\kappa}{\sqrt{1+\beta_w^{-1}}} - \frac{\beta_w^{-1}}{\sqrt{1+\kappa}} \right). \tag{4.19}$$

There are two things to note from this expression in comparison to the quasi-active point-neuron variance (4.9): (i) the functional dependence on (β_w, κ) is qualitatively different, and (ii) it does not depend on any spatial parameters. The first observation is similar to how the infinite and point-neuron variances differ for the passive membrane when coloured noise is introduced.

4.3.2 Infinite Dendrite Variances, Coloured-Noise

Deriving the variances for coloured noise in the quasi-active infinite dendrite follows the same procedure as white noise. Substituting the coloured-noise form of $\hat{s}(k,\omega)$ into (4.15) and integrating with respect to ω first we find

$$\begin{aligned} K(\Delta) &= \frac{\sigma_s^2 \beta_s}{\pi} \int_{-\infty}^{\infty} \frac{(c_w + \beta_w k^2) e^{ik\Delta}}{[1+\beta_w(1+k^2)](1+\kappa+k^2)(c_s+\beta_s k^2)} \mathrm{d}k, \\ c_w &= \frac{\beta_w + \beta_s(1+\beta_w) + \beta_w^2(1+\kappa)}{\beta_w + \beta_s}, \\ c_s &= \frac{\beta_s + \beta_w(1+\beta_s) + \beta_s^2(1+\kappa)}{\beta_w + \beta_s}. \end{aligned} \tag{4.20}$$

Splitting this into partial fractions and performing the k-integral gives three terms

$$K(\Delta) = \sigma_s^2 \beta_s \left[\frac{\eta_w e^{-|\Delta|\sqrt{1+\beta_w^{-1}}}}{\sqrt{1+\beta_w^{-1}}} + \frac{\eta_\kappa e^{-|\Delta|\sqrt{1+\kappa}}}{\sqrt{1+\kappa}} + \frac{\eta_s e^{-|\Delta|\sqrt{c_s\beta_s^{-1}}}}{\sqrt{c_s\beta_s^{-1}}} \right], \tag{4.21}$$

where the constants $\eta_w,\ \eta_\kappa,\ \eta_s$ are used for compactness and are given by

$$\eta_w = \frac{\beta_w^3 \kappa}{(\kappa\beta_w - 1)[\beta_w^2 + \beta_s^2(\kappa\beta_w - 1)]}, \quad \eta_\kappa = -\frac{1}{\kappa\beta_w - 1}, \quad \eta_s = \frac{\beta_s^2 - \beta_w^2}{\beta_w^2 + \beta_s^2(\kappa\beta_w - 1)}, \tag{4.22}$$

and as in previous cases the variance is obtained by setting $\Delta = 0$ in (4.21)

$$\sigma_v^2 = \sigma_s^2 \beta_s \left[\frac{\eta_w}{\sqrt{1+\beta_w^{-1}}} + \frac{\eta_\kappa}{\sqrt{1+\kappa}} + \frac{\eta_s}{\sqrt{c_s\beta_s^{-1}}} \right]. \tag{4.23}$$

The derivative variance follows from the relation between the white and coloured noise variances introduced in Chapter 2 (2.17)

$$\sigma_{\dot{v}}^2 = \frac{\sigma_s^2}{\beta_s}\left[\frac{1}{\sqrt{1+\beta_w^{-1}}}\left(\frac{\kappa\beta_w}{\kappa\beta_w - 1} - \eta_w\right) - \frac{\eta_s}{\sqrt{c_s\beta_s^{-1}}}\right]. \tag{4.24}$$

We compare the white- and coloured-noise spatial autocovariance of the quasi-active infinite dendrite in Figure 4.3. For both noise types, decreasing β_w such that the active current responds more quickly to fluctuations decreases the effective length constant. This makes sense, as the active current with $\kappa > 0$ and lower β_w dampens fluctuations from the equilibrium potential at each point along the dendrite more quickly, thus decreasing the length over which fluctuations can be correlated. Similarly, increasing κ also increases the effective length constant, though this effect is less pronounced.

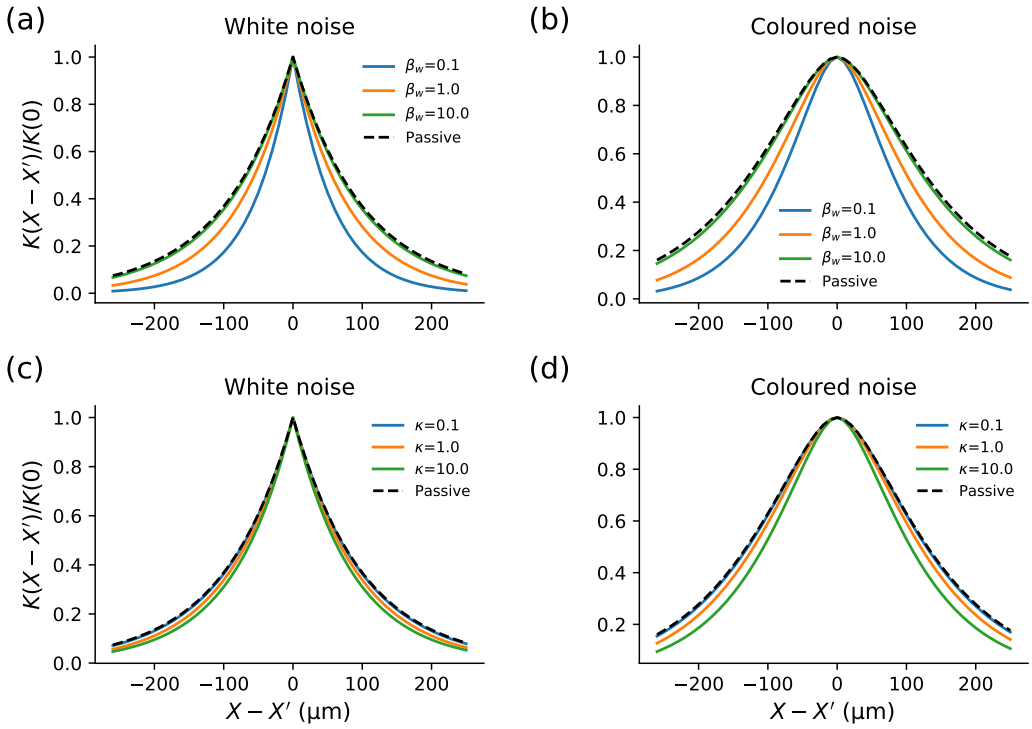

Figure 4.3: The effective length constant of an infinite dendrite is reduced by restorative currents. Here the spatial autocovariance is plotted for the infinite dendrite with white (4.18) and coloured noise (4.21). (a, b) show that a faster active current (decreasing β_w) decreases the extent of spatial correlations, while (c, d) show that increasing κ decreases the extent of correlations. The passive temporal autocovariances are calculated from (2.30) and (2.35) for white and coloured noise respectively. Other parameters: (a-d) $\lambda = 100\mu$m, $\beta_s = 0.5$, (a-b) $\kappa = 2.5$ (c-d) $\beta_w = 2.5$.

For the variances in both the point neuron and the infinite dendrite, decreasing κ and decreasing β_w increases σ_v^2, Figure 4.4(a). However, $\sigma_{\dot{v}}^2$ varies non-monotonically with β_w, with Figure 4.4(b) showing that $\sigma_{\dot{v}}^2$ initially increases and then decreases gradually towards the passive value. This also means that $\sigma_{\dot{v}}^2$ decreases with increasing κ for small β_w but increases with increasing κ for larger β_w, with the switch between these regimes at $\beta_w \sim \beta_s$. We should note however that the relative variations in $\sigma_{\dot{v}}^2$ with the quasi-active parameters are quite small, especially compared to the much larger relative changes in σ_v^2. The more significant difference is between the two models themselves, with the infinite dendrite having lower σ_v^2 and higher $\sigma_{\dot{v}}^2$ than the point neuron, just as was found for the passive membrane, section 2.3.2.

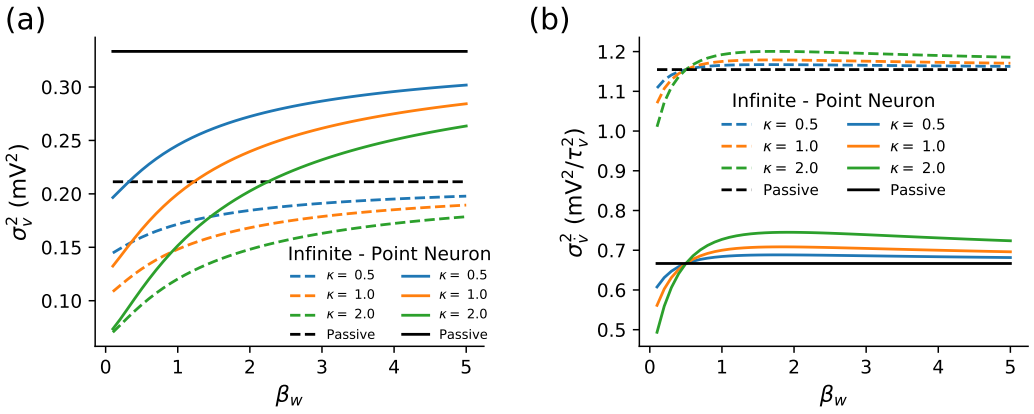

Figure 4.4: Comparing the variances of the quasi-active point neuron (4.12, 4.13) and infinite dendrite (4.23, 4.24) shows that: (a) for both models increasing κ and decreasing β_w increases σ_v^2, (b) $\sigma_{\dot{v}}^2$ initially increases with β_w before decreasing towards the passive value and $\sigma_{\dot{v}}^2$ increases with κ for $\beta_w > \beta_s$. The passive values of $\sigma_{\dot{v}}^2$ in (b) are given by (2.16) and (2.36) for the point and infinite neurons respectively. Other parameters: $\beta_s = 0.5$, $\sigma_s = 1\text{mV}$.

4.3.3 Infinite Dendrite, Firing Rate

In the subthreshold regime, the firing rate increases with increasing β_w (Figure 4.5 a) and decreasing κ (Figure 4.5b), which makes sense as the variance increases for both of these parameter changes. We also note good agreement between the upcrossing approximation and the simulated threshold-reset rate. The upcrossing approximation is more accurate at $\beta_s = 0.5$, $(v_{\text{th}} - \langle v \rangle)/\sigma_v \sim 3$ for the quasi-active infinite dendrite in comparison with the passive infinite dendrite, as detailed in Figure C.7 of Appendix C.2.2.

Like the passive case, we see that in comparison with the point neuron,

the firing rate is lower for the same input parameters in the infinite dendrite. In addition, the upcrossing approximation is generally less accurate with a smaller parameter space in which it can be reliably applied.

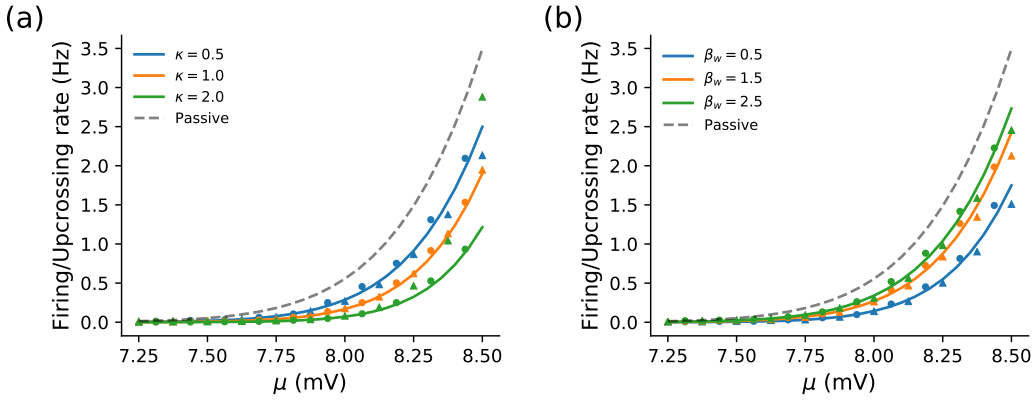

Figure 4.5: The subthreshold firing rate of the quasi-active infinite dendrite (a) increases with higher β_w and (b) decreases with higher κ, except when the neuron is near-threshold. Solid lines show the theoretical upcrossing rate obtained via substitution of (4.23) and (4.24) into (2.1), while circles and triangles indicate values from upcrossing and threshold-reset simulations respectively. Other Parameters: (a-b) $\tau_v = 10\text{ms}$, $\tau_s = 5\text{ms}$, $\sigma_s = 1.5\text{mV}$, $v_{\text{th}} = 10\text{mV}$, (a) $\kappa = 0.55$, (b) $\beta_w = 1.5$.

4.4 Quasi-Active Finite Sealed Dendrite

4.4.1 Sealed Dendrite Variances, White-Noise

Using our previous results from the quasi-active infinite dendrite and the passive sealed dendrite, section 2.5, we can deduce that the variance for the sealed active cable is calculated from the expression

$$\sigma_v^2 = \frac{\sigma_{\text{WN}}^2}{\pi} \sum_{m=-\infty}^{\infty} \int_{-\infty}^{\infty} e^{2ikml}(e^{2ikx} + 1) \frac{1 + \beta_w(1 + \kappa + k^2)}{[1 + \beta_w(1 + k^2)](1 + \kappa + k^2)} \mathrm{d}k, \tag{4.25}$$

which ultimately reduces to

$$\sigma_v^2 = \sigma_{\text{WN}}^2 \frac{\beta_w \kappa C(x; \beta_w^{-1}) - C(x; \kappa)}{\beta_w \kappa - 1}, \tag{4.26}$$

where we recall that $C(x; \zeta)$ was defined in Chapter 2 (2.47). From the infinite dendrite (4.19) and (4.26), we can infer that decreasing κ and increasing β_w increases σ_v^2 at all positions on the sealed dendrite. Furthermore, Figure 4.6 shows that the relative variance profile $\sigma_v^2(x)/\sigma_v^2(0)$ decreases with increasing κ and decreasing

β_w. However, large changes in either variable are required to make a significant difference. In comparison with the passive sealed dendrite in section 2.5.1, we can conclude that the decrease in $\sigma_v^2(x)/\sigma_v^2(0)$ from stronger quasi-active currents means that not only can the semi-infinite approximation still be used for $L = 1000\mu$m and $\lambda \leq 200\mu$m, but that the validity of this approximation is enhanced when restorative linearised active currents are present.

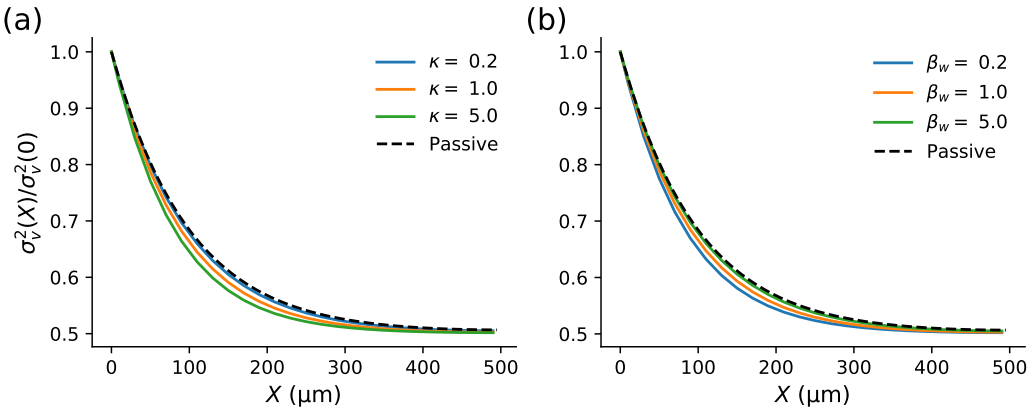

Figure 4.6: The relative white-noise variance in the quasi-active sealed dendrite (4.26) decreases at all positions with (a) increasing κ and (b) decreasing β_w. The passive sealed variance is given by (2.46). Other parameters: (a-b) $L = 1000\mu$m $\lambda = 200\mu$m, $\sigma_{\text{WN}} = 1$mV, (a) $\beta_w = 1.5$, (b) $\kappa = 0.55$.

4.4.2 Sealed Dendrite Variances, Coloured-Noise

Again following the passive sealed cable and the infinite active cable we can start from the sum

$$\sigma_v^2 = \sigma_s^2 \beta_s \sum_{m=-\infty}^{\infty} \left\{ \frac{\eta_w \left(e^{-|2ml|\sqrt{1+\beta_w^{-1}}} + e^{-|2ml+2x|\sqrt{1+\beta_w^{-1}}} \right)}{\sqrt{1+\beta_w^{-1}}} + \ldots \right\}, \tag{4.27}$$

where the constants η_w, η_κ, η_s and c_s have the same meanings as in the infinite active section (4.20,4.22). Collecting these terms as before, we find the variance

$$\sigma_v^2(x) = \sigma_s^2 \beta_s \left[\eta_w C(x; \beta_w^{-1}) + \eta_\kappa C(x; \kappa) + \eta_s C(x; c_s \beta_s^{-1} - 1) \right]. \tag{4.28}$$

Similarly the derivative variance is given by

$$\sigma_v^2(x) = \frac{\sigma_s^2}{\beta_s} \left\{ \left(\frac{\kappa \beta_w}{\kappa \beta_w - 1} - \eta_w \right) C(x; \beta_w^{-1}) - \eta_s C(x; c_s \beta_s^{-1} - 1) \right\}. \tag{4.29}$$

The variation of the relative variances, $\sigma_v^2(x)/\sigma_v^2(0)$ and $\sigma_{\dot{v}}^2(x)/\sigma_{\dot{v}}^2(0)$, with the quasi-active parameters (β_w, κ) is shown in Figure 4.7. While increasing κ and decreasing β_w decreases the effective length constant, differences are only visible in the spatial profile of the variances for very large changes in the parameters. Furthermore, we can see that σ_v^2 is more susceptible to changes in the quasi-active parameters than $\sigma_{\dot{v}}^2$. In particular, $\sigma_{\dot{v}}^2$ is almost constant with changes in β_w, Figure 4.7(d). As in the case of the infinite dendrite, section 4.3.2, $\sigma_{\dot{v}}^2$ peaks for $\beta_w \sim 1.5$ rather than monotonically varying. All of these changes occur at every spatial position on the sealed dendrite.

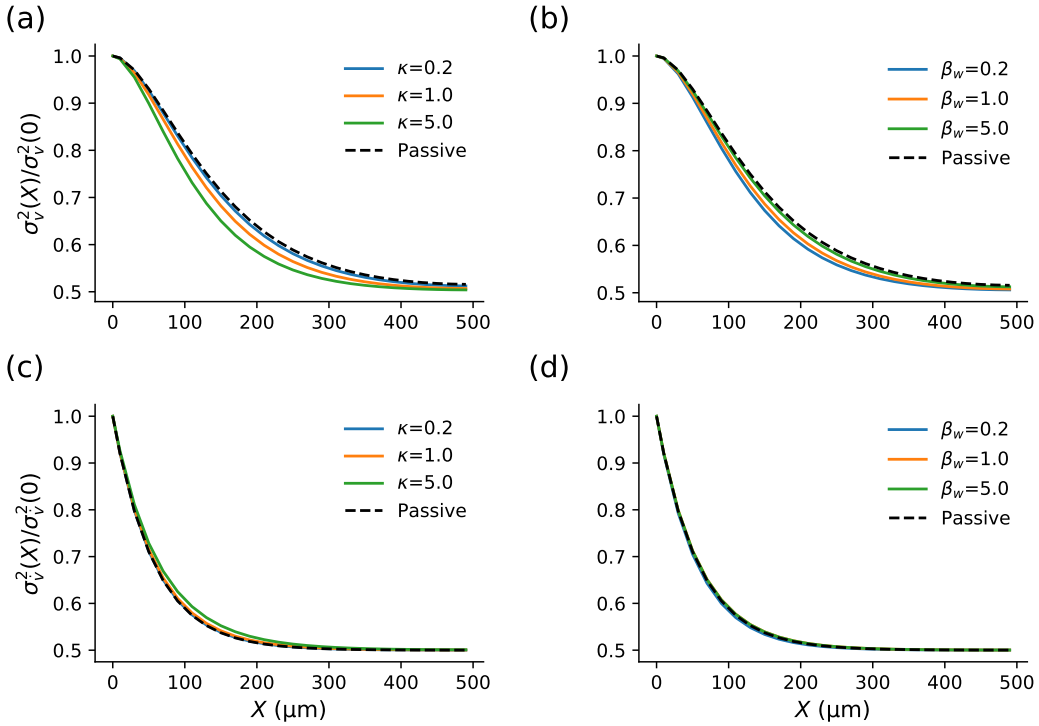

Figure 4.7: The relative coloured-noise variance (4.28) in the quasi-active sealed dendrite decreases at all positions with (a) increasing κ and (b) decreasing β_w. The coloured-noise derivative variance (4.29) (c) increases with increasing κ and (d) peaks at $\beta_w \sim 1.5$ for the chosen set of parameters. However, σ_v^2 is far more sensitive both to changes in κ and β_w than $\sigma_{\dot{v}}^2$, which by comparison is close to constant. σ_v^2 and $\sigma_{\dot{v}}^2$ for the passive sealed dendrite are given by (2.52) and (2.53) respectively. Other parameters: (a-d) $L = 1000\mu$m, $\lambda = 200\mu$m, $\beta_s = 0.5$, (a, c) $\beta_w = 1.5$, (b, d) $\kappa = 0.55$.

These results show that quasi-active currents do not significantly change our ability to approximate long dendrites as being semi-infinite in extent. In fact, the

reduction in the effective length constant from κ and β_w gives the semi-infinite approximation greater accuracy.

4.5 Quasi-Active Ball-and-Stick Model

For models with a soma, we assume that the soma receives no active currents. This is in approximate agreement with the far lower density of I_h channels found in the somata of pyramidal cells as compared with the dendrites [51, 57, 58].

As we recall from section 2.7.2, the passive ball-and-stick neuron has a spatially varying mean. This means that one could choose to linearise the active current about $\langle V(x)\rangle_0$, which in models with a spatially homogeneous mean was always equal to E_{0h}. However as one can infer from the derivation of the linearisation in section 1.3.4, this would lead to spatially varying quasi-active parameters such as τ_w and κ, as well as making λ and τ_v spatially varying as they ultimately depend on n^*. To avoid this complication, and to allow for a more direct comparison with previous spatial models, we will instead linearise about the constant value of E_{0h} throughout the whole quasi-active dendrite. This represents the equilibrium potential at the distal dendritic end, $X = \infty$, and has the same value as previous spatial models. This is further justified if the mean varies little with X about the equilibrium (V^*, n^*). Therefore we can write our cable and quasi-active equations as in (4.14).

Due to the lack of active currents at the soma, the boundary condition at $x = 0$ remains as in the passive case

$$\beta_\sigma \frac{\mathrm{d}v_\sigma}{\mathrm{d}t} = -v_\sigma + \rho \left.\frac{\partial v}{\partial x}\right|_{x=0}, \tag{4.30}$$

however we must stress that while identical mathematically, the physiological interpretation of β_σ and ρ differs slightly from the passive membrane due to the influence of the active current on the effective dendritic membrane conductance g_0.

As in the passive membrane, the ball-and-stick neuron can be analysed using the Green's function in the temporal Fourier domain, $\tilde{\mathcal{G}}(x, y; \omega)$. We can straightforwardly translate the passive neuron Green's functions into quasi-active ones by replacing γ_1 with γ_{h1}. In the case of the ball-and-stick model, this substitution of γ_{h1} into (2.93) yields

$$\tilde{\mathcal{G}}(x, y; \omega) = \frac{e^{-|x-y|\gamma_{h1}}}{2\gamma_{h1}} + \frac{e^{-|x+y|\gamma_{h1}}}{2\gamma_{h1}} \left(\frac{\rho\gamma_{h1} - \gamma_\sigma^2}{\rho\gamma_{h1} + \gamma_\sigma^2}\right). \tag{4.31}$$

4.5.1 Ball-and-Stick Model, Mean

With mean synaptic drive component μ, $\langle v \rangle$ is given by applying the input $\tilde{I}(y;\omega) = 2\pi\delta(\omega)\mu[1+\kappa/(1+i\omega\beta_w)]$. In terms of the Green's function integral this means

$$\begin{aligned}\langle v(x)\rangle &= \mu(1+\kappa)\int_0^\infty \tilde{\mathcal{G}}(x,y;0)\mathrm{d}y \\ &= \frac{\mu(1+\kappa)}{2\sqrt{1+\kappa}}\int_0^\infty e^{-|x-y|\sqrt{1+\kappa}} + e^{-|x+y|\sqrt{1+\kappa}}\left(\frac{\rho\sqrt{1+\kappa}-1}{\rho\sqrt{1+\kappa}+1}\right) \\ \langle v(x)\rangle &= \mu\left(1-\frac{e^{-x\sqrt{1+\kappa}}}{\rho\sqrt{1+\kappa}+1}\right). \end{aligned} \tag{4.32}$$

This shows that the linearised active current affects the mean through the coupling parameter κ. For higher κ the effective length constant decreases, which causes the mean to increase more quickly to the bulk value as x increases, Figure 4.8(a). Furthermore, increasing κ and ρ also increases the mean at the soma ($x = 0$), which will converge to μ as $\kappa \to \infty$ or $\kappa \to \infty$, Figure 4.8(b).

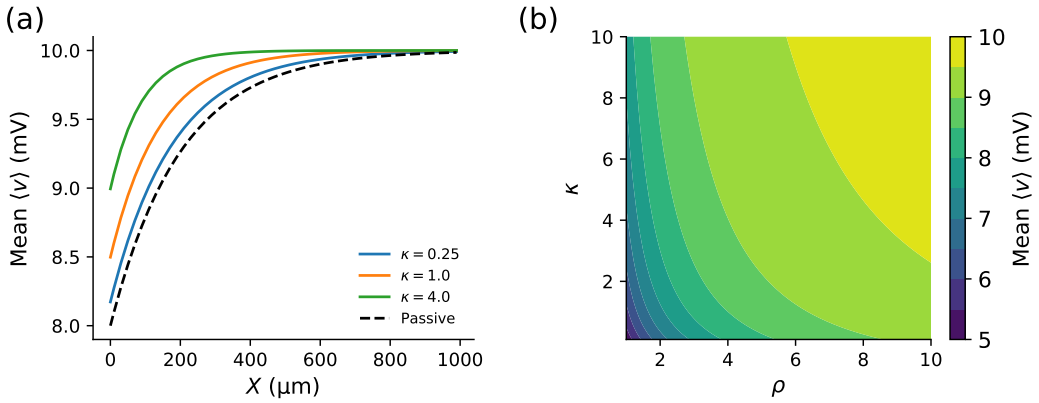

Figure 4.8: The mean potential of the quasi-active ball-and-stick model neuron (4.32) (a) increases with increasing κ. (b) The mean at the soma ($X = 0$) increases towards μ for increasing ρ and κ. The passive mean is calculated from (2.96). Other parameters: (a, b) $\lambda = 200\mu$m, $\mu = 10$mV (a) $\rho = 4$.

4.5.2 Ball-and-Stick Model, Variances

In agreement with previous spatial models, increasing κ and decreasing β_w decreases the variance Figure 4.9(a, b) at all positions in the ball-and-stick model. The location of the peak in variance (seen for the passive ball-and-stick model in section 2.7.3) increases with both increasing κ and β_w. The derivative variance (not shown) increases monotonically with distance from the soma.

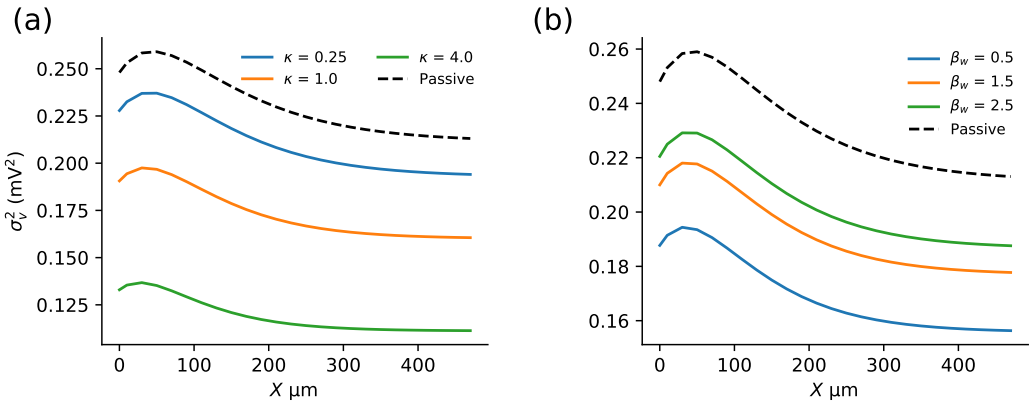

Figure 4.9: The variance in the quasi-active ball-and-stick model from (4.31) in (2.77) decreases with (a) increasing κ and (b) increasing β_w, while increasing the derivative variance at all positions of the ball-and-stick model neuron. The passive variance is given by integration of (2.93) in (2.77). Other parameters: (a-b) $\lambda = 200\mu$m, $\rho = 4$, $\beta_\sigma = 7/6$, $\mu = 10$mV (a) $\beta_w = 1.5$, (b) $\kappa = 0.55$.

4.5.3 Ball-and-Stick Model, Firing Rate

The dependence of the mean on κ gives the firing rate an interesting dependence on the quasi-active parameters. We see in Figure 4.10(a) that for lower μ ($\lesssim 8$ mV), increasing κ decreases the firing rate, while for high μ, increasing κ increases the firing rate. This is because as μ is larger, reducing the difference between the mean and threshold has a more significant effect on increasing the firing rate than the corresponding variance reduction does on decreasing it. On the other hand, increasing β_w always increases the firing rate for the same subthreshold range of μ as it has no effect on the mean, Figure 4.10(b). The quasi-active firing rate does not converge to the passive firing rate when $\beta_w \to \infty$ however, because the mean potential is still affected by κ in this limit as we saw in (4.32).

We investigate the effect of κ on the upcrossing rate in more detail by fixing $\mu = 8$ mV and calculating the upcrossing rate for a wide range of κ and β_w. Figure 4.10(c) shows that for lower β_w, increasing κ decreases the firing rate, while for higher β_w, increasing κ increases the firing rate. This can be explained by considering that for low β_w, the variance will already be low, and thus further reductions to σ_v^2 by increasing κ will not be offset by the corresponding increase in the mean. On the other hand, at higher β_w, the variance starts from a higher position, and thus reductions from increasing κ will be compensated by the increase in $\langle v \rangle$. If we had chosen a lower value of μ, then the region for which κ decreases the upcrossing rate would be larger, and vice versa had we chosen a larger value of μ.

Further exploration of varying ρ reveals that, if the upcrossing rate initially increases with κ, then it generally decreases slightly as κ increases further, giving a non-monotonic profile. This is because the effect of the mean on κ eventually saturates, as can be seen from (4.32). To see how this is affected by morphology, we varied the somatic size with ρ and noted the value of κ which maximised the upcrossing rate. Figure 4.10(d) shows that for larger ρ (smaller somata), the value of κ that maximises firing is lower. This makes sense, as for larger ρ, $\langle v \rangle$ increases towards μ. This makes the increase in the mean from increasing κ less significant. We also see that for lower μ, $\kappa_{\max} = 0$, whilst for higher μ, $\kappa_{\max}$ increases.

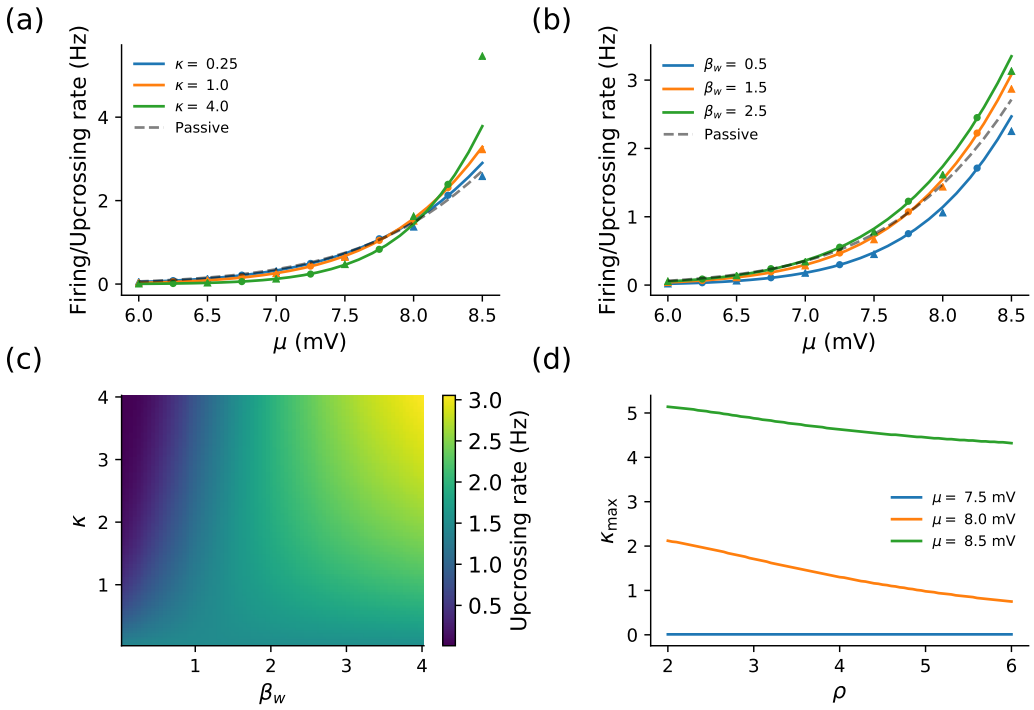

Figure 4.10: The firing rate of the quasi-active ball-and-stick neuron: (a) increases with increasing κ for larger μ (where its increase of the mean is more significant) but decreases with smaller μ (where its decrease of the variance is more significant); (b) always increases with increasing β_w. (c) Keeping μ constant, increasing κ decreases the upcrossing rate for low β_w and increases it for high β_w. (d) The value of κ which maximises the upcrossing rate, $\kappa_{\max}$, decreases with ρ (smaller somata). Solid lines and the heatmap in (c) show the theoretical upcrossing rate (2.1), while circles and triangles denote upcrossing and threshold-reset simulations respectively. Other parameters: (a-d) $\lambda = 200\mu$m, $\beta_\sigma = 7/6$, $\sigma_s = 3$mV (a-c) $\rho = 4$, (a-b) $\mu = 10$mV (a, d) $\beta_w = 1.5$, (b) $\kappa = 0.55$, (c) $\mu = 8$ mV.

4.6 Quasi-Active Dendrite-and-Axon Model

We will now explore a model with a quasi-active dendrite and passive axon. As this is also a case where the mean is no longer spatially homogeneous, we will continue to assume the active current is linearised about the resting potential at the distal dendritic end throughout the dendrite. The dimensionless cable equations are

$$\frac{\partial v_1}{\partial t} = \mu_1 - v_1 + \frac{\partial^2 v_1}{\partial x_1^2} + s_1 - \kappa_1 w_1, \quad \beta_\alpha \frac{\partial v_\alpha}{\partial t} = -v_\alpha + \frac{\partial^2 v_\alpha}{\partial x_\alpha^2}, \tag{4.33}$$

where we have denoted the linearised active current as w_1 to show how this can be extended for multiple dendrites as we shall see later.

The Green's functions in the Fourier domain for (4.33) now obey

$$i\omega\tilde{\mathcal{G}}_{11}(x_1, y_1; \omega) = -\tilde{\mathcal{G}}_{11} + \frac{\partial^2 \tilde{\mathcal{G}}_{11}}{\partial x_1^2} - \frac{\kappa_1 \tilde{\mathcal{G}}_{11}}{1 + i\omega\beta_w} + \delta(x_1 - y_1), \tag{4.34}$$

$$i\omega\beta_\alpha\tilde{\mathcal{G}}_{\alpha 1}(x_\alpha, y_1; \omega) = -\tilde{\mathcal{G}}_{\alpha 1} + \frac{\partial^2 \tilde{\mathcal{G}}_{\alpha 1}}{\partial x_\alpha^2}, \tag{4.35}$$

which after collecting the Green's functions in terms of γ_h (which we denote here as γ_{h1}) and $\gamma_\alpha = \sqrt{1 + i\omega\beta_\alpha}$ gives

$$\gamma_{h1}^2\tilde{\mathcal{G}}_{11} = \frac{\partial^2 \tilde{\mathcal{G}}_{11}}{\partial x_{11}^2} + \delta(x_1 - y_1), \quad \gamma_\alpha^2\tilde{\mathcal{G}}_{\alpha 1} = \frac{\partial^2 \tilde{\mathcal{G}}_{\alpha 1}}{\partial x_\alpha^2}. \tag{4.36}$$

These Green's functions obey the same equations as the passive case (2.58), but γ_1 has been replaced with γ_{h1}. Since the boundary conditions are also the same, the Green's functions will also be the same as (2.64) but with γ_1 replaced with γ_{h1}

$$\tilde{\mathcal{G}}_{11}(x_1, y_1; \omega) = \frac{e^{-|x_1 - y_1|\gamma_{h1}}}{2\gamma_{h1}} + \frac{e^{-|x_1 + y_1|\gamma_{h1}}}{2\gamma_{h1}} \left(\frac{\beta_\alpha^2\lambda_1^3\gamma_{h1} - \lambda_\alpha^3\gamma_\alpha}{\beta_\alpha^2\lambda_1^3\gamma_{h1} + \lambda_\alpha^3\gamma_\alpha} \right), \tag{4.37}$$

$$\tilde{\mathcal{G}}_{\alpha 1}(x_\alpha, y_1; \omega) = \frac{\beta_\alpha^2\lambda_1^3 e^{-(x_\alpha\gamma_\alpha + y_1\gamma_{h1})}}{\beta_\alpha^2\lambda_1^3\gamma_{h1} + \lambda_\alpha^3\gamma_\alpha}. \tag{4.38}$$

4.6.1 Dendrite-and-Axon, Mean

With synaptic input in the dendrite only, the axonal mean is given by

$$\begin{aligned} \langle v_\alpha(x_\alpha)\rangle &= \mu \int_0^\infty \mathrm{d}y_1 \int_{-\infty}^\infty \tilde{\mathcal{G}}_{\alpha 1}(x_\alpha, y_1; \omega) \left[1 + \frac{\kappa}{1 + i\omega\beta_w}\right] \delta(\omega) e^{i\omega t} \mathrm{d}\omega \\ &= \langle v_\alpha(x_\alpha)\rangle = \mu(1 + \kappa) \int_0^\infty \tilde{\mathcal{G}}(x_\alpha, y_1; 0) \mathrm{d}y_1, \end{aligned} \tag{4.39}$$

which is the general equation for the mean contribution from a quasi-active structure, akin to the passive general mean equation in Chapter 2 (2.71). With a single dendrite and axon, recalling that $\gamma_{h1}(\omega = 0) = \sqrt{1+\kappa}$, we have

$$\langle v_\alpha(x_\alpha)\rangle = \frac{\mu\beta_\alpha^2\lambda_1^3\sqrt{1+\kappa}}{\beta_\alpha^2\lambda_1^3\sqrt{1+\kappa}+\lambda_\alpha^3}e^{-x_\alpha}, \tag{4.40}$$

where we see that the coupling parameter κ has an effect while β_w does not. Furthermore, the relative spatial decay of the mean with length along the axon is unaffected by the linearised active current in the dendrite, however the magnitude increases towards μe^{-x_α} as κ increases. Similarly the mean in the dendrite is given by

$$\langle v_1(x_1)\rangle = \mu\left(1 - \frac{\lambda_\alpha^3 e^{-x_1\sqrt{1+\kappa}}}{\beta_\alpha^2\lambda_1^3\sqrt{1+\kappa}+\lambda_\alpha^3}\right). \tag{4.41}$$

The effect of scaling κ is shown in Figure 4.11, where we see that increasing κ increases the mean at all positions along the dendrite and axon. Since these differences in the axon can be difficult to see clearly in Figure 4.11(a), we show the mean as a function of κ for fixed values of X in Figure 4.11(b). This panel shows that changes in the axonal mean with κ are much smaller than changes due to position. Despite this, we shall see later for the firing rate that even these small changes cannot be neglected.

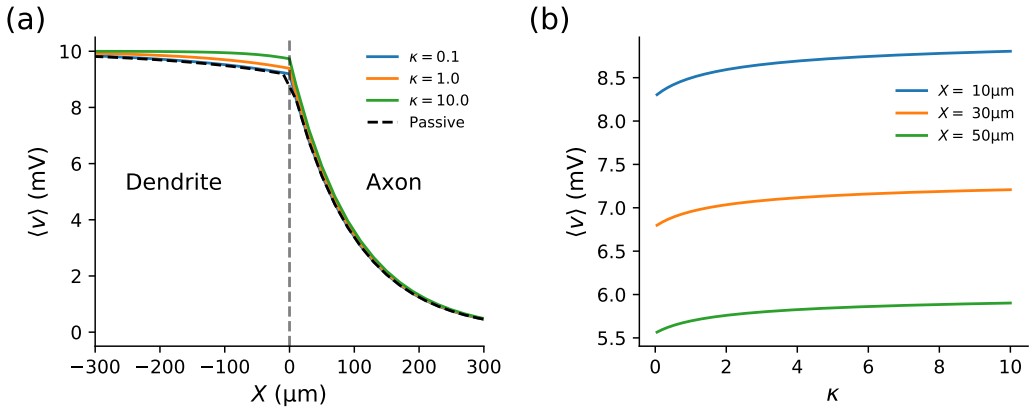

Figure 4.11: For the mean voltage in the quasi-active dendrite-and-axon model (4.41): (a) Increasing κ increases the mean at all positions along the axon but does not affect the relative spatial decay. The mean in the dendrite also increases as κ increases. (b) The difference in $\langle v\rangle$ is relatively small with κ compared to small changes in position X_α. We have used the convention of negative values of X for the dendrite and positive values for the axon. The passive mean is calculated from (2.72, 2.73) . Other parameters: $\lambda_1 = 200\mu$m, $\lambda_\alpha = 100\mu$m, $\mu = 10$mV.

4.6.2 Dendrite-and-Axon, Variances

Analogous to the passive dendrite-and-axon model 2.85, the variances can be obtained via integration of $|\tilde{\mathcal{G}}(x_\alpha, y_1; \omega)|^2$

$$\sigma_v^2(x_\alpha) = \frac{2\sigma_s^2\beta_s}{\pi}\int_{-\infty}^{\infty} \frac{\beta_\alpha^4\lambda_1^6 e^{-x_\alpha z_\alpha}}{z_{h1}|\beta_\alpha\lambda_1^3\gamma_{h1} + \lambda_\alpha^3\gamma_\alpha|^2(1+\omega^2\beta_s^2)}\mathrm{d}\omega. \tag{4.42}$$

As in the single-neurite models, Figure 4.12 shows that σ_v^2 in the axon increases at all positions with increasing β_w and decreasing κ. Again, σ_v^2 has a non-monotonic relationship with β_w and increases with increasing κ, but this variation is very minor so is not shown here.

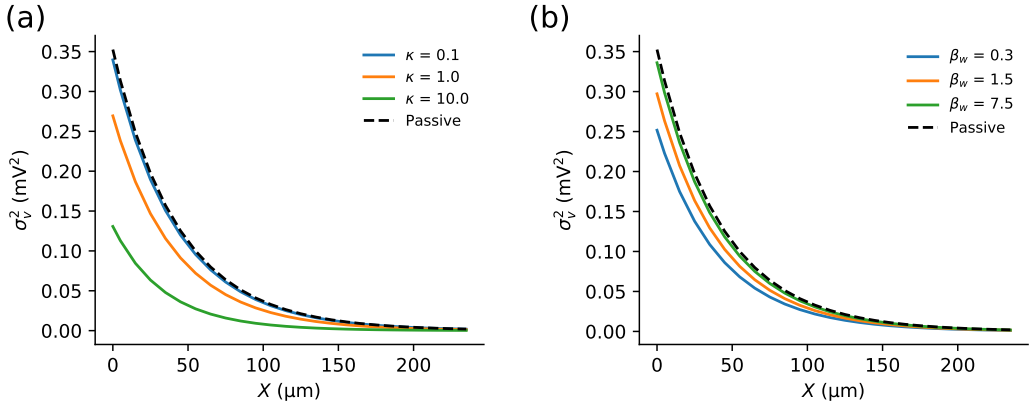

Figure 4.12: For the variance in the quasi-active dendrite-and-axon model (4.42) (a) decreasing κ and (b) increasing β_w increase the variance at all positions along the axon. The passive variance is given by (2.85). Other parameters: $\beta_s = 0.5$, $\sigma_s = 1\text{mV}$.

4.6.3 Dendrite-and-Axon, Firing Rate

Due to the influence of κ on the mean, the upcrossing rate decreases with κ for lower μ and initially increases with κ for higher μ, Figure 4.13(a). In general, the relationship for higher μ is non-monotonic, peaking at higher κ for larger subthreshold values of μ. Furthermore, for larger λ_α this non-monotonic dependence of the firing rate on κ will start for lower values of μ. This is because the increase in mean from increased κ from (4.40) will be able to propagate further along the axon. Increasing β_w always increases the firing rate when the mean is not near threshold, Figure 4.13(b). However, the firing rate does not converge to the passive case as $\beta_w \to \infty$ due to the fact that κ affects the mean even in this limit (4.40).

In the passive model for $X_{\text{th}} > 0$, there was a non-monotonic relationship

between the upcrossing rate and ratio of the axonal to dendritic radii, a_α/a_1, Figure 2.11(c). Fixing μ, we varied κ to see how the ratio for maximal subthreshold upcrossing changes. Figure 4.10(c) shows that the optimal a_α/a_1 increases for increased κ and equivalently the value of κ for maximal subthreshold upcrossing, $\kappa_{\max}$, increases with a_α/a_1. We show the $\kappa_{\max}$ for different $\lambda_\alpha \propto \sqrt{a_\alpha/a_1}$ in Figure 4.10(d).

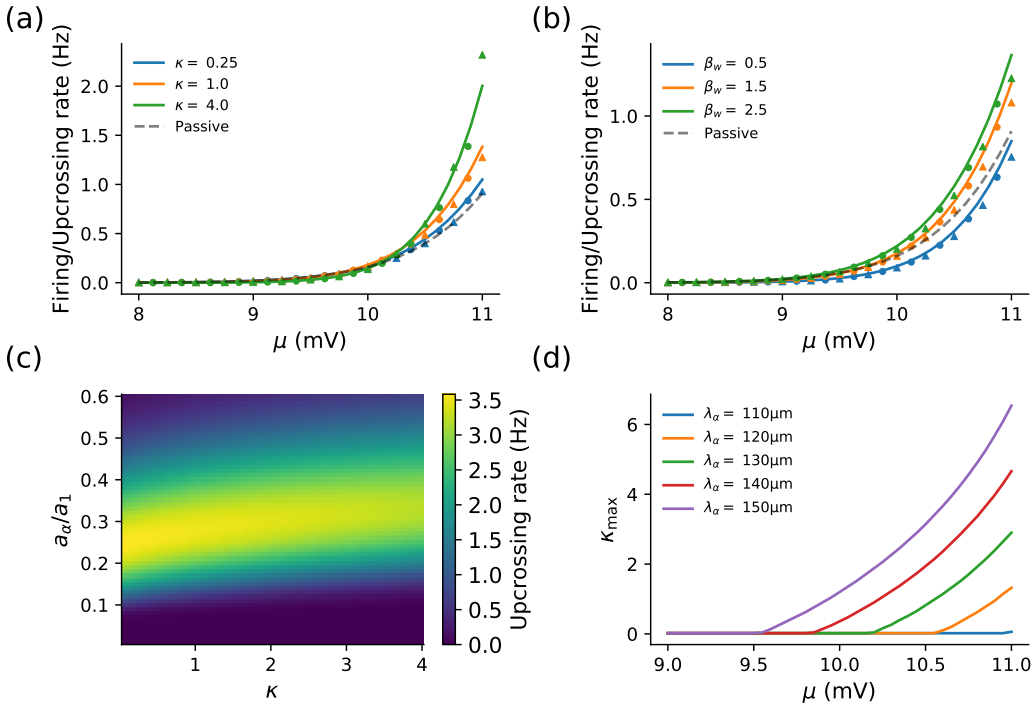

Figure 4.13: For the quasi-active dendrite-and-axon model: (a) The firing rate initially increases with increasing κ for higher μ and λ_α. (b) Increasing β_w increases the firing rate for all μ not near threshold. (c) The radius ratio a_α/a_1 that maximises the subthreshold upcrossing rate increases as κ increases. (d) Increasing λ_α increases the value of κ which maximises the upcrossing rate, $\kappa_{\max}$, and allows it to be non-zero at lower μ. Solid lines and the heatmap in (c) show theoretical upcrossing values calculated from (2.1), while circles and triangles represents values from simulations. Other parameters: (a-d) $\lambda_1 = 200\mu$m, $\beta_s = 0.5$, $\sigma_s = 3$mV, $v_{\text{th}} = 10$mV, $X_{\text{th}} = 30\mu$m, (a-b) $\lambda_\alpha = 150\mu$m, (a, c, d) $\beta_w = 1.5$, (b) $\kappa = 0.55$, (c) $\mu = 11$mV.

Next, we looked at how the radius ratio a_α/a_1 that produces maximal subthreshold upcrossing varies depending on κ and the absolute trigger position X_{th}. We confirm that $\max(a_\alpha/a_1)$ increases with κ for different values of X_{th}, Figure 4.14(a). Like in the passive neuron, $\max(a_\alpha/a_1)$ increases as the trigger position is moved further down the axon. Finally, we looked at the effect that the axon has on the firing rate when compared to a semi-infinite active cable. As in section 2.6.5,

we put the trigger position at $X = 0$. Figure 4.14(b) shows that the same size axon decreases the upcrossing rate more significantly for stronger active currents. This is because at $x = 0$ with an axon, the variance reduction from higher κ is more important for the upcrossing rate than the relative increase in the mean. This is also reflected in the simulated firing rate.

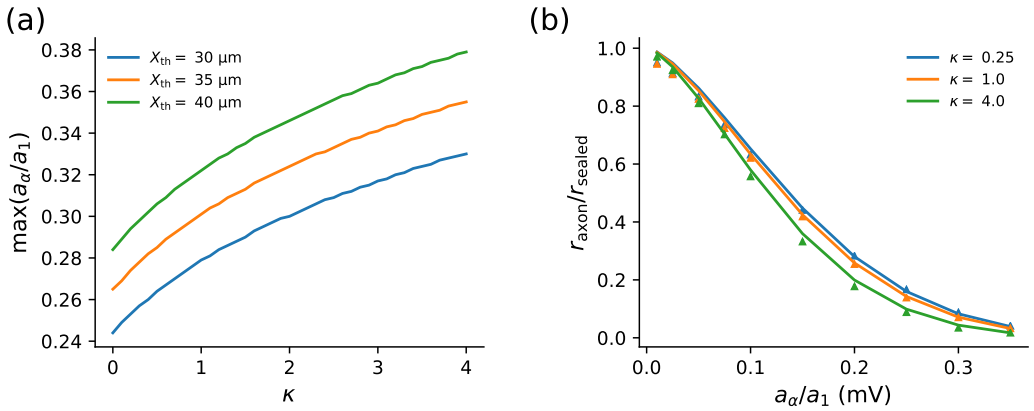

Figure 4.14: (a) Increasing the coupling strength κ in the quasi-active dendrite-and-axon model increases the axonal radius which maximises the upcrossing rate when $X_{\text{th}} > 0$. (b) When $X_{\text{th}} = 0$, increasing κ causes the upcrossing rate to decrease more with a wider axon. Solid lines indicate theoretical upcrossing results from (2.1) while triangles in (b) show values from threshold-reset simulations. Other parameters: (a-b) $\lambda_1 = 200\mu$m, $\beta_s = 0.5$, $\sigma_s = 3$mV, (a) $\mu = 11$ mV, (b) $\mu = 5$ mV.

4.7 Multiple Quasi-Active Dendrites and Axon

With multiple quasi-active dendrites, we consider the linearised restorative currents in each dendrite to have the same parameters, but each has its own quasi-active state variable w_j. Each w_j will differ between the dendrites due to the voltage fluctuations caused by the between-dendrite independent stochastic drive. Thus for n dendrites and an axon

$$\frac{\partial v_j}{\partial t} = \mu - v_j + \frac{\partial^2 v_j}{\partial x_j^2} + s_j - \kappa w_j, \quad \beta_\alpha \frac{\partial v_\alpha}{\partial t} = -v_\alpha + \frac{\partial^2 v_\alpha}{\partial x_\alpha^2},$$
$$\beta_w \frac{\partial w_j}{\partial t} = v_j - \mu - w_j, \quad j = 1, 2, ..., n, \tag{4.43}$$

where the boundary conditions at $x = 0$ are as in the passive case (2.101).

The sum-over-trips formalism introduced in section 2.8 has previously been applied to branching quasi-active dendrites [104]. Therefore we can use this to find

the segment factor for n quasi-active dendrites and a passive axon meeting at a node

$$\tilde{f}_{1h} = \frac{\beta_\alpha^2 \lambda_1^3 \gamma_{h1}}{n\beta_\alpha^2 \lambda_1^3 \gamma_{h1} + \lambda_\alpha^3 \gamma_\alpha}, \tag{4.44}$$

and hence the Green's function for the axonal voltage response to an input signal into a single dendrite is

$$\tilde{\mathcal{G}}_{\alpha 1}(x_\alpha, y_1; \omega) = \frac{\tilde{f}_{1h}}{\gamma_{h1}} e^{-(x_\alpha \gamma_\alpha + y_1 \gamma_{h1})} = \frac{\beta_\alpha^2 \lambda_1^3}{n\beta_\alpha^2 \lambda_1^3 \gamma_{h1} + \lambda_\alpha^3 \gamma_\alpha} e^{-(x_\alpha \gamma_\alpha + y_1 \gamma_{h1})}. \tag{4.45}$$

4.7.1 Multiple Dendrites and Axon, Mean

From the mean calculation in the axon from a single quasi-active dendrite (4.39), and noting that the mean contributions from each dendrite sum linearly, we can calculate the mean as

$$\begin{aligned} \langle v_\alpha(x_\alpha) \rangle &= \sum_{j=1}^{n} \mu(1+\kappa) \int_0^\infty \tilde{\mathcal{G}}_{\alpha j}(x_\alpha, y_j; 0) \mathrm{d}y_j \\ \langle v_\alpha(x_\alpha) \rangle &= \frac{n\mu\beta_\alpha^2 \lambda_1^3 \sqrt{1+\kappa}}{n\beta_\alpha^2 \lambda_1^3 \sqrt{1+\kappa} + \lambda_\alpha^3} e^{-x_\alpha}. \end{aligned} \tag{4.46}$$

The mean converges to μe^{-x_α} as n increases, as seen for passive dendrites, Figure 4.15(a). However, the relative increase in the mean as n increases is smaller as κ is larger, Figure 4.15(b). This makes sense as the limits of $\langle v_\alpha \rangle$ are the same as $n \to \infty$ and $\kappa \to \infty$, so higher κ puts the mean closer to the limiting value.

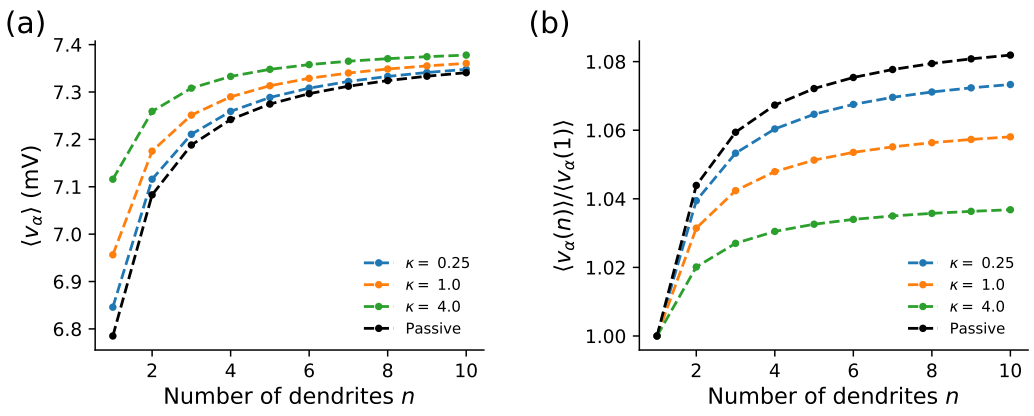

Figure 4.15: (a) For n quasi-active dendrites and a passive axon, increasing both κ and n increase the mean (4.46), however (b) shows that the relative increase of the mean with n is larger for smaller κ. The mean for passive dendrites is given by (2.111). Other parameters $\lambda_1 = 200\mu$m, $\lambda_\alpha = 100\mu$m, $X_\alpha = 30\mu$m, $\mu = 10$mV.

4.7.2 Multiple Dendrites and Axon, Variances

Variance contributions from each dendrite also add linearly, as we saw for the passive membrane in section 2.8.3. This means for the overall axonal variance

$$\begin{aligned}\sigma_{v_\alpha}^2 &= \sum_{j=1}^{n} \frac{2\sigma_s^2\beta_s}{\pi} \int_{-\infty}^{\infty} \frac{\mathrm{d}\omega}{1+\omega^2\beta_s^2} \int_0^{\infty} |\tilde{\mathcal{G}}_{\alpha j}(x_\alpha, y_j; \omega)|^2 \mathrm{d}y_j \\ &= \frac{2n\sigma_s^2\beta_s}{\pi} \int_{-\infty}^{\infty} \frac{e^{-x_\alpha z_\alpha}\mathrm{d}\omega}{z_\alpha(1+\omega^2\beta_s^2)|n\beta_\alpha^2\lambda_1^3\gamma_{h1} + \lambda_\alpha^3\gamma_\alpha|^2},\end{aligned} \tag{4.47}$$

and similarly for $\sigma_{\dot{v}_\alpha}^2$. For all β_w and κ, both steady-state variances decrease monotonically with dendritic number n, similar to passive dendrites in section 2.8. Furthermore, increasing κ and β_w has the same qualitative effect on the variances as other spatial models (decreasing and increasing σ_v^2 respectively), Figure 4.16(a, b). Figure 4.16(c, d) show that $\sigma_{\dot{v}_\alpha}/\sigma_{v_\alpha}$ is almost constant with n for a range of β_w and κ, similar to n passive dendrites and an axon in section 2.8.3.

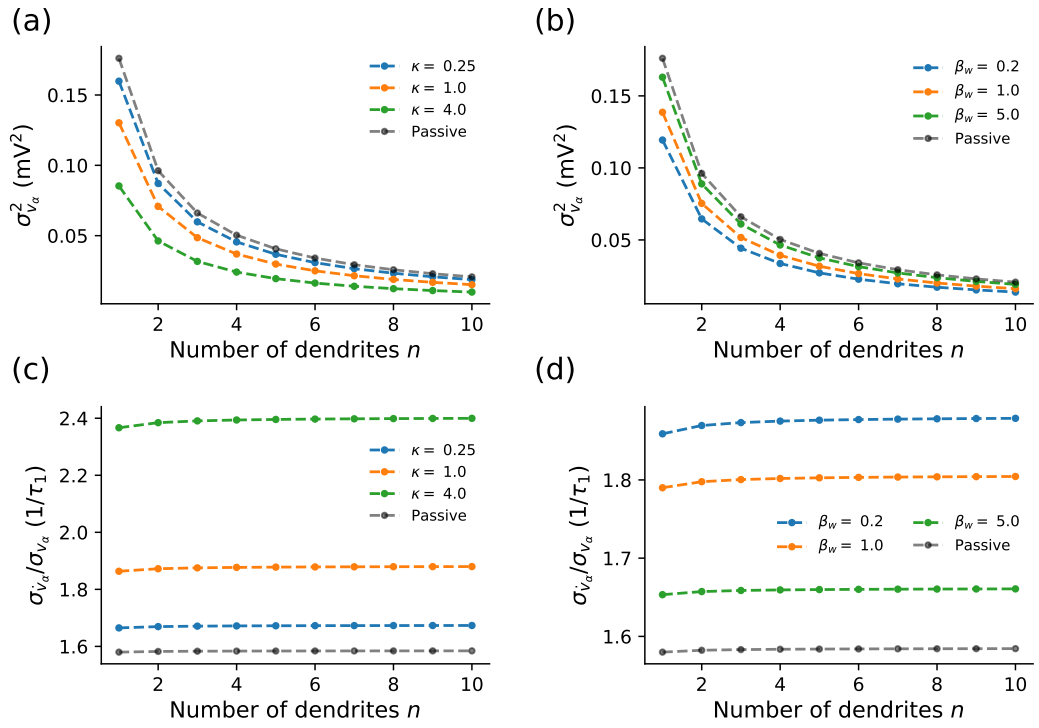

Figure 4.16: The axonal variance with n quasi-active dendrites (4.47) (a) decreases monotonically with dendritic number n and κ, while (b) increases with β_w. The ratio $\sigma_{\dot{v}}/\sigma_v$ remains almost constant with n across a range of (c) κ and (d) β_w. The passive variance is from 2.116. Other parameters: (a-d) $\lambda_1 = 200\mu$m, $\lambda_\alpha = 100\mu$m, $\beta_\alpha = 7/6$, $X_\alpha = 30\mu$m, $\beta_s = 0.5$, $\sigma_s = 1$mV, (a, c) $\beta_w = 1.5$, (b, d) $\kappa = 0.55$.

4.7.3 Multiple Dendrites and Axon, Firing Rate

Since κ affects both the mean and the variance, we focussed on this quasi-active parameter for n dendrites. From section 2.8, we also chose a value of λ_α which gives rise to a non-monotonic dependence of the firing rate on n. We see in Figure 4.17(a) that for lower κ the firing and upcrossing rates are first maximised for 1, 2 then 3 dendrites as μ increases, much like for passive dendrites. However, for higher κ, Figure 4.17(b), the ranges of μ for which the firing rate is highest for $n = 1$ and $n = 2$ dendrites is larger. A comparison of the relative magnitudes of the firing rates between (a) and (b) shows this is due to an increase in the firing rates of $n = 1$ and $n = 2$ while for $n = 3$ the firing rate has not changed as much.

We investigated the dependence of the upcrossing rate on n and κ in more detail by fixing $\mu = 11$mV. Figure 4.17(c) reveals that for lower numbers of dendrites, increasing κ initially increases the upcrossing rate, with a non-monotonic dependency noticeable for very high κ (not shown). For higher n however, increasing κ monotonically decreases the upcrossing rate. These relationships can be explained by recalling that increasing both n and κ increase the mean and decrease the variance in the axon. However, we saw in (4.46) that the mean saturates with both parameters and increases more strongly with n than κ. Therefore, for higher n, the increase in $\langle v_\alpha \rangle$ caused by increasing κ will have a lesser effect on the firing rate than the corresponding decrease in $\sigma^2_{v_\alpha}$.

Finally, we show the number of dendrites that maximises the upcrossing rate as a function of κ and the axon-to-dendrite radius ratio a_α/a_1 in Figure 4.17(d). Here we see, similar to the passive neuron, that $n = 1$ maximises the upcrossing rate for a thinner axon. As the axon becomes thicker, $n_{\max}$ increases, with the additional effect that $n_{\max}$ is higher for lower κ. This can be explained for the same reasons as the previous panel; higher κ means that $\langle v_\alpha(x_\alpha) \rangle$ for $n = 1$ is higher and that increasing n will have a smaller relative impact on the mean for higher κ.

These results imply that a more strongly coupled linearised restorative current leads to a smaller number of dendrites being favoured for subthreshold firing. Thus, we should expect that if a neuron has dendrites with active currents, then, if its morphology is tuned to maximise fluctuation-driven subthreshold firing, it should have fewer dendrites when compared with a passive neuron or one with weaker active currents.

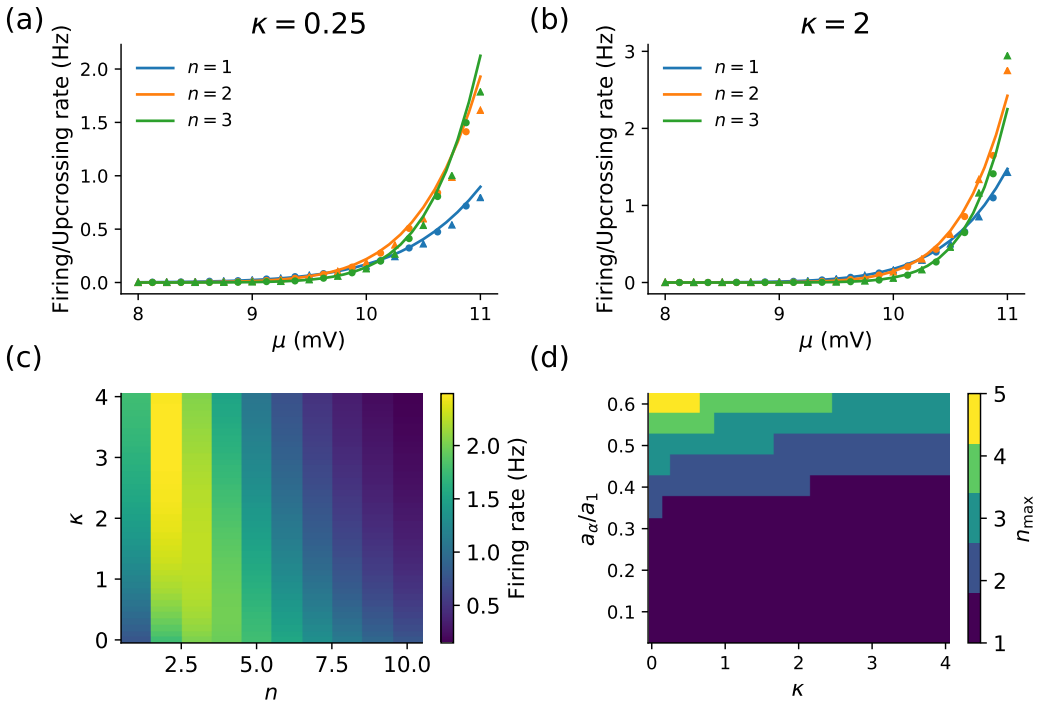

Figure 4.17: The firing rate for n quasi-active dendrites and an axon (a) is maximised for $n = 3$ when $\kappa = 0.25$ and for higher μ. (b) Whilst for $\kappa = 2$, the range of μ for which $n = 1$ and $n = 2$ dendrites maximises the firing rate is larger. (c) For $\mu = 11$, as n increases the upcrossing rate is maximised for lower κ. (d) As seen for passive dendrites, wider axons (higher a_α/a_1) causes the upcrossing rate to be maximised for a higher n. Increasing κ reduces the maximal n for subthreshold firing. Solid lines in (a, b) and the heatmaps in (c, d) denote values calculated from the theoretical upcrossing rate given by (2.1), whilst circles and triangles indicate values obtained via upcrossing and threshold-reset simulations respectively. Other parameters: (a-d) $\lambda_1 = 200\mu$m, $\beta_w = 1.5$, $\beta_s = 0.5$, $\sigma_s = 3$ mV, $v_{\text{th}} = 10$mV (a-b) $\lambda_\alpha = 150\mu$m, (c-d) $\mu = 11$ mV

4.8 Summary

In this chapter we have seen that quasi-active membranes can be straightforwardly incorporated into the framework for spatially extended neuron models driven by stochastic synaptic drive developed in Chapter 2. The restorative linearised current narrows the the temporal autocovariance profile of the quasi-active point neuron (section 4.2), while for spatial-neuron models we showed that the quasi-active parameters changed the effective length constants for the spatial autocorrelation (section 4.3), an effect similar to that calculated in [65,160] for the subthreshold voltage response. Analysis of the sealed dendrite (section 4.4) revealed that this meant we

can make the semi-infinite approximation more accurately than for passive membranes. For all models studied, decreasing the relative quasi-active time constant β_w and increasing the coupling parameter κ decreased the variance at all spatial locations, while having a much smaller effect on the variance of the time derivative.

From these effects on the variances, for models with a spatially homogeneous mean, the presence of a restorative quasi-active current reduced the firing rate compared to the passive membrane for the same input parameters. This is because the linearised restorative current provides negative feedback to voltage excursions from the mean. Furthermore, the accuracy of the upcrossing approximation was higher than the passive membrane case.

When the steady-state mean was spatially varying, as in the dendrite-and-axon, ball-and-stick, multiple dendrites and axon models (sections 4.5, 4.6 and 4.7), increasing κ increased the steady-state mean. This enabled the coupling parameter to have non-monotonic effect on the firing rate, with larger κ being favoured by a larger somatic size, a wider axonal radius, and a lower number of dendrites. Equivalently, this effects shows that more strongly quasi-active membranes (higher κ): increase the optimal axonal radius for subthreshold firing, increase the relative firing-rate reduction of an axon, and decrease the number of dendrites which maximises fluctuation-driven firing.

Chapter 5

Quasi-Active Neurons: Dynamic Response

5.1 Introduction

Voltage-gated currents can have a significant effect on the dynamic neuronal response. Focusing again on I_h, it has been experimentally observed that I_h adds subthreshold voltage resonance to cortical pyramidal cells at frequencies of $\sim$ 5Hz, similar to the theta EEG frequency band [61,62]. Furthermore, it has been measured experimentally [60] and calculated theoretically [105–107] that firing-rate resonance occurs at similar frequencies to the subthreshold resonance. Modelling studies have demonstrated that the subthreshold resonant frequency is affected by spatial separation between the point of applied input and point of measurement [65, 103, 160], and that quasi-active currents affect the resonant frequency of the produced local field potentials (LFPs) [66]. Various different functional roles of theta oscillations have been proposed, including pattern recognition, working memory [28], sequence learning [161], and navigation [162].

However, the effect of spatial separation and morphology on the firing-rate resonance induced by voltage-gated currents have not yet been investigated. This chapter uses the framework established in Chapter 3 of calculating the dynamic upcrossing-rate response to modulation of a localised current, the synaptic mean and variance of quasi-active spatial-neuron models.

5.2 Quasi-Active Point Neuron Modulation

When modulation is applied to a quasi-active neuron, since we still linearise the active current about the steady-state resting value E_{h0} (as opposed to the time-varying mean value), no oscillatory modulation terms enter the equation of the quasi-active current w. This is the case for both modulation arising from an external current and from modulation to the presynaptic drive, and applies to all the models studied in this chapter. Since the amplitude of oscillations of each modulation type is set to be small, we assume that the approximation of linearity for the active current in section 1.3.4 still holds as it did for small stochastic fluctuations in the voltage.

5.2.1 Subthreshold Response

The subthreshold response is obtained by generalising the input s to I and expressing the deviation of the potential from the steady-state mean, $u = v - \langle v \rangle_0$, in terms of s in the Fourier domain. This gives

$$i\omega\tilde{u} = -\tilde{u} - \kappa\tilde{w} + \tilde{I}, \qquad i\omega\beta_w\tilde{w} = \tilde{u} - \tilde{w}, \tag{5.1}$$

which after rearranging yields

$$\tilde{u}(\omega) = \frac{1 + i\omega\beta_w}{(1 + i\omega)(1 + i\omega\beta_w) + \kappa}\tilde{I}(\omega) = \tilde{Z}(\omega)\tilde{I}(\omega), \tag{5.2}$$

where we have defined the subthreshold response as the dimensionless quantity $\tilde{Z}(\omega) = \tilde{u}(\omega)/\tilde{I}(\omega)$. When $|\tilde{Z}(\omega)| > |\tilde{Z}(0)|$ for some range of ω, we refer to this as subthreshold resonance, with the value of ω for which $|\tilde{Z}(\omega)|$ is maximised as the subthreshold resonant frequency ω_s. Where resonance exists, we use the subthreshold quality factor, $Q_s = |\tilde{Z}(\omega_s)|/|\tilde{Z}(0)|$ to quantify the relative height of the resonant peak. Of greatest interest to us however is the phase zero frequency. We can see in Figure 5.1(c) that $\tilde{Z}(\omega)$ has a phase zero for larger β_w and κ.

5.2.2 Point Neuron, Current Modulation

When current modulation is applied to a quasi-active point neuron, our equations become

$$\frac{\mathrm{d}u}{\mathrm{d}t} = -u + s - \kappa w + \epsilon_c e^{i\Omega t}, \quad \beta_w \frac{\mathrm{d}w}{\mathrm{d}t} = u - w, \tag{5.3}$$

$$\beta_s \frac{\mathrm{d}s}{\mathrm{d}t} = -s + \sigma_s \sqrt{2\beta_s}\xi_s(t). \tag{5.4}$$

Taking Fourier transforms in time yields

$$\tilde{u}(\omega) = \frac{1 + i\omega\beta_w}{\kappa + (1 + i\omega)(1 + i\omega\beta_w)} \left[\frac{\sigma_s\sqrt{2\beta_s}\tilde{\xi}_s(\omega)}{1 + i\omega\beta_s} + 2\pi\epsilon_c\delta(\omega - \Omega) \right], \tag{5.5}$$

from which we can see that the prefactor of the equation for $\tilde{u}$ is equivalent to the subthreshold voltage frequency response (5.2). For restorative quasi-active currents, it is known that the subthreshold response can exhibit resonance and the connection between subthreshold and firing-rate resonance has been explored previously for point-neuron models [105–107]. From (5.5) it is straightforward to find the oscillatory first-moment coefficients as

$$\langle u \rangle_1 = \frac{1 + i\Omega\beta_w}{\kappa + (1 + i\Omega)(1 + i\Omega\beta_w)}, \quad \langle \dot{u} \rangle_1 = i\Omega \langle u \rangle_1, \tag{5.6}$$

which is simply the subthreshold response evaluated at $\omega = \Omega$. Substituting these first moments into the general equation for the dynamic upcrossing-rate response due to current modulation from the passive dynamic chapter (3.10) yields

$$\frac{r_{1c}}{r_0} = \frac{1 + i\Omega\beta_w}{\kappa + (1 + i\Omega)(1 + i\Omega\beta_w)} \left(\frac{u_{\mathrm{th}}}{\sigma_u^2} + \frac{i\Omega}{\sigma_{\dot{u}}} \sqrt{\frac{\pi}{2}} \right), \tag{5.7}$$

with the steady-state variances provided in the previous chapter by (4.12) and (4.13). The low- and high-frequency limits are both finite and given by

$$\Lambda_0 = \frac{u_{\mathrm{th}}}{\sigma_u^2(\kappa + 1)}, \quad \Lambda_\infty = \frac{1}{\sigma_{\dot{u}}} \sqrt{\frac{\pi}{2}}, \tag{5.8}$$

which differ subtly from the passive point neuron (3.20) in the presence of κ in Λ_0 and the different value of $\sigma_{\dot{u}}$ due to the quasi-active parameters (4.13).

Increasing β_w increases the amplitude of the upcrossing-rate response and allows for a resonant peak, Figure 5.1(a). When there is such as resonance there can also be a phase zero, which increases in frequency with β_w, Figure 5.1(b). Con-

vergence to the passive response seen in Chapter 3, is attained as $\beta_w \to \infty$, causing the resonant peak and phase zero frequencies to converge zero. Another passive limit is obtained as $\beta_w \to 0$, when the active current responds instantaneously to changes in potential. Substituting $w = u$ into (5.3) shows that this reduces the effective timescale by a factor of $1 + \kappa$, which, given that σ_u^2 is fixed, is also the factor by which Λ_0 is reduced in comparison to the passive point neuron (3.20).

In comparison with the subthreshold response, phase zeros are attained more easily and are at a similar frequency except for high κ and low β_w, Figure 5.1(c, d). This similarity of the phase zeros between the subthreshold response and the current modulation upcrossing-rate response agrees with the analysis in [105–107]. Furthermore, we can also see that $\kappa \sim 0.5$ and $\beta_w > 1$ yields subthreshold and upcrossing phase zeros with frequencies 1-10 Hz, similar to experimental findings for I_h resonance and lying in the theta frequency band [60–62].

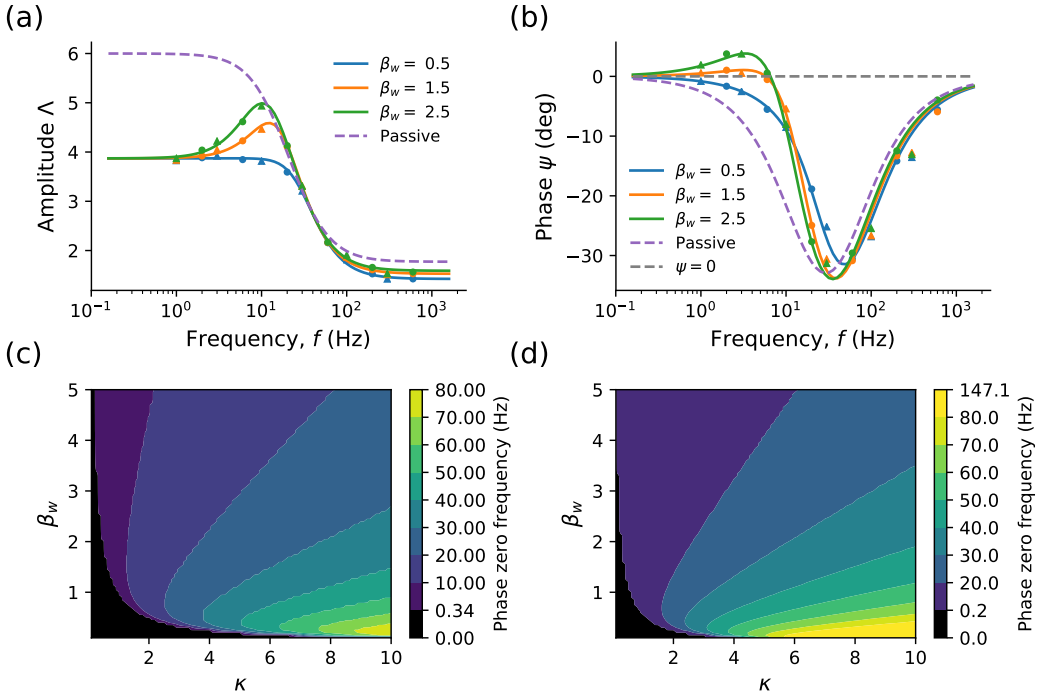

Figure 5.1: For current modulation applied to the quasi-active point-neuron model, as β_w decreases, (a) the resonance and (b) the phase zero of the firing-rate response gradually disappear. (c) The subthreshold response (5.2) shows a phase zero for higher β_w and κ which increases with both parameters. (d) In comparison, with current modulation the minimum β_w and κ for phase zeros is lower and the phase zero frequency for low β_w and higher κ is higher. The solid lines of (a, b) and the phase zero contours of (d) represent the theoretical upcrossing-rate response (5.7), the dashed lines the response for the passive model (3.19), while circles and triangles denote upcrossing and threshold-reset simulations respectively. Other parameters: (a-d) $\tau_v = 10\text{ms}$, $\tau_s = 5\text{ms}$, $u_{\text{th}}/\sigma_u = 3$, (a-b) $\kappa = 0.55$.

5.2.3 Point Neuron, Synaptic Mean Modulation

For synaptic mean modulation applied to a quasi-active point neuron, we have

$$\frac{\mathrm{d}u}{\mathrm{d}t} = -u + s - \kappa w + \frac{\epsilon_m}{1 + i\Omega\beta_s} e^{i\Omega t}, \quad \beta_w \frac{\mathrm{d}w}{\mathrm{d}t} = u - w, \tag{5.9}$$

$$\beta_s \frac{\mathrm{d}s}{\mathrm{d}t} = -s + \sigma_s \sqrt{2\beta_s}\xi_s(t). \tag{5.10}$$

From the prior calculation of the first-moment coefficients for current modulation, it is straightforward to see that for synaptic mean modulation we simply divide $\langle u \rangle_1$

and $\langle \dot{u} \rangle_1$ by $1 + i\Omega\beta_s$, giving

$$\langle u \rangle_1 = \frac{1 + i\Omega\beta_w}{[\kappa + (1 + i\Omega)(1 + i\Omega\beta_w)](1 + i\Omega\beta_s)}, \quad \langle \dot{u} \rangle_1 = i\Omega \langle u \rangle_1. \tag{5.11}$$

Substituting these first moments into general dynamic upcrossing response for mean modulation (3.10) gives

$$\frac{r_{1m}}{r_0} = \frac{1 + i\Omega\beta_w}{(1 + i\Omega\beta_s)[\kappa + (1 + i\Omega)(1 + i\Omega\beta_w)]} \left(\frac{u_{\text{th}}}{\sigma_u^2} + \frac{i\Omega}{\sigma_{\dot{u}}} \sqrt{\frac{\pi}{2}} \right). \tag{5.12}$$

As we saw for mean modulation in the passive point neuron, the synaptic filtering has the effect of making the high-frequency limit of the amplitude tend to zero with phase $\psi_\infty = -\pi/2$.

We see in Figure 5.2(a) that the resonant peak is at approximately the same position as in current modulation, but that the peak is of a lower amplitude. Similarly in Figure 5.2(b) we see that phase zeros still exist, but at much lower frequencies than current modulation. Looking more closely at the theoretically predicted phase zeros for two values of β_s in Figure 5.2 (c, d), we see that the phase zeros are at lower frequencies compared with current modulation across the whole quasi-active parameter range (β_w, κ). Furthermore, a higher value of β_w is required for the existence of phase zeros, meaning that for $\kappa \sim 0.5$, $\beta_w > 3$ is required to achieve theta-band phase zeros.

In addition, increasing β_s translates the region that allows phase zeros to higher values of β_w, with $\beta_w > \beta_s$ a necessary (but not sufficient) condition for phase zeros. This can be inferred from (5.11): we need the rising phase numerator term of $(1 + i\Omega\beta_w)$ to be active at low frequencies before the falling phase denominator term of $(1 + i\Omega\beta_s)$ in order to get a temporary phase increase in $\langle u \rangle_1$. Recalling from section 3.2.2 that it was not possible to achieve a phase zero from the passive point neuron with synaptic mean modulation when the upcrossing approximation applies, it is therefore only possible via linearised restorative currents to achieve a phase zero.

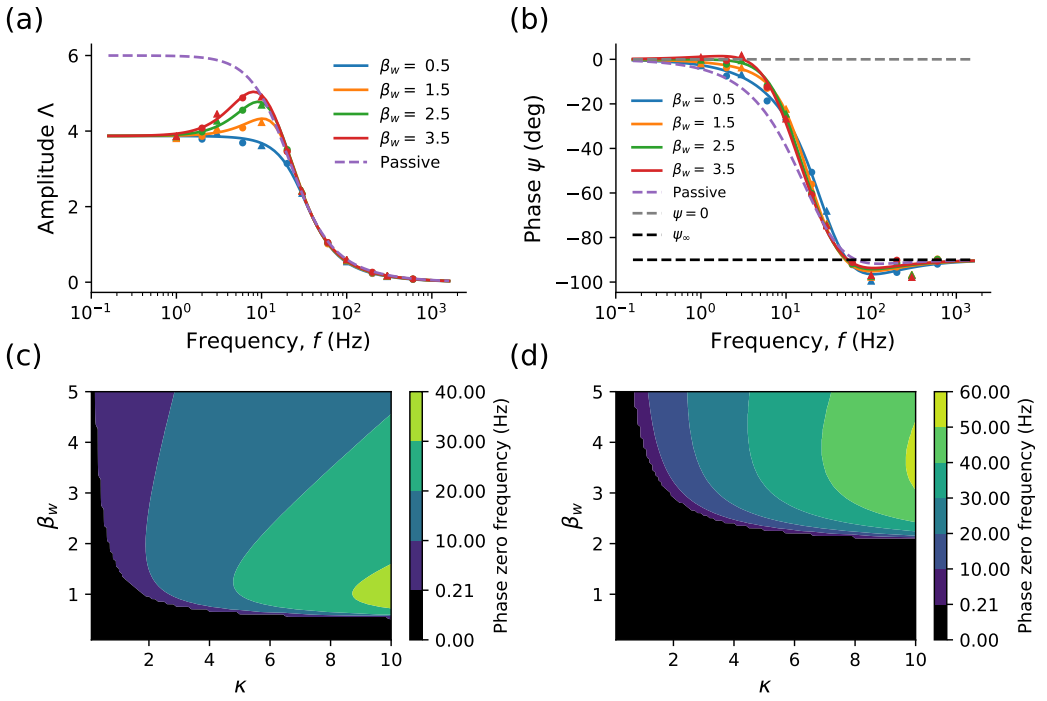

Figure 5.2: With synaptic mean modulation applied to the quasi-active point-neuron model, as β_w decreases, the (a) resonance and (b) phase zero of the firing-rate response gradually disappear. (c) When $\beta_s = 0.5$ the existence of a phase zero requires larger κ and especially β_w than for current modulation. (d) With $\beta_s = 2.0$, the region of (β_w, κ) that allows phase zeros is translate to higher β_w. Solid lines and the phase zero contours represent the theoretical upcrossing-rate response (5.12), dashed lines the passive response (3.24), while circles and triangles denote upcrossing and threshold-reset simulations respectively. Other parameters: (a-d) $\tau_s = 5$ms, $u_{\text{th}}/\sigma_u = 3$ (a-b) $\tau_v = 10$ms, $\kappa = 0.55$.

5.2.4 Point Neuron, Variance Modulation

With variance modulation applied to the cable, the response for u is

$$u(t) = \frac{\sigma_s\sqrt{2\beta_s}}{2\pi}\int_{-\infty}^{\infty}\frac{\tilde{Z}(\omega)[\tilde{\xi}_s(\omega)+\epsilon_v\tilde{\xi}_s(\omega-\Omega)]}{1+i\omega\beta_s}e^{i\omega t}\mathrm{d}\omega, \tag{5.13}$$

from which, following a same procedure as the passive membrane (see section 3.2.3), we can extract $[\sigma_u^2]_1$ as

$$[\sigma_u^2]_1 = \frac{2\sigma_s^2\beta_s}{\pi}\int_{-\infty}^{\infty}\frac{\tilde{Z}(\omega)\tilde{Z}(\Omega-\omega)}{1+i\Omega\beta_s+\omega(\omega-\Omega)\beta_s^2}\mathrm{d}\omega, \tag{5.14}$$

and similarly for $[\sigma^2_{\dot{u}}]_1$ and $[\sigma_{u\dot{u}}]_1$ by multiplying the integrand of (A.76) by $\omega(\omega-\Omega)$ and $i\omega$ respectively. These variances can be calculated in closed form, but are algebraically verbose so we refer the reader to Appendix A.4.4 (A.76, A.80, A.83) for their exact form. With all the oscillatory variances, we can calculate the dynamic upcrossing-rate response r_{1v}/r_0 using the general formula in Chapter 3 (3.15). The low- and high-frequency limits have the same form as the passive point neuron (3.36, 3.38) with

$$\Lambda_0 = \frac{u^2_{\text{th}}}{[\sigma^2_u]_0}, \quad \Lambda_\infty = \frac{2\sigma^2_s}{\Omega\beta_s[\sigma^2_{\dot{u}}]_0}, \quad \psi_\infty = -\frac{\pi}{2}. \tag{5.15}$$

Furthermore, unlike current and synaptic mean modulation and like variance modulation for passive models (section 3.2.3), a peak higher than the low-frequency limit Λ_0 is not observed in the quasi-active point neuron for $u_{\text{th}}/[\sigma_u]_0 = 3$. However, for strong coupling κ, a sharp high-frequency peak in Λ lower than the low-frequency limit Λ_0 emerges. The frequency and sharpness of this peak increases with κ, and this peak also has the effect of increasing the half-amplitude frequency $\Omega_{1/2}$ as shown later by the dashed lines in Figure 5.5(a). However, it is important to note that this peak does not cause a phase zero, as shown in Figure 5.5(b).

The cause of both this lack of resonance and this high-frequency peak is due to r_{1v}/r_0 being dominated by the r_{13} term of variance modulation (3.15), as is the case when $u_{\text{th}}/[\sigma_u]_0$ is high enough for the upcrossing approximation to valid. The only Ω-dependent part of r_{13} is $[\sigma^2_u]_1$, which acts as a low-pass filter with a high-frequency peak for higher κ. Intuition as to why $[\sigma^2_u]_1$ has this high-frequency peak can be gained from the behaviour of the shifted subthreshold response $\tilde{Z}(\Omega-\omega)$ in (A.76). We saw that $\tilde{Z}(\omega)$ has a phase zero, and thus a resonant peak, in Figure 5.1(c). Shifting this peak by Ω can make the minimum of $|\tilde{Z}(\Omega-\omega)|$ and maximum of $|\tilde{Z}(\omega)|$ overlap, leading to the minimum in $[\sigma^2_u]_1$, or make the maxima overlap, leading to the maximum in $[\sigma^2_u]_1$ (see Appendix C.4.1).

5.3 Quasi-Active Infinite Dendrite Modulation

5.3.1 Infinite Dendrite, Local Current Modulation

For current modulation applied at a single location x_c, the response at $x = 0$ is given in terms of the Green's function as we saw for the passive dendrite, $\langle u\rangle_1 =$

$\tilde{\mathcal{G}}(0, x_c; \Omega)$. Where for the infinite quasi-active dendrite we have

$$\tilde{\mathcal{G}}(x, y; \omega) = \frac{e^{-|x-y|\gamma_h}}{2\gamma_h}. \tag{5.16}$$

Substituting the first moments into (3.10), this means that the dynamic upcrossing-rate response for local current modulation is

$$\frac{r_{1c}}{r_0} = \frac{e^{-|x_c|\Gamma_h}}{2\Gamma_h}\left(\frac{u_{\text{th}}^2}{\sigma_u^2} + \frac{i\Omega}{\sigma_{\dot{u}}}\sqrt{\frac{\pi}{2}}\right), \tag{5.17}$$

where $\Gamma_h = \gamma_h(\Omega)$ and this has the same form as local current modulation to the passive infinite dendrite (3.44) but with Γ replaced with Γ_h.

Figure 5.3(a) shows a resonant peak for larger β_w as we saw for current modulation in the quasi-active point neuron and Figure 5.3(b) shows that there are potentially three phase zeros: a low-frequency phase zero associated arising from the active current, and two high-frequency phase zeros arising from current modulation which we saw in passive spatial models in Chapter 3.

By varying β_w and the dimensionless position of current modulation x_c, we see in Figure 5.3(c) that increasing x_c always reduces the phase zero frequency, and that this phase zero varies non-monotonically with β_w, as found previously for current and synaptic mean modulation applied to the quasi-active point neuron. We also see that the minimum value of β_w required for the first phase zero to appear increases slightly from $\beta_w \sim 1$ to $\beta_w \sim 1.3$ as x_c increases from 0 to 0.5. Conversely, for the second phase zero we see in Figure 5.3(d) that x_c has a much more profound effect similar to that seen in the passive infinite dendrite, increasing the frequency of the second phase zero until it is eliminated at $x_c \sim 0.17$. Increasing β_w lowers the frequency of this phase zero and slightly increases the maximum value of x_c that allows for it.

The fact that β_w more strongly affects the first phase zero while x_c more strongly affects the second (and also third) phase zero, forms part of a general theme we will find throughout this chapter for current modulation: quasi-active parameters (β_w, κ) mainly affect the first phase zero while morphological parameters (x_c, λ, ρ) mainly affect the high frequency phase zeros. However, there is some weak interaction of the quasi-active parameters on the higher frequency phase zeros and vice versa.

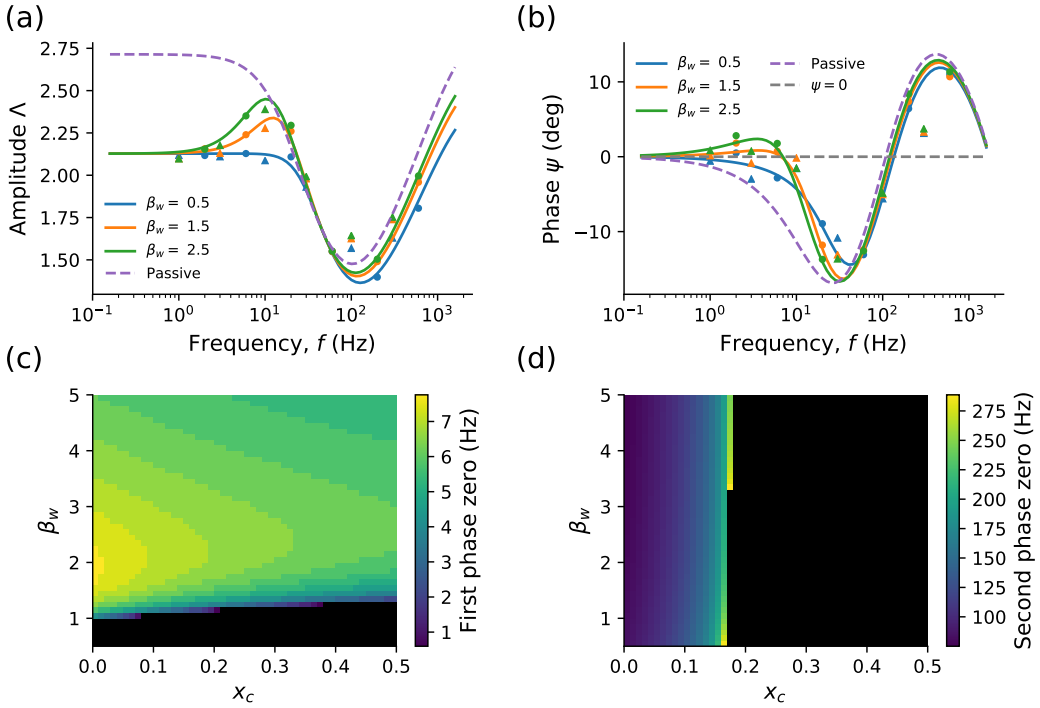

Figure 5.3: Increasing β_w for local current modulation applied to a quasi-active infinite dendrite (a) yields a resonant peak in the amplitude (b) allows for a first low-frequency phase zero and decreases the second high-frequency phase zero. (c) The first phase zero requires a slightly higher value of β_w for larger x_c. (d) The range of x_c for which the second phase zero exists is only slightly affected by β_w. Solid lines and phase zero contours are from the theoretical upcrossing-rate response (5.17), dashed lines represent the passive response (3.44), while circles and triangles represent values from upcrossing and threshold-reset simulations respectively. Other parameters: (a-d) $\lambda = 100\mu$m, $\tau_v = 10$ms, $\tau_s = 5$ms, $\kappa = 0.55$, $u_{\text{th}}/\sigma_u = 3$, (a-b) $X_c = 10\mu$m.

5.3.2 Infinite Dendrite, Synaptic Mean Modulation

As in the passive case, we can obtain the dynamic mean coefficient for the quasi-active infinite dendrite by taking Fourier transforms in space and time. Inverting this and then taking the expectation yields

$$\langle u(x,t)\rangle = \frac{\epsilon_m}{1+i\Omega\beta_s}\int_{-\infty}^{\infty} e^{ikx}\mathrm{d}k \int_{-\infty}^{\infty} \frac{(1+i\omega\beta_w)\delta(\omega-\Omega)\delta(k)}{(1+i\omega+k^2)(1+i\omega\beta_w)+\kappa} e^{i\omega t}\mathrm{d}\omega, \quad (5.18)$$

from which we can resolve the integral to give the prefactor $\langle u \rangle_1$

$$\langle u \rangle_1 = \frac{1 + i\Omega\beta_w}{(1 + i\Omega\beta_s)[(1 + i\Omega)(1 + i\Omega\beta_w) + \kappa]}. \tag{5.19}$$

As in the passive case, the quasi-active infinite dendrite with synaptic mean modulation has the same value of $\langle u \rangle_1$ as the corresponding point-neuron model. Hence the upcrossing-rate response will also have the same form as (5.12). Despite this, there are subtle differences in both the phase zeros in the dynamic response. Figure 5.4 shows that while there is a peak in Λ for the same values of β_w as the point neuron, higher β_w is required for phase zeros also to be present.

When we look at larger range of quasi-active parameters, Figure 5.4(c) shows that the cutoff frequency for both the point and infinite neuron models varies little with $\beta_w > 0.5$ and increases more notably with κ. This shows that the coupling of the linearised restorative current is more important than its timescale for the bandwidth of a quasi-active population. The phase zero frequency initially increases with β_w before peaking and also increases monotonically with κ, Figure 5.4(d). This means that quasi-active neurons with more strongly coupled restorative currents will tend to synchronise at higher frequencies.

The differences in cutoff and phase zero frequencies between the point and infinite models are small, with the infinite neuron having a < 5Hz lower cutoff and < 1Hz lower phase zero frequencies across the whole parameter range. The more significant difference between the two models is that higher values of κ and β_w are required for the infinite dendrite for the phase zero to exist.

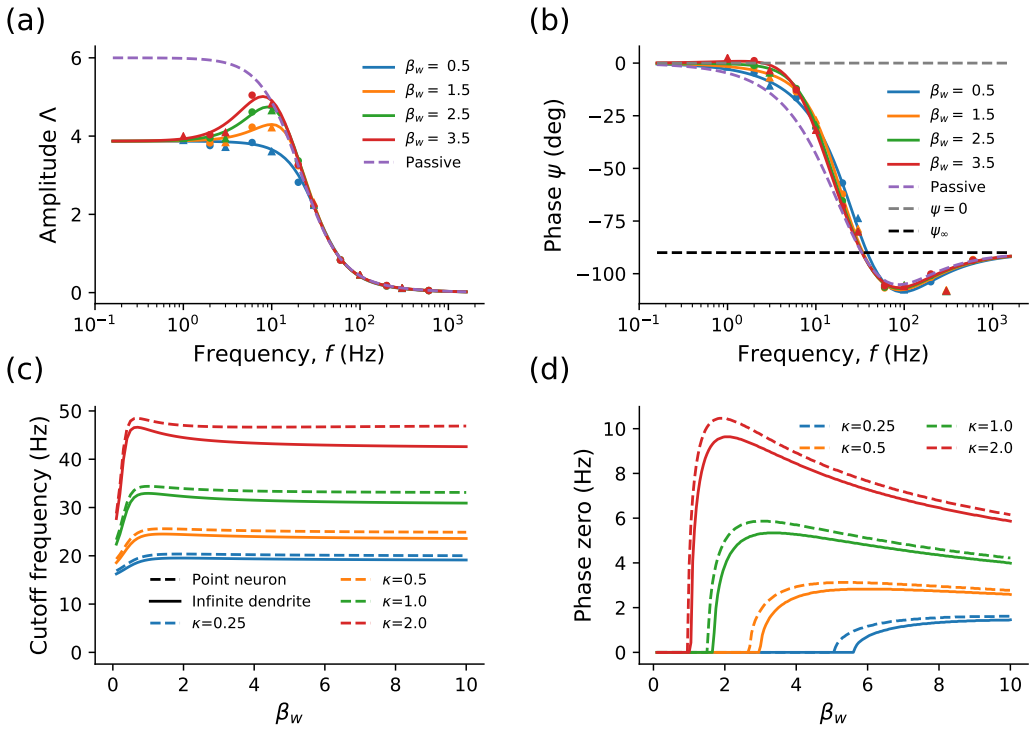

Figure 5.4: For synaptic mean modulation applied to the quasi-active infinite dendrite, as β_w decreases, (a) the amplitude resonance and (b) the phase zero of the firing-rate response disappears. Solid and dashed lines represent the theoretical quasi-active(5.12) and passive (3.24) upcrossing-rate responses respectively , while circles and triangles denote upcrossing and threshold-reset simulations respectively. (c) The cutoff frequency increases with κ but is roughly constant for $\beta_w > 0.5$. (d) The phase zero frequency initially increases with β_w before reaching a maximum. In (c, d) dashed lines show frequencies for mean modulation applied to quasi-active point neurons (5.12). Higher values of β_w and κ are required for the phase zero for the infinite dendrite compared to the point neuron. Other parameters: (a-d) $\beta_s = 0.5$, $u_{\text{th}}/\sigma_u = 3$, (a-b) $\kappa = 0.55$.

5.3.3 Infinite Dendrite, Variance Modulation

For spatially extended neurons, we recall from Chapter 3 that coefficients for the dynamic variances are given by (3.80, 3.82, 3.83). Denoting $\gamma_h(\Omega - \omega) = \overline{\Gamma}_h$ and $\overline{z}_h = \gamma_h + \overline{\Gamma}_h$, we show the calculation of $[\sigma_u^2]_1$ for the quasi-active dendrite as an

illustrative example

$$[\sigma_u^2]_1 = \frac{4\sigma_s^2\beta_s}{\pi}\int_{-\infty}^{\infty}\mathrm{d}\omega\int_{-\infty}^{\infty}\frac{\tilde{\mathcal{G}}(x,y;\omega)\tilde{\mathcal{G}}(x,y;\Omega-\omega)}{1+\omega(\omega-\Omega)\beta_s^2+i\Omega\beta_s}\mathrm{d}y$$
$$= \frac{2\sigma_s^2\beta_s}{\pi}\int_{-\infty}^{\infty}\frac{\mathrm{d}\omega}{\overline{z}_h\gamma_h\overline{\Gamma}_h[1+\omega(\omega-\Omega)\beta_s^2+i\Omega\beta_s]}. \tag{5.20}$$

As in the passive membrane case and the quasi-active point neuron, $[\sigma_{\dot{u}}^2]_1$ and $[\sigma_{u\dot{u}}]_1$ can be obtained by multiplying the integrand by $\omega(\omega-\Omega)$ and $i\omega$ respectively.

For the quasi-active infinite dendrite, the amplitude and phase of the firing-rate response for variance modulation are generally similar to that seen for the quasi-active point neuron. We observe in Figure 5.5(c, d) that for high κ a peak in Λ and ψ emerges at high frequencies, as in the point neuron, Figure 5.5(a,b). Compared with the point neuron, these peaks are less prominent. This is not because Λ is lower at the peaks for the infinite dendrite, but rather because the preceding minimum is higher. This is due to the slower decay in amplitude for the infinite dendrite, as we saw in the passive case for the higher cutoff frequency when $\beta_s > 1$ (section 3.3.3).

The increase in half amplitude frequency is still retained, shown by the dashed line for $\frac{1}{2}\Lambda_0$ in Figure 5.5(c). Closer examination of the change in Λ with κ reveals that the cutoff frequency Ω_c decreases despite $\Omega_{1/2}$ increasing. Thus, depending on the decay in amplitude which counts as the neuronal population faithfully encoding the modulating signal, one can either consider stronger quasi-active coupling to increase (from $\Omega_{1/2}$) or decrease (from Ω_c) the bandwidth. We will refer to this effect as increasing the *dampened* bandwidth of the firing-rate response.

At high frequencies the phase responses for the point and infinite neurons also differ, with the high-frequency limits unchanged from their passive values of $\psi_\infty = -\pi/2$ for the point neuron and $\psi_\infty = -\pi/4$ for the infinite dendrite, Figure 5.5 (b, d).

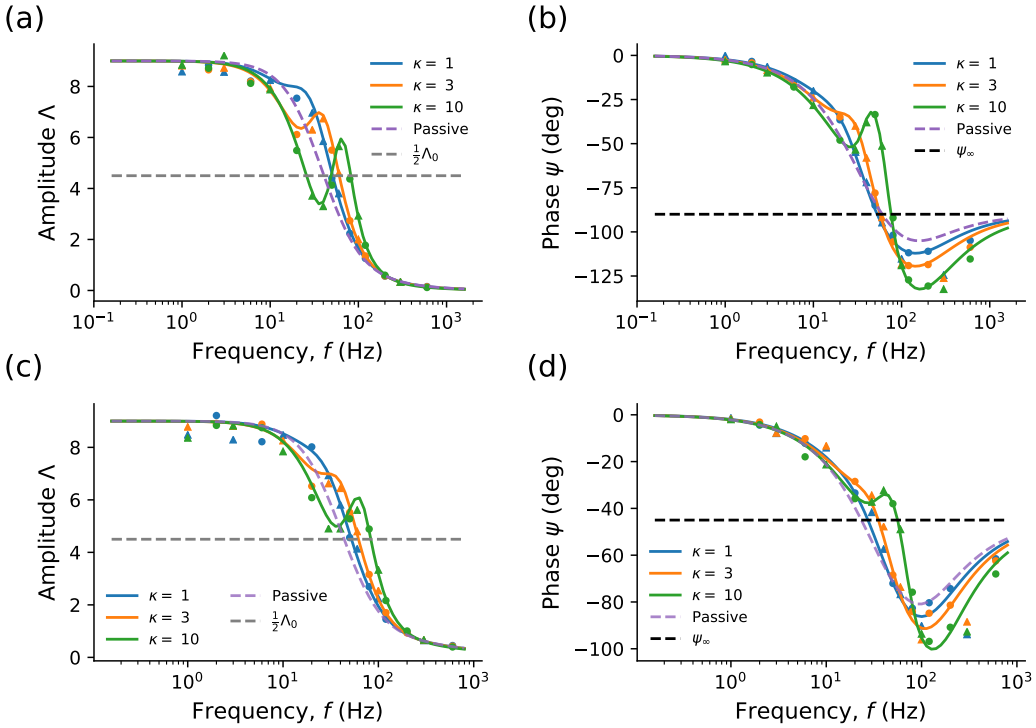

Figure 5.5: For variance modulation, (a, c) amplitude and (b, d) phase peaks appear when κ is large, and occur at similar frequencies for the (a, b) quasi-active point neuron and (c, d) infinite dendrite. These peaks in amplitude and phase are more prominent for the point neuron, however the half-amplitude ($\Lambda = \frac{1}{2}\Lambda_0$) dampened bandwidth increases in both cases. Solid and dashed lines denote the theoretical quasi-active and passive upcrossing-rate responses (3.15) respectively, while circles and triangles represent upcrossing and threshold-reset simulations respectively. Other parameters: (a-d) $\beta_w = 2.5$, $\beta_s = 0.5$, $u_{\text{th}}/[\sigma_u]_0 = 3$, (c-d) $\lambda = 100\mu$m.

Since further morphological factors such as a substantial soma and an axon will add a further passive load to the neuron, we can predict (and have verified, see Appendix C.4) that this quasi-active amplitude and phase peak will only be dampened for more complex morphologies. In addition, we saw in Chapter 3, that the effects of a substantial soma and an axon had very minor effects on variance modulation in the passive neuron. We will therefore not include variance modulation for other quasi-active neuronal morphologies in this chapter.

5.4 Quasi-Active Ball-and-Stick Modulation

5.4.1 Ball-and-Stick Model, Local Current Modulation

Based on the calculation of the first-moment coefficients for the passive ball-and-stick neuron, we can deduce that $\langle u \rangle_1$ and $\langle \dot{u} \rangle_1$ are as in the passive case (3.68) but with Γ_1 replaced with Γ_{h1}. For current modulation at the soma therefore

$$\langle u \rangle_1 = \frac{\rho}{\rho \Gamma_{h1} + \Gamma_\sigma^2}, \quad \Gamma_\sigma^2 = 1 + i\Omega\beta_\sigma, \tag{5.21}$$

and hence the upcrossing-rate response is given by

$$\frac{r_{1c}}{r_0} = \frac{\rho}{\rho \Gamma_{h1} + \Gamma_\sigma^2} \left(\frac{u_{\text{th}}}{\sigma_u^2} + \frac{i\Omega}{\sigma_{\dot{u}}} \sqrt{\frac{\pi}{2}} \right). \tag{5.22}$$

While for the passive neuron we only observed a single phase zero, the quasi-active resonance at lower frequencies that means that two phase zeros can now be present. As in the passive case, we changed the dendritic dominance factor ρ to see the effect of neuronal size on these phase zeros. Figure 5.6 shows that decreasing ρ (a larger soma) leads to the lower phase zero decreasing and the higher phase zero increasing, with both eventually disappearing when ρ becomes sufficiently small. The former effect can be intuitively explained by the fact that the soma is passive with no quasi-active current, hence decreasing ρ increases the ratio of passive to quasi-active load conductance. Further, we see that in (5.21) that decreasing ρ makes the $\rho\Gamma_{h1}$ term less important than the Γ_σ^2 term.

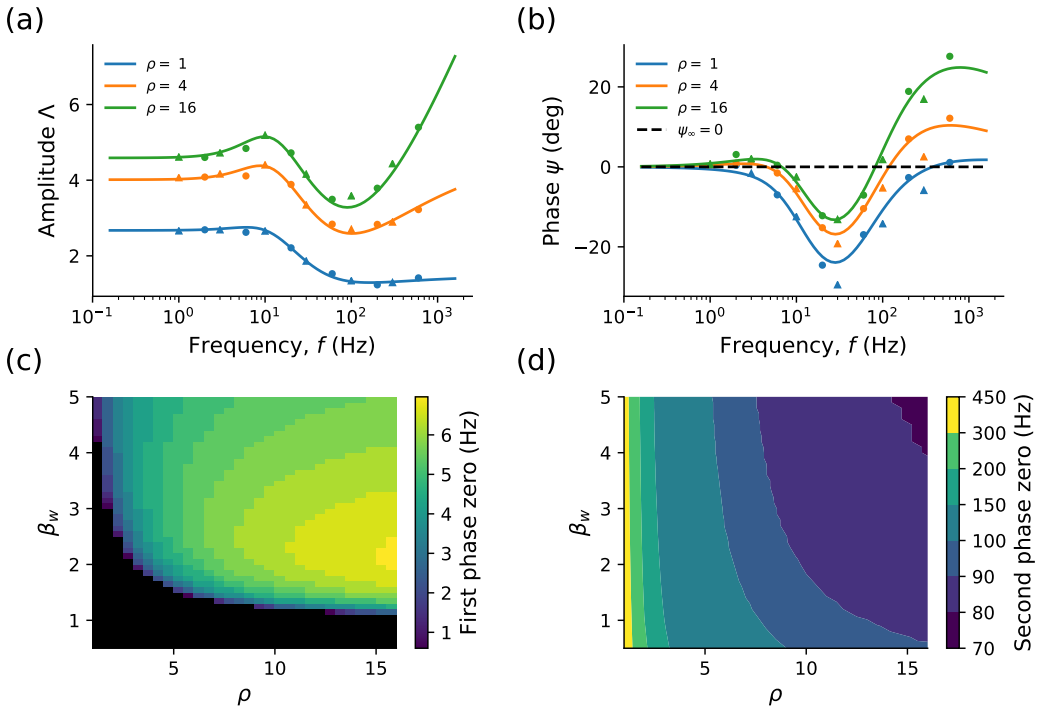

Figure 5.6: For current modulation applied to the soma of a quasi-active ball-and-stick neuron, a larger soma (a) lowers the firing rate amplitude across all frequencies and (b) eventually eliminates both the low- and high-frequency phase zeros. (c) A higher value of β_w is required for the first phase zero with a larger soma. (d) Increasing ρ increases the frequency of the second phase zero towards that seen for the semi-infinite dendrite, while lowering β_w has a slight lowering effect most noticeable at low ρ. Solid lines and phase zero contours are from the theoretical upcrossing-rate response (5.22) while circles and triangles denote upcrossing and reset simulations respectively. Other parameters: (a-d) $\beta_\sigma = 7/6$, $\beta_s = 0.5$, $u_{\text{th}}/\sigma_u = 3$, $\kappa = 0.55$, (a-b) $\beta_w = 2.5$.

5.4.2 Ball-and-Stick Model, Synaptic Mean Modulation

With synaptic mean modulation, substitution of Γ_1 with Γ_{h1}, means that the first-moment coefficient at the soma is given by

$$\langle u \rangle_1 = \frac{\rho}{\Gamma_{h1}(1 + i\Omega\beta_s)(\rho\Gamma_{h1} + \Gamma_\sigma^2)}, \tag{5.23}$$

and hence for the upcrossing-rate response

$$\frac{r_{1m}}{r_0} = \frac{\rho}{\Gamma_{h1}(1 + i\Omega\beta_s)(\rho\Gamma_{h1} + \Gamma_\sigma^2)} \left(\frac{u_{\text{th}}}{\sigma_u^2} + \frac{i\Omega}{\sigma_{\dot{u}}} \sqrt{\frac{\pi}{2}} \right). \tag{5.24}$$

As in previous cases for synaptic mean modulation applied to quasi-active structures, both a resonant peak and phase zero can be attained for higher β_w and κ. Here we show the effect of the relative somatic size, parametrised by ρ, on this firing-rate resonance. Like the passive case, Figure 5.7(a) shows that decreasing ρ reduces Λ at all frequencies, including the resonant peak. While Figure 5.7(b) illustrates that the phase zero can be reduced in frequency then eliminated with lower ρ.

When investigating these effects in more detail, we first see in Figure 5.7(c) that the quality factor increases with ρ, demonstrating that both the relative and absolute resonant peak amplitude are affected by somatic size. Next we find in Figure 5.7(d) that the phase zero increases with ρ and that a lower value of κ is required for the phase zero to exist. Both of these increasing trends saturate towards the limit given by a semi-infinite dendrite and can be intuitively explained by the fact that decreasing ρ increases the relative proportion of passive conductance to the neuron. Furthermore, given that $\beta_\sigma \sim 1$, the frequency at which $\angle\, \Gamma_\sigma^2 = -\pi/4$ is $\sim$ 16Hz, which is close enough to the quasi-active resonant frequency to have an impact.

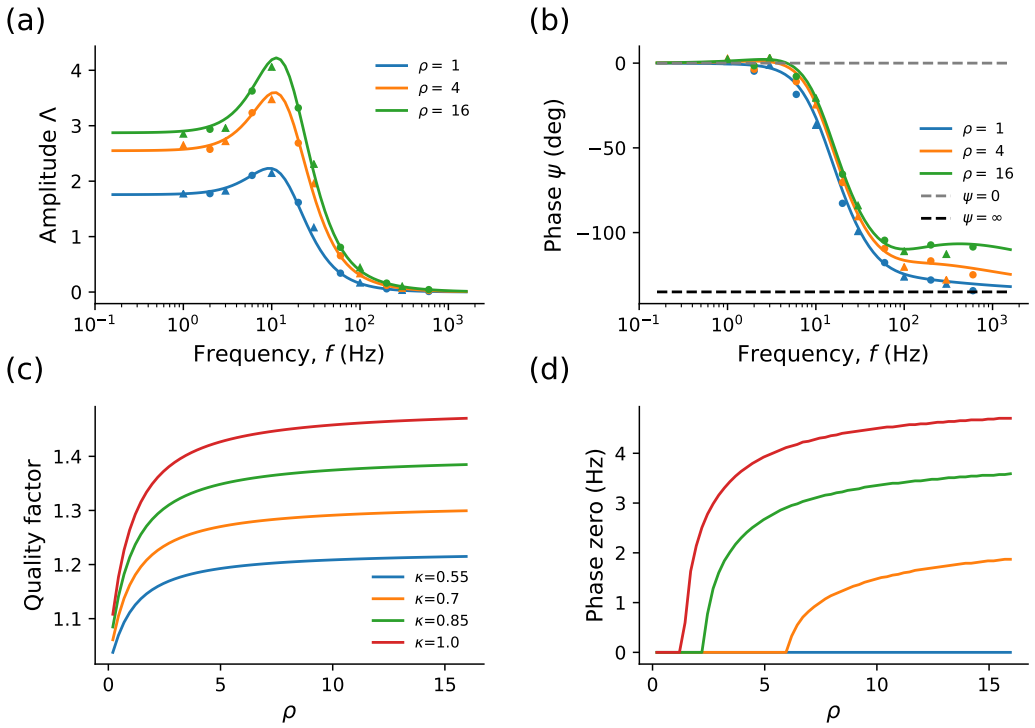

Figure 5.7: With synaptic mean modulation applied to the quasi-active ball-and-stick neuron, decreasing ρ (a) decreases the amplitude at all frequencies, and (b) decreases the phase at all frequencies, lowering the phase zero frequency. (c) Closer inspection of the amplitude shows that the quality factor of the resonant peak increases with ρ for a range of κ. (d) Decreasing ρ and κ decreases the phase zero frequency and eventually eliminates it entirely. Solid lines show the theoretical upcrossing-rate response (5.24) while circles and triangles denote upcrossing and threshold-reset simulations respectively. Other parameters: (a-d) $\beta_w = 2.5$, $\beta_\sigma = 7/6$, $\beta_s = 0.5$, $u_{\text{th}}/\sigma_u = 3$ (a-b) $\kappa = 1$.

5.5 Quasi-Active Dendrite-and-Axon Modulation

5.5.1 Dendrite-and-Axon, Local Current Modulation

With the dendrite-and-axon model, we apply current modulation at the nominal soma ($x = 0$) where the two neurites meet as in the passive neuron. We can obtain the coefficient for the modulated mean by replacing Γ_1 in the passive dendrite-and-axon model (3.85) with Γ_{h1} to yield

$$\langle u \rangle_1 = \frac{\beta_\alpha^2 \lambda_1^3 e^{-x_{\text{th}}\Gamma_\alpha}}{\beta_\alpha^2 \lambda_1^3 \Gamma_{h1} + \lambda_\alpha^3 \Gamma_\alpha}, \tag{5.25}$$

giving the dynamic upcrossing-rate response as

$$\frac{r_{1c}}{r_0} = \frac{\beta_\alpha^2 \lambda_1^3 e^{-x_{\text{th}}\Gamma_\alpha}}{\beta_\alpha^2 \lambda_1^3 \Gamma_{h1} + \lambda_\alpha^3 \Gamma_\alpha} \left(\frac{u_{\text{th}}}{\sigma_u^2} + \frac{i\Omega}{\sigma_{\dot{u}}} \sqrt{\frac{\pi}{2}} \right). \tag{5.26}$$

As in the passive dendrite-and-axon model and the quasi-active infinite dendrite, we vary the separation between point of modulation and the trigger position X_{th}. Figure 5.8(a) shows the amplitude starts decaying at lower frequencies after the resonant sag for higher X_{th}, while the phase in Figure 5.8(b) shows that the low-frequency phase zero is far less affected by X_{th} than the second phase zero.

Looking at these phase zeros more closely as a function of the dimensionfull trigger position X_{th} and β_w, we see in Figure 5.8(c) that larger X_{th} causes higher β_w to be required for the first phase zero. In contrast to current modulation in the quasi-active infinite dendrite (Figure 5.3(c)), we note that x_{th} has a more significant effect on the minimal β_w required and the reduction on the phase zero frequency. Figure 5.8(d) reveals that the second phase zero is eliminated for $x_{\text{th}} \gtrsim 0.18$. While β_w has an almost unnoticeable effect on the existence of the second phase zero, like the infinite dendrite, increasing β_w lowers its frequency.

The reason why x_{th} in the quasi-active dendrite-and-axon model has a different effect on the dynamic response than x_c in the quasi-active infinite dendrite is due to the presence of Γ_α in the exponent rather than Γ_{h1}. This makes the spatial filtering effect passive rather than quasi-active. Since $|\Gamma_\alpha| < |\Gamma_{h1}|$ for low frequencies and $|\Gamma_\alpha| > |\Gamma_{h1}|$ at high frequencies (given $\beta_\alpha > 1$), this makes the spatial filtering effect stronger for the dendrite-and-axon model near the first phase zero and weaker near the second phase zero.

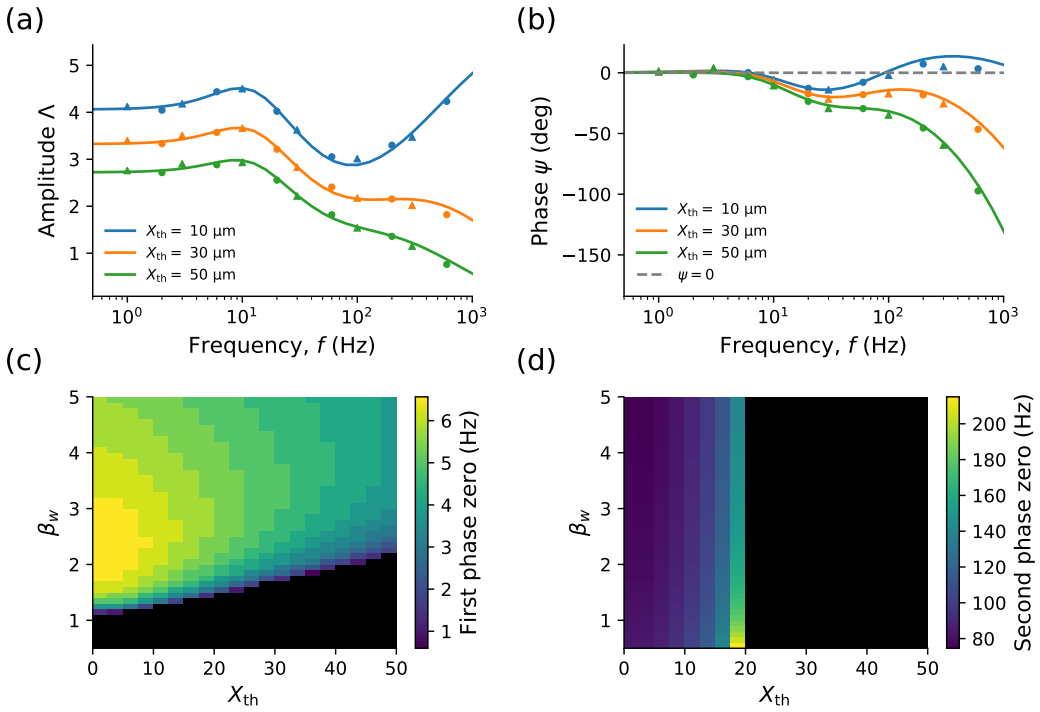

Figure 5.8: For current modulation applied locally to the quasi-active dendrite-and-axon model, increasing the trigger position: (a) decreases the amplitude across all frequencies and initiates high-frequency decay sooner, (b) reduces the phase at all frequencies, eventually removing (c) the low-frequency phase zero and (d) the high-frequency phase zero. Solid lines and phase zero contours are from the theoretical upcrossing-rate response (5.26), while circles and triangles denote upcrossing and threshold-reset simulations respectively. Other parameters: $\lambda_1 = 200\mu$m, $\lambda_\alpha = 100\mu$m, $\beta_\alpha = 7/6$, $\beta_w = 2.5$ $\kappa = 0.55$, $\beta_s = 0.5$, $u_{\rm th}/\sigma_u = 3$.

5.5.2 Dendrite-and-Axon, Synaptic Mean Modulation

With synaptic mean modulation, substitution of Γ_{h1} for Γ_1 in (3.87) gives the oscillatory mean coefficient as

$$\langle u \rangle_1 = \frac{\beta_\alpha^2 \lambda_1^3 e^{-x_{\rm th}\Gamma_\alpha}}{(1 + i\Omega\beta_s)(\beta_\alpha^2 \lambda_1^3 \Gamma_{h1}^2 + \lambda_\alpha^3 \Gamma_\alpha \Gamma_{h1})}, \tag{5.27}$$

therefore giving the dynamic upcrossing-rate response as

$$\frac{r_{1m}}{r_0} = \frac{\beta_\alpha^2 \lambda_1^3 e^{-x_{\rm th}\Gamma_\alpha}}{(1 + i\Omega\beta_s)(\beta_\alpha^2 \lambda_1^3 \Gamma_{h1}^2 + \lambda_\alpha^3 \Gamma_\alpha \Gamma_{h1})} \left(\frac{u_{\rm th}}{\sigma_u^2} + \sqrt{\frac{\pi}{2}} \right). \tag{5.28}$$

In comparison with the infinite dendrite, we see that by setting $x_{\rm th} = 0$ in (5.27) that the quasi-active influence on the frequency response for the dendrite-and-axon

model is lessened in comparison by the $\Gamma_\alpha \Gamma_{h1}$ term in the denominator, especially in terms of the phase. Letting $\lambda_\alpha \to 0$ on the other hand yields the response for the infinite dendrite (5.19)

As in previous cases for synaptic mean modulation, we observe in Figure 5.9(a, b) that there is an amplitude peak and potentially a phase zero associated with the quasi-active current. By adjusting β_w and X_{th}, one can show that the quality factor Q decreases with increasing X_{th} and decreasing β_w but these variations are generally quite small.

As in previous comparisons between current and synaptic mean modulation, the phase zero requires higher β_w or κ to exist due to synaptic filtering. Thus we expect that the dependence of the phase zero on x_{th} and β_w to be similar to that seen for current modulation in Figure 5.8(c), with increasing x_{th} leading to higher β_w required for the phase zero. This is shown in Figure 5.9(d), with $\beta_w > 5.5$ required for phase zeros even for $X_{\text{th}} = 0$.

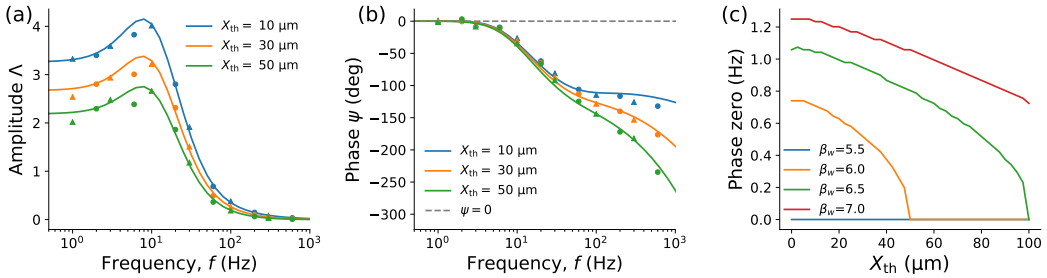

Figure 5.9: For synaptic mean modulation applied to the quasi-active dendrite-and-axon model, increasing the trigger position decrease both the (a) amplitude and (b) phase at all frequencies. (c) Slow active currents ($\beta_w > 5.5$) are required for phase zeros and the phase zero frequency decreases with increasing X_{th}. Solid lines show the theoretical upcrossing-rate response (5.28) while circles and triangles indicate upcrossing and threshold-reset simulations respectively. Other parameters: (a-c) $\lambda_1 = 200\mu\text{m}$, $\lambda_\alpha = 100\mu\text{m}$, $\beta_\alpha = 7/6$, $\kappa = 0.55$, $\beta_s = 0.5$, $u_{\text{th}}/\sigma_u = 3$, (a-b) $\beta_w = 3.5$.

5.6 Summary

For all the models studied in this chapter, the dynamic firing-rate response for synaptic mean modulation showed a low-frequency resonant peak enabled by similar quasi-active parameters as the subthreshold voltage resonance (sections 5.2.3, 5.3.2, 5.4.2, 5.5.2). Occurring at 1-10 Hz, this quasi-active resonance lies in the range of the experimentally observed resonance in some pyramidal cells [60–62] and theta oscillations [144, 162]. A phase zero did not always exist with a resonant peak

however, and spatial extent made the phase zero more difficult to attain due to the higher derivative variance $\sigma_{\dot{u}}^2$. This resonance was never observed for variance modulation due to the fact that the oscillatory variances are calculated by a convolution of the subthreshold response (section 5.2.4).

With current modulation applied to a single location in a spatial model (sections 5.3.1, 5.4.1, 5.5.1), two additional high-frequency phase zeros are possible like the passive models in Chapter 3, in addition to a low-frequency quasi-active phase zero. The values of these high-frequency phase zeros are affected slightly by the quasi-active parameters, though not to the same relative degree as the first quasi-active phase zero. Conversely, morphological parameters such as the somatic size, axonal radius and trigger position have a larger impact the high-frequency phase zeros than the low frequency phase zero. The presence of both low- and high-frequency phase zeros is of physiological relevance due to experimental evidence suggesting coexistence and coupling between theta and high-gamma oscillations in the cortex [155], which are present for spatial working memory tasks [163] and the disruption this coupling may play a role in schizophrenia [156].

For very strong coupling, an amplitude peak was observed in all models with variance modulation at high frequencies (sections 5.2.4, 5.3.3). This peak increases the half-amplitude frequency $\Omega_{1/2}$, showing that restorative active currents increase the bandwidth of neuronal populations subject to variance modulation. However, recalling that $\kappa \sim 0.1 - 2$ for I_h [57, 59], as this peak requires larger values of κ it is unclear whether this behaviour would be observed experimentally.

Chapter 6

Conclusions

While prior research either models the effect of morphology on deterministic firing [135, 164], or fluctuation-driven firing in point-neuron models [5, 7, 9, 96, 101, 151], in this thesis we have developed an approximate analytical framework to examine the effects of morphology on fluctuation-driven firing. Previous theoretical studies in this area are sparse, usually limited to calculation of the subthreshold moments [77, 125], two-compartment rather than spatially continuous models [10–12], or synaptic drive applied to only a single point [126, 127].

In this thesis we have seen how a level-crossing formula based on the work of Rice [110], can be extended from point-neuron models, as done by Tchumatchenko [111] and Badel [9], to approximate the fluctuation-driven firing rate in spatially continuous neuron models. Furthermore, we found that spatial distribution of synaptic drive produces qualitatively different steady-state firing rates and dynamic firing-rate responses from point-neuron models for both passive and quasi-active membranes.

6.1 Steady-State Firing Rate

In Chapters 2 and 4, we showed that the steady-state fluctuation-driven firing rates in passive and quasi-active spatial neuron models have a fundamentally different form to point-neuron models (sections 2.2.3, 2.3.3, 4.2.3, 4.3.3). In contrast, the deterministic limit for spatial models where drive is distributed across the whole structure was the same, showing that firing rate is more sensitive to neuronal morphology if it is fluctuation-driven. Furthermore, for models where the mean was spatially homogeneous such as the infinite dendrite, the upcrossing and simulated firing rates at the nominal soma were independent of all spatial parameters such as

the length constant.

With models where the mean was no longer spatially homogeneous, increasing some morphological parameters, such as axonal radius (sections 2.6) and the number of dendrites (section 2.8), and the quasi-active coupling strength (sections 4.5, 4.6, 4.7), increased the mean but decreased the variance. This often led to non-monotonic variations in the upcrossing and simulated firing rates with these parameters that depended on the mean synaptic drive. The addition of an electrically substantial soma (sections 2.7, 2.8, 4.5) affected both the morphological and quasi-active parameters that maximised the fluctuation-driven firing rate, for example a larger soma increased the optimal axonal radius, number of dendrites and quasi-active coupling. There is also interaction between the quasi-active and morphological parameters for this optimum. For example, a higher coupling strength leads to a lower dendritic number and higher axonal radius that maximise fluctuation-driven firing.

These effects imply that neuronal morphology and active currents can be tuned to maximise fluctuation-driven firing. As discussed earlier, both morphology and active currents differ between cell classes [31, 32] and species [42, 159]. In particular, it would be interesting to see if there are any correlations between the morphology of the AIS and the number or strength of I_h channels.

6.2 Dynamic Response

Previous theoretical studies have largely focussed on how the type of noise [101,165] and spiking mechanisms [96,101] have affected the dynamic firing-rate response, with some focus being place on models with a few compartments [11, 12]. The research shown here in Chapters 3 and 5 shows novel insights into how spatial extent, both in the model and the distribution of the noise, affect various aspects of the dynamic firing-rate response. These include the cutoff frequency, existence of phase zeros, and the high-frequency limit.

For the dynamic response, several differences from the point-neuron model and new types of frequency responses were found for each modulation type. With current modulation applied locally, we saw that finite high-frequency phase zeros were present even for the passive membrane (sections 3.3.1, 3.5.1, 3.6.1). In addition, the frequency and existence of phase zeros were significantly altered by the spatial separation between the trigger and modulation positions, as well as the somatic size. This implies that the spatial separation between the soma and the position of AP initiation in the AIS plays a significant role in how neuronal populations process

signals and how they might synchronise. This could help explain the experimentally observed ultrafast response of cortical populations [85–87, 148].

On the other hand, in passive models synaptic mean (sections 3.2.2, 3.3.2, 3.5.2, 3.6.2) and variance modulation (sections 3.2.3, 3.3.3, 3.5.3, 3.6.3) never produced resonances or phase zeros in the region for which the upcrossing method is valid. Across various different models, variance modulation gives a cutoff frequency approximately twice that of mean modulation, in qualitative agreement with some experiments [148, 150], although the cutoff frequency in our case was much lower at around 10-30 Hz. Furthermore, for both modulation types we also found that changes to morphology such as length constants, soma size and trigger position, did not significantly alter the cutoff frequency. However with variance modulation we found different high-frequency phase limits from the point-neuron model which were significantly changed by the morphology, as summarised in Table 6.1.

The dynamic firing-rate response was substantially different for quasi-active membranes. Low-frequency resonances and phase zeros were found across all morphologies for synaptic mean (sections 5.2.3, 5.3.2, 5.4.2, 5.5.2) and local current modulation (sections 5.2.2, 5.3.1, 5.4.1, 5.5.1). Being in the 1-10Hz range, these low-frequency phase zeros are in a similar frequency range to the resonances induced by I_h in pyramidal cells [60–62] and the theta frequency band. Furthermore, we found that morphological factors such as the somatic and axonal size affect the low-frequency phase zero for local current and synaptic mean modulation, while quasi-active parameters affected the high-frequency phase zeros in current modulation. The presence of both low- and high-frequency phase zeros in the case of local current modulation is particularly interesting in light of experimentally observed cross-frequency coupling between theta and gamma bands [155, 163].

The low-frequency phase zero induced by the quasi-active parameters was not present for variance modulation however (sections 5.2.4, 5.3.3). Instead, strong quasi-active coupling for variance modulation produced a local high-frequency peak in amplitude and phase. While this effect is not usually strong enough to increase the cutoff frequency, it does increase or add an additional half-amplitude frequency. This shows that the quasi-active coupling increases the effective bandwidth of dampened signals.

Model	Local Current	Synaptic Mean	Variance
Point Neuron	0	$-\pi/2$	$-\pi/2$
Infinite Dendrite	$\pi/4$	$-\pi/2$	$-\pi/4$
Ball-and-Stick	0	$-3\pi/4$	$-3\pi/4$
Dendrite-and-Axon	undetermined	undetermined	undetermined

Table 6.1: High-frequency phase limits ψ_∞ for the dynamic upcrossing-rate responses of the spatial models examined in this thesis for each type of modulation. For the infinite dendrite the limit shown is for when the spatial separation between modulation input and the trigger position is zero. The limit shown for the dendrite-and-axon model assumes the trigger position is placed a finite distance along the axon.

6.3 Future Work

6.3.1 Separation of Synaptic Drive

In Chapter 3 we found that synaptic mean and variance modulation in the passive point neuron did not produce resonances in the same parameter range as in [9] due to the fact that we have combined both excitatory and inhibitory synaptic drive in our models. Separating the synaptic drive into excitatory and inhibitory components with their own distinct time constants would allow us to see the effect of the different time constants on the dynamic response in spatial models.

With the synaptic drive separated, one can also look at removing the Gaussian approximation and replacing the drive with a shot noise process. It has been observed that the effect of individual synaptic inputs is not always small as required by the Gaussian approximation, but can sometimes have a large effect (> 5 mV) on the transmembrane potential [166–168]. Previous theoretical research has shown that shot noise processes yield different firing-rate responses to Gaussian noise drive in point-neuron models [165, 169, 170] . Furthermore, some of the approaches in this thesis can be retained, as an upcrossing rate in response to shot noise is calculable [171]. Therefore, following the initial tests in Appendix C.1 of the Gaussian approximation in spatial models, one could examine how the firing-rate responses due to shot-noise drive are influenced by spatial structure.

6.3.2 Non-Uniform Neurites

In this thesis, all neurites were one-dimensional with uniform membrane properties and applied synaptic drive. However, in reality many of these properties will vary

along the neuritic length. One example noted in Chapter 1 is that the dendrites and axon often significantly taper in various neurons [31, 172, 173], and that cable theory has been adapted to account for tapered neurites [45–48]. Since dendritic tapering in particular is thought to have functional implications [48,174], it would be informative to see how it affects fluctuation-driven firing with synapses distributed across the tapered dendrites.

For quasi-active membranes, a non-uniformity that can be added is to generalise the distribution of linearised active currents. This can more accurately model I_h currents in pyramidal cells for example, for which the concentration in certain cell classes increases exponentially with distance from the soma [51, 57, 58]. While this would lead to additional modelling complications, such as position-dependent membrane time and length constants, it is theoretically manageable in this framework.

After separating synaptic drive into excitatory and inhibitory components, the synaptic drive can be applied non-uniformly. This can be done to represent the fact that as excitatory synapses are generally distributed across the dendrites, while inhibitory synapses are more locally focused on specific regions depending on the inhibitory cell type [23]. The different spatial filtering of distributed excitatory drive and localised inhibitory drive will alter the steady-state upcrossing rate and the dynamic upcrossing-rate response.

6.3.3 Network Structure

In this thesis we have considered spatial-neuron models representative of a population with background synaptic drive which is independent of the population-averaged firing rate. However, in neuronal networks the level of synaptic input will be affected by the population response due to recurrent activity. Research has been conducted that examines how recurrent activity affects global oscillations and synchrony in the population firing rate [5, 175–177]. Incorporating the dynamic effects of spatial extent into recurrent network models will affect network oscillations due to its effect on low- and high-frequency phase zeros of the dynamic response. Though in a recurrent network the frequency of in-phase oscillations will be complicated by propagation delays, the morphological dependence of phase zeros can, in principle, be adjusted to account for this.

Furthermore, neurons are not usually connected homogeneously but often stereotypically in motifs [167, 178, 179], which simulations have shown can create some computational differences [180]. With the synaptic drive from certain presynaptic cells in the motif localised to given areas on the postsynaptic cell, the frame-

work developed here gives a starting point to look at how spatial structure influences the firing-rate properties of neuronal motifs.

6.3.4 Population Heterogeneity

By considering our spatial-neuron model to be part of a similar population, we in effect assume that all neurons in the population have identical parameters. However, experimental research has shown there to be variation in electrophysiological parameters of pyramidal neurons of the same layer [181] and heterogeneity of the firing rate to the input statistics [182]. An extension of this work is therefore to see the effect of imposing heterogeneity onto the neuronal parameters, which as pointed out in [118] is equivalent to adding frozen noise onto the model.

6.3.5 Active Currents

We have mostly focussed on a single active current linearised in the subthreshold regime, with I_h the physiological current we have had in mind. However other subthreshold active currents can be included such as the persistent sodium current I_{Nap} [67, 68] and the slow potassium current I_{Ks} [67], as has been modelled for the point neuron in [105]. So long as the quasi-active approximation can be applied to incorporate each additional current, an arbitrary number be included in this framework.

The ion channels modelled by active currents often open randomly, adding a form of stochasticity termed channel noise to the system [183]. While the intensity of channel noise is thought to be less than from synaptic drive, it may still affect spike timing and be occasionally sufficient to initiate APs [78, 184, 185]. Various methods have been explored which incorporate channel noise into neuronal models [77, 186, 187], including in spatial models with dendrites [188, 189]. Given certain modelling assumptions such as linearity, channel noise could be included into the framework developed here.

When the active currents are highly nonlinear, for example in the spiking dynamics in the AIS or dendritic spikes, then quasi-active approximation can no longer be used. Therefore, other frameworks have been used for spatial models of nonlinear neurites [95, 190–193]. However, the voltage variances calculated for linear dendrite may still allow approximation of the firing rate in a similar manner to the point-neuron EIF model [118].

6.3.6 Experimental Application

Due to the requirement of delivering controllable spatially distributed stimulation to a neuron, it is difficult to find suitable experimental results *in vitro* or *in vivo* in the literature which correspond to the results presented here. However, recent advances in optogenetics and multiple, parallel intracellular recordings make the prospect of *in vivo*-like stimulation at arbitrary dendritic locations feasible [194–197].

These future experiments would inform us for which biophysical conditions - such as neuronal class, amplitude of synaptic drive and active currents - the various modelling assumptions made in this framework are appropriate. With these conditions established, the framework developed in this thesis would allow us to predict the firing-rate response of any neuron that satisfies them given its morphology, and hence grant insight into the fluctuation-driven functional differences between neuronal morphologies.

Appendix A

Analytical Methods

A.1 Derivation of the Upcrossing Rate

To determine the rate at which the potential $v(x,t)$ crosses a threshold value v_{th} with positive time derivative $\dot{v}$, we look at a small section in time $[t, t+\mathrm{d}t)$ for a fixed spatial position x. In this section, the curve of v crosses the value $v = 0$ (used instead of v_{th} for simplicity) between (x,t) and $(x, t+\mathrm{d}t)$. Since this time interval is small, one can assume that the derivative $\dot{v}$ is constant. Therefore, the time at which $v = 0$ is given by $t - v_i/\dot{v}$, where $v_i = v(x,t)$. This means we can write the inequality illustrated in Figure A.1a

$$t < t - v_i/\dot{v} < t + \mathrm{d}t, \tag{A.1}$$

where clearly v_i and $\dot{v}$ must have opposite signs. If we are looking at upcrossings, then we suppose that $\dot{v}$ is positive and can write

$$-\dot{v}\mathrm{d}t < v_i < 0. \tag{A.2}$$

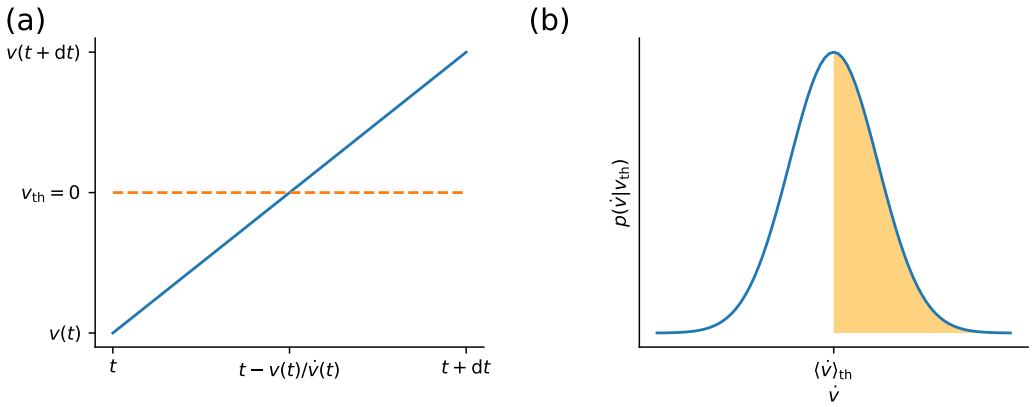

Figure A.1: (a) Diagram showing a section $[t, t+\mathrm{d}t)$ over which the upcrossing rate is derived. (b) Both $\langle v\rangle$ and $\langle\dot{v}\rangle_{\mathrm{th}}$ have a Gaussian distribution. For upcrossings we are interested in the shaded area for which $\dot{v} > 0$.

Given a probability density function of v, $p(v, \dot{v}; x, t)$, the probability that the curve will pass through 0 with positive gradient in $[t, t+\mathrm{d}t)$ is

$$P = \int_0^\infty \mathrm{d}\dot{v} \int_{-\dot{v}\mathrm{d}t}^0 p(v, \dot{v})\mathrm{d}v \approx \mathrm{d}t \int_0^\infty p(0, \dot{v})\dot{v}\mathrm{d}\dot{v}, \tag{A.3}$$

where we perform the v integral by noticing that v is very close to 0 in $[t, t+\mathrm{d}t)$. This means that the rate, $r = \mathrm{d}P/\mathrm{d}t$, at which the potential crosses zero, or indeed any threshold v_{th}, is given by (Rice's formula) [110]

$$r = \int_0^\infty p(v_{\mathrm{th}}, \dot{v})\dot{v}\mathrm{d}\dot{v}. \tag{A.4}$$

Since in general v and $\dot{v}$ are not independent, by Bayes' theorem the joint distribution $p(v_{\mathrm{th}}, \dot{v}) = p(v_{\mathrm{th}})p(\dot{v}|v_{\mathrm{th}})$. From this, if we suppose that both v and $\dot{v}$ have a Gaussian distribution

$$p(v_{\mathrm{th}}) = \frac{1}{\sigma_v\sqrt{2\pi}} \exp\left[-\frac{(v_{\mathrm{th}} - \langle v\rangle)^2}{2\sigma_v^2}\right], \quad \sigma_v^2 = \langle(v - \langle v\rangle)^2\rangle, \tag{A.5}$$

$$p(\dot{v}|v_{\mathrm{th}}) = \frac{1}{[\sigma_{\dot{v}}]_{\mathrm{th}}\sqrt{2\pi}} \exp\left[-\frac{(\dot{v} - \langle\dot{v}\rangle_{\mathrm{th}})^2}{2[\sigma_{\dot{v}}]_{\mathrm{th}}^2}\right], \quad \langle\dot{v}\rangle_{\mathrm{th}} = \langle\dot{v}|v = v_{\mathrm{th}}\rangle, \tag{A.6}$$

$$[\sigma_{\dot{v}}]_{\mathrm{th}}^2 = \langle(\dot{v} - \langle\dot{v}\rangle|v = v_{\mathrm{th}})^2\rangle. \tag{A.7}$$

Substitution for $p(v_{\rm th},\dot{v})$ into (A.4) gives

$$r=\frac{1}{2\pi\sigma_v[\sigma_{\dot{v}}]_{\rm th}}\exp\left[-\frac{(v_{\rm th}-\langle v\rangle)^2}{2\sigma_v^2}\right]\int_0^\infty \dot{v}\exp\left[-\frac{(\dot{v}-\langle\dot{v}\rangle_{\rm th})^2}{2[\sigma_{\dot{v}}]_{\rm th}^2}\right]\mathrm{d}\dot{v}, \tag{A.8}$$

where the integral can be evaluated by letting $x=\dot{v}-\langle\dot{v}\rangle_{\rm th}$,

$$\begin{aligned}\int_0^\infty \dot{v}\exp\left[-\frac{(\dot{v}-\langle\dot{v}\rangle_{\rm th})^2}{2[\sigma_{\dot{v}}]_{\rm th}^2}\right]\mathrm{d}\dot{v}&=\int_{-\langle\dot{v}\rangle_{\rm th}}^\infty (x+\langle\dot{v}\rangle_{\rm th})\exp\left[-\frac{x^2}{2[\sigma_{\dot{v}}]_{\rm th}^2}\right]\mathrm{d}x\\ =[\sigma_{\dot{v}}]_{\rm th}^2\exp\left[-\frac{\langle\dot{v}\rangle_{\rm th}^2}{2[\sigma_{\dot{v}}]_{\rm th}^2}\right]&+\langle\dot{v}\rangle_{\rm th}\sqrt{\frac{\pi[\sigma_{\dot{v}}]_{\rm th}^2}{2}}+\langle\dot{v}\rangle_{\rm th}[\sigma_{\dot{v}}]_{\rm th}\sqrt{\frac{\pi}{2}}\,\mathrm{erf}\left[\frac{\langle\dot{v}\rangle_{\rm th}}{[\sigma_{\dot{v}}]_{\rm th}\sqrt{2}}\right].\end{aligned} \tag{A.9}$$

Hence with $\eta=\langle\dot{v}\rangle_{\rm th}/([\sigma_{\dot{v}}]_{\rm th}\sqrt{2})$, the upcrossing rate can be simplifies to the same expression given by Badel [9]

$$r=\frac{[\sigma_{\dot{v}}]_{\rm th}}{2\pi\sigma_v}\exp\left[-\frac{(v_{\rm th}-\langle v\rangle)^2}{2\sigma_v^2}\right][e^{-\eta^2}+\eta\sqrt{\pi}(1+\mathrm{erf}\,\eta)], \tag{A.10}$$

The conditional moments, $\langle\dot{v}\rangle_{\rm th}$ and $[\sigma_{\dot{v}}]_{\rm th}$, can be found by introducing a new variable $z=\dot{v}+\alpha v$. Supposing that z is independent of v this means that $\langle zv\rangle=\langle z\rangle\langle v\rangle$, which can be used to find the value of the fixed parameter α

$$\begin{aligned}\langle zv\rangle=\langle\dot{v}v\rangle+\alpha\langle v^2\rangle,\quad \langle z\rangle\langle v\rangle=\langle\dot{v}\rangle\langle v\rangle+\alpha\langle v\rangle^2\\ \alpha(\langle v^2\rangle-\langle v\rangle^2)=-(\langle\dot{v}v\rangle-\langle\dot{v}\rangle\langle v\rangle),\quad \therefore\alpha=-\,\mathrm{cov}(v,\dot{v})/\sigma_v^2.\end{aligned} \tag{A.11}$$

With this α, independence of z and v means that $\langle z\rangle=\langle z\rangle_{\rm th}$. Hence $\langle\dot{v}\rangle_{\rm th}$ can be found by equating the two

$$\begin{aligned}\langle z\rangle=\langle\dot{v}\rangle-\frac{\mathrm{cov}(v,\dot{v})\langle v\rangle}{\sigma_v^2},\quad \langle z\rangle_{\rm th}=\langle\dot{v}\rangle_{\rm th}-\frac{\mathrm{cov}(v,\dot{v})v_{\rm th}}{\sigma_v^2},\\ \langle\dot{v}\rangle_{\rm th}=\langle\dot{v}\rangle+\frac{\mathrm{cov}(v,\dot{v})(v_{\rm th}-\langle v\rangle)}{\sigma_v^2}.\end{aligned} \tag{A.12}$$

Furthermore, it also follows that the second moments of z are equal, that is $\sigma_z^2=[\sigma_z^2]_{\rm th}$. This can be used to find $[\sigma_{\dot{v}}]_{\rm th}$

$$\sigma_z^2=\langle z^2\rangle-\langle z\rangle^2=\sigma_{\dot{v}}^2+2\alpha\,\mathrm{cov}(v,\dot{v})+\alpha^2\sigma_v^2 \tag{A.13}$$

$$\begin{aligned}[\sigma_z^2]_{\rm th}&=\langle z^2\rangle_{\rm th}-\langle z\rangle_{\rm th}^2\\ &=\langle\dot{v}^2\rangle_{\rm th}+2\alpha\langle\dot{v}\rangle_{\rm th}v_{\rm th}+\alpha^2v_{\rm th}^2-\langle\dot{v}\rangle_{\rm th}^2-2\alpha\langle\dot{v}\rangle_{\rm th}v_{\rm th}-\alpha^2v_{\rm th}^2=[\sigma_{\dot{v}}^2]_{\rm th}\end{aligned} \tag{A.14}$$

$$[\sigma_{\dot{v}}^2]_{\rm th}=\sigma_{\dot{v}}^2+2\alpha\,\mathrm{cov}(v,\dot{v})+\alpha^2\sigma_v^2=\sigma_{\dot{v}}^2-\frac{\mathrm{cov}(v,\dot{v})^2}{\sigma_v^2}. \tag{A.15}$$

A.2 Sum-over-trips Formalism

The sum-over-trips method can be used to derive the Green's function for a dendritic structure in either the time [137, 198] or frequency [103, 104, 199] domain. Here we detail the method in the frequency domain following the steps shown in [103, 104, 199]. We start with the fundamental Green's function for the infinite cable, $\tilde{\mathcal{G}}_\infty(z;\omega)$. For a trip from neurite i to neurite j that has length x_i in neurite i and length y_j in neurite j, the fundamental function is

$$\tilde{\mathcal{G}}_\infty(z = x_i\gamma_i + y_j\gamma_j;\omega) = \frac{e^{-(x_i\gamma_i + y_j\gamma_j)}}{2\gamma_i}. \tag{A.16}$$

Here $\gamma_j = \sqrt{1 + i\omega\beta_j}$, where β_j is the relative time constant in neurite j, and z is a complex trip length. Each trip has complex coefficient A_q, with the overall Green's function being given by the sum of the Green's functions for the individual trips [103],

$$\tilde{\mathcal{G}}_{ij}(x_i, y_j;\omega) = \sum_q A_q \tilde{\mathcal{G}}_\infty(z_q;\omega). \tag{A.17}$$

The coefficients A_q are calculated in terms of the input admittance of neurite j, $Y_j(\omega)$, relative to the input admittance of all structures (soma and neurites) that contact the same node. This is termed the segment factor and for m neurites that emanate from a node with a soma, it is given by

$$\tilde{f}_j = \frac{Y_j(\omega)}{Y_\sigma(\omega) + \sum_{i=1}^m Y_i(\omega)}, \quad Y_j(\omega) = G_{\lambda_j}\gamma_j, \quad Y_\sigma(\omega) = G_\sigma\gamma_\sigma^2. \tag{A.18}$$

From this definition of the segment factor, the rules for calculating the coefficients A_q are as follows:

1. A trip starts at x_i and ends at y_j. Trips starting at x_i may start travelling in either direction along i but can only change direction at a node or terminal.

2. Trips may go through x_i or y_j numerous times before ending at y_j.

3. The trip coefficient A_q starts at 1 and is multiplied by a factor at each reflection or transmission through a node.

4. When a trip reaches a terminal (whether sealed or killed), it is reflected and the trip reverses direction. Multiply A_q by +1 for a sealed end and -1 for a killed end.

5. When a trip passes through a node from neurite k to neurite m ($k \neq m$), multiply A_q by $2\tilde{f}_m$.

6. When a trip is reflected back at node from neurite k, multiply A_q by $2\tilde{f}_k - 1$.

Since we only have a single node in all the models we examine in this thesis, the application of these rules becomes quite simple. However, this general sum-over-trips approach demonstrates that the framework used here can be applied to arbitrarily complex neuronal branching structures.

A.3 Oscillatory Presynaptic Drive

A.3.1 Point Neuron

For modulated presynaptic input, we consider the rate at which pulses arrive to consist of a fixed component and a component oscillating at angular frequency Ω,

$$r_s = r_{s0} + r_{s1}e^{i\Omega T}. \tag{A.19}$$

If the point neuron has n_s synapses, then the average number of pulses arriving in a time Δ is now time-dependent

$$N_s = n_s(r_{s0} + r_{s1}e^{i\Omega T})\Delta_T. \tag{A.20}$$

For a passive point neuron with filtered synaptic noise, with the Gaussian approximation the conductance evolves as follows

$$\tau_s \frac{\mathrm{d}g_s}{\mathrm{d}T} = -g_s + \tau_s \Delta_g n_s (r_{s0} + r_{s1}e^{i\Omega T}) + \tau_s \Delta_g \sqrt{n_s(r_{s0} + r_{s1}e^{i\Omega T})}\xi_s(T). \tag{A.21}$$

As in earlier sections we will split the conductance into a stochastic fluctuating component, g_{sF}, and a deterministic component, $\langle g_s \rangle$, with $g_s = g_{sF} + \langle g_s \rangle$. Taking the mean of the conductance yields

$$\langle g_s(T) \rangle = \tau_s \Delta_g n_s \left(r_{s0} + \frac{r_{s1}e^{i\Omega T}}{1 + i\Omega\tau_s} \right), \tag{A.22}$$

hence we can split the synaptic conductance mean into a steady term, $\langle g_s \rangle_0$, and an oscillatory term with complex prefactor $\langle g_s \rangle_1$

$$\langle g_s \rangle = \langle g_s \rangle_0 + \langle g_s \rangle_1 e^{i\Omega T}, \quad \langle g_s \rangle_1 = \frac{r_{s1}\langle g_s \rangle_0}{r_{s0}(1 + i\Omega\tau_s)}. \tag{A.23}$$

For the point neuron, the potential evolves as

$$C_{\mathrm{m}}\frac{\mathrm{d}V}{\mathrm{d}T} = g_L(E_L - V) + g_s(E_s - V). \tag{A.24}$$

Similar to the steady-state case, we let $V = \langle V\rangle_0 + u$, where $\langle V\rangle_0$ is the steady state mean component and u is the combined fluctuating and oscillatory voltage. Note that u is different to v_F defined in the previous chapter because it is not zero-mean in general. This means that we have

$$C_{\mathrm{m}}\frac{\mathrm{d}\langle V\rangle_0}{\mathrm{d}T} = g_L(E_L - \langle V\rangle_0) + \langle g_s\rangle_0(E_s - \langle V\rangle_0). \tag{A.25}$$

With $g_0 = g_L + \langle g_s\rangle_0$, $E_0 = (g_L E_L + \langle g_s\rangle_0 E_s)/g_0$, $\tau_v = c_{\mathrm{m}}/g_0$ and $\mu = E_0 - E_L$ as in the steady-state case, in the long time limit we obtain $\langle V\rangle_0 = E_0$. If we now look at the other component of the voltage with the oscillatory and fluctuating conductances $\langle g_s\rangle_1$ and g_{sF} respectively

$$\tau_v\frac{\mathrm{d}u}{\mathrm{d}T} = -u + \frac{\langle g_s\rangle_1 e^{i\Omega T} + g_{sF}}{g_0}(E_s - E_0 - u), \tag{A.26}$$

we find this reduces to (assuming $u \times g_{sF}$ is small)

$$\tau_v\frac{\mathrm{d}u}{\mathrm{d}T} = -\left(1 + \frac{\langle g_s\rangle_1}{g_0}e^{i\Omega T}\right)u + \frac{\langle g_s\rangle_1}{g_0}(E_s - E_0)e^{i\Omega T} + \frac{g_{sF}}{g_0}(E_s - E_0). \tag{A.27}$$

The equation for the fluctuating synaptic conductance is given by

$$\tau_s\frac{\mathrm{d}g_{sF}}{\mathrm{d}T} = -g_{sF} + \tau_s\Delta_g\sqrt{n_s}\sqrt{r_{s0} + r_{s1}e^{i\Omega T}}\xi_s(T). \tag{A.28}$$

If we assume that r_{s1}/r_{s0} is small, then this is approximately equivalent to

$$\tau_s\frac{\mathrm{d}g_{sF}}{\mathrm{d}T} = -g_{sF} + \tau_s\Delta_g\sqrt{n_s r_{s0}}\left(1 + \frac{r_{s1}}{2r_{s0}}e^{i\Omega T}\right)\xi_s(T). \tag{A.29}$$

Letting $s = (E_s - E_0)g_{sF}/g_0$ and $\sigma_s = (E_s - E_0)\Delta_g/g_0\sqrt{\tau_s n_s r_{s0}/2}$, we can simplify both the potential and conductance equations to

$$\tau_v\frac{\mathrm{d}u}{\mathrm{d}T} = -\left(1 + \tilde{\epsilon}_p e^{i\Omega T}\right)u + \tilde{\epsilon}_m e^{i\Omega T} + s \tag{A.30}$$

$$\tau_s\frac{\mathrm{d}s}{\mathrm{d}T} = -s + \sigma_s\sqrt{2\tau_s}\left(1 + \epsilon_v e^{i\Omega T}\right)\xi_s(T), \tag{A.31}$$

where the complex modulation prefactors are given by

$$\epsilon_v = \frac{r_{s1}}{2r_{s0}}, \quad \tilde{\epsilon}_p = \frac{r_{s1}\langle g_s\rangle_0}{r_{s0}g_0(1+i\Omega\tau_s)}, \quad \tilde{\epsilon}_m = \frac{r_{s1}\langle g_s\rangle_0(E_s-E_0)}{r_{s0}g_0(1+i\Omega\tau_s)} = \frac{\epsilon_m}{1+i\Omega\tau_s}. \quad \text{(A.32)}$$

We can typically neglect $\tilde{\epsilon}_p$ due to the product $u \times \langle g_s\rangle_1$ being between small amplitude oscillations and small stochastic fluctuations. Furthermore, due to the large factor of $E_s - E_0$, $|\tilde{\epsilon}_m| >> |\tilde{\epsilon}_p|$, so modulations of the mean of u will be dominated by $\tilde{\epsilon}_m$. Taking this into account, we can simplify the equations further by making time dimensionless with $T = t\tau_0$, $\beta_s = \tau_s/\tau_v$ and $\Omega T \to \Omega t$, yielding

$$\frac{\mathrm{d}u}{\mathrm{d}t} = -u + \frac{\epsilon_m}{1+i\Omega\beta_s}e^{i\Omega t} + s \quad \text{(A.33)}$$

$$\beta_s\frac{\mathrm{d}s}{\mathrm{d}t} = -s + \sigma_s\sqrt{2\beta_s}(1+\epsilon_v e^{i\Omega t})\xi_s(t). \quad \text{(A.34)}$$

A.3.2 Spatially Extended Neuron

For a spatially extended neuron, the equation for the synaptic conductance per unit area with modulated presynaptic arrival rate is given by

$$\tau_s\frac{\partial g_s}{\partial T} = -g_s + \tau_s\Delta_g\varrho_s r_s + \tau_s\Delta_g\sqrt{\frac{\varrho_s(r_{s0}+r_{s1}e^{i\Omega T})}{2\pi a}}\xi_s(X,T). \quad \text{(A.35)}$$

Splitting the synaptic conductance in the same way as for the point neuron, the components of the synaptic conductance are

$$\langle g_s\rangle_0 = \tau_s\Delta_g\varrho_s r_{s0}, \quad \langle g_s\rangle_1 = \frac{r_{s1}\langle g_s\rangle_0}{r_{s0}(1+i\Omega\tau_s)}. \quad \text{(A.36)}$$

For the potential, we split as before, making the cable equation in terms of the steady-state deterministic component

$$c_\mathrm{m}\frac{\partial\langle V\rangle_0}{\partial T} = g_L(E_L - \langle V\rangle_0) + \langle g_s\rangle_0(E_s - \langle V\rangle_0) + g_L\lambda_L^2\frac{\partial^2 V}{\partial X^2}. \quad \text{(A.37)}$$

With g_0 and E_0 defined as before, we obtain the time-invariant constants τ_v and λ, as in the case for a constant presynaptic firing rate. Turning to the equation for u

$$\begin{aligned} c_\mathrm{m}\frac{\partial u}{\partial T} &= -g_L v + (E_s - \langle V\rangle_0)(\langle g_s\rangle_1 e^{i\Omega T} + g_{sF}) - (\langle g_s\rangle_0 + \langle g_s\rangle_1 e^{i\Omega T})v + g_L\lambda_L^2\frac{\partial^2 u}{\partial X^2} \\ \tau_v\frac{\partial u}{\partial T} &= -\left(1 + \frac{\langle g_s\rangle_1 e^{i\Omega T}}{g_0}\right)u + \frac{E_s - \langle V\rangle_0}{g_0}\left(g_{sF} + \langle g_s\rangle_1 e^{i\Omega T}\right) + \lambda^2\frac{\partial^2 u}{\partial X^2}. \end{aligned} \quad \text{(A.38)}$$

Returning to the synaptic conductance, the fluctuating component with the square-root expanded to first order obeys

$$\tau_s \frac{\partial g_{sF}}{\partial T} \approx -g_{sF} + \tau_s \Delta_g \sqrt{\frac{\varrho_s r_{s0}}{2\pi a}} \left(1 + \frac{r_{s1}}{2r_{s0}} e^{i\Omega T}\right) \xi_s(X,T). \tag{A.39}$$

Rescaling the synaptic conductance with $s = g_{sF}(E_s - E_0)/g_0$, space with $X = x\lambda$ and time with $T = \tau_v t$, we find

$$\beta_s \frac{\partial s}{\partial t} = -s + 2\sigma_s \sqrt{\beta_s}(1 + \epsilon_v e^{i\Omega t})\xi_s(x,t), \tag{A.40}$$

where σ_s has the same definition as the spatial model for constant presynaptic drive and ϵ_v is given earlier in (A.32). Neglecting the multiplicative modulation term represented for the point neuron by $\tilde{\epsilon}_p$, we can thus finally write the cable equation for u as

$$\frac{\partial u}{\partial t} = -u + \frac{\epsilon_m(x)}{1 + i\Omega\beta_s} e^{i\Omega t} + \frac{E_s - \langle V(x)\rangle_0}{E_s - E_0} s + \frac{\partial^2 u}{\partial x^2}, \tag{A.41}$$

where ϵ_m can in principle be spatially varying

$$\tilde{\epsilon}_m(x) = \frac{\langle g_s\rangle_1}{g_0}(E_s - \langle V(x)\rangle_0) = \frac{r_{s1}\langle g_s\rangle_0 (E_s - \langle V\rangle_0(x))}{r_{s0} g_0 (1 + i\Omega\beta_s)}. \tag{A.42}$$

However as before we make the approximation $(E_s - \langle V(x)\rangle_0)/(E_s - E_0) \approx 1$, which causes ϵ_m to be spatially uniform and equivalent to the point-neuron definition in (A.32).

A.4 Specific Derivations of Moments

A.4.1 Sealed Dendrite Correlator

$$\begin{aligned}
\langle \hat{\xi}_s(\omega,k)\hat{\xi}_s(-\omega',-k')\rangle &= \delta(\omega-\omega')\int_{-\infty}^{\infty} e^{ikx}\mathrm{d}x \\
&\quad \times \int_{-\infty}^{\infty} e^{-ik'x'} \sum_{m=-\infty}^{\infty} \delta(x - x' + 2ml) + \delta(x + x' + 2ml)\mathrm{d}x' \\
\langle \hat{\xi}_s(\omega,k)\hat{\xi}_s(-\omega' - k')\rangle &= \delta(\omega-\omega') \sum_{m=-\infty}^{\infty} \int_{-\infty}^{\infty} [e^{i(k-k')x} + e^{i(k+k')x}] e^{2ik'ml}\mathrm{d}x \\
\langle \hat{\xi}_s(\omega,k)\hat{\xi}_s(-\omega',-k')\rangle &= \delta(\omega-\omega') \sum_{m=-\infty}^{\infty} [\delta(k-k') + \delta(k+k')] e^{2ik'ml}.
\end{aligned} \tag{A.43}$$

A.4.2 Passive Infinite Dendrite Temporal Autocovariance

$$K(\tau) = \sigma_s^2 \beta_s \Bigg\{ \operatorname{erfc}(\sqrt{|\tau|}) + e^{-|\tau|\beta_s^{-1}} \frac{\sqrt{1+\beta_s^{-1}} - \sqrt{1-\beta_s^{-1}}}{2\sqrt{1+\beta_s^{-1}}\sqrt{1-\beta_s^{-1}}}$$
$$- e^{-|\tau|\beta_s^{-1}} \frac{\operatorname{erfc}\left[\sqrt{|\tau|(1-\beta_s^{-1})}\right]}{2\sqrt{1-\beta_s^{-1}}} - e^{|\tau|\beta_s^{-1}} \frac{\operatorname{erfc}\left[\sqrt{|\tau|(1+\beta_s^{-1})}\right]}{2\sqrt{1+\beta_s^{-1}}} \Bigg\},\ \beta_s > 1$$
$$K(\tau) = \sigma_s^2 \beta_s \Bigg\{ \operatorname{erfc}(\sqrt{|\tau|}) - \frac{e^{-|\tau|\beta_s^{-1}}}{2\sqrt{1+\beta_s^{-1}}} + e^{-|\tau|\beta_s^{-1}} \frac{\operatorname{erfi}\left[\sqrt{|\tau|(\beta_s^{-1}-1)}\right]}{2\sqrt{\beta_s^{-1}-1}}$$
$$- e^{|\tau|\beta_s^{-1}} \frac{\operatorname{erfc}\left[\sqrt{|\tau|(1+\beta_s^{-1})}\right]}{2\sqrt{1+\beta_s^{-1}}} \Bigg\},\ \beta_s < 1. \tag{A.44}$$

While this correlator is algebraically complicated, we can see the $\operatorname{erfc}(\sqrt{|\tau|})$ term that was also seen in the autocovariance for white noise (2.29).

A.4.3 Passive Dendrite-and-Axon White-Noise Variances

The axonal voltage variance is computed from the integral (2.81)

$$\sigma_{v_\alpha}^2(x_\alpha) = \frac{2\sigma_w^2}{\pi} \int_{-\infty}^{\infty} \frac{\beta_\alpha^4 \lambda_1^6 e^{-x_\alpha z_\alpha}}{z_1 |\beta_\alpha^2 \lambda_1^3 \gamma_1 + \lambda_\alpha^3 \gamma_\alpha|^2} \mathrm{d}\omega. \tag{A.45}$$

When $g_1 = g_\alpha$ and $\lambda_1 = \lambda_\alpha$, this can be resolved in terms of modified Bessel functions of the second kind K_n and modified Struve functions L_ν

$$\sigma_{v_\alpha}^2(x_\alpha) = \sigma_{v_\alpha}^2(0) \left\{ 1 - 2x_\alpha [K_0(2x_\alpha) L_{-1}(2x_\alpha) + K_1(2x_\alpha) L_0(2x_\alpha)] \right\}, \tag{A.46}$$
$$L_\nu(x) = \sum_{m=0}^{\infty} \frac{(x/2)^{2m+\nu+1}}{\Gamma(m+3/2)\Gamma(\nu+m+3/2)}. \tag{A.47}$$

For the derivative variance, one must compute the integral 2.84

$$\sigma_{\dot{v}_\alpha}^2(x_\alpha) = \frac{2\sigma_w^2}{\pi} \int_{-\infty}^{\infty} \frac{\omega^2 \beta_\alpha^4 \lambda_1^6 e^{-x_\alpha z_\alpha}}{z_1 |\beta_\alpha^2 \lambda_1^3 \gamma_1 + \lambda_\alpha^3 \gamma_\alpha|^2} \mathrm{d}\omega, \tag{A.48}$$

which for $g_1 = g_\alpha$ can be reduced to

$$\sigma_{\dot{v}_\alpha}^2(x_\alpha) = \frac{2\sigma_w^2}{\pi} \left(\frac{\lambda_1^3}{\lambda_1 + \lambda_\alpha} \right)^2 \int_{-\infty}^{\infty} \frac{\omega^2 e^{-x_\alpha z}}{z|\gamma|^2} \mathrm{d}\omega. \tag{A.49}$$

Using the substitutions $\omega = \sinh\eta$ and $q = \cosh(\eta/2)$, we can resolve the integral for the equal conductance case in terms of a modified Bessel function of the second kind, K_2 [200, p. 917]

$$\begin{aligned}\sigma^2_{\dot{v}_\alpha}(x_\alpha) &= \frac{16\sigma_w^2}{\pi}\left(\frac{\lambda_1^3}{\lambda_1^3+\lambda_\alpha^3}\right)^2\int_1^\infty q\sqrt{q^2-1}e^{-2x_\alpha q}\mathrm{d}q,\\ &= \frac{8\sigma_w^2}{\pi x_\alpha}\left(\frac{\lambda_1^3}{\lambda_1^3+\lambda_\alpha^3}\right)^2 K_2(2x_\alpha).\end{aligned} \tag{A.50}$$

A.4.4 Quasi-Active Point Neuron Second Moments

White Noise Autocovariance

We start from the quasi-active point neuron with white noise input and the mean removed

$$\frac{\mathrm{d}u}{\mathrm{d}t} = -u - \kappa w + \sigma_w\sqrt{2}\xi_s(t), \quad \beta_w\frac{\mathrm{d}w}{\mathrm{d}t} = u - w. \tag{A.51}$$

After performing temporal Fourier transforms, this can be rearranged to give an expression for $\tilde{u}$

$$\tilde{u}(\omega) = \frac{\sigma_w\sqrt{2}(1+i\omega\beta_w)\tilde{\xi}_s(\omega)}{(1+i\omega\beta_w)(1+i\omega)+\kappa} = \sigma_w\sqrt{2}\tilde{A}(\omega)\tilde{\xi}_s(\omega). \tag{A.52}$$

Denoting the inverse transform of $\tilde{A}(\omega)$ as $A(t)$, we can invert to give an equation for $u(t)$ by using the convolution theorem

$$u(t) = \sigma_w\sqrt{2}\int_{-\infty}^{\infty} A(t-s)\xi_s(t')\mathrm{d}t', \tag{A.53}$$

where $A(t)$ can be found using the known Fourier transforms

$$e^{-at}\cos(ht)\theta(t) \to \frac{i\omega+a}{(i\omega+a)^2+h^2}, \quad e^{-at}\sin(ht)\theta(t) \to \frac{h}{(i\omega+a)+h^2}. \tag{A.54}$$

Hence we have

$$\begin{aligned}A(t) &= e^{-at}[\cos(ht) + b\sin(ht)]\theta(t) + \overline{A}(t)\theta(t),\\ a &= \frac{1+\beta_w}{2\beta_w}, \quad h^2 = \frac{1+\kappa}{\beta_w} - a^2, \quad b = \frac{1/\beta_w - a}{h},\end{aligned} \tag{A.55}$$

meaning that for the temporal autocovariance we have

$$\begin{aligned}\langle v(t)v(t+\tau)\rangle = K(\tau) &= 2\sigma_w^2 \int_{-\infty}^{\infty} A(t+\tau-t')A(t-t')\mathrm{d}t' \\ &= 2\sigma_w^2 \int_{-\infty}^{\min(t,t+\tau)} \overline{A}(t+\tau-t')A(t-t')\mathrm{d}t', \end{aligned} \tag{A.56}$$

which after assuming that $\tau > 0$ yields

$$\begin{aligned}K(\tau) = \sigma_w^2 e^{-a\tau}\big\{&[2a^2+2abh+(1+b^2)h^2]\cos(h\tau) \\ &+ a[2ab+(b^2-1)h]\sin(h\tau)\big\}/[2a(a^2+h^2)]. \end{aligned} \tag{A.57}$$

Substituting for the constants a, b and h finally gives

$$\begin{aligned}K(\tau) = \sigma_w^2 e^{-(1+\beta_w^{-1})\frac{\tau}{2}}\big\{&(1+\beta_w+\kappa\beta_w)\cos(h\tau) \\ &+ \tfrac{1}{2h}(1+\beta_w)(\beta_w^{-1}-1-\kappa)\sin(h\tau)\big\}/[(1+\beta_w)(1+\kappa)]. \end{aligned} \tag{A.58}$$

White Noise Variance

The white noise variance can be obtained by setting $\tau = 0$ in (A.58)

$$\sigma_v^2 = \sigma_w^2 \frac{1+\beta_w(1+\kappa)}{(1+\beta_w)(1+\kappa)}. \tag{A.59}$$

Coloured Noise Autocovariance

Starting from the quasi-active point neuron equation with coloured noise in terms of the zero-mean potential u

$$\frac{\mathrm{d}u}{\mathrm{d}t} = -u + s - \kappa w, \quad \beta_s \frac{\mathrm{d}s}{\mathrm{d}t} = -s + \sigma_s\sqrt{2\beta_s}\xi_s(t), \quad \beta_w \frac{\mathrm{d}w}{\mathrm{d}t} = u - w, \tag{A.60}$$

which after taking temporal Fourier transforms yields

$$\tilde{u}(\omega) = \frac{\sigma_s\sqrt{2\beta_s}(1+i\omega\beta_w)\tilde{\xi}_s(\omega)}{(1+i\omega\beta_s)[(1+i\omega\beta_w)(1+i\omega)+\kappa]} = \sigma_s\sqrt{2\beta_s}\tilde{A}(\omega)\tilde{B}(\omega)\tilde{\xi}_s(\omega). \tag{A.61}$$

We can thus follow a similar procedure to the white noise case, but now we have a double convolution upon taking the inverse transform

$$u(t) = \sigma_s\sqrt{2\beta_s}\int_{-\infty}^{\infty}\xi(t')dt'\int_{-\infty}^{\infty}A(t'')B(t-t'-t'')\mathrm{d}t'', \tag{A.62}$$

where $B(t) = \theta(t)\beta_s^{-1}e^{-t\beta_s^{-1}}$. Substituting the step functions we arrive at

$$\begin{aligned} u(t) &= \sigma_s\sqrt{2\beta_s}\int_{-\infty}^{t}\xi(t')\mathrm{d}t'\int_{0}^{t-t'}\overline{A}(t'')B(t-t'-t'')\mathrm{d}t'' \\ &= \sigma_s\sqrt{2\beta_s}\int_{-\infty}^{t}\xi(t')F(t-t')\mathrm{d}t', \end{aligned} \tag{A.63}$$

and therefore the autocovariance can be written as

$$K(\tau) = 2\sigma_s^2\beta_s\int_{-\infty}^{t}F(t-t')F(t+\tau-t') = 2\sigma_s^2\beta_s\int_{0}^{\infty}F(q)F(q+\tau)\mathrm{d}q. \tag{A.64}$$

Using the same definitions of a, b and h as in (A.55), we can obtain $F(q)$ as

$$\begin{aligned} F(q) = \big[e^{-\beta_s^{-1}q}(\beta_s a + \beta_s bh - 1) + e^{-aq}\big\{ &-(\beta_s a + \beta_s bh - 1)\cos(hq) \\ &+ [b(1-\beta_s a) + \beta_s h]\sin(hq)\big\}\big]/[(\beta_s a - 1)^2 + \beta_s^2 h^2], \end{aligned} \tag{A.65}$$

which if $F(q) = c_0 e^{-\beta_s^{-1}q} - c_0 e^{-aq}[\cos(\Omega q) + c_1\sin(\Omega q)]$, then the integral is

$$\begin{aligned} \int_0^\infty F(q)F(q+\tau)\mathrm{d}q = &-\frac{\beta_s c_0^2 e^{-a\tau}\left\{(1+\beta_s a + c_1 h)\cos(h\tau) + [(1+\beta_s a)c_1 - h]\sin(h\tau)\right\}}{(1+\beta_s a)^2 + \beta_s^2 h^2} \\ &+ \frac{c_0^2 e^{-a\tau}\left\{[2a^2 + 2ac_1 h + (1+c_1^2)h^2]\cos(h\tau) + a[2ac_1 + (c_1^2-1)h]\sin(h\tau)\right\}}{4a(a^2+h^2)} \\ &+ \frac{\beta_s c_0^2 e^{-\beta_s^{-1}\tau}}{2} - \frac{\beta_s c_0^2 e^{-\beta_s^{-1}\tau}(1+\beta_s a + c_1 h)}{(1+\beta_s a)^2 + \beta_s^2 h^2}. \end{aligned} \tag{A.66}$$

Substitution of this integral into (A.64) finally yields the temporal autocovariance.

Coloured Noise Variance

Setting $\tau = 0$ in (A.66) gives

$$\int_0^\infty F(q)^2\mathrm{d}q = \frac{\beta_s c_0^2}{2} + \frac{c_0^2[2a^2 + 2ac_1 h + (1+c_1^2)h^2]}{4a(a^2+h^2)}, \tag{A.67}$$

where we note that c_0 and c_1 are given by

$$c_0 = \frac{\beta_s a + \beta_s bh - 1}{(\beta_s a - 1)^2 + \beta_s^2 h^2}, \quad c_1 = \frac{\beta_s h + b(1-\beta_s a)}{\beta_s a + \beta_s bh - 1}. \tag{A.68}$$

Thus substituting the values of a, b and h from (A.55) gives the variance as

$$\sigma_v^2 = \frac{\sigma_s^2\beta_s}{(1+\beta_w)(1+\kappa)}\frac{\beta_w + \beta_s(1+\beta_w) + \beta_w^2(1+\kappa)}{\beta_w + \beta_s(1+\beta_w) + \beta_s^2(1+\kappa)}. \tag{A.69}$$

Variance Modulation Second Moments

Variance

To calculate the dynamic second moments for the quasi-active membrane, we extend the approach used in the steady-state. This means that we start from the Fourier transform of u

$$\tilde{u}(\omega) = \sigma_s \sqrt{2\beta_s} \tilde{A}(\omega)\tilde{B}(\omega)[\tilde{\xi}_s(\omega) + \epsilon_v \tilde{\xi}_s(\omega - \Omega)]. \tag{A.70}$$

Double convolution can again be used to invert the equation, but now we note the Fourier transform pair

$$e^{i\Omega t}\tilde{\xi}_s(t) \to \tilde{\xi}_s(\omega - \Omega), \tag{A.71}$$

which thus yields

$$u(t) = \sigma_s \sqrt{2\beta_s} \int_{-\infty}^{\infty} (1 + \epsilon_v e^{i\Omega t'})\xi_s(t')\mathrm{d}t' \int_{-\infty}^{\infty} A(t'')B(t - t' - t'')\mathrm{d}t'', \tag{A.72}$$

where we note that $A(t)$ has the form given in (A.55) with the same constants a, b and h, and $B(t) = \theta(t)e^{-t/\beta_s}/\beta_s$. After putting in the step functions, we can simplify the double-convolution to

$$u(t) = \sigma_s \sqrt{2\beta_s} \int_{-\infty}^{t} (1 + \epsilon_v e^{i\Omega t'})\xi(s)\mathrm{d}t'' \int_{0}^{t-t'} \overline{A}(t'')\overline{B}(t - t' - t'')\mathrm{d}t'' \tag{A.73}$$

$$= \sigma_s \sqrt{2\beta_s} \int_{-\infty}^{t} (1 + \epsilon_v e^{i\Omega t'})\xi(t')F(t - t')\mathrm{d}t', \tag{A.74}$$

where we know from the steady-state case that $F(q)$ is given by (A.65). Hence the overall variance is

$$\sigma_u^2 = 2\sigma_s^2\beta_s \int_{-\infty}^{t} F(t - t')^2\mathrm{d}t' + 4\sigma_s^2\beta_s\epsilon_v \int_{-\infty}^{t} F(t - t')^2 e^{i\Omega t'}\mathrm{d}t' + O(\epsilon_v^2), \tag{A.75}$$

which upon substituting $q = t - t'$ yields the oscillatory second moment coefficient in an integral which has closed form

$$\begin{aligned}[\sigma_u^2]_1 &= 4\sigma_s^2\beta_s \int_0^\infty F(q)^2 e^{-i\Omega q}\mathrm{d}q \\ &= 8\sigma_s^2\beta_s\big\{(2a+i\Omega)(1+a\beta_s+i\Omega\beta_s) + bh(2+4a\beta_s+3i\Omega\beta_s) \\ &+ h^2[2+i\Omega\beta_s+b^2(2+4a\beta_s+3i\Omega\beta_s)]/(2a+i\Omega)\big\} \\ &/\big\{(2+i\Omega\beta_s)[(2a+i\Omega)^2+4h^2][(1+a\beta_s+i\Omega\beta_s)^2+\beta_s^2h^2]\big\}.\end{aligned} \tag{A.76}$$

Substituting the original system parameters gives the denominator as

$$\begin{aligned}D(\Omega) &= (2+i\Omega\beta_s)[4\beta_w^{-1}(1+\kappa)+i\Omega(1+\beta_w^{-1})-\Omega^2] \\ &\times [1+\beta_s(1+\beta_w^{-1})+\beta_s^2\beta_w^{-1}(1+\kappa)+i\Omega\beta_s(2+\beta_s(1+\beta_w^{-1}))-\Omega^2\beta_s^2].\end{aligned} \tag{A.77}$$

Derivative Variance

$\dot{u}$ can be written in a similar manner, but with a new definition of $\tilde{B}(\omega)$

$$\tilde{B}'(\omega) = \frac{i\omega}{1+i\omega\beta_s}, \quad B'(t) = \frac{\delta(t)}{\beta_s} - \frac{\theta(t)e^{-t/\beta_s}}{\beta_s^2}. \tag{A.78}$$

This means that we have for $\dot{u}$

$$\begin{aligned}\tilde{\dot{u}}(\omega) &= \sigma_s\sqrt{2\beta_s}\tilde{A}(\omega)\tilde{B}'(\omega)[\tilde{\xi}_s(\omega)+\epsilon_v\tilde{\xi}_s(\omega-\Omega)], \\ \dot{u}(t) &= \sigma_s\sqrt{2\beta_s}\int_{-\infty}^{\infty}(1+\epsilon_v e^{i\Omega t'})\xi_s(t')\mathrm{d}t'\int_{-\infty}^{\infty}A(\tau)B'(t-t'-t'')\mathrm{d}t'' \\ &= \frac{\sigma_s\sqrt{2\beta_s}}{\beta_s}\int_{-\infty}^{t}(1+\epsilon_v e^{i\Omega t'})\xi_s(t')\left[\overline{A}(t-t')-F(t-t')\right]\mathrm{d}t'.\end{aligned} \tag{A.79}$$

From this expression we can see that the coefficient for the dynamic derivative variance is given by

$$[\sigma_{\dot{u}}^2]_1 = \frac{4\sigma_s^2}{\beta_s}\int_0^\infty [\overline{A}(q) - F(q)]^2 \mathrm{d}q \tag{A.80}$$

$$\begin{aligned}
&= \frac{4\sigma_s^2}{D(\Omega)}\Big\{(2a+i\Omega)(1+a\beta_s+i\Omega\beta_s)[2a+i\Omega(1+a\beta_s+i\Omega\beta_s)] \\
&+ 2bh\beta_s[2a(a+i\Omega) - \Omega^2 + (a+i\Omega)^2 i\Omega\beta_s] \\
&+ \frac{h^2}{2a+i\Omega}\big\{2a^2\beta_s(b^2+3)(2+i\Omega\beta_s) + 4ai\Omega\beta_s[b^2+5+i\Omega\beta_s(b^2+2)] \\
&+ 4(2a+i\Omega) - \Omega^2\beta_s[8+3i\Omega\beta_s+2b^2(1+i\Omega\beta_s)]\big\} \\
&+ 2b\beta_s h^3(2+i\Omega\beta_s) + \frac{2\beta_s w^4(b^2+1)(2+i\Omega\beta_s)}{2a+i\Omega}\Big\}.
\end{aligned} \tag{A.81}$$

Covariance

For the covariance we simply multiply the expressions for $u(t)$ and $\dot{u}(t)$ together and take the expectation

$$\langle u(t)\dot{u}(t)\rangle = 2\sigma_s^2\int_{-\infty}^t (1 + 2\epsilon_v e^{i\Omega s} + O(\epsilon_v^2))F(t-s)[\overline{A}(t-s) - F(t-s)]\mathrm{d}s. \tag{A.82}$$

Since we found earlier in the steady-state section that the integral of $\overline{A}(q)F(q)$ is the same as $F(q)^2$, only the oscillating term will remain from this integral, which is

$$[\sigma_{u\dot{u}}]_1 = 4\sigma_s^2\int_0^\infty F(q)[\overline{A}(q) - F(q)]e^{-i\Omega q}\mathrm{d}q \tag{A.83}$$

$$\begin{aligned}
&= \frac{4\sigma_s^2}{D(\Omega)}\Big\{(2a+i\Omega)(1+a\beta_s+i\Omega\beta_s) + bh(2+4a\beta_s+3i\Omega\beta_s) \\
&+ \frac{h^2[(2+i\Omega\beta_s) + b^2(2+4a\beta_s+3i\Omega\beta_s)]}{2a+i\Omega}\Big\}
\end{aligned} \tag{A.84}$$

A.4.5 Quasi-Active Infinite Dendrite Second Moments

Taking Fourier transforms in time and space of the quasi-active cable equation (4.14) with white noise, $s = 2\sigma_w\xi_s(x,t)$, gives the fluctuating voltage as

$$\hat{v}_F(k,\omega) = \frac{2\sigma_w(1+i\omega\beta_w)\hat{\xi}_s(k,\omega)}{(1+k^2+i\omega)(1+i\omega\beta_w)+\kappa} = 2\sigma_w\hat{A}(k,\omega)\hat{\xi}_s(k,\omega). \tag{A.85}$$

Using the convolution theorem in time and inverting in space gives

$$v_F(x,t) = \frac{\sigma_w}{\pi}\int_{-\infty}^{\infty} e^{ikx}\mathrm{d}k \int_{-\infty}^{\infty} \tilde{A}(t-t',k)\tilde{\xi}_s(k,t')\mathrm{d}t', \tag{A.86}$$

where $\tilde{A}(t,k)$ has the same form as $A(t)$ for the point neuron (A.55), but now a, h and b are k-dependent

$$a = \frac{1+k^2+\beta_w^{-1}}{2}, \quad h^2 = \frac{1+k^2+\kappa}{\beta_w} - a^2, \quad b = \frac{\beta_w^{-1}-a}{h}. \tag{A.87}$$

The spatial autocovariance can be calculated from (A.86) via multiplication by $v_F(x',t)$ and taking the expectation

$$\begin{aligned}\langle v_F(x,t)v_F(x',t)\rangle &= \frac{2\sigma_w^2}{\pi}\int_{-\infty}^{\infty} e^{ik(x-x')}\mathrm{d}k \int_0^{\infty} \tilde{A}(q,k)^2\mathrm{d}q \\ &= \frac{\sigma_w^2}{\pi}\int_{-\infty}^{\infty} e^{ik(x-x')}\frac{\beta_w^{-1}+1+\kappa+k^2}{(1+\beta_w^{-1}+k^2)(1+\kappa+k^2)}\mathrm{d}k,\end{aligned} \tag{A.88}$$

where we first used the change of variable $q = t - t'$. Resolving the k-integral yields the spatial autocovariance $K(x-x')$

$$K(x-x') = \frac{\sigma_w^2}{\kappa-\beta_w^{-1}}\left(\frac{\kappa e^{-|x-x'|\sqrt{1+\beta_w^{-1}}}}{\sqrt{1+\beta_w^{-1}}} - \beta_w^{-1}\frac{e^{-|x-x'|\sqrt{1+\kappa}}}{\sqrt{1+\kappa}}\right) \tag{A.89}$$

A.5 Somatic Synaptic Drive

If we let $I_{s\sigma} = G_s(E_{s\sigma} - V_\sigma)$ be a general synaptic input and take the diffusion approximation as in the case of the dendritic synaptic drive

$$\tau_{s\sigma}\frac{\mathrm{d}G_s}{\mathrm{d}T} = \langle G_s\rangle - G_s + A_\sigma\tau_{s\sigma}\Delta_{g\sigma}\sqrt{\frac{\varrho_{s\sigma}r_{s\sigma}}{A_\sigma}}\xi_{s\sigma}(T), \tag{A.90}$$

where A_σ is the soma surface area, $\tau_{s\sigma}$ is the synaptic time constant, $\Delta_{g\sigma}$ is the conductance change caused by each synaptic pulse, $\varrho_{s\sigma}$ is the density of synapses on the soma, and r_{s0} is the presynaptic arrival rate. Splitting the somatic voltage and synaptic conductance into deterministic and fluctuating parts as in chapter 2, we obtain the effective soma conductance G_σ and the effective resting potential E_σ. Dividing (2.86) by G_σ and defining the neuritic dominance factor as $\rho = G_\lambda/G_\sigma$ [44],

we obtain

$$\tau_\sigma \frac{\mathrm{d}V_\sigma}{\mathrm{d}T} = E_\sigma - V_\sigma + \rho\lambda_1 \left.\frac{\partial V}{\partial X}\right|_{X=0} + s_\sigma, \tag{A.91}$$

where $\tau_\sigma = C_\sigma/G_\sigma$ is the effective somatic membrane time constant and $s_\sigma = (E_{s\sigma} - \langle V_\sigma \rangle)G_{sF}/G_\sigma$, which has dynamics described by

$$\tau_{s\sigma} \frac{\mathrm{d}s_\sigma}{\mathrm{d}T} = -s_\sigma + \sigma_{s\sigma}\sqrt{2\tau_{s\sigma}}\xi_{s\sigma}(T). \tag{A.92}$$

Here we can rescale space and time in terms of the dendrite, defining $\beta_\sigma = \tau_\sigma/\tau_v$ and $\beta_{s\sigma} = \tau_{s\sigma}/\tau_v$, measure all voltages from E_L with $\mu_\sigma = E_\sigma - E_L$ (assuming the dendrite and soma have the same leak current rest potential),

$$\beta_\sigma \frac{\mathrm{d}v_\sigma}{\mathrm{d}t} = \mu_\sigma - v_\sigma + \rho \left.\frac{\partial v}{\partial x}\right|_{x=0} + s_\sigma \tag{A.93}$$

$$\beta_{s\sigma} \frac{\mathrm{d}s_\sigma}{\mathrm{d}t} = -s_\sigma + \sigma_{s\sigma}\sqrt{2\beta_{s\sigma}}\xi_{s\sigma}(t). \tag{A.94}$$

Appendix B

Numerical Methods

B.1 Simulation of Stochastic Partial Differential Equations

B.1.1 Forward Euler Method

The forward Euler method is explicit in time and looks to the next time step Δ_T. We measure v at half-integer spatial steps Δ_X and $\partial v/\partial X$ at integer spatial steps in order to directly enforce the sealed-end boundary condition ($\partial v/\partial X|_{X=0} = 0$) present for semi-infinite and finite dendrites. Hence, with fixed, temporal and spatial step sizes Δ_T and Δ_X, $v((k+\frac{1}{2})\Delta_X, i\Delta_T) = v^i_{k+1/2}$ and $\partial v/\partial X(k\Delta_X, i\Delta_T) = \partial_X v^i_k$. The numerical algorithm used to generate v is thus as follows

$$\begin{aligned} v^{i+1}_{k+1/2} &= v^i_{k+1/2} + \frac{\Delta_T}{\tau_v}\left[\mu - v^i_{k+1/2} + \frac{\lambda^2}{\Delta_X}(\partial_X v^i_k - \partial_X v^i_{k+1}) + s^i_{k+1/2}\right], \\ \partial_X v^{i+1}_k &= \frac{v^{i+1}_{k+1/2} - v^{i+1}_{k-1/2}}{\Delta_X}. \end{aligned} \tag{B.1}$$

For white noise the synaptic drive is discretised as if we were applying the Euler-Maruyama method to an SDE with $s^i_{k+1/2} = 2\sigma_w\psi^i_k/\sqrt{\Delta_T}$, where ψ^i_k is a zero-mean unit variance Gaussian number that is independently generated at each time step i and each spatial location k. While for coloured noise we have

$$s^{i+1}_{k+1/2} = s^i_{k+1/2} + \frac{\Delta_T}{\tau_s}\left(-s^i_{k+1/2} + 2\sigma_s\sqrt{\frac{\lambda\tau_s}{\Delta_X\Delta_T}}\psi^i_k\right). \tag{B.2}$$

Boundary Conditions

Throughout this thesis a range of boundary conditions are used for the different morphologies. The sealed end in the semi-infinite and sealed dendrites is easiest to implement, especially as we evaluate the derivative at integer steps in Δ_X

$$\left.\frac{\partial v}{\partial X}\right|_{X=0} = 0 \;\rightarrow\; \partial_X v_0^i = 0. \tag{B.3}$$

Where we also use the sealed end boundary condition for the far end of an infinite or semi-infinite dendrite for convenience.

For the case of n dendrites and an axon meeting where there is only a nominal soma, our numerical implementation of the boundary condition is derived from Kirchoff's current law applied to the axial current

$$\frac{\lambda_\alpha}{R_{\lambda_\alpha}}\partial_X v_{(\alpha,0)}^{i+1} + \sum_{j=1}^{n}\frac{\lambda_j}{R_{\lambda_j}}\partial_X v_{(j,0)}^{i+1} = 0, \tag{B.4}$$

which after assuming identical dendrites, substituting for R_λ and $g_1/g_\alpha = \beta_\alpha$ yields

$$\lambda_\alpha^4\partial_X v_{(\alpha,0)}^{i+1} + \beta_\alpha^2\lambda_1^4\sum_{j=1}^{n}\partial_X v_{(j,0)}^{i+1} = 0. \tag{B.5}$$

The spatial derivatives at $X = 0$ can be calculated to first order in Δ_{Xj} in terms of $v_{(j,1/2)}$ and v_0

$$\partial_X v_{(j,0)}^{i+1} = \frac{2}{\Delta_{Xj}}(v_{(j,1/2)}^{i+1} - v_0^{i+1}), \tag{B.6}$$

where v_0 lacks the additional subscript j since by continuity of potential it is the same on each neurite ($v_{(1,0)} = v_{(2,0)} = ... = v_0$). This scheme can support different spatial step sizes Δ_{Xj} in each neurite, but for simplicity from hereon we suppose just two spatial step sizes: Δ_{X1} for the dendrites and $\Delta_{X\alpha}$ for the axon. By first calculating $v_{(j,1/2)}^{i+1}$ from (B.1), we then substitute (B.6) into (B.5) and rearrange in terms of v_0

$$\frac{2\lambda_\alpha^4}{\Delta_{X\alpha}}(v_{(\alpha,1/2)}^{i+1} - v_0^{i+1}) + \frac{2\beta_\alpha^2\lambda_1^4}{\Delta_{X1}}\sum_{j=1}^{n}(v_{(j,1/2)}^{i+1} - v_0^{i+1}) = 0$$

$$v_0^{i+1}\left(\frac{\lambda_\alpha^4}{\Delta_{X\alpha}} + n\frac{\beta_\alpha^2\lambda_1^4}{\Delta_{X1}}\right) = \frac{\lambda_\alpha^4}{\Delta_{X\alpha}}v_{(\alpha,1/2)}^{i+1} + \frac{\beta_\alpha^2\lambda_1^4}{\Delta_{X1}}\sum_{j=1}^{n}v_{(j,1/2)}^{i+1}. \tag{B.7}$$

After calculating v_0, one can then proceed to calculate each $\partial_X v^{i+1}_{(j,0)}$, thus calculating everything required for this boundary condition.

The somatic boundary condition is more complicated, as both v and $\partial_x v$ are required at $X = 0$. In this instance we first calculate v^{i+1}_σ using a forward time step, which for generality we show with n dendrites and an axon

$$v^{i+1}_\sigma = v^i_\sigma + \frac{\Delta_T}{\tau_\sigma}\left[-v^i_\sigma + \rho_\alpha\lambda_\alpha\partial_X v^i_{(\alpha,0)} + \sum_{j=1}^{n}\rho_j\lambda_j\partial_X v^i_{(j,0)}\right], \tag{B.8}$$

where we have introduced the notation $v^i_{(j,k)}$ to indicate spatial position $k\Delta_X$ on neurite j at time $i\Delta_T$. The next steps are to calculate $v^{i+1}_{(j,1/2)}$ by equation (B.1) and then calculate $\partial_X v^{i+1}_{(j,0)}$ via (B.6).

Finally, we must consider the effect of applying an external input current $I_{\text{ext}}(T)$ (for example current modulation in section 3.6.1) at a node where dendrites meet at $X = 0$. For generality we first consider the case with an electrically substantial soma

$$\tau_\sigma\frac{\mathrm{d}v_\sigma}{\mathrm{d}T} = -v_\sigma + \rho_\alpha\lambda_\alpha\left.\frac{\partial v_\alpha}{\partial X_\alpha}\right|_{X_\alpha=0} + \sum_{j=1}^{n}\rho_j\lambda_j\left.\frac{\partial v_j}{\partial X_j}\right|_{X_j=0} + \rho_1 I_{\text{ext}}(T), \tag{B.9}$$

where the prefactor ρ_1 to the external current makes it equivalent to $I(T)$ applied at $X_1 = 0$ on dendrite 1. It is straightforward to see how discretisation of (B.9) leads to a form of calculating v^{i+1}_σ as in (B.8). For a nominal soma, we use the fact that $\rho_j = 2\pi a_j\lambda_j g_j/(g_\sigma A_\sigma)$ and take the somatic area $A_\sigma = 0$ to yield

$$2\pi a_\alpha\lambda_\alpha^2 g_\alpha\left.\frac{\partial v_\alpha}{\partial X_\alpha}\right|_{X_\alpha=0} + \sum_{j=1}^{n}2\pi a_j\lambda_j^2 g_j\left.\frac{\partial v_j}{\partial X_j}\right|_{X_j=0} + 2\pi a_1\lambda_1 g_1 I_{\text{ext}}(T) = 0, \tag{B.10}$$

which after assuming identical dendrites and noting $a_1/a_\alpha = \beta_\alpha\lambda_1^2/\lambda_\alpha^2$ gives

$$\lambda_\alpha^4\left.\frac{\partial v_\alpha}{\partial X_\alpha}\right|_{X_\alpha=0} + \beta_\alpha^2\lambda_1^4\sum_{j=1}^{n}\left.\frac{\partial v_j}{\partial X_j}\right|_{X_j=0} + \beta_\alpha^2\lambda_1^3 I_{\text{ext}}(t) = 0. \tag{B.11}$$

This equation can then be discretised in the same manner as (B.4) and rearranged to ultimately yield

$$v_0^{i+1}\left(\frac{\lambda_\alpha^4}{\Delta_{X\alpha}} + n\frac{\beta_\alpha^2\lambda_1^4}{\Delta_{X1}}\right) = \frac{\lambda_\alpha^4}{\Delta_{X\alpha}}v^{i+1}_{(\alpha,1/2)} + \frac{\beta_\alpha^2\lambda_1^4}{\Delta_{X1}}\sum_{j=1}^{n}v^{i+1}_{(j,1/2)} + \frac{\beta_\alpha^2\lambda_1^3}{2}I^{i+1}. \tag{B.12}$$

Threshold and Reset

For threshold-reset simulations, the trigger position X_{th} is given a single discrete location. If the initial calculation of the potential at the trigger position exceeds threshold, then the potential and spatial derivative at all locations in all the neurites is reset

$$\text{If} \quad v_{X_{\text{th}}}^{i+1} > v_{\text{th}}, \text{ then} \quad v_{(j,k+1/2)}^{i+1} = v_{\text{re}}, \quad \partial_X v_{j,k}^{i+1} = 0 \quad \forall j,k. \tag{B.13}$$

Note that neither the synaptic variable s or the quasi-active variable w are reset.

B.1.2 Fourier Mode Decomposition

An approach employed by Tuckwell [201] is to decompose the voltage, synaptic drive and noise into Fourier modes with spatial eigenfunctions $\phi_n(x)$

$$\begin{aligned} v(x,t) &= \sum_{n=0}^{\infty} \phi_n(x) v_n(t), \quad s(x,t) = \sum_{n=0}^{\infty} \phi_n(x) s_n(t), \\ \xi(x,t) &= \sum_{n=0}^{\infty} \phi_n(x) \xi_n(t), \end{aligned} \tag{B.14}$$

where in this subsection we will describe space and time in terms of dimensionless variables (x,t). For a quasi-active cable, we can decompose w_n in the same manner. As mentioned in the main text, this decomposition can be used as an alternative approach for finding the second moments analytically. Where possible eigenfunctions $\phi_n(x)$ are chosen to be orthonormal to each other (but see [202])

$$\int_{\mathcal{R}} \phi_n(x)\phi_m(x)\mathrm{d}x = \delta_{mn}, \tag{B.15}$$

where δ_{mn} is the Kronecker delta function. For a cable of dimensionless length l with sealed ends we find

$$\phi_n(x) = \begin{cases} \frac{1}{\sqrt{l}}, & n = 0 \\ \sqrt{\frac{2}{l}} \cos\left(\frac{n\pi x}{l}\right), & n = 1,2,3,... \end{cases}. \tag{B.16}$$

Substituting (B.14) into the passive cable equation, we find for a single mode the $\phi_n(x)$ factors cancel (as required for an eigenfunction)

$$\frac{\mathrm{d}v_n}{\mathrm{d}t} = -\mu_n v_n + s_n, \quad \mu_n = 1 + \frac{n^2\pi^2}{l^2}. \tag{B.17}$$

Here μ_n is the eigenvalue associate with eigenfunction ϕ_n. For white noise $s_n = 2\sigma_w \xi_n(t)$, while for coloured noise

$$\beta_s \frac{\mathrm{d}s_n}{\mathrm{d}t} = -s_n + 2\sigma_s \sqrt{\beta_s} \xi_n(t). \tag{B.18}$$

Note that we have converted an SPDE to a SDE. This means that rather than generating v at different spatial positions and times, we generate v at different modes and times. Once we have a reasonable number of modes, we can substitute the generated $v_n(t)$ into (B.14) and choose any position x to acquire the voltage. Thus this method has the advantage of arbitrary spatial fidelity. Furthermore, we avoid the von Neumann stability criterion by reducing the problem to an SDE and can thus choose higher Δ_t thus reducing simulation speed. However, it should be noted that we still have a stability condition that depends on Δ_t, n and l. Applying the Euler-Maruyama method to (B.17), we obtain

$$v_n(t + \Delta_t) = (1 - \mu_n \Delta_t) v_n(t) + \Delta_t s_n(t). \tag{B.19}$$

To ensure that the voltage tends back towards the mean, for the discretised equation we require $|1 - \mu_n \Delta_t| < 1$. To illustrate, we substitute in μ_n for the sealed dendrite and look at when instability occurs for $(1 - \mu_n \Delta_t) < -1$

$$1 - \left(1 + \frac{n^2 \pi^2}{l^2}\right) \Delta_t < -1. \tag{B.20}$$

This shows that instability is made easier for larger Δ_t, higher n and lower l. In fact, given high enough n, the numerical scheme becomes unstable. This is important as it gives an upper limit for mode simulation; simulating modes above this value of n will introduce inaccuracies.

While this method is mathematically elegant and can be computationally more convenient than the forward Euler method, its biggest disadvantage is that it is much more difficult to apply to morphologies with an electrically significant soma, axon or branching dendrites.

B.2 Dynamic Response Simulation

Due to the linearity of the cable equation and the small amplitude dynamic response, if we let the input have K oscillatory terms each at a different frequency Ω_j with

input amplitude ϵ_j and phase ψ_j

$$I(t) = I_0 + \sum_{j=1}^{K} \epsilon_j I_j \sin(\Omega_j t + \psi_j), \tag{B.21}$$

provided that every ϵ_j is small and that the sum of ϵ_j is small, the output firing rate will have the form

$$r(t) = r_0 + \sum_{j=1}^{K} \epsilon_j r_j \sin(\Omega_j t + \phi_j + \psi_j). \tag{B.22}$$

Each simulation yields a spike train $\chi(t)$, where $\chi(t) = 1$ if there is a spike at t and zero otherwise. These simulations may be repeated R times to give an experimental probability of spiking $\langle \chi(t) \rangle_R$. With time regularly discretised with time-step Δt, an approximation of the instantaneous firing rate is given by

$$\hat{r}(t) = \frac{\langle \chi(t) \rangle_R}{\Delta t}. \tag{B.23}$$

The discrete Fourier transform method we employ involves multiplying the (B.23) by an exponential at the frequency we wish to extract, Ω_k, and integrated over the duration of the simulation T

$$\mathcal{I} = \int_0^T e^{i\Omega_k t} \hat{r}(t) dt = \int_0^T e^{i\Omega_k t} \left[\hat{r}_0 + \sum_{j=1}^{K} \epsilon_j \hat{r}_j \sin(\Omega_j t + \hat{\phi}_j + \psi_j) \right] \mathrm{d}t. \tag{B.24}$$

Note that we know the input amplitudes ϵ_j and phases ψ_j, but the output amplitudes $\hat{r}_j$ and $\hat{r}_j$ are estimates from the simulation. If we let T be an integer number of periods of *all* of the input frequencies (implying that each input frequency is an integer multiple of the lowest frequency), then we can utilise the following relations

$$\int_0^{n_j P_j} \sin(\Omega_j t) \sin(\Omega_k t) \mathrm{d}t = \delta_{jk} \frac{n_j P_j}{2} = \int_0^{n_j P_j} \cos(\Omega_j t) \cos(\Omega_k t) \mathrm{d}t. \tag{B.25}$$

Separating out the phase using the compound angle formula

$$\sin(\Omega_j t + \hat{\phi}_j + \psi_j) = \sin(\Omega_j t) \cos(\hat{\phi}_j + \psi_j) + \cos(\Omega_j t) \sin(\hat{\phi}_j + \psi_j), \tag{B.26}$$

the integral (B.24) becomes

$$\mathcal{I} = \frac{n_k P_k \epsilon_k \hat{r}_k}{2} \left[i \cos(\hat{\phi}_k + \psi_k) + \sin(\hat{\phi}_k + \psi_k) \right] = \frac{iT \epsilon_k \hat{r}_k}{2} e^{-i(\hat{\phi}_k + \psi_k)}. \tag{B.27}$$

We can discretise the Fourier transform (B.24) as

$$\mathcal{I} \approx \sum_m e^{i\Omega_k t_m} \hat{r}(t_m) \Delta t = \hat{\mathcal{I}}, \tag{B.28}$$

which thus means we can extract the amplitude and phase estimates for frequency k as

$$|\hat{r}_k| = \frac{2}{\epsilon_k T} |\hat{\mathcal{I}}|, \quad \hat{\phi}_k = \frac{\pi}{2} - \psi_k - \arg\left(\hat{\mathcal{I}}\right). \tag{B.29}$$

This method shows how we can choose the amplitudes and phase so that all frequencies have the same effective output amplitude $\epsilon_k r_k$ and effective phase $\phi_k + \psi_k$. Supposing that we want to fix all the outputs to have the same amplitude and phase as $k = 1$, then this implies that

$$\epsilon_k = \epsilon_1 \frac{r_1}{r_k}, \quad \psi_k = \phi_1 + \psi_1 - \phi_k, \tag{B.30}$$

where here r_k and ϕ_k are the theoretically predicted values.

Appendix C

Additional Results

C.1 Verification of the Diffusion Approximation

While the diffusion approximation used for incoming synaptic drive has been tested for point-neuron models [84,165,169], relatively less studied is a comparison between a spatially distributed shot-noise process and a Gaussian one (though see [203] for a mathematically rigorous proof of convergence). A key feature of the Gaussian approximation to synaptic drive is that the distribution of the potential v itself becomes Gaussian in distribution. This is assumed by the upcrossing formulae given in this thesis. While one can match the voltage mean $\langle v \rangle$ and standard deviation σ_v between a shot noise process and a Gaussian one, the distribution from shot noise will be positively skewed. Therefore, we test the validity of the diffusion approximation by simulating a spatial shot-noise process and measuring the skew of v, which should approach the Gaussian value of zero.

C.1.1 White Noise

With a white shot-noise process of fixed amplitude Δ_v and spatially uniform arrival rate r_s, the cable equation for the potential measured from E_L is

$$\tau_v \frac{\partial v}{\partial t} = -v + \lambda^2 \frac{\partial^2 v}{\partial X^2} + \Delta_v \tau_v \lambda \sum_{\{T_{sk}\}} \delta(T - T_{sk}) \delta(X - X_{sk}) \tag{C.1}$$

The voltage standard deviation σ_v is varied between simulations, while $\langle v \rangle = \Delta_v \tau_v r_s$ is kept constant. As expected, the voltage distribution from shot noise becomes more symmetric as $\langle v \rangle / \sigma_v$ increases, Figure C.1. The skew is always positive and converges to zero as $\sim (\langle v \rangle / \sigma_v)^{-1}$, Figure C.1(d).

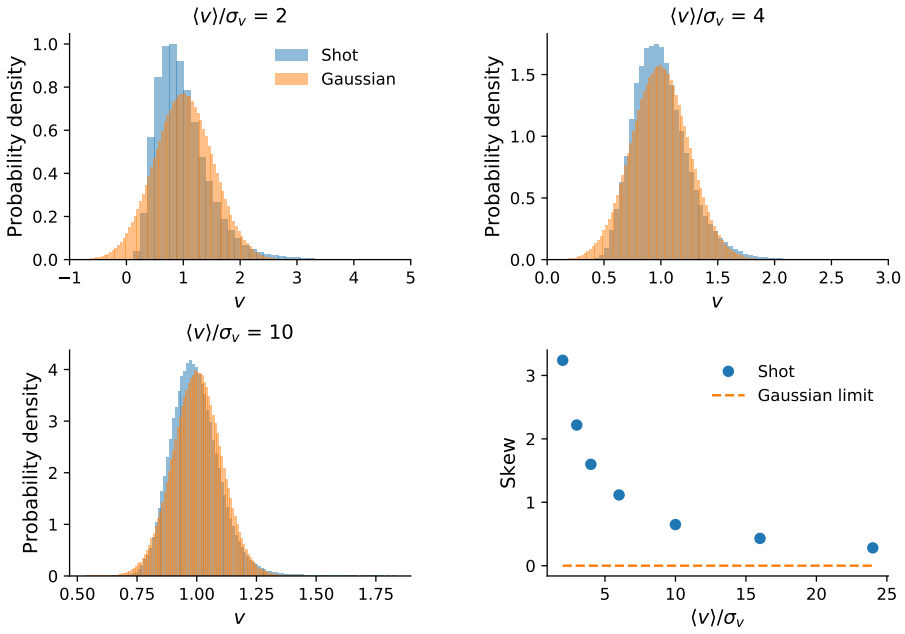

Figure C.1: A comparison of the voltage distributions from white shot-noise drive to white Gaussian drive shows that $\langle v \rangle / \sigma_v >> 1$ is required for the diffusion approximation to be applicable.

C.1.2 Coloured Noise

For coloured shot-noise drive of fixed synaptic amplitude Δ_s, the equations of interest are

$$\tau_v \frac{\partial v}{\partial t} = -v + \lambda^2 \frac{\partial^2 v}{\partial X^2} + s(x,t), \quad \tau_s \frac{\partial s}{\partial t} = -s + \Delta_s \tau_s \lambda \sum_{\{T_{sk}\}} \delta(T - T_{sk}) \delta(X - X_{sk}) \tag{C.2}$$

For this case, we instead focus on the ratio between the mean of the synaptic variable μ_s (which should equal $\langle v \rangle$) to the synaptic noise intensity σ_s. This is because the diffusion approximation is applied to the equation for the synaptic conductance rather than the voltage itself. However, we still measure the effectiveness of the diffusion approximation in terms of the skew of the voltage distribution. We find that convergence to the Gaussian distribution is much faster for coloured-noise drive as compared with white-noise drive, Figure C.2.

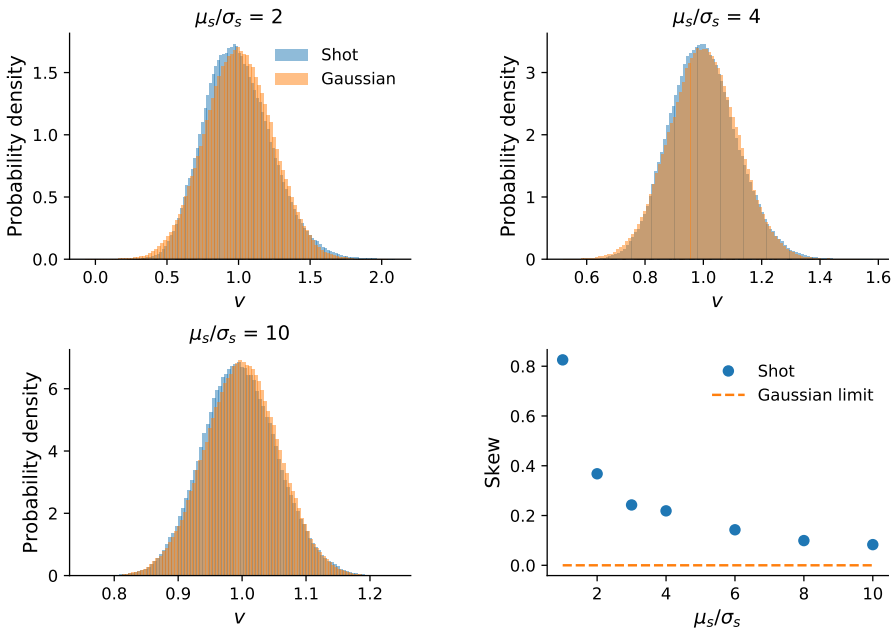

Figure C.2: A comparison of the voltage distributions coloured shot-noise drive to coloured Gaussian drive shows that $\mu_s/\sigma_s >> 1$ is required for the diffusion approximation to be applicable, though convergence is much faster than for white-noise drive.

C.2 Validity of the Upcrossing Approximation

The accuracy of the upcrossing method was calculated in a manner similar to [9] but parametrized differently. This was determined calculating the relative error ε_r between simulated upcrossing rate $\hat{r}_{\text{uc}}$ and the simulated threshold-reset rate $\hat{r}_{\text{tr}}$, i.e.

$$\varepsilon_r = \frac{\hat{r}_{\text{uc}} - \hat{r}_{\text{tr}}}{\hat{r}_{\text{tr}}}. \tag{C.3}$$

Thus $\varepsilon_r < 0$ indicates that the upcrossing approximation underestimates the true firing rate while $\varepsilon_r > 0$ shows an overestimate.

Each simulation was performed in terms of dimensionless parameters, in particular: the distance between the threshold and the mean in terms of the voltage variance, $(v_{\text{th}} - \langle v \rangle)/\sigma_v$, the relative synaptic timescale $\beta_s = \tau_s/\tau_v$, the relative somatic time constant $\beta_\sigma = \tau_\sigma/\tau_1$, the dendritic dominance factor ρ, the dimensionless trigger position $x_{\text{th}}/\lambda_\alpha$, and the relative axonal size λ_α/λ_1.

C.2.1 Passive Neurons

Point Neuron and Infinite Dendrite

For $(v_{\text{th}} - \mu)/\sigma_v = 3$, there is a larger range of β_s for the point-neuron model than the infinite dendrite for which the upcrossing approximation is within 10% of the threshold-reset rate. The exact quantitative reasons this seem beyond obvious considerations of spatial discretisation and likely requires highly complicated analysis to uncover.

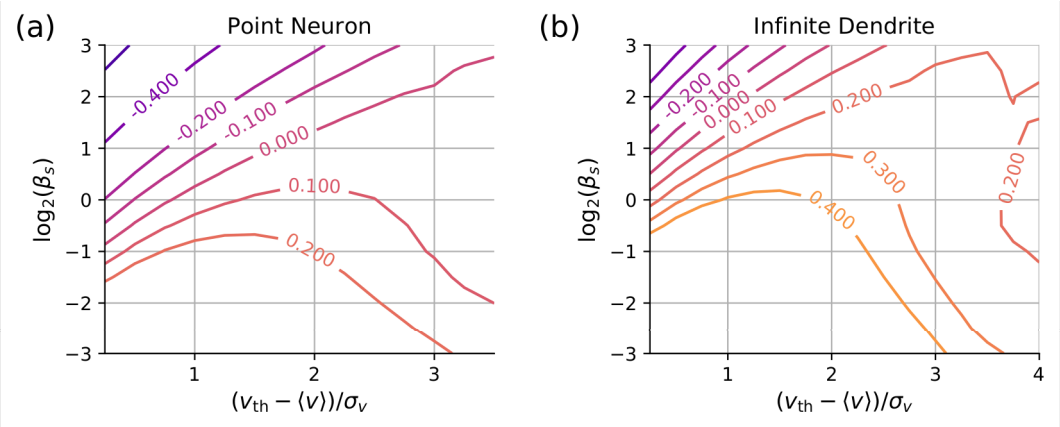

Figure C.3: With contours showing the relative error of upcrossing simulations (C.3): (a) For the point neuron, the upcrossing method approximates the threshold-reset process best for higher relative threshold, $(v_{\text{th}} - \mu)/\sigma_v$ and for $\beta_s \sim 1$. (b) The upcrossing method approximates the threshold-reset process well over a narrower window at higher β_s for the infinite dendrite than the point neuron.

Dendrite-and-Axon Model

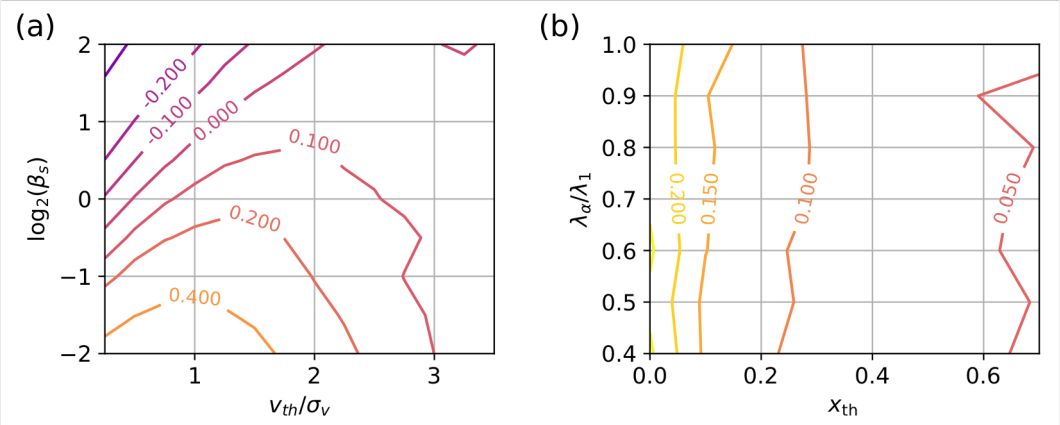

Figure C.4: Contours showing the relative error of the passive dendrite-and-axon model. (a) With the addition of the passive axon and a trigger position of $X_{\text{th}} = 30\mu$m, the area for which the relative error is around 10% is broader than the infinite dendrite. (b) Focussing on $(v_{\text{th}} - \langle v \rangle)/\sigma_v = 3$ and $\beta_s = 0.5$, the relative error decreases as dimensionless trigger position x_{th} is moved further along the axon, while remaining reasonably invariant to the relative axonal size λ_α/λ_1. Other parameters: (a-b) $\lambda_1 = 200\mu$m, (a) $\lambda_\alpha = 100\mu$m.

Ball-and-Stick Model

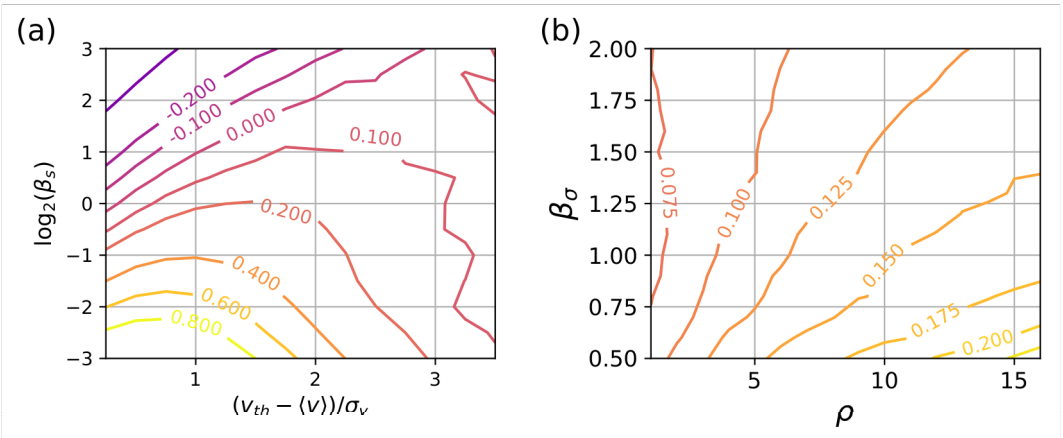

Figure C.5: For the passive ball-and-stick model, the relative error of the upcrossing approximation is (a) lower than the infinite dendrite case for a broader range of β_s and $(v_{\text{th}}-\langle v\rangle)/\sigma_v$ for $\rho = 4$, $\beta_\sigma = 7/6$. (b) Investigating the effect of the soma around the point $(v_{\text{th}} - \langle v\rangle)/\sigma_v = 3$, $\beta_s = 0.5$, increasing the somatic size (lower ρ) and time constant (larger β_0) increases the accuracy of the upcrossing approximation.

C.2.2 Quasi-Active Neurons

Point neuron

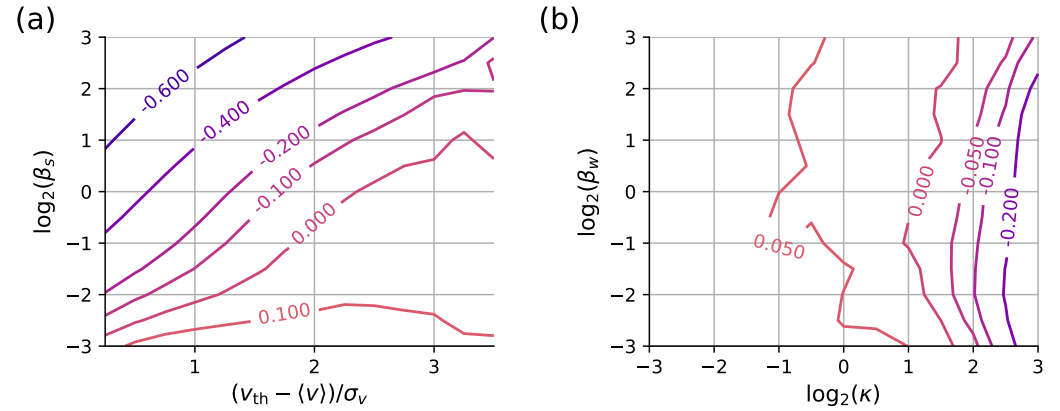

Figure C.6: With contours showing the relative error between upcrossing and threshold-reset simulations for the quasi-active point-neuron model: (a) The linearised active current shifts the area of maximal accuracy of the upcrossing method to smaller β_s. (b) The relative error of the upcrossing method is reasonably stable across a range of κ and β_w, and is more sensitive to changes in κ, especially as it increases. The relative error is smallest for $\kappa \sim 2$. Other parameters: (a-b) $v_{\text{th}} = 10\text{mV}$, (a) $\beta_w = 1.5$, $\kappa = 0.55$, (b) $(v_{\text{th}} - \langle v\rangle)/\sigma_v = 3$, $\beta_s = 0.5$.

Infinite Dendrite

These panels show that the presence of an active current moves the area of good approximation to lower values of β_s (c.f. 2.3 in Chapter 2), and that stronger coupling reduces the error of the approximation up to $\kappa \sim 4$.

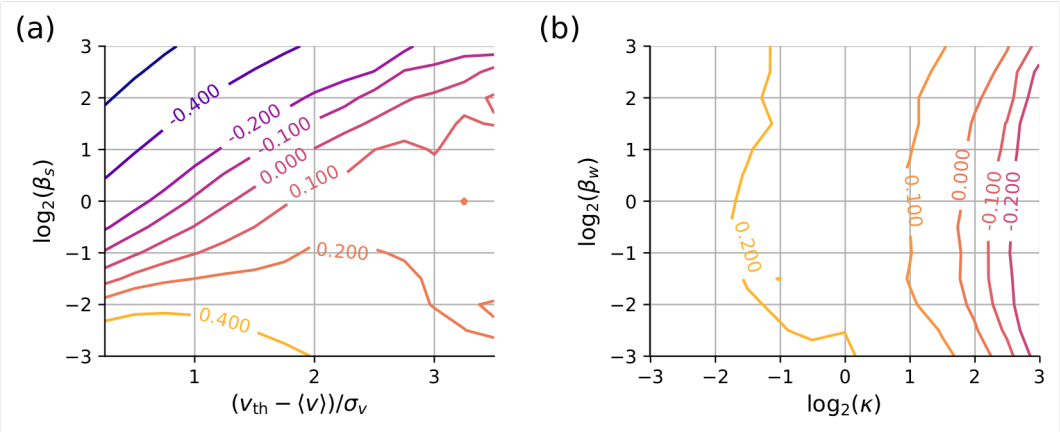

Figure C.7: (a) The upcrossing method for the quasi-active dendrite is more accurate over the passive dendrite with respect to β_s and $(v_{\text{th}} - \langle v \rangle)/\sigma_v$. (b) κ has a stronger influence over the upcrossing accuracy than β_w, with accuracy highest for $\kappa \sim 2$. Other parameters: (a) $\beta_w = 1.5$, $\kappa = 0.55$, (b) $(v_{\text{th}} - \langle v \rangle)/\sigma_v = 3$.

C.3 Multiple Dendrites and Axon: Dynamic Response

With multiple dendrites, we can choose a different phase and frequency for each input dendrite. However, we are operating under the linear approximation with small amplitude oscillations, this would simply be a superposition of inputs. Thus for this model we will largely focus on first the effect of a single modulation frequency in one of n dendrites and then apply this to all n dendrites.

C.3.1 Current Modulation

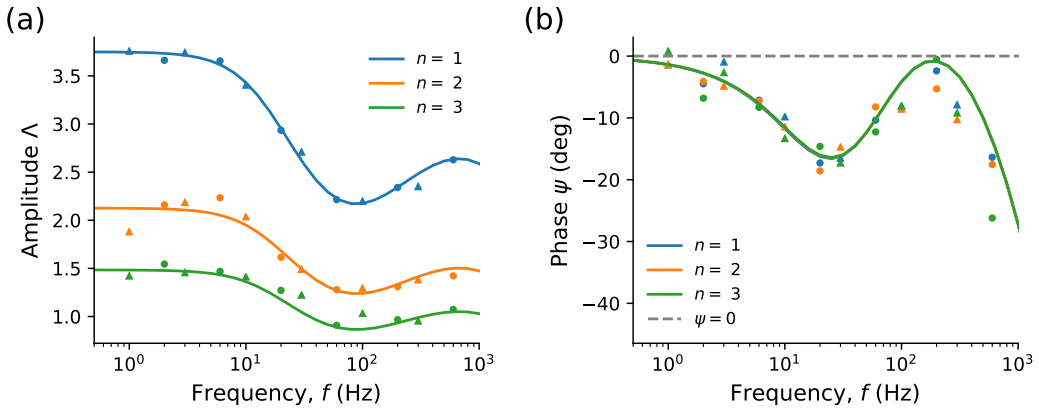

Figure C.8: (a) For current modulation at $x_c = 0$ with multiple dendrites, the dynamic firing response amplitude decreases with n. (b) The phase remains practically unchanged with n. Solid lines show the theoretical upcrossing-rate response, while circle and triangles denote upcrossing and threshold-reset simulations respectively. Other parameters: $\tau_1 = 10\text{ms}$, $\tau_s = 5\text{ms}$, $\lambda_1 = 200\mu\text{m}$, $\lambda_\alpha = 100\mu\text{m}$, $\beta_\alpha = 7/6$, $u_{\text{th}}/\sigma_u = 3$, $X_{\text{th}} = 30\mu\text{m}$

C.3.2 Mean Modulation

The oscillatory amplitude of the axonal mean from modulation at one of n dendrites is given by

$$\langle u \rangle_1 = \frac{\beta_\alpha^2 \lambda_1^3 e^{-x_{\text{th}}\Gamma_\alpha}}{\Gamma_1(1 + i\Omega\beta_s)(n\beta_\alpha^2\lambda_1^3\Gamma_1 + \lambda_\alpha^3\Gamma_\alpha)}. \tag{C.4}$$

If we apply the same oscillatory input along each dendrite, then we simply scale this result by n. For this particular case, as $n \to \infty$, we obtain $\langle u \rangle_1 \to e^{-x_{\text{th}}\Gamma_\alpha}/[(1 + i\Omega\beta_s)\Gamma_1^2]$. This limit shows that the axonal load becomes negligible for large n but the path length along the axon from the soma retains its effect on the mean.

Remarkably, we find that for fixed u_{th}/σ_u that while the magnitude Λ increases monotonically across all frequencies towards a finite limit with n, the phase ψ remains virtually unchanged, as shown in Figure C.9. The increase in Λ with n increases as the axonal length constant λ_α increases, though the overall effect is still quite small.

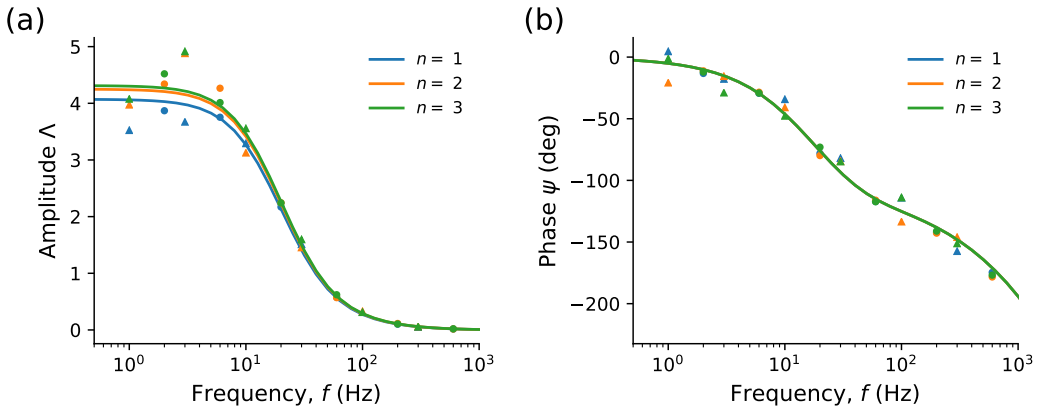

Figure C.9: (a) For mean modulation in multiple dendrites, the dynamic firing response increases slightly with dendritic number n. (b) However the phase remains unchanged. Solid lines show the theoretical upcrossing-rate response, while circle and triangles denote upcrossing and threshold-reset simulations respectively. Other parameters: $\tau_1 = 10\text{ms}$, $\tau_s = 5\text{ms}$, $\lambda_1 = 200\mu\text{m}$, $\lambda_\alpha = 100\mu\text{m}$, $\beta_\alpha = 7/6$, $u_{\text{th}}/\sigma_u = 3$, $X_{\text{th}} = 30\mu\text{m}$

C.3.3 Variance Modulation

For variance modulation, the second moments can be obtained by multiplying (3.90) by n and using the n-dendrite Green's function. We see in Figure C.10 that for a fixed steady-state variance $[\sigma_u^2]_0$ and $u_{\text{th}}/[\sigma_u]$, the dynamic response is virtually identical with n in both amplitude and phase.

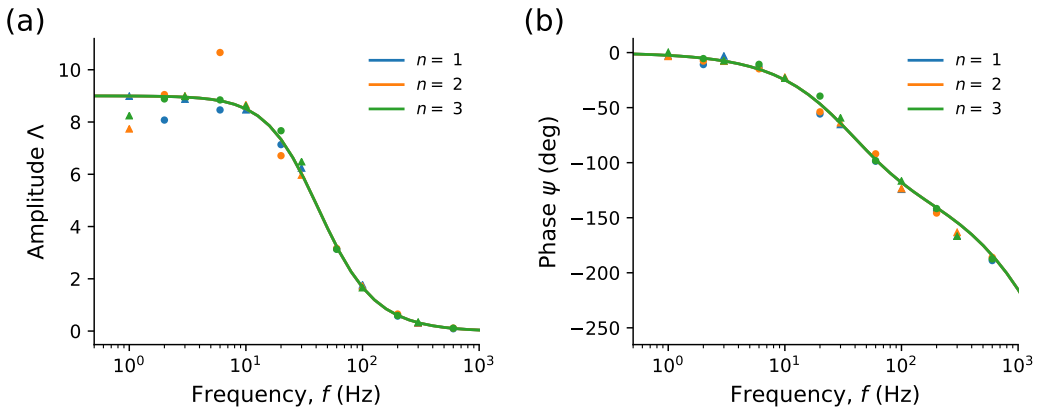

Figure C.10: For variance modulation in multiple dendrites, the dynamic firing response does not change with dendritic number n. Solid lines show the theoretical upcrossing-rate response, while circle and triangles denote upcrossing and threshold-reset simulations respectively. Parameters: $\tau_1 = 10\text{ms}$, $\tau_s = 5\text{ms}$, $\lambda_1 = 200\mu\text{m}$, $\lambda_\alpha = 100\mu\text{m}$, $\beta_\alpha = 7/6$, $u_{\text{th}}/\sigma_u = 3$, $X_{\text{th}} = 30\mu\text{m}$.

C.4 Variance Modulation in Quasi-Active Neurons

C.4.1 Point-Neuron Model Analysis

Here we show in Figure C.11(a) the of the magnitude of the shifted subthreshold response $|\tilde{Z}(\Omega-\omega)|$ (5.2) for three values of Ω. The integrand of $[\sigma_u^2]_0$ is proportional to $\tilde{Z}(\Omega-\omega)Z(\omega)$ (A.76), and in Figure C.11(b) we see that the area under the curve is highest for $\Omega = 0$ (corresponding to the low-frequency limit), then followed by $\Omega = 4$ (roughly corresponding to the peak in Figure 5.5(a)), and with $\Omega = 2$ being the smallest of the three values chosen (roughly corresponding to the trough in Figure 5.5(a)).

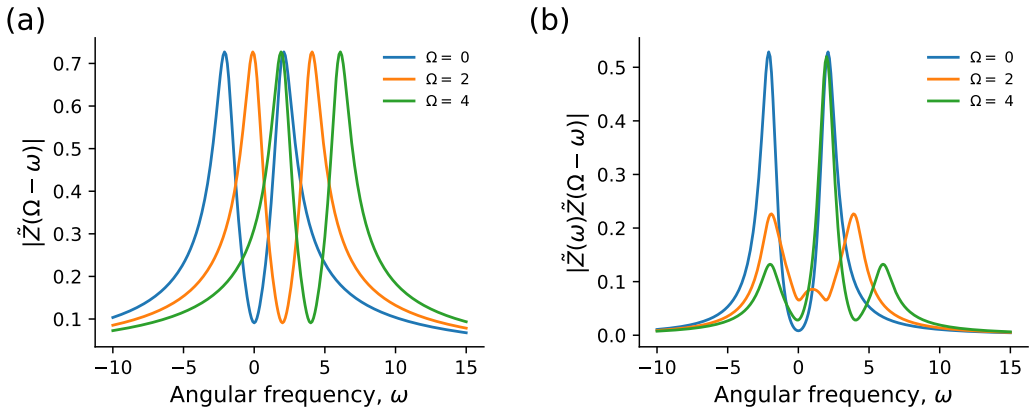

Figure C.11: (a) The subthreshold response magnitude $|\tilde{Z}|$ (5.2) for the quasi-active point-neuron model is shown when the minimum has been shifted to align with the positive maximum ($\Omega = 2$) and when the lower maximum has been shifted to align with the positive maximum ($\Omega = 4$). (b) The product $|\tilde{Z}(\omega)\tilde{Z}(\Omega-\omega)|$is predictably lowest for the $\Omega = 2$ case and increases again for the $\Omega = 4$ shift. $\kappa = 10$, $\beta_w = 2.5$ are used to make the peaks prominent.

C.4.2 Ball-and-Stick Model

With variance modulation applied to the quasi-active ball-and-stick model we set the parameters to have the same values as the infinite model and set $\kappa = 10$ to recreate the high-frequency amplitude peak. As we decrease ρ we see in Figure C.12 that this peak frequency decreases, becoming less noticeable compared to the general low-pass filter curve.

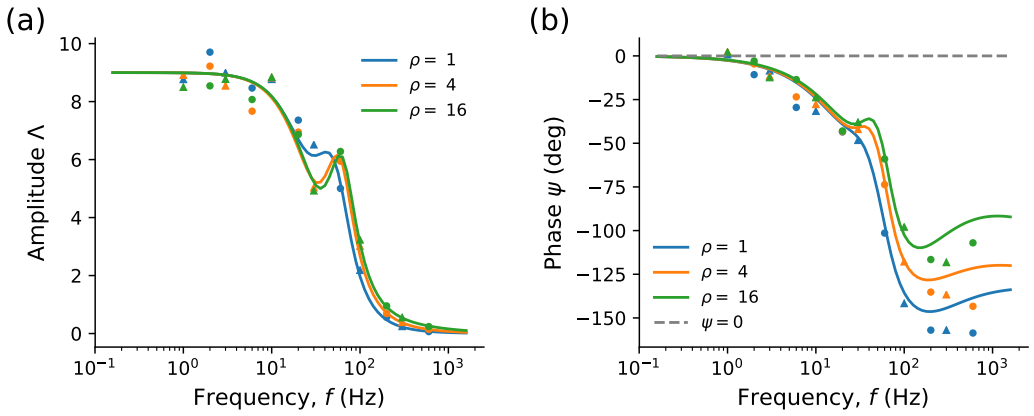

Figure C.12: For variance modulation applied to the quasi-active ball-and-stick neuron, decreasing ρ (a) reduces the prominence of the amplitude peak and (b) causes the phase to decay more quickly. Solid lines show the theoretical upcrossing-rate response, while circle and triangles denote upcrossing and threshold-reset simulations respectively. Other parameters: $\lambda = 100\mu$m, $\beta_\sigma = 7/6$, $\beta_w = 2.5$, $\kappa = 10$, $\beta_s = 0.5$, $u_{\text{th}}/[\sigma_u]_0 = 3$.

C.4.3 Dendrite-and-Axon Model

With variance modulation applied to the quasi-active dendrite and passive axon model, we note from Figure C.13 that the trigger position has very little effect on the amplitude and only affects the phase at high frequencies.

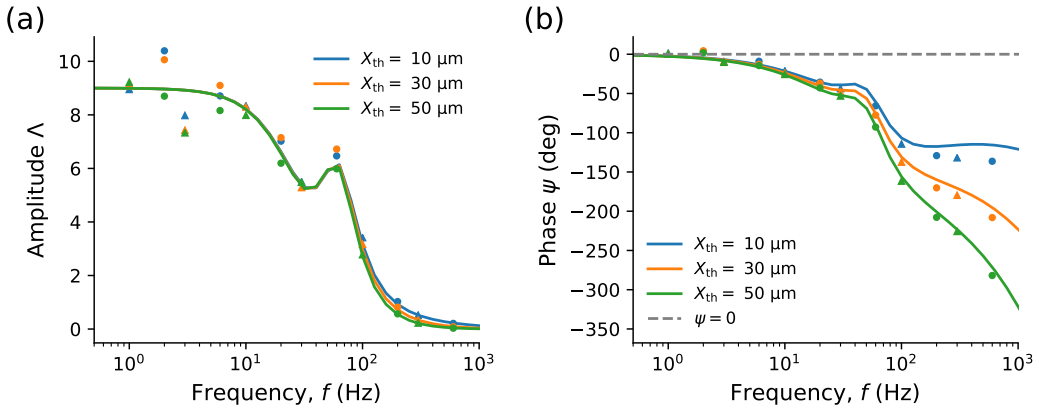

Figure C.13: Increasing the trigger position for variance modulation applied to the quasi-active dendrite and passive axon: (a) has little effect on the amplitude, (b) causes the phase to decrease more rapidly. Solid lines show the theoretical upcrossing-rate response, while circle and triangles denote upcrossing and threshold-reset simulations respectively. Other parameters: $\lambda_1 = 200\mu$m, $\lambda_\alpha = 100\mu$m, $\beta_\alpha = 7/6$, $\beta_w = 2.5$, $\kappa = 10$, $\beta_s = 0.5$, $u_{\text{th}}/\sigma_u = 3$.

Bibliography

[1] W. W. Lytton, "Computer modelling of epilepsy," *Nature Reviews Neuroscience*, vol. 9, pp. 626–637, Aug. 2008.

[2] P. J. Uhlhaas and W. Singer, "Abnormal neural oscillations and synchrony in schizophrenia," *Nature Reviews Neuroscience*, vol. 11, no. 2, pp. 100–113, 2010.

[3] H. Bergman and G. Deuschl, "Pathophysiology of Parkinson's disease: From clinical neurology to basic neuroscience and back," *Movement Disorders*, vol. 17, pp. S28–S40, Mar. 2002.

[4] D. Hassabis, D. Kumaran, C. Summerfield, and M. Botvinick, "Neuroscience-Inspired Artificial Intelligence," *Neuron*, vol. 95, pp. 245–258, July 2017.

[5] N. Brunel and V. Hakim, "Fast global oscillations in networks of integrate-and-fire neurons with low firing rates," *Neural computation*, vol. 11, no. 7, pp. 1621–1671, 1999.

[6] B. Lindner and L. Schimansky-Geier, "Transmission of Noise Coded versus Additive Signals through a Neuronal Ensemble," *Physical Review Letters*, vol. 86, pp. 2934–2937, Apr. 2001.

[7] A. N. Burkitt, "A review of the integrate-and-fire neuron model: I. Homogeneous synaptic input," *Biological Cybernetics*, vol. 95, no. 1, pp. 1–19, 2006.

[8] A. N. Burkitt, "A review of the integrate-and-fire neuron model: II. Inhomogeneous synaptic input and network properties," *Biological Cybernetics*, vol. 95, pp. 97–112, Aug. 2006.

[9] L. Badel, "Firing statistics and correlations in spiking neurons: A level-crossing approach," *Physical Review E - Statistical, Nonlinear, and Soft Matter Physics*, vol. 84, no. 4, 2011.

[10] P. Lánský and R. Rodriguez, "Two-compartment stochastic model of a neuron," *Physica D: Nonlinear Phenomena*, vol. 132, pp. 267–286, July 1999.

[11] S. Ostojic, G. Szapiro, E. Schwartz, B. Barbour, N. Brunel, and V. Hakim, "Neuronal morphology generates high-frequency firing resonance," *Journal of Neuroscience*, vol. 35, no. 18, pp. 7056–7068, 2015.

[12] J. Ladenbauer and K. Obermayer, "Weak electric fields promote resonance in neuronal spiking activity: Analytical results from two-compartment cell and network models," *PLOS Computational Biology*, vol. 15, p. e1006974, Apr. 2019.

[13] S. Petersen and O. Sporns, "Brain Networks and Cognitive Architectures," *Neuron*, vol. 88, pp. 207–219, Oct. 2015.

[14] R. S. Cajal, *Histology of the Nervous System of Man and Vertebrates (History of Neuroscience, No 6)(2 Volume Set)*. Oxford: Oxford University Press, 1995.

[15] C. Thome, T. Kelly, A. Yanez, C. Schultz, M. Engelhardt, S. Cambridge, M. Both, A. Draguhn, H. Beck, and A. Egorov, "Axon-Carrying Dendrites Convey Privileged Synaptic Input in Hippocampal Neurons," *Neuron*, vol. 83, pp. 1418–1430, Sept. 2014.

[16] M. S. Hamada, S. Goethals, S. I. D. Vries, R. Brette, and M. H. P. Kole, "Covariation of axon initial segment location and dendritic tree normalizes the somatic action potential," *PNAS*, vol. 113, no. 51, 2016.

[17] D. Schmitz, S. Schuchmann, A. Fisahn, A. Draguhn, E. H. Buhl, E. Petrasch-Parwez, R. Dermietzel, U. Heinemann, and R. D. Traub, "Axo-Axonal Coupling: A Novel Mechanism for Ultrafast Neuronal Communication," *Neuron*, vol. 31, no. 5, pp. 831–840, 2001.

[18] M. London and M. Häusser, "Dendritic Computation," *Annual Review of Neuroscience*, vol. 28, pp. 503–532, 2005.

[19] N. Spruston, "Pyramidal neurons : dendritic structure and synaptic integration," *Nature Reviews Neuroscience*, vol. 9, pp. 206–221, 2008.

[20] T. Branco and M. Husser, "The single dendritic branch as a fundamental functional unit in the nervous system," *Current Opinion in Neurobiology*, vol. 20, pp. 494–502, Aug. 2010.

[21] H. Cuntz, M. Remme, and B. Torben-Nielsen, *The computing dendrite*, vol. 10. Springer, 2014.

[22] C. Grienberger, X. Chen, and A. Konnerth, "Dendritic function in vivo," *Trends in Neurosciences*, vol. 38, pp. 45–54, Jan. 2015.

[23] H. Markram, M. Toledo-Rodriguez, Y. Wang, A. Gupta, G. Silberberg, and C. Wu, "Interneurons of the neocortical inhibitory system," *Nature Reviews Neuroscience*, vol. 5, no. 10, pp. 793–807, 2004.

[24] C. A. Anastassiou, R. Perin, H. Markram, and C. Koch, "Ephaptic coupling of cortical neurons," *Nature neuroscience*, vol. 14, no. 2, pp. 217–223, 2011.

[25] G. N. Elston, "Cortex, Cognition and the Cell: New Insights into the Pyramidal Neuron and Prefrontal Function," *Cerebral Cortex*, vol. 13, pp. 1124–1138, Nov. 2003.

[26] M. Wehr and A. M. Zador, "Balanced inhibition underlies tuning and sharpens spike timing in auditory cortex," *Nature*, vol. 426, pp. 442–446, Nov. 2003.

[27] C. Poo and J. S. Isaacson, "Odor Representations in Olfactory Cortex: Sparse Coding, Global Inhibition, and Oscillations," *Neuron*, vol. 62, pp. 850–861, June 2009.

[28] P. Sauseng, B. Griesmayr, R. Freunberger, and W. Klimesch, "Control mechanisms in working memory: A possible function of EEG theta oscillations," *Neuroscience & Biobehavioral Reviews*, vol. 34, pp. 1015–1022, June 2010.

[29] M. Abeles, "Corticonics: Neural circuits of the cerebral cortex," ch. 1, pp. 49–59, Cambridge University Press, 1991.

[30] A. U. Larkman, "Dendritic Morphology of Pyramidal Neurones of the Visual Cortex of the Rat: III. Spine Distributions," *the Journal of Comparative Neurology*, vol. 306, pp. 332–343, 1991.

[31] A. Larkman and A. Mason, "Correlations between morphology and electrophysiology of pyramidal neurons in slices of rat visual cortex. I. Establishment of cell classes," *The Journal of Neuroscience*, vol. 10, pp. 1407–1414, May 1990.

[32] K. I. van Aerde and D. Feldmeyer, "Morphological and Physiological Characterization of Pyramidal Neuron Subtypes in Rat Medial Prefrontal Cortex," *Cerebral Cortex*, vol. 25, pp. 788–805, Oct. 2013.

[33] S. Ramaswamy and H. Markram, "Anatomy and physiology of the thick-tufted layer 5 pyramidal neuron," *Frontiers in Cellular Neuroscience*, vol. 9, June 2015.

[34] H. Mohan, M. B. Verhoog, K. K. Doreswamy, G. Eyal, R. Aardse, B. N. Lodder, N. A. Goriounova, B. Asamoah, A. C. B. Brakspear, C. Groot, S. van der Sluis, G. Testa-Silva, J. Obermayer, Z. S. Boudewijns, R. T. Narayanan, J. C. Baayen, I. Segev, H. D. Mansvelder, and C. P. de Kock, "Dendritic and Axonal Architecture of Individual Pyramidal Neurons across Layers of Adult Human Neocortex," *Cerebral Cortex*, vol. 25, pp. 4839–4853, Dec. 2015.

[35] G. Eyal, M. B. Verhoog, G. Testa-Silva, Y. Deitcher, R. Benavides-Piccione, J. DeFelipe, C. P. J. de Kock, H. D. Mansvelder, and I. Segev, "Human Cortical Pyramidal Neurons: From Spines to Spikes via Models," *Frontiers in Cellular Neuroscience*, vol. 12, June 2018.

[36] K. J. Stratford, K. Tarczy-Hornoch, K. A. C. Martin, N. J. Bannister, and J. J. B. Jack, "Excitatory synaptic inputs to spiny stellate cells in cat visual cortex," *Nature*, vol. 382, pp. 258–261, July 1996.

[37] H. C. Tuckwell, "Time-dependent cable theory for nerve cylinders and dendritic trees," in *Introduction to theoretical neurobiology: volume 1, linear cable theory and dendritic structure*, ch. 2, pp. 33–84, Cambridge University Press, 1988.

[38] D. Johnston and S. M.-S. Wu, "Foundations of cellular neurophysiology," ch. 2, pp. 9–38, MIT press, 1994.

[39] D. E. Goldman, "Potential, impedance, and rectification in membranes," *The Journal of general physiology*, vol. 27, no. 1, pp. 37–60, 1943.

[40] A. L. Hodgkin and B. Katz, "The effect of sodium ions on the electrical activity of the giant axon of the squid," *The Journal of physiology*, vol. 108, no. 1, pp. 37–77, 1949.

[41] W. Hu and B. P. Bean, "Differential Control of Axonal and Somatic Resting Potential by Voltage-Dependent Conductances in Cortical Layer 5 Pyramidal Neurons," *Neuron*, vol. 97, pp. 1315–1326.e3, Mar. 2018.

[42] L. Beaulieu-Laroche, E. H. Toloza, M.-S. van der Goes, M. Lafourcade, D. Barnagian, Z. M. Williams, E. N. Eskandar, M. P. Frosch, S. S. Cash, and M. T.

Harnett, "Enhanced Dendritic Compartmentalization in Human Cortical Neurons," *Cell*, vol. 175, pp. 643–651.e14, Oct. 2018.

[43] W. F. Pickard, "A contribution to the electromagnetic theory of the unmyelinated axon," *Mathematical Biosciences*, vol. 2, pp. 111–121, Jan. 1968.

[44] W. Rall, "Core conductor theory and cable properties of neurons," *Comprehensive Physiology*, pp. 39–97, 2011.

[45] W. Rall, "Theory of Physiological Properties of Dendrites," *Annals of the New York Academy of Sciences*, vol. 96, no. 4, pp. 1071–1092, 1962.

[46] J. J. B. Jack, D. Noble, and R. W. Tsien, "Mathematical models of the nerve cell," in *Electric current flow in excitable cells*, ch. 7, pp. 131–224, Clarendon Press Oxford, 1975.

[47] R. R. Poznanski, "A generalized tapering equivalent cable model for dendritic neurons," *Bulletin of Mathematical Biology*, vol. 53, no. 3, pp. 457–467, 1991.

[48] A. D. Bird and H. Cuntz, "Optimal Current Transfer in Dendrites," *PLOS Computational Biology*, vol. 12, p. e1004897, May 2016.

[49] N. S. Koshlyakov, M. M. Smirnov, and E. B. Gilner in *Differential Equations of Mathematical Physics*, ch. 5, pp. 70–79, Interscience, New York, 1964.

[50] A. L. Hodgkin and A. F. Huxley, "A quantitative description of membrane current and its application to conduction and excitation in nerve," *The Journal of Physiology*, vol. 117, pp. 500–544, Aug. 1952.

[51] T. Berger, M. E. Larkum, and H.-R. Lscher, "High I_{h} Channel Density in the Distal Apical Dendrite of Layer V Pyramidal Cells Increases Bidirectional Attenuation of EPSPs," *Journal of Neurophysiology*, vol. 85, pp. 855–868, Feb. 2001.

[52] R. B. Robinson and S. A. Siegelbaum, "Hyperpolarization-Activated Cation Currents: From Molecules to Physiological Function," *Annual Review of Physiology*, vol. 65, pp. 453–480, Mar. 2003.

[53] M. H. P. Kole, S. Hallermann, and G. J. Stuart, "Single I h Channels in Pyramidal Neuron Dendrites : Properties , Distribution , and Impact on Action Potential Output," *Journal of Neuroscience*, vol. 26, no. 6, pp. 1677–1687, 2006.

[54] N. P. Poolos, M. Migliore, and D. Johnston, "Pharmacological upregulation of h-channels reduces the excitability of pyramidal neuron dendrites," *Nature neuroscience*, vol. 5, no. 8, pp. 767–774, 2002.

[55] J. C. DiFrancesco and D. DiFrancesco, "Dysfunctional HCN ion channels in neurological diseases," *Frontiers in Cellular Neuroscience*, vol. 6, Mar. 2015.

[56] J. Lehnhoff, U. Strauss, S. Wierschke, S. Grosser, E. Pollali, U. C. Schneider, M. Holtkamp, C. Dehnicke, and R. A. Deisz, "The anticonvulsant lamotrigine enhances Ih in layer 2/3 neocortical pyramidal neurons of patients with pharmacoresistant epilepsy," *Neuropharmacology*, vol. 144, pp. 58–69, Jan. 2019.

[57] J. C. Magee, "Dendritic Hyperpolarization-Activated Currents Modify the Integrative Properties of Hippocampal CA1 Pyramidal Neurons," *The Journal of Neuroscience*, vol. 18, pp. 7613–7624, Oct. 1998.

[58] S. R. Williams and G. J. Stuart, "Site Independence of EPSP Time Course Is Mediated by Dendritic I_{h} in Neocortical Pyramidal Neurons," *Journal of Neurophysiology*, vol. 83, pp. 3177–3182, May 2000.

[59] K. Angelo, M. London, S. R. Christensen, and M. Häusser, "Local and Global Effects of Ih Distribution in Dendrites of Mammalian Neurons," *Journal of Neuroscience*, vol. 27, pp. 8643–8653, Aug. 2007.

[60] F. G. Pike, R. S. Goddard, J. M. Suckling, P. Ganter, N. Kasthuri, and O. Paulsen, "Distinct frequency preferences of different types of rat hippocampal neurones in response to oscillatory input currents," *The Journal of Physiology*, vol. 529, pp. 205–213, Nov. 2000.

[61] H. Hu, K. Vervaeke, and J. F. Storm, "Two forms of electrical resonance at theta frequencies , generated by M-current , h-current and persistent Na^+ current in rat hippocampal pyramidal cells," pp. 783–805, 2002.

[62] D. Ulrich, "Dendritic Resonance in Rat Neocortical Pyramidal Cells," *Journal of Neurophysiology*, vol. 87, no. 6, pp. 2753–2759, 2002.

[63] F. Aspart, M. W. H. Remme, and K. Obermayer, "Differential polarization of cortical pyramidal neuron dendrites through weak extracellular fields," *PLOS Computational Biology*, vol. 14, p. e1006124, May 2018.

[64] W. J. Spain, P. C. Schwindt, and W. E. Crill, "Anomalous rectification in neurons from cat sensorimotor cortex in vitro," *Journal of Neurophysiology*, vol. 57, pp. 1555–1576, May 1987.

[65] C. Koch, "Cable theory in neurons with active, linearized membranes," *Biological Cybernetics*, vol. 50, no. 1, pp. 15–33, 1984.

[66] T. V. Ness, M. W. Remme, and G. T. Einevoll, "Active subthreshold dendritic conductances shape the local field potential," *The Journal of physiology*, vol. 594, no. 13, pp. 3809–3825, 2016.

[67] Y. Gutfreund, Y. Yarom, and I. Segev, "Subthreshold oscillations and resonant frequency in guinea-pig cortical neurons: physiology and modelling.," *The Journal of Physiology*, vol. 483, pp. 621–640, Mar. 1995.

[68] N. Agrawal, B. Hamam, J. Magistretti, A. Alonso, and D. Ragsdale, "Persistent sodium channel activity mediates subthreshold membrane potential oscillations and low-threshold spikes in rat entorhinal cortex layer V neurons," *Neuroscience*, vol. 102, pp. 53–64, Jan. 2001.

[69] H. Markram and B. Sakmann, "Calcium transients in dendrites of neocortical neurons evoked by single subthreshold excitatory postsynaptic potentials via low-voltage-activated calcium channels.," *Proceedings of the National Academy of Sciences*, vol. 91, pp. 5207–5211, May 1994.

[70] J. Schiller, Y. Schiller, G. Stuart, and B. Sakmann, "Calcium action potentials restricted to distal apical dendrites of rat neocortical pyramidal neurons," *The Journal of Physiology*, vol. 505, pp. 605–616, Dec. 1997.

[71] F. Helmchen, K. Svoboda, W. Denk, and D. W. Tank, "In vivo dendritic calcium dynamics in deep-layer cortical pyramidal neurons," *Nature Neuroscience*, vol. 2, pp. 989–996, Nov. 1999.

[72] M. E. Larkum, J. J. Zhu, and B. Sakmann, "A new cellular mechanism for coupling inputs arriving at different cortical layers," *Nature*, vol. 398, no. 6725, pp. 338–341, 1999.

[73] D. Johnston and S. M.-S. Wu, "Foundations of cellular neurophysiology," ch. 11, pp. 287–322, MIT press, 1994.

[74] `https://commons.wikimedia.org/wiki/File:Synapse_Illustration2_tweaked.svg`.

[75] W. R. Softky and C. Koch, "The highly irregular firing of cortical cells is inconsistent with temporal integration of random EPSPs," *The Journal of Neuroscience*, vol. 13, pp. 334–350, Jan. 1993.

[76] G. R. Holt, W. R. Softky, C. Koch, and R. J. Douglas, "Comparison of discharge variability in vitro and in vivo in cat visual cortex neurons," *Journal of neurophysiology*, vol. 75, no. 5, pp. 1806–1814, 1996.

[77] A. Manwani and C. Koch, "Detecting and Estimating Signals in Noisy Cable Structures, I: Neuronal Noise Sources," *Neural Computation*, vol. 11, no. 8, pp. 1797–1829, 1999.

[78] A. A. Faisal, L. P. J. Selen, and D. M. Wolpert, "Noise in the nervous system.," *Nature Reviews Neuroscience*, vol. 9, pp. 292–303, 2008.

[79] F. Ventriglia and V. Di Maio, "Stochastic fluctuations of the synaptic function," *Biosystems*, vol. 67, pp. 287–294, Oct. 2002.

[80] M. Häusser and A. Roth, "Estimating the Time Course of the Excitatory Synaptic Conductance in Neocortical Pyramidal Cells Using a Novel Voltage Jump Method," *The Journal of Neuroscience*, vol. 17, pp. 7606–7625, Oct. 1997.

[81] M. N. Shadlen and W. T. Newsome, "The Variable Discharge of Cortical Neurons: Implications for Connectivity, Computation, and Information Coding," *The Journal of Neuroscience*, vol. 18, pp. 3870–3896, May 1998.

[82] A. Compte, C. Constantinidis, J. Tegnr, S. Raghavachari, M. V. Chafee, P. S. Goldman-Rakic, and X.-J. Wang, "Temporally Irregular Mnemonic Persistent Activity in Prefrontal Neurons of Monkeys During a Delayed Response Task," *Journal of Neurophysiology*, vol. 90, pp. 3441–3454, Nov. 2003.

[83] W. Gerstner and W. M. Kistler, "Spiking neuron models: Single neurons, populations, plasticity," ch. 5, Cambridge university press, 2002.

[84] M. J. E. Richardson and W. Gerstner, "Synaptic Shot Noise and Conductance Fluctuations Affect the Membrane Voltage with Equal Significance," *Neural computation*, vol. 947, pp. 923–947, 2005.

[85] H. Köndgen, C. Geisler, S. Fusi, X.-J. Wang, H.-R. Lüscher, and M. Giugliano, "The dynamical response properties of neocortical neurons to temporally modulated noisy inputs in vitro," *Cerebral cortex*, vol. 18, no. 9, pp. 2086–2097, 2008.

[86] V. Ilin, A. Malyshev, F. Wolf, and M. Volgushev, "Fast Computations in Cortical Ensembles Require Rapid Initiation of Action Potentials," *Journal of Neuroscience*, vol. 33, pp. 2281–2292, Feb. 2013.

[87] T. Tchumatchenko, A. Malyshev, F. Wolf, and M. Volgushev, "Ultrafast Population Encoding by Cortical Neurons," *Journal of Neuroscience*, vol. 31, no. 34, pp. 12171–12179, 2011.

[88] G. Testa-Silva, M. B. Verhoog, D. Linaro, C. P. J. de Kock, J. C. Baayen, R. M. Meredith, C. I. De Zeeuw, M. Giugliano, and H. D. Mansvelder, "High Bandwidth Synaptic Communication and Frequency Tracking in Human Neocortex," *PLoS Biology*, vol. 12, no. 11, p. e1002007, 2014.

[89] L. Bindman, T. Meyer, and C. Prince, "Comparison of the electrical properties of neocortical neurones in slices in vitro and in the anaesthetized rat," *Experimental Brain Research*, vol. 69, Feb. 1988.

[90] D. Paré, E. Shink, H. Gaudreau, A. Destexhe, and E. J. Lang, "Impact of Spontaneous Synaptic Activity on the Resting Properties of Cat Neocortical Pyramidal Neurons In Vivo," *Journal of Neurophysiology*, vol. 79, pp. 1450–1460, Mar. 1998.

[91] M. Häusser and B. A. Clark, "Tonic Synaptic Inhibition Modulates Neuronal Output Pattern and Spatiotemporal Synaptic Integration," *Neuron*, vol. 19, pp. 665–678, Sept. 1997.

[92] A. Destexhe and D. Paré, "Impact of Network Activity on the Integrative Properties of Neocortical Pyramidal Neurons In Vivo," *Journal of Neurophysiology*, vol. 81, pp. 1531–1547, Apr. 1999.

[93] W. R. Holmes and C. D. Woody, "Effects of uniform and non-uniform synaptic activation-distributions on the cable properties of modeled cortical pyramidal neurons," *Brain Research*, vol. 505, pp. 12–22, Dec. 1989.

[94] Q. Bernander and R. J. Douglas, "Synaptic background activity influences spatiotemporal integration in single pyramidal cells," *Proceedings of the National Academy of Sciences*, vol. 88, pp. 11569–11573, 1991.

[95] M. Rudolph and A. Destexhe, "A Fast-Conducting, Stochastic Integrative Mode for Neocortical Neurons *In Vivo*," *The Journal of Neuroscience*, vol. 23, pp. 2466–2476, Mar. 2003.

[96] M. J. E. Richardson, "Firing-rate response of linear and nonlinear integrate-and-fire neurons to modulated current-based and conductance-based synaptic drive," *Physical Review E - Statistical, Nonlinear, and Soft Matter Physics*, vol. 76, no. 2, pp. 1–15, 2007.

[97] L. M. Palmer and G. J. Stuart, "Site of action potential initiation in layer 5 pyramidal neurons," *Journal of Neuroscience*, vol. 26, no. 6, pp. 1854–1863, 2006.

[98] Y. Shu, A. Duque, Y. Yu, B. Haider, and D. A. McCormick, "Properties of action-potential initiation in neocortical pyramidal cells: evidence from whole cell axon recordings.," *Journal of Neurophysiology*, vol. 97, no. 1, pp. 746–60, 2007.

[99] Data with permission from Emily Hill.

[100] N. Brunel and P. E. Latham, "Firing Rate of the Noisy Quadratic Integrate-and-Fire Neuron," *Neural Computation*, vol. 15, pp. 2281–2306, Oct. 2003.

[101] N. Fourcaud-Trocmé, D. Hansel, C. Van Vreeswijk, and N. Brunel, "How spike generation mechanisms determine the neuronal response to fluctuating inputs," *Journal of Neuroscience*, vol. 23, no. 37, pp. 11628–11640, 2003.

[102] E. M. Izhikevich, "Resonate-and-fire neurons," *Neural Networks*, vol. 14, no. 6-7, pp. 883–894, 2001.

[103] S. Coombes, Y. Timofeeva, C. M. Svensson, G. J. Lord, K. Josić, S. J. Cox, and C. M. Colbert, "Branching dendrites with resonant membrane: a "sum-over-trips" approach," *Biological Cybernetics*, vol. 97, no. 2, pp. 137–149, 2007.

[104] L. Yihe and Y. Timofeeva, "Response functions for electrically coupled neuronal network: a method of local point matching and its applications," *Biological cybernetics*, vol. 110, no. 2-3, pp. 117–133, 2016.

[105] M. J. Richardson, N. Brunel, and V. Hakim, "From subthreshold to firing-rate resonance," *Journal of neurophysiology*, vol. 89, no. 5, pp. 2538–2554, 2003.

[106] T. Tchumatchenko and C. Clopath, "Oscillations emerging from noise-driven steady state in networks with electrical synapses and subthreshold resonance," *Nature communications*, vol. 5, 2014.

[107] M. Puelma Touzel and F. Wolf, "Complete Firing-Rate Response of Neurons with Complex Intrinsic Dynamics," *PLoS Computational Biology*, vol. 11, no. 12, pp. 1–43, 2015.

[108] J. A. Goldberg, C. A. Deister, and C. J. Wilson, "Response Properties and Synchronization of Rhythmically Firing Dendritic Neurons," *Journal of Neurophysiology*, vol. 97, pp. 208–219, Jan. 2007.

[109] Y. Timofeeva, "Travelling waves in a model of quasi-active dendrites with active spines," *Physica D: Nonlinear Phenomena*, vol. 239, no. 9, pp. 494–503, 2010.

[110] S. O. Rice, "Mathematical analysis of random noise Part III," *The Bell System Technical Journal*, vol. 24, no. 1, pp. 46–156, 1945.

[111] T. Tchumatchenko, A. Malyshev, T. Geisel, M. Volgushev, and F. Wolf, "Correlations and synchrony in threshold neuron models," *Physical Review Letters*, vol. 104, no. 5, p. 058102, 2010.

[112] E. Di Bernardino, J. León, and T. Tchumatchenko, "Cross-Correlations and Joint Gaussianity in Multivariate Level Crossing Models," *The Journal of Mathematical Neuroscience*, vol. 4, no. 1, p. 22, 2014.

[113] L. Yang and M.-S. Alouini, "Level crossing rate over multiple independent random processes: An extension of the applicability of the rice formula," *IEEE Transactions on Wireless Communications*, vol. 6, no. 12, 2007.

[114] A. Baxevani, K. Podgórski, and I. Rychlik, "Velocities for moving random surfaces," *Probabilistic Engineering Mechanics*, vol. 18, no. 3, pp. 251–271, 2003.

[115] F. Shahbazi, S. Sobhanian, M. R. R. Tabar, S. Khorram, G. Frootan, and H. Zahed, "Level crossing analysis of growing surfaces," *Journal of Physics A: Mathematical and General*, vol. 36, no. 10, p. 2517, 2003.

[116] N. Brunel and S. Sergi, "Firing frequency of leaky integrate-and-fire neurons with synaptic current dynamics," *Journal of Theoretical Biology*, vol. 195, no. 1, pp. 87–95, 1998.

[117] N. Brunel, F. S. Chance, N. Fourcaud, and L. F. Abbott, "Effects of synaptic noise and filtering on the frequency response of spiking neurons," *Physical Review Letters*, vol. 86, no. 10, pp. 2186–2189, 2001.

[118] A. K. Alijani and M. J. E. Richardson, "Rate response of neurons subject to fast or frozen noise: From stochastic and homogeneous to deterministic and heterogeneous populations," *Physical Review E*, vol. 84, July 2011.

[119] A. L. Barth and J. F. Poulet, "Experimental evidence for sparse firing in the neocortex," *Trends in Neurosciences*, vol. 35, pp. 345–355, June 2012.

[120] G. Buzsáki and K. Mizuseki, "The log-dynamic brain: how skewed distributions affect network operations," *Nature Reviews Neuroscience*, vol. 15, pp. 264–278, Apr. 2014.

[121] M. S. Grubb and J. Burrone, "Activity-dependent relocation of the axon initial segment fine-tunes neuronal excitability," *Nature*, vol. 465, pp. 1070–1074, June 2010.

[122] M. H. P. Kole and G. J. Stuart, "Signal Processing in the Axon Initial Segment," *Neuron*, vol. 73, no. 2, pp. 235–247, 2012.

[123] J. A. Perge, J. E. Niven, E. Mugnaini, V. Balasubramanian, and P. Sterling, "Why Do Axons Differ in Caliber?," *Journal of Neuroscience*, vol. 32, pp. 626–638, Jan. 2012.

[124] M. London, A. Roth, L. Beeren, M. Husser, and P. E. Latham, "Sensitivity to perturbations in vivo implies high noise and suggests rate coding in cortex," *Nature*, vol. 466, pp. 123–127, July 2010.

[125] H. C. Tuckwell and J. B. Walsh, "Random currents through nerve membranes - I. Uniform poisson or white noise current in one-dimensional cables," *Biological Cybernetics*, vol. 49, no. 2, pp. 99–110, 1983.

[126] G. Eyal, H. D. Mansvelder, C. P. de Kock, and I. Segev, "Dendrites impact the encoding capabilities of the axon," *Journal of Neuroscience*, vol. 34, no. 24, pp. 8063–8071, 2014.

[127] F. Aspart, J. Ladenbauer, and K. Obermayer, "Extending integrate-and-fire model neurons to account for the effects of weak electric fields and input filtering mediated by the dendrite," *PLOS Computational Biology*, vol. 12, pp. 1–29, 11 2016.

[128] H. Cuntz, A. D. Bird, M. Beining, M. Schneider, L. Mediavilla, F. Z. Hoffmann, T. Deller, and P. Jedlicka, "A general principle of dendritic constancy a neurons size and shape invariant excitability," *bioRxiv*, Oct. 2019.

[129] W. Rall, "Branching dendritic trees and motoneuron membrane resistivity," *Experimental Neurology*, vol. 1, no. 5, pp. 491–527, 1959.

[130] R. P. Gowers, Y. Timofeeva, and M. J. E. Richardson, "Low-rate firing limit for neurons with axon, soma and dendrites driven by spatially distributed stochastic synapses," *bioRxiv*, June 2019.

[131] G. Adomian, "Stochastic systems," ch. 2, pp. 64–72, Academic Press, 1983.

[132] J. T. Rubinstein, "Analytical theory for extracellular electrical stimulation of nerve with focal electrodes," *Biophysical Journal*, vol. 60, no. 3, pp. 538–555, 1991.

[133] J. P. Meeks and S. Mennerick, "Action Potential Initiation and Propagation in CA3 Pyramidal Axons," *Journal of Neurophysiology*, vol. 97, pp. 3460–3472, May 2007.

[134] D. Debanne, E. Campanac, A. Bialowas, and E. Carlier, "Axon Physiology," *Physiological Reviews*, vol. 91, pp. 555–602, 2011.

[135] Z. F. Mainen and T. J. Sejnowski, "Influence of dendritic structure on firing pattern in model neocortical neurons," *Nature*, vol. 382, no. July, pp. 1–4, 1996.

[136] M. Migliore, M. Ferrante, G. A. Ascoli, M. Ferrante, and G. A. A. Signal, "Signal Propagation in Oblique Dendrites of CA1 Pyramidal Cells," *Journal of Neurophysiology*, vol. 94, no. 6, pp. 4145–4155, 2005.

[137] L. F. Abbott, E. Farhi, and S. Gutmann, "The path integral for dendritic trees," *Biological Cybernetics*, vol. 66, no. 1, pp. 49–60, 1991.

[138] F. Höfflin, A. Jack, C. Riedel, J. Mack-Bucher, J. Roos, C. Corcelli, C. Schultz, P. Wahle, and M. Engelhardt, "Heterogeneity of the Axon Initial Segment in Interneurons and Pyramidal Cells of Rodent Visual Cortex," *Frontiers in Cellular Neuroscience*, vol. 11, Nov. 2017.

[139] A. van Ooyen, J. Duijnhouwer, M. W. H. Remme, and J. van Pelt, "The effect of dendritic topology ion firing patterns in model neurons," *Neurocomputing*, vol. 13, pp. 311–325, 2002.

[140] H. Cuntz, A. Borst, and I. Segev, "Optimization principles of dendritic structure," *Theoretical Biology and Medical Modelling*, vol. 4, pp. 1–8, 2007.

[141] D. Breuer, M. Timme, and R.-M. Memmesheimer, "Statistical physics of neural systems with nonadditive dendritic coupling," *Physical Review X*, vol. 4, no. 1, p. 011053, 2014.

[142] S. Jarvis, K. Nikolic, and S. R. Schultz, "Neuronal gain modulability is determined by dendritic morphology: A computational optogenetic study," *PLOS Computational Biology*, vol. 14, no. 3, p. e1006027, 2018.

[143] G. Buzsáki, "Neuronal Oscillations in Cortical Networks," *Science*, vol. 304, pp. 1926–1929, June 2004.

[144] X.-J. Wang, "Neurophysiological and Computational Principles of Cortical Rhythms in Cognition," *Physiological Reviews*, vol. 90, pp. 1195–1268, July 2010.

[145] F. Amzica and M. Steriade, "Short- and long-range neuronal synchronization of the slow (< 1 Hz) cortical oscillation," *Journal of Neurophysiology*, vol. 73, pp. 20–38, Jan. 1995.

[146] S. Ray, N. E. Crone, E. Niebur, P. J. Franaszczuk, and S. S. Hsiao, "Neural Correlates of High-Gamma Oscillations (60-200 Hz) in Macaque Local Field Potentials and Their Potential Implications in Electrocorticography," *Journal of Neuroscience*, vol. 28, pp. 11526–11536, Nov. 2008.

[147] L.-E. Martinet, G. Fiddyment, J. R. Madsen, E. N. Eskandar, W. Truccolo, U. T. Eden, S. S. Cash, and M. A. Kramer, "Human seizures couple across spatial scales through travelling wave dynamics," *Nature Communications*, vol. 8, p. 14896, Apr. 2017.

[148] C. Boucsein, T. Tetzlaff, R. Meier, A. Aertsen, and B. Naundorf, "Dynamical response properties of neocortical neuron ensembles: multiplicative versus additive noise," *Journal of Neuroscience*, vol. 29, no. 4, pp. 1006–1010, 2009.

[149] J. Doose, G. Doron, M. Brecht, and B. Lindner, "Noisy Juxtacellular Stimulation In Vivo Leads to Reliable Spiking and Reveals High-Frequency Coding in Single Neurons," *Journal of Neuroscience*, vol. 36, pp. 11120–11132, Oct. 2016.

[150] G. Silberberg, M. Bethge, H. Markram, K. Pawelzik, and M. Tsodyks, "Dynamics of Population Rate Codes in Ensembles of Neocortical Neurons," *Journal of Neurophysiology*, vol. 91, pp. 704–709, Feb. 2004.

[151] T. Tchumatchenko and F. Wolf, "Representation of dynamical stimuli in populations of threshold neurons," *PLoS Computational Biology*, vol. 7, no. 10, 2011.

[152] D. Linaro, I. Biró, and M. Giugliano, "Dynamical response properties of neocortical neurons to conductance-driven time-varying inputs," *European Journal of Neuroscience*, vol. 47, no. 1, pp. 17–32, 2018.

[153] W. Wei and F. Wolf, "Spike onset dynamics and response speed in neuronal populations," *Physical Review Letters*, vol. 106, no. 8, pp. 1–4, 2011.

[154] J. Pressley and T. W. Troyer, "The Dynamics of Integrate-and-Fire: Mean Versus Variance Modulations and Dependence on Baseline Parameters," *Neural Computation*, vol. 23, pp. 1234–1247, May 2011.

[155] R. T. Canolty, E. Edwards, S. S. Dalal, M. Soltani, S. S. Nagarajan, H. E. Kirsch, M. S. Berger, N. M. Barbaro, and R. T. Knight, "High Gamma Power Is Phase-Locked to Theta Oscillations in Human Neocortex," *Science*, vol. 313, pp. 1626–1628, 2006.

[156] J. Lisman and G. Buzsáki, "A Neural Coding Scheme Formed by the Combined Function of Gamma and Theta Oscillations," *Schizophrenia Bulletin*, vol. 34, pp. 974–980, July 2008.

[157] B. Hutcheon, R. M. Miura, and E. Puil, "Subthreshold membrane resonance in neocortical neurons," *Journal of Neurophysiology*, vol. 76, pp. 683–697, Aug. 1996.

[158] J. B. Bullis, T. D. Jones, and N. P. Poolos, "Reversed somatodendritic I_{h} gradient in a class of rat hippocampal neurons with pyramidal morphology: I_{h} in PLP neurons," *The Journal of Physiology*, vol. 579, pp. 431–443, Mar. 2007.

[159] Y. Deitcher, G. Eyal, L. Kanari, M. B. Verhoog, G. A. Atenekeng Kahou, H. D. Mansvelder, C. P. J. de Kock, and I. Segev, "Comprehensive Morpho-Electrotonic Analysis Shows 2 Distinct Classes of L2 and L3 Pyramidal Neurons in Human Temporal Cortex," *Cerebral Cortex*, vol. 27, pp. 5398–5414, Nov. 2017.

[160] J. Laudanski, B. Torben-Nielsen, I. Segev, and S. Shamma, "Spatially distributed dendritic resonance selectively filters synaptic input," *PLoS Comput Biol*, vol. 10, no. 8, p. e1003775, 2014.

[161] J. P. Roach, A. Pidde, E. Katz, J. Wu, N. Ognjanovski, S. J. Aton, and M. R. Zochowski, "Resonance with subthreshold oscillatory drive organizes activity and optimizes learning in neural networks," *Proceedings of the National Academy of Sciences*, vol. 115, pp. E3017–E3025, Mar. 2018.

[162] M. Lengyel, Z. Huhn, and P. Érdi, "Computational theories on the function of theta oscillations," *Biological Cybernetics*, vol. 92, pp. 393–408, June 2005.

[163] I. Alekseichuk, Z. Turi, G. A. deLara, A. Antal, and W. Paulus, "Spatial Working Memory in Humans Depends on Theta and High Gamma Synchronization in the Prefrontal Cortex," *Current Biology*, vol. 26, pp. 1513–1521, June 2016.

[164] R. A. J. van Elburg and A. van Ooyen, "Impact of Dendritic Size and Dendritic Topology on Burst Firing in Pyramidal Cells," *PLoS Computational Biology*, vol. 6, p. e1000781, May 2010.

[165] M. J. E. Richardson and R. Swarbrick, "Firing-rate response of a neuron receiving excitatory and inhibitory synaptic shot noise," *Physical Review Letters*, vol. 105, no. 17, pp. 1–4, 2010.

[166] H. Markram, J. Lübke, M. Frotscher, A. Roth, and B. Sakmann, "Physiology and anatomy of synaptic connections between thick tufted pyramidal neurones in the developing rat neocortex.," *The Journal of physiology*, vol. 500, no. 2, pp. 409–440, 1997.

[167] S. Song, P. J. Sjöström, M. Reigl, S. Nelson, and D. B. Chklovskii, "Highly nonrandom features of synaptic connectivity in local cortical circuits," *PLoS biology*, vol. 3, no. 3, p. e68, 2005.

[168] S. Lefort, C. Tomm, J.-C. F. Sarria, and C. C. Petersen, "The excitatory neuronal network of the c2 barrel column in mouse primary somatosensory cortex," *Neuron*, vol. 61, no. 2, pp. 301–316, 2009.

[169] F. Droste and B. Lindner, "Exact analytical results for integrate-and-fire neurons driven by excitatory shot noise," *Journal of computational neuroscience*, vol. 43, no. 1, pp. 81–91, 2017.

[170] M. J. E. Richardson, "Spike shape and synaptic-amplitude distribution interact to set the high-frequency firing-rate response of neuronal populations," *Physical Review E*, vol. 98, Oct. 2018.

[171] E. Daly and A. Porporato, "Effect of different jump distributions on the dynamics of jump processes," *Physical Review E*, vol. 81, no. 6, p. 061133, 2010.

[172] A. U. Larkman, "Dendritic morphology of pyramidal neurones of the visual cortex of the rat: I. Branching patterns," *The Journal of Comparative Neurology*, vol. 306, pp. 307–319, Apr. 1991.

[173] Y. Kubota, F. Karube, M. Nomura, A. T. Gulledge, A. Mochizuki, A. Schertel, and Y. Kawaguchi, "Conserved properties of dendritic trees in four cortical interneuron subtypes," *Scientific Reports*, vol. 1, Dec. 2011.

[174] M. Ferrante, M. Migliore, and G. A. Ascoli, "Functional Impact of Dendritic Branch-Point Morphology," *Journal of Neuroscience*, vol. 33, pp. 2156–2165, Jan. 2013.

[175] N. Brunel, "Dynamics of sparsely connected networks of excitatory and inhibitory spiking neurons," *Journal of computational neuroscience*, vol. 8, no. 3, pp. 183–208, 2000.

[176] S. Ostojic, "Two types of asynchronous activity in networks of excitatory and inhibitory spiking neurons," *Nature neuroscience*, vol. 17, no. 4, p. 594, 2014.

[177] M. Mattia, M. Biggio, A. Galluzzi, and M. Storace, "Dimensional reduction in networks of non-Markovian spiking neurons: Equivalence of synaptic filtering and heterogeneous propagation delays," *PLOS Computational Biology*, vol. 15, p. e1007404, Oct. 2019.

[178] G. Silberberg, A. Gupta, and H. Markram, "Stereotypy in neocortical microcircuits," *Trends in neurosciences*, vol. 25, no. 5, pp. 227–230, 2002.

[179] W.-C. A. Lee, V. Bonin, M. Reed, B. J. Graham, G. Hood, K. Glattfelder, and R. C. Reid, "Anatomy and function of an excitatory network in the visual cortex," *Nature*, vol. 532, no. 7599, p. 370, 2016.

[180] S. Haeusler, K. Schuch, and W. Maass, "Motif distribution, dynamical properties, and computational performance of two data-based cortical microcircuit templates," *Journal of Physiology-Paris*, vol. 103, no. 1-2, pp. 73–87, 2009.

[181] P. M. Harrison, L. Badel, M. J. Wall, and M. J. Richardson, "Experimentally verified parameter sets for modelling heterogeneous neocortical pyramidal-cell populations," *PLoS Comput Biol*, vol. 11, no. 8, p. e1004165, 2015.

[182] Y. Zerlaut, B. Teleńczuk, C. Deleuze, T. Bal, G. Ouanounou, and A. Destexhe, "Heterogeneous firing rate response of mouse layer V pyramidal neurons in the fluctuation-driven regime," *Journal of Physiology*, vol. 594, no. 13, pp. 3791–3808, 2016.

[183] J. A. White, J. T. Rubinstein, and A. R. Kay, "Channel noise in neurons," *Trends in neurosciences*, vol. 23, no. 3, pp. 131–137, 2000.

[184] C. C. Chow and J. A. White, "Spontaneous action potentials due to channel fluctuations.," *Biophysical journal*, vol. 71, no. 6, p. 3013, 1996.

[185] M. Van Rossum, B. J. O'Brien, and R. G. Smith, "Effects of noise on the spike timing precision of retinal ganglion cells," *Journal of neurophysiology*, vol. 89, no. 5, pp. 2406–2419, 2003.

[186] J. H. Goldwyn and E. Shea-Brown, "The what and where of adding channel noise to the hodgkin-huxley equations," *PLoS computational biology*, vol. 7, no. 11, 2011.

[187] D. Linaro, M. Storace, and M. Giugliano, "Accurate and fast simulation of channel noise in conductance-based model neurons by diffusion approximation," *PLoS computational biology*, vol. 7, no. 3, 2011.

[188] R. C. Cannon, C. O'Donnell, and M. F. Nolan, "Stochastic ion channel gating in dendritic neurons: morphology dependence and probabilistic synaptic activation of dendritic spikes," *PLoS computational biology*, vol. 6, no. 8, 2010.

[189] C. ODonnell and M. C. van Rossum, "Spontaneous action potentials and neural coding in unmyelinated axons," *Neural computation*, vol. 27, no. 4, pp. 801–818, 2015.

[190] Y. Timofeeva, G. J. Lord, and S. Coombes, "Dendritic cable with active spines: A modelling study in the spike-diffuse-spike framework," *Neurocomputing*, vol. 69, pp. 1058–1061, 2006.

[191] H. C. Tuckwell, "Nonlinear effects in white-noise driven spatial diffusion: General analytical results and probabilities of exceeding threshold," *Physica A: Statistical Mechanics and its Applications*, vol. 387, no. 7, pp. 1455–1463, 2008.

[192] T. Górski, R. Veltz, M. Galtier, H. Fragnaud, J. S. Goldman, B. Teleńczuk, and A. Destexhe, "Dendritic sodium spikes endow neurons with inverse firing rate response to correlated synaptic activity," *Journal of computational neuroscience*, vol. 45, no. 3, pp. 223–234, 2018.

[193] S. Goethals and R. Brette, "Theoretical relation between axon initial segment geometry and excitability," *BioRxiv*, p. 834671, 2019.

[194] A. M. Packer, B. Roska, and M. Häusser, "Targeting neurons and photons for optogenetics," *Nature Neuroscience*, vol. 16, no. 7, p. 805, 2013.

[195] A. Malyshev, R. Goz, J. J. LoTurco, and M. Volgushev, "Advantages and limitations of the use of optogenetic approach in studying fast-scale spike encoding," *PLOS One*, vol. 10, no. 4, p. e0122286, 2015.

[196] L. Ferrarese, J.-S. Jouhanneau, M. W. Remme, J. Kremkow, G. Katona, B. Rózsa, S. Schreiber, and J. F. Poulet, "Dendrite-Specific Amplification of Weak Synaptic Input during Network Activity In Vivo," *Cell Reports*, vol. 24, pp. 3455–3465.e5, Sept. 2018.

[197] L. Tiroshi and J. A. Goldberg, "Population dynamics and entrainment of basal ganglia pacemakers are shaped by their dendritic arbors," *PLOS Computational Biology*, vol. 15, no. 2, p. e1006782, 2019.

[198] P. C. Bressloff, V. M. Dwyer, and M. J. Kearney, "A 'sum-over-paths' approach to diffusion on trees," *Journal of Physics A: Mathematical and General*, vol. 29, no. 9, p. 1881, 1996.

[199] Y. Timofeeva and S. Coombes, "Response of gap junction-coupled dendrites: A sum-over-trips approach," in *The Computing Dendrite*, pp. 449–464, Springer, 2014.

[200] I. S. Gradshteyn and I. M. Ryzhik, *Table of integrals, series, and products*. Academic press, 2007.

[201] H. C. Tuckwell, "Spatial neuron model with two-parameter OrnsteinUhlenbeck input current," *Physica A: Statistical Mechanics and its Applications*, vol. 368, pp. 495–510, Aug. 2006.

[202] J. Evans, G. Kember, and G. Major, "Techniques for obtaining analytical solutions to the multicylinder somatic shunt cable model for passive neurones," *Biophysical Journal*, vol. 63, pp. 350–365, Aug. 1992.

[203] J. B. Walsh, "A stochastic model of neural response," *Advances in applied probability*, vol. 13, no. 2, pp. 231–281, 1981.